



**Tiago Gomes  
da Silveira**

**All-optical processing systems based  
on semiconductor optical amplifiers**





**Tiago Gomes  
da Silveira**

**All-optical processing systems based  
on semiconductor optical amplifiers**

Dissertação apresentada à Universidade de Aveiro para cumprimento dos requisitos necessários à obtenção do grau de Doutor em Engenharia Electrotécnica, realizada sob a orientação científica do Doutor António Luís Jesus Teixeira, Professor Associado do Departamento de Electrónica, Telecomunicações e Informática da Universidade de Aveiro e do Doutor Paulo Miguel Nepomuceno Pereira Monteiro, Professor Associado do Departamento de Electrónica, Telecomunicações e Informática da Universidade de Aveiro.

Apoio financeiro do POCTI no âmbito  
do III Quadro Comunitário de Apoio.

Apoio financeiro da FCT e do FSE no  
âmbito do III Quadro Comunitário de  
Apoio.





Para os meus pais,  
Orlando e Helena.



## **o júri**

presidente

**Prof. Doutor Luís Castro**  
professor catedrático na Universidade de Aveiro

**Prof. Doutor Henrique José Almeida da Silva**  
professor associado na Universidade de Coimbra

**Prof. Doutora Maria Carmo Raposo de Medeiros**  
Professora associada na Universidade do Algarve

**Doutor Giorgio Maria Tosi-Beleffi**  
Investigador no Ministério Italiano de Desenvolvimento Económico

**Prof. Doutor Paulo Miguel Nepomuceno Monteiro**  
professor associado na Universidade de Aveiro

**Prof. Doutor António Luís Jesus Teixeira**  
professor associado na Universidade de Aveiro



**agradecimentos** Agradeço ao meu orientador, Doutor António Teixeira pelo permanente entusiasmo, por me fazer acreditar que “o Tiago resolve” e por me abrir as portas do mundo; ao meu co-orientador, Doutor Paulo Monteiro por me ter trazido para as telecomunicações e por acreditar em mim, mesmo quando ainda era um “imberbe” aluno de licenciatura.

Ao Daniel Fonseca agradeço o doloroso pragmatismo, a imensa paciência na revisão de artigos e as frutíferas discussões sobre tantas ideias. Ao Ruben Luís estou grato por ter sido um elemento chave no meu crescimento como cientista e como engenheiro. Ao Rui Morais e ao Rui Meleiro agradeço o companheirismo e a colaboração no laboratório. Agradeço à Ni Yan pela frutífera colaboração e por mostrar que até na ciência há um lado colorido. Ao Doutor Giorgio Tosi-Beleffi e ao Davide Forin agradeço pelo empréstimo de material experimental e pelas discussões, essenciais à realização de alguns dos testes experimentais. Ao Doutor Naoya Wada e à sua equipa estou grato por me terem aberto a porta do seu laboratório e por me terem feito sentir em casa a dez mil quilómetros de distância. Agradeço ao Mestre João Prata pela ajuda no laboratório, especialmente durante a realização do protótipo VSB.

Agradeço ao Instituto de Telecomunicações de Aveiro e à Nokia Siemens Networks por me terem acolhido e por terem possibilitado este trabalho.

Ao Álvaro Carvalho agradeço porque não me deixou desistir desta tese, por me facilitar a gestão de tempo e sobretudo me ter ajudado a descobrir a minha verdadeira vocação.

Ao meu tio e amigo, Paulo Silveira, agradeço pela inspiração, por ter levantado a fasquia e por há quinze anos atrás me ter emprestado uma caixa cheia de cassetes, que foi a semente para a banda sonora desta tese e da minha vida.

À Ana agradeço o apoio e discussão nos primeiros trabalhos experimentais; a revisão da tese; a companhia em tantas vésperas de conferências, enquanto ensaiava as apresentações; a motivação e o sacrifício durante os meses finais de escrita em que eu “não levantava uma palha”; por me fazer ser maior do que sou; e sobretudo por dar sentido e alegria a cada um dos meus dias.

Aos meus amigos de sempre e à minha família, agradecerei pessoalmente.

Porque não sei de palavras para agradecer aos meus pais o sacrifício, apoio, inspiração e amizade, lhes dedico esta tese.



## palavras-chave

Amplificador óptico de semiconductor (SOA), modulação cruzada de ganho, modulação cruzada de fase, processamento óptico, interferômetro de Mach Zehnder com SOA, modulação óptica de banda lateral residual, conversão de formato de impulso, regeneração, conversão de formato de modulação, multiplexagem por divisão no comprimento de onda

## resumo

Nesta tese investigam-se e desenvolvem-se dispositivos para processamento integralmente óptico em redes com multiplexagem densa por divisão no comprimento de onda (DWDM). O principal objectivo das redes DWDM é transportar e distribuir um espectro óptico densamente multiplexado com sinais de débito binário ultra elevado, ao longo de centenas ou milhares de quilómetros de fibra óptica. Estes sinais devem ser transportados e encaminhados no domínio óptico de forma transparente, sem conversões óptico-eléctrico-ópticas (OEO), evitando as suas limitações e custos. A tecnologia baseada em amplificadores ópticos de semiconductor (SOA) é promissora graças aos seus efeitos não-lineares ultra-rápidos e eficientes, ao potencial para integração, reduzido consumo de potência e custos.

Conversores de comprimento de onda são o elemento óptico básico para aumentar a capacidade da rede e evitar o bloqueio de comprimentos de onda. Neste trabalho, são estudados e analisados experimentalmente métodos para aumentar a largura de banda operacional de conversores de modulação cruzada de ganho (XGM), a fim de permitir a operação do SOA para além das suas limitações físicas. Conversão de um comprimento de onda, e conversão simultânea de múltiplos comprimentos de onda são testadas, usando interferómetros de Mach-Zehnder com SOA.

As redes DWDM de alto débito binário requerem formatos de modulação optimizados, com elevada tolerância aos efeitos nefastos da fibra, e reduzida ocupação espectral. Para esse efeito, é vital desenvolver conversores integralmente ópticos de formatos de modulação, a fim de permitir a interligação entre as redes já instaladas, que operam com modulação de intensidade, e as redes modernas, que utilizam formatos de modulação avançados. No âmbito deste trabalho é proposto um conversor integralmente óptico de formato entre modulação óptica de banda lateral dupla e modulação óptica de banda lateral residual; este é caracterizado através de simulação e experimentalmente. Adicionalmente, é proposto um conversor para formato de portadora suprimida, através de XGM e modulação cruzada de fase.

A interligação entre as redes de transporte com débito binário ultra-elevado e as redes de acesso com débito binário reduzido requer conversão óptica de formato de impulso entre retorno-a-zero (RZ) e não-RZ. São aqui propostas e investigadas duas estruturas distintas: uma baseada em filtragem desalinhada do sinal convertido por XGM; uma segunda utiliza as dinâmicas do laser interno de um SOA com ganho limitado (GC-SOA).

Regeneração integralmente óptica é essencial para reduzir os custos das redes. Dois esquemas distintos são utilizados para regeneração: uma estrutura baseada em MZI-SOA, e um método no qual o laser interno de um GC-SOA é modulado com o sinal distorcido a regenerar.

A maioria dos esquemas referidos é testada experimentalmente a 40 Gb/s, com potencial para aplicação a débitos binários superiores, demonstrado que os SOA são uma tecnologia basilar para as redes ópticas do futuro.





## keywords

Semiconductor optical amplifiers (SOA), cross-gain modulation (XGM), cross-phase modulation (XPM), all-optical processing, Mach-Zehnder interferometer with SOA (MZI-SOA), optical vestigial sideband (OVSB), pulse format conversion, modulation format conversion, regeneration, wavelength division multiplexing (WDM), optical time division multiplexing (OTDM).

## abstract

This thesis investigates and develops all-optical processing devices for wavelength division multiplexing networks (WDM) of the future. The ultimate goal of optical networks is to transport and deliver a densely multiplexed spectrum, populated by ultra-high bit rate signals over hundreds or thousands of kilometers of optical fiber. Such signals should be transported and routed transparently in the optical domain, without recurring to optic-electro-optic (OEO) conversions, avoiding its limitations and costs. Semiconductor optical amplifier (SOA) based technology is a promising building block due to its inherent ultra-fast and efficient non-linear effects, potential for integration, low power consumption and cost.

Wavelength converters are the basic optical functionality to increase the network throughput and avoid wavelength blocking. Methods to increase the operation bandwidth of cross-gain modulation (XGM) converters are studied and experimentally assessed to enable operation beyond the physical constraints of SOA. Single and multi-wavelength conversion exploiting cross-phase modulation (XPM) in Mach-Zehnder interferometer with semiconductor optical amplifiers (MZI-SOA) is tested.

High bit rate DWDM networks require optimized modulation formats with enhanced tolerance to fiber impairments and reduced spectral tolerance. As a consequence, it is crucial to develop all-optical modulation formats between legacy on-off-keying networks and networks employing advanced modulation formats. An all-optical format converter between optical double sideband (ODSB) and optical vestigial sideband (OVSB) based on SOA self-phase modulation is proposed and thoroughly characterized by simulations and experimental tests. A converter, which uses a mix of XGM and XPM to allow simultaneous pulse and modulation format conversion to the carrier suppressed format, is proposed.

The interface between ultra-high bit rate transport networks and lower bit rate access networks requires optical pulse format conversions between return-to-zero (RZ) and non-return-to-zero (NRZ). Two different structures are proposed and investigated. The first is based on detuned filtering of XPM converted signal; while the second uses the dynamics of the internal laser of a gain-clamped SOA.

All-optical regeneration is one of the most sought functionalities to reduce network costs. Regeneration is achieved in this work through two simple setups: a MZI-SOA based structure, and a method in which the internal laser from a GC-SOA is modulated with the input distorted signal.

Most applications are experimentally validated at 40 Gb/s, with potential for even higher bit rates, demonstrating that SOA can be one of the key elements for the next generation of optical networks.



# Index

Index .....	1
List of acronyms and abbreviations .....	5
List of symbols .....	11
Chapter 1 Introduction .....	15
1.1 Context .....	15
1.2 Motivation .....	16
1.3 Thesis objectives and outline .....	18
1.4 Main contributions .....	20
Chapter 2 Semiconductor optical amplifiers .....	23
2.1 Motivation .....	23
2.2 Historical development .....	23
2.3 Principle of SOA operation .....	24
2.4 Design of SOA .....	25
2.4.1 Materials and structures for the active layer .....	27
2.4.2 Semiconductor optical amplifiers with specific design .....	28
Reflective semiconductor optical amplifier (R-SOA) .....	28
Multi-electrode semiconductor optical amplifier (ME-SOA) .....	29
2.5 Gain and phase dynamics in SOA .....	29
2.6 Modelling of signal amplification in SOA .....	32
2.6.1 Gain dynamics .....	34
2.6.1.1 Inter-band processes .....	35
2.6.1.2 Intra-band processes .....	36
2.6.2 Phase dynamics .....	37
2.7 SOA simulation tool .....	38
2.8 Gain-clamped semiconductor optical amplifiers .....	40
2.9 Applications of SOA .....	42
Linear Amplifier .....	43
Optical modulator and detector .....	44
Wavelength Conversion .....	44
Logic gates .....	45
Multiplexing and add-drop multiplexing .....	46
Clock Recovery and Regeneration .....	46
Pulse and modulation format conversion .....	47

Other applications .....	47
2.10 Summary .....	47
Chapter 3 Wavelength Conversion .....	49
3.1 Motivation .....	49
3.2 Wavelength conversion techniques with SOA .....	52
3.2.1 Cross gain modulation .....	52
3.2.2 Cross phase modulation .....	53
3.2.2.1 Filter assisted XPM wavelength conversion .....	54
3.2.2.2 XPM converters with standard-mode interferometric structures .....	56
Mach-Zehnder interferometer with SOA (MZI-SOA) .....	56
Michelson interferometer with SOA (MI-SOA) .....	57
3.2.2.3 XPM converters with differential-mode interferometric structures .....	58
Differential mode MZI-SOA .....	59
Semiconductor Laser in a Loop Mirror .....	60
Delayed-Interference Signal Converter .....	61
Comparison with fiber based interferometer structures .....	62
3.2.2.4 Gain Transparent Operation .....	63
3.2.3 Four-wave mixing .....	63
3.2.4 Cross-Polarization Rotation .....	65
3.3 Enhancement of cross gain modulation bandwidth .....	66
3.3.1 Decrease of the SOA effective carrier lifetime .....	66
3.3.2 XGM bandwidth enhancement by detuned filtering .....	69
3.3.2.1 Operation principle .....	69
3.3.2.2 Simulation tests and filter optimization .....	71
10 Gb/s results .....	71
40 Gb/s results .....	77
3.3.2.3 Experimental validation .....	78
10 Gb/s results .....	79
20 Gb/s results .....	80
40Gb/s results .....	81
3.4 Filter assisted wavelength conversion in GC-SOA .....	82
3.5 Experimental characterization of MZI-SOA based wavelength converter .....	88
Static characterization .....	89
Standard mode characterization .....	91
Differential mode characterization .....	93
Comparison between standard and differential modes .....	94
3.6 Multi wavelength conversion .....	95
3.6.1 Experimental results .....	96
3.7 Summary .....	102
Chapter 4 Modulation format conversion .....	105
4.1 Motivation .....	105
4.2 Format modulation conversion from oDSB to oVSB .....	108
4.2.1 Introduction to optical sideband suppressed signals .....	108
4.2.1.1 Feasible oSSB and oVSB transmitters .....	109

Electro-optical SSB / VSB generation .....	109
All-optical SSB / VSB generation.....	110
4.2.1.2 Transmission of oSSB signals over dispersive fiber .....	110
4.2.1.3 Electrical dispersion compensation .....	111
4.2.2 All-optical generation of VSB signals with SOA.....	113
4.2.2.1 Impact of non-ideal phase modulation in sideband suppression .....	115
4.2.2.2 SOA based converter operation principle.....	117
4.2.3 Converter operation assessment .....	119
4.2.3.1 Results at 10 Gb/s .....	120
Tolerance to power variations of data signal and CW probe signal.....	121
Input signal extinction ratio.....	123
Input signal wavelength.....	124
Transmission tests .....	124
Electrical dispersion compensation after direct detection .....	126
4.2.3.2 Results at 40 Gb/s .....	130
Performance with slow SOA device.....	130
Back-to-back performance and sideband suppression with fast SOA device ....	132
Transmission results .....	133
4.3 On-off keying to CSRZ converter .....	136
4.3.1 Operation Principle.....	136
4.3.2 40 Gb/s simulation tests.....	140
4.3.2.1 CSRZ generation with SOA .....	140
4.3.2.2 Comparison with common transmitter .....	143
4.3.2.3 NRZ to CSRZ converter robustness to input signal variations .....	146
4.3.3 40 Gb/s single- and multi-channel experimental validation.....	149
4.4 Summary.....	153
Chapter 5 Pulse format conversions between RZ and NRZ .....	155
5.1 Motivation .....	155
5.2 RZ to NRZ converter with SOA and detuned filtering .....	157
5.2.1 Pulse format conversion based only on detuned filtering.....	157
5.2.1.1 Operation principle .....	157
5.2.1.2 Simulation results .....	159
5.2.2 Pulse format and wavelength conversion based on SOA and detuned filtering	165
5.2.2.1 Operation principle .....	166
5.2.2.2 Simulation tests and optimization .....	167
40 Gb/s conversion with fast SOA device.....	167
40 Gb/s conversion with slow SOA device.....	175
5.2.2.3 Experimental validation.....	177
40 Gb/s conversion with fast SOA device.....	177
10 Gb/s conversion with slow SOA device.....	184
5.3 RZ to NRZ pulse converter with GC-SOA .....	185
5.3.1 Operation principle .....	185
5.3.2 10 Gb/s experimental results .....	187
5.4 Summary.....	193

Chapter 6	Optical regeneration .....	195
6.1	Motivation.....	195
6.2	All-optical regeneration techniques in SOA.....	197
6.2.1	Non-linear gate .....	197
6.2.2	Clock recovery .....	201
6.3	2R Regeneration of OCDMA with MZI-SOA .....	202
6.3.1	Experimental Setup and Operation Principle .....	205
6.3.2	Experimental OCDMA Regeneration Results .....	206
6.4	2R Regenerator using a GC-SOA.....	209
6.4.1	Operation principle.....	209
6.4.2	Experimental regeneration of a distorted signal.....	211
6.5	Summary.....	215
Chapter 7	Conclusions.....	217
7.1	Summary and conclusions .....	217
7.2	Directions for future work .....	221
References	.....	223
Appendix I	Publications by the author.....	241
	List of work published in the scope of this thesis.....	241
	Patents.....	241
	Journals .....	241
	International peer-reviewed conferences .....	242
	Local conferences .....	244
	Other publications .....	244
	Journals .....	244
	International peer-reviewed conferences .....	245
	Local conferences .....	246
Appendix II	SOA devices used in this work.....	249
Appendix III	Performance assessment in simulations .....	253
Appendix IV	Optimization and development of a prototype to convert optical DSB to VSB .....	255
	10 Gb/s prototype.....	256
	Equipment characterization and optimization .....	257
	Laser characterization .....	257
	Photo-detector characterization.....	258
	CW power optimization .....	259
	Final prototype and results.....	260
	Back-to-back results.....	260
	VSB signal generation after transmission over fiber .....	263
	40 Gb/s prototype.....	265

# List of acronyms and abbreviations

<b>Notation</b>	<b>Description</b>
ADC	analog to digital converter
AMI	alternate mark inversion
AOWC	All optical wavelength converters / conversion
ARC	anti-reflection coating
ASE	amplified spontaneous emission noise
BER	bit error rate
BR	bit rate
BP	bit period
BW	bandwidth
CATV	cable television (originally community antenna television)
c.c.	complex conjugate
CC	carrier cooling
CD	chromatic dispersion
CDP	carrier density pulsation
CH	carrier heating
CLK	clock
CS	carrier suppressed
CSRZ	carrier suppressed return-to-zero modulation format
CW	continuous wave
DBR	distributed Bragg reflector

DC	direct current
DEMUX	demultiplexer
DFB	distributed feedback
DFP	dispersion flattened fiber
DH	double heterostructure
DISC	delayed-interference signal converter
DPSK	differential binary phase shift keying modulation format
DQPSK	differential quadrature phase shift keying modulation format
CP-QPSK	coherent-detected polarization-multiplexed quadrature phase shift keying modulation format
CSRZ	carrier-suppressed return-to-zero modulation format
DSB	double sideband
DWDM	dense wavelength division multiplexing
EDC	electrical dispersion compensation
EDFA	erbium doped fiber amplifier
EOP	eye opening penalty
ER	extinction ratio
FBG	fiber Bragg grating
FCA	free carrier absorption
FP	Fabry Perot
FPF	Fabry-Perot filter
FP-SOA	Fabry Perot semiconductor optical amplifier
FWHM	full-width at half maximum
FWM	four-wave mixing
GC-SOA	gain clamped semiconductor optical amplifier
GVD	group velocity dispersion



---

HNLF	highly non-linear fiber
IL	insertion loss
IM	intensity modulated
ISOL	isolator
MAI	multiple access interference
MEOP	modified eye opening penalty
ME-SOA	multi electrode semiconductor optical amplifier
MI-SOA	Michelson interferometer with semiconductor optical amplifier
MLLD	model locked laser diode
MQW	multi-quantum well
MWC	multi-channel wavelength conversion
MZ	Mach-Zehnder
MZI-SOA	Mach-Zehnder interferometer with semiconductor optical amplifiers
MZM	Mach-Zehnder Modulator
NF	noise figure
NOLM	non-linear optical loop mirror
NPS	Non-linear polarization switching
NRZ	non-return-to-zero
OCDMA	optical code division multiple access
ODC	optical dispersion compensation
oDSB	optical double sideband modulation format
OEO	optical-electro-optical
OEWC	optoelectronic wavelength conversion
OF	optical filter
OOK	on-off-keying
OBS	optical burst switching

OPS	optical packet switching
OSA	optical spectrum analyser
OSNR	optical signal to noise ratio
oSSB	optical single sideband modulation format
OTDM	optical time division multiplexing
oVSB	optical vestigial sideband modulation format
PBS	polarization beam splitter
PC	polarization controller
PD	photo-detector
PDL	polarization dependent loss
PIC	peripheral interface controller
PLC	planar lightwave circuit
PM	phase modulation; power monitor
PMD	polarization mode dispersion
PON	passive optical network
PPLN	periodically poled lithium niobate
PRBS	pseudo-random bit sequence
PS	phase shift
Q-factor	quality factor
QD-SOA	quantum-dot semiconductor optical amplifier
QW	quantum well
RC	raised cosine
RES	resolution
RF	radio frequency
RoF	radio over fiber
R-SOA	reflective semiconductor optical amplifier

---

RZ	return-to-zero
SCM	sub-carrier multiplexed
SGM	self gain modulation
SHB	spectral hole burning
SHG	second harmonic generation
SL	Semiconductor laser
SLA	semiconductor laser amplifiers
SLALOM	Sagnac interferometer with an asymmetrically placed semiconductor optical amplifier
SLED	Superluminescent Light Emitting Diodes
SLPM	spatial light phase modulator
SOA	Semiconductor optical amplifier
SPM	self-phase modulation
SSB	single sideband
SSFBG	super-structured fiber Bragg grating
SSMF	Standard single mode fiber
SSR	sideband suppression ratio
SWC	single-channel wavelength conversion
TDM	time division multiplexing
TE	transversal electric
TF	transfer function; transversal filter
TM	transversal magnetic
TOAD	terahertz optical asymmetric demultiplexer
TPA	two photon absorption
TW-SOA	traveling wave semiconductor optical amplifier
UOC	ultra-fast optical clock

VDL	variable delay line
VOA	variable optical attenuator
VODL	variable optical delay line
WC	wavelength converters / wavelength conversion
WDM	wavelength division multiplexing
XAM	cross-absorption modulation
XGM	cross gain modulation
XPM	cross phase modulation
XPR	cross polarization rotation
1R	regeneration: reamplification
2R	regeneration: reamplification and reshaping
3R	regeneration: reamplification, reshaping, and retiming
SC	single conversion
DC	dual conversion
QC	quadruple conversion
LAN	local area networks
QoS	quality of service

# List of symbols

Notation	Abbreviation
$\alpha_{\text{int}}$	absorption coefficient in SOA by the internal waveguide loss
$m(t)$	ac coupled electrical information signal
$L$	active layer length
$V$	active layer volume
$C_{\text{Auger}}$	Auger recombination coefficient
$S$	average photon density inside the active region
$I_j$	bias current of section j
$T_B$	Bit period
$N$	carrier density
$N_{\text{tr}}$	carrier density at transparency
$\tau_s$	carrier lifetime
$R_{\text{ASE}}$	carrier recombination stimulated by spontaneous emitted photons
$\epsilon_{\text{CH}}$	CH nonlinear gain compression factor
$\tau_{\text{CH}}$	CH relaxation time
c.c.	complex conjugate
$\sigma$	conductivity of the medium
$\Gamma$	confinement factor
*	convolution operator

---

$dg/dN$	differential gain coefficient
$D$	Dispersion parameter
$H_{fiber}$	Dispersive fiber transfer function
$\tau_{eff}$	effective carrier lifetime
$\bar{n}$	effective mode index
$E$	electrical field vector of the optical field
$\epsilon_0$	electrical permittivity of free space
$q$	electron charge
$N$	free carrier density in the conduction band or carrier density
$f$	frequency
$W$	full width at half maximum
$G$	Gain
$g_{CH}$	gain associated with CH
$g_{SHB}$	gain associated with SHB
$g_{TPA}$	gain associated with TPA
$g_T$	gain coefficient
$n_g$	Group index
$v_g$	group velocity
$m_H$	Hilbert transform of the information signal
$I$	injected current
$IL_{in}$	Input losses
$S_{in}$	input photon density
$\Phi_{in}$	(Input) signal phase

---

$\nabla^2$	Laplacian operator
$\alpha_{CH}$	linewidth enhancement factor for CH
$\alpha_{SHB}$	linewidth enhancement factor for SHB
$\alpha_N$	linewidth enhancement factors for CDP
$g_N$	material gain (gain associated with intra-band processes)
$z$	Modulation depth
$f_{mod}$	modulation frequency
$\Delta N$	modulation of carrier density
$\gamma$	non-linear parameter
$A_{NR}$	non-radiative processes coefficient
$M$	Number of sections
$A$	optical signal envelope
$w$	optical signal angular frequency
$\lambda$	optical signal wavelength
$\beta_i$	Order $i$ coefficient of the Taylor approximation to the propagation constant
$IL_{out}$	Output losses
$S_{out}$	output photon density
$\phi$	phase modulation
$h$	Plank constant
$P$	polarization density
$\hat{x}$	polarization unit vector
$x, y, z$	position coordinates (Cartesian coordinates)
$\beta$	Propagation constant

---

$\alpha$	roll-off factor
$\epsilon_{\text{SHB}}$	SHB nonlinear gain compression factor
$\Phi$	Signal phase
$P$	Signal power
$A_{\text{DSB}}$	Slowly varying envelope associated with an optical double sideband signal
$A_{\text{SSB}}$	Slowly varying envelope associated with an optical single sideband signal
$A$	Slowly varying envelope associated with the optical pulse
$P_{\text{in}}$	SOA input power
$c$	speed of light in vacuum
$B_{\text{SP}}$	spontaneous emission coefficient
$R_{\text{REC}}$	spontaneous recombination rate
$R_{\text{ST}}$	stimulated recombination rate
$\tilde{\chi}$	susceptibility
$t, t'$	time
$N_{\text{st}}$	unsaturated carrier density
$k_0$	vacuum wave number
$F$	Waveguide mode distribution
$R_{\text{ST}}$	stimulated recombination rate
$R_{\text{REC}}$	spontaneous recombination rate
$\tau$	delay
$\Delta x$	difference in distance



# Chapter 1

## Introduction

### *1.1 Context*

It is outstanding to analyse statistics of International Telecommunications Union which report, for example, that the percentage of world-wide mobile phone subscribers has grown from round 5% of world population in 1998 to an estimated 61 % in 2008 [1]. Similarly, broadband home internet connections have exploded: only 10 years ago typical home connection was just 52 Kb/s; while today 200 Mb/s are commonly offered below €100 per month [2]. Even more impressive is to look back to the middle of the 20<sup>th</sup> century, where information was sent only by wire or radio. The remarkable growth in bandwidth has been feeding the burst of new internet applications, such as peer-to-peer, YouTube, MySpace, messaging, FaceBook, Twitter, Google earth, on-line gaming, etc; TV services like high-definition, 3D, and pay-per-view are also a reality in most homes. All these services and applications have dramatically changed the paradigm of communication between human beings. People want to be connected to *everyone, everywhere, at all time*.

This revolution could only be possible because of optical fiber communications. In the 1970's microwave communication systems were limited to only 100 (Mb/s)/km [3]. Such limitation was eliminated with the deployment of optical fibers and especially after the invention of the Erbium doped fiber amplifier (EDFA) [4]. In the last two decades, optical time division multiplexing (OTDM) and wavelength division multiplexed (WDM) networks, together with advanced modulation formats, have led to an explosion of the bit rate-distance product. Research records are now around 117 000 Tb/km [5]. Commercial

systems are keeping up: Nokia Siemens Networks plans to provide 96 x 100 Gb/s systems during 2011 and have already an eye in 400 Gb/s per channel [6].

Although deployed transmission capacity is only one step behind research, most signal processing, such as wavelength conversion, routing, and regeneration are still done in the electrical domain. Electrical signal processing may be the next impairment to the *Holy Grail* of service providers, which is to increase available bandwidth at the lowest costs possible. The price of a single regenerator for 40 Gb/s is today several times the cost of an EDFA, for example; and the high electrical consumption of electrical processing systems is becoming a major concern for operators [7]. All-optical processing is expected to overcome such limitations and to lead optical communications to the next level. However, all-optical processing is not yet a reliable solution; therefore, it is considered a key research topic.

The main objective of this thesis is to contribute to the study and development of all-optical processing devices, focusing on some of the decisive requirements of commercial systems: low cost, simplicity and robustness.

## 1.2 Motivation

The functionalities required from an optical network are increasing rapidly. Years ago it was sufficient that an optical system would transmit high volumes of information over large distances. Nowadays, it is also required that the optical network performs signal processing over the information being transported.

Optical networks are now a mix of dense wavelength division multiplexing, and optical time division multiplexing [8], [9]. In DWDM several signals at different wavelengths are combined in the same optical fiber with outstanding spectral efficiency. Latest reports present efficiencies in the order of 7.7 b/s/Hz by the use of optical frequency division multiplexing [10]. OTDM consists in interleaving several incoming signals in the same wavelength, reaching ultra-high per-channel bit rates. Currently, all this information is processed in the electrical domain to achieve the required functionalities, which consist mostly in:

- Wavelength conversion: where an input signal at wavelength  $\lambda_1$  is converted to  $\lambda_2$ . Wavelength converters are key devices to increase network throughput and avoid wavelength blocking.
- Regeneration: optical signals are distorted by several impairments in fiber transmission (such as dispersion, non-linearities, polarization mode dispersion (PMD), noise from amplification) and in the switching nodes (tight filtering, crosstalk, etc.). Regeneration consists in converting a distorted signal in an undistorted one.
- Format conversion: different network scenarios require different optical modulation or pulse format. Therefore, the nodes at the edge of such networks are required to convert the optical signals to the appropriate format.

Performing such operations in the electrical domain generally leads to a *bottleneck-effect*, since the optical transmission capacity and costs keep improving but the processing capabilities are limited by slower, more expensive and in general less efficient electronics. It becomes urgent to develop all-optical functionalities which will enable the ultimate goal of building true fully optical routers. Besides the aforementioned essential functionalities, the following are also mandatory:

- Add-drop multiplexing: since OTDM carries the information of several users, it is required to add / extract channels at switching nodes.
- Switching: the optical signal is switched through the network from the transmitter to the end receiver. The information required for the switching is carried together with the optical signal (e.g. label). Such information should be extracted and added from the optical signal without optical-electro-optical (OEO) conversions.
- Optical memory: required to store the optical signal while the several processing functionalities are performed.
- Optical logic: logical functions are the basis of any processing system.

All-optical functionalities are usually achieved by exploiting the non-linear characteristics of optical mediums. Most research has focused on optical fiber, (mostly highly non-linear fibers [11]) and semiconductor optical amplifiers (SOA) [12] as non-linear mediums. In fiber, the interaction between the signals and the medium is called non-resonant [13] and has an ultra-fast response time (in the order of the femto-seconds); however, the efficiency is usually low, since the non-linear coefficients are relatively low. As a consequence high input optical power or large interaction lengths (hundreds of meters) are commonly required to achieve reasonable non-linearity. On the other hand, SOA have a much higher non-linear coefficient [13], but the temporal response of its non-linear applications is limited to tens or hundreds of picoseconds by slow carrier dynamics. Nevertheless, ultra-fast SOA operation is being enabled using, for example, a Mach-Zehnder Interferometer structure with SOA in each arm (MZI-SOA), operated in a differential mode. SOA have also the advantage of being integrable, have potential for low cost, provide optical gain, are stable, and can be operated with very simple schemes. State-of-the-art research demonstrates simple operations at ultra-high bit rates, such as wavelength conversion at 640 Gb/s [14], or add-drop multiplexing at 160 Gb/s [15]. However, it is still essential to investigate and develop more complex functionalities which will enable the true and effective all-optical processing capabilities of the networks of the future.

### *1.3 Thesis objectives and outline*

The objective of this thesis is to contribute for the development of all-optical functionalities, which may constitute the building blocks for the all-optical routers of the future. It is not the objective of this work to propose or develop a routing solution, as research is not yet at the level where realistic all-optical routers can be developed. We focus on surpassing the SOA inherent limitations, such as slow response time or signal degradation due to intra-channel distortion, and on developing some of the urgent network requirements, such as wavelength converters, pulse and modulation format converters, and regenerators.

This thesis is organized in five chapters where several SOA based functionalities are investigated, the present introduction chapter, and a conclusion chapter.

**Chapter 2** presents an overview of the fifty year history behind SOA developments. An overview of the principle behind amplification in semiconductor materials is delivered, and techniques employed for the design of more efficient SOA. Different SOA-based solutions, like multi-electrode SOA (ME-SOA), gain-clamped SOA (GC-SOA) or reflective SOA (R-SOA) are revised and different network applications are pointed for each of them. The non-linear behavior of SOA is detailed regarding gain and phase dynamics. Such dynamics are the base of all applications studied throughout this work. The simulation model considered in the rest of this work is presented. This chapter includes also the state-of-the-art regarding several applications of SOA.

**Chapter 3** is focused in wavelength conversion. This is most basic all-optical functionality and the principles behind it are fundamental for the development of other processing functionalities. Wavelength converters are divided in four main groups, depending on the main non-linear effect involved: cross-phase modulation (XPM), cross-gain modulation (XGM), cross-polarization rotation (XPR), and four-wave mixing (FWM). From these, cross-phase modulation and cross-gain modulation are chosen to perform most of the functionalities along this thesis, due to their superior characteristics: robustness to variations in the input signal like polarization, power and wavelength; allow simple processing schemes, which operate at ultra-high bit rates; versatile configurations can be obtained by combining these two non-linear effects. We experimentally demonstrate methods to enhance the operation bandwidth of XGM based on detuned filtering. A method to convert phase modulation to intensity modulation, based on detuned optical filtering, is applied for the first time in a gain-clamped SOA wavelength converter. Phase-to-intensity conversion in a MZI-SOA is experimentally characterized at 10 Gb/s and 40 Gb/s 1 to 4 multi-wavelength conversion in MZI-SOA is experimentally demonstrated.

In **Chapter 4** two novel format converters are proposed. First, a format modulation converter from optical double sideband (oDSB) to optical vestigial sideband (oVSB) is presented. The converter is based on self-phase modulation (SPM) non-linear effect. The converter operation is enhanced by the use of a continuous wave signal (CW) holding beam, which avoids distortion caused by self-gain modulation (SGM). Operation is

demonstrated by simulations and experiments at 10 Gb/s and at 40 Gb/s. After characterization in back-to-back, the converted signal is transported over optical fiber to assess its transmission properties. Two scenarios are considered: without any optical or electrical dispersion compensation (ODC and EDC), and with simple EDC. A second modulation format converter, from on-off keying to carrier suppressed return-to-zero, is proposed. The proposed scheme, which exploits the interaction between XGM and XPM in a SOA, is first compared via simulations with the common transmitter. Afterwards, single- and multi-channel operation up to four channels are experimentally assessed at 40 Gb/s.

**Chapter 5** focuses on format conversions between return-to-zero (RZ) and non-return-to-zero (NRZ) pulse formats. Two schemes to convert RZ to NRZ are proposed and experimentally demonstrated. The first uses a detuned optical filter and XPM in a SOA. The optical filter shape is optimized and approximated by Gaussian filters. Characterization is presented at 10 Gb/s and at 40 Gb/s. The second method employs a two stage structure: in the first stage the gain-clamped SOA internal laser is modulated with the data signal; the second stage consists in XGM in a common SOA. Demonstration is presented at 10 Gb/s for different pulse width at input.

Optical regeneration is studied in **chapter 6**. A MZI-SOA structure is employed for the first time to suppress multiple access interference (MAI) noise of coherent 8 chip 10 Gb/s OCDMA signals. A novel 2R regeneration scheme is proposed, which uses the modulation of the internal laser of a gain-clamped SOA. This regenerator is experimentally tested at 2.5 Gb/s.

**Chapter 7** delivers a summary of the work and the main conclusions. Proposals for future work are also presented.

## *1.4 Main contributions*

The most important results presented in this thesis are:

- Study of the cross-gain modulation (XGM) bandwidth limitation imposed by the effective carrier lifetime.

- Exploitation of a scheme which employs detuned optical filtering to convert phase to intensity and enhance up to 40 Gb/s the modulation bandwidth of a SOA device originally designed for operation at 2.5 Gb/s.
- Investigation of a wavelength converter based on cross-phase modulation (XPM) in a Mach-Zehnder interferometer with SOA (MZI-SOA). Operation is enabled over single and multi-input signals at 40 Gb/s. This work resulted from collaboration with the Technical University of Eindhoven, Netherlands.
- XPM wavelength conversion in a gain-clamped SOA is proposed and assessed at 10 Gb/s.
- A novel all-optical converter between optical double sideband (ODSB) and optical vestigial sideband (OVSB) is proposed and demonstrated at 10 Gb/s and 40 Gb/s. To the authors knowledge this is the first true all-optical converter between these modulation formats that does not require optical filtering. The converter is characterized regarding robustness to optical fiber transmission and application in real networks.
- Characterization of return-to-zero (RZ) to non-return-to-zero (NRZ) pulse format converter based on detuned filtering of a XPM signal with demonstration at 10 Gb/s and 40 Gb/s.
- Proposal of a scheme to convert RZ to NRZ based on modulation of the internal laser of a gain-clamped SOA and assessment of its performance at 10 Gb/s with ultra-short input optical pulses. This work was developed in a joint collaboration with ISCOM, Rome, Italy.
- Proposal and implementation of converter from NRZ to RZ with simultaneous format conversion to carrier-suppressed. Experimental demonstration over 40 Gb/s single and multi-input.

- Regeneration of multi-access interference (MAI) of an optical coded division multi access (OCDMA) signal with MZI-SOA. This work was developed in a joint collaboration with NICT, Tokyo, Japan.
- Proposal of the use of gain-clamped SOA to obtain true 2R regeneration and demonstration at 2.5 Gb/s.

From this work resulted a total of three patent applications, eight journal papers, nineteen international conference papers, and five national conference papers. Appendix I lists the contributions resultant from this work.

Effective research can not be done without sharing of knowledge, ideas, and facilities. This work includes the result of four collaborations: with University College of London (UCL), to characterize the dynamic response of SOA; with ISCOM, Rome, to explore the immense potentials of gain-clamped SOA; with the Technical University of Eindhoven (TuE) to experimentally develop efficient multi-wavelength applications; and with NICT, Japan to demonstrate the application of SOA-based devices in OCDMA networks.

The work developed has been framed in a PhD program in an industrial environment at Nokia Siemens Networks (NSN) Portugal, S. A. (formerly Siemens, S. A.). NSN is one of the main optical network vendors in the market and leads research and development (R&D) of optical network solutions. As a consequence, this work has been earthbound by the premises and requirements of a demanding industry: low costs, simplicity, robustness, and potential for fast integration in real products. Some evidences of this link are the three patent applications filed during the development of this work, the development of a prototype for a modulation format converter, used internally in NSN in comparison with other solutions (detailed in appendix IV), and a very strong focus on the cost, simplicity and robustness of solutions.



# Chapter 2

## Semiconductor optical amplifiers

### *2.1 Motivation*

Semiconductor optical amplifiers (SOA) are the key device for the all-optical processing functionalities studied and proposed in this thesis. This chapter presents an overview of the history behind the development of SOA and of some basic design principles to optimize its characteristics. Propagation of optical signals in SOA is analysed via gain and phase dynamics. The simulation model utilized throughout this work is detailed, which includes intra- and inter-band effects. Finally, the most relevant linear and non-linear applications of SOA are presented.

### *2.2 Historical development*

The development of semiconductor optical amplifiers (SOA) is closely related to progresses in semiconductor lasers (SL) technology. The first SOA were regular laser diodes biased below threshold [12]: SOA are also known as semiconductor laser amplifiers (SLA) in the early literature [16], [17], [18]. In 1966, anti-reflection coatings (ARC) were proposed to reduce the optical feedback and allow amplification of infrared light [19]. The double heterostructure was demonstrated in 1969 and led to significant improvements in both lasers and SOA, such as enabling operation at room temperature [20]. Whilst first studies focused AlGaAs SOA, operating in the 830 nm range [21], in the 80's decade InP/InGaAsP SOA were designed for operation in the 1300 nm and 1550 nm ranges [16].

By the second half of the 80's the first transmission tests employing SOA as in-line amplifiers were reported [22]; however, in 1987 the Erbium doped fiber amplifier (EDFA) was invented [4] and began to compete with SOA for linear amplification purposes. The first true travelling wave SOA (TW-SOA) are reported in the end of the 80's [17]. These devices are enabled by developments in anti-reflection coatings and feature low polarization sensitivity – one of the main drawbacks of early SOA. By mid 90's the first semiconductor amplifiers featuring simultaneously high gain, high saturation power, and low polarization dependence are reported [23]. More recently, quantum-dot SOA (QD-SOA) have been developed to provide higher cross signal independence, lower biasing currents and wider operation bandwidths, along with other advantages [24].

Currently, SOA are presented as enabling devices for low cost amplification and processing in access networks [25], [26], since these can be used in photonic integrated circuits [27], allowing integration with several other optical components – passive or active. Moreover, SOA are compact, electrically pumped, have a large optical bandwidth, and allow flexibility in the choice of the peak gain wavelength. Due to their non-linear characteristics and fast response, SOA are also key devices for state-of-the-art all-optical processing at ultra-high bit rates (BR) [28].

The increase in the per channel bit rate and in the total number of wavelength multiplexed channels are exhausting the electrical processing capabilities of networks. Electrical processing at ultra high bit rates, such as 40 Gb/s and superior has high costs, footprint and energy consumption [29]. As a consequence, all-optical processing is currently one of the key research topics in optical networks [30].

### *2.3 Principle of SOA operation*

The operation of semiconductor optical amplifiers requires bringing together a p-type semiconductor and an n-type semiconductor to form a p-n junction. The denominations n- and p-type refer to the semiconductor doping with impurities that have an excess valence electron or one less valence electron, respectively, when compared to the

semiconductor atoms [31]. Figure 2-1 depicts the energy band of a p-n junction. In thermal equilibrium, the Fermi level<sup>1</sup> must be continuous across the junction (also known as depletion region). Under such condition, the charged particles set an electrical field that prevents diffusion of electrons and holes across the depletion region (Figure 2-1 a)). By applying an external electrical voltage, the built-in electrical field is reduced, resulting in diffusion of electrons and holes across the depletion region. When an electron and a hole are present in the same region, recombination can occur, and a photon is produced. A photon may be generated through stimulated or spontaneous emission. *Spontaneous emission* originates photons with random phase and frequency; these are essentially noise and contribute to reduce the optical gain. On the other hand, *stimulated emission* is the mechanism responsible for the optical gain: the newly generated photon is identical to an emitting photon. Besides the radiative mechanisms, referred before, in a semiconductor material electrons and holes can also recombine non-radiatively. These recombinations are not beneficial to the amplifier operation, thus efforts are made to its minimization.

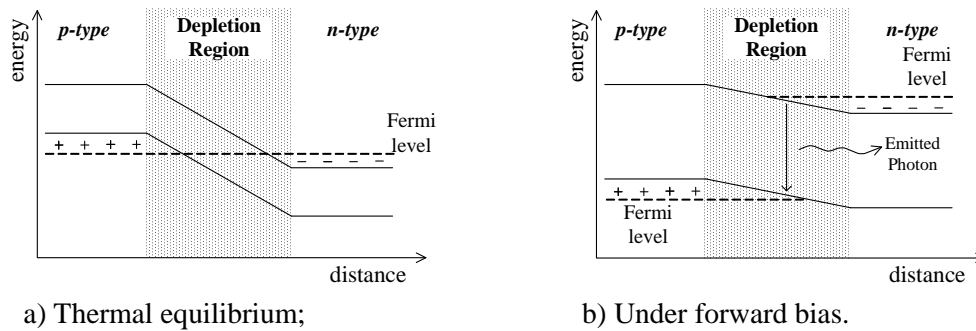


Figure 2-1: Energy band diagram of a homojunction p-n junction [31].

## 2.4 Design of SOA

Since the development of the first SOA devices, efforts have been made to improve their characteristics [12] for application in optical networks. Ideally, an optical amplifier should feature the following characteristics:

<sup>1</sup> The Fermi Level is defined as the highest occupied molecular orbital in the valence band at 0 K

- High gain, bandwidth, and saturation power;
- Negligible reflections at the end facets;
- Efficient coupling at the input and output;
- Polarization independent amplification;
- Low spontaneous emission noise;
- Low bias current sensitivity; and low temperature dependence.

To meet such requirements, it is required to optimize the SOA design. The SOA structure is usually a double heterostructure [31], where the active layer is sandwiched between layers with different band gap energies. This configuration enables better confinement of the carriers to the active region, improving the device efficiency. Undesired reflections can be minimized through the simultaneous use of several methods, which have enabled reflectivities lower than  $10^{-5}$  [32]:

- Use of antireflection coating (ARC) at the end facets of the device [33];
- Utilizing angled facet structure, where the active region is not perpendicular to the facet cleavage plane [34];
- Guard a transparent region between the active layer and the active region end facets: window-facet structure [35].

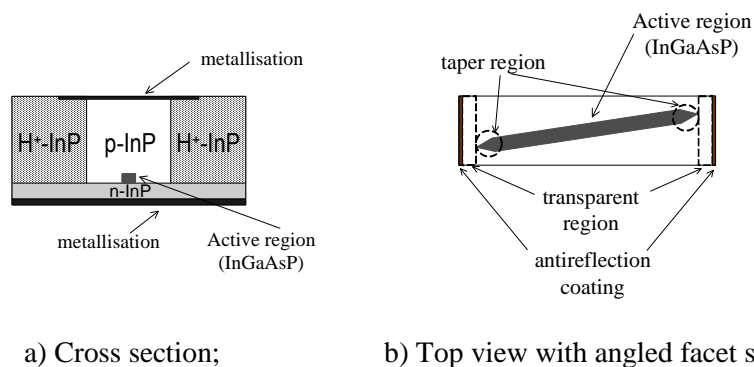


Figure 2-2. Schematic representation of a buried ridge stripe SOA [13].

Polarization independence is usually achieved by the use of a waveguide with a square cross section (and taper region to improve coupling efficiency). Other techniques can also be employed to enable polarization independence: ridge-waveguide SOA, and

structures based on strained materials. In Figure 2-2 a schematic representation of a buried ridge stripe SOA is depicted, showing some of the design techniques referred before [13].

Semiconductor optical amplifiers are often classified in two main types depending on the facet reflectivity [18]: Fabry Perot (FP) amplifiers and travelling wave amplifiers (TW). A FP-SOA is a resonant amplifier while TW-SOA features reduced facet reflectivity. Due to their characteristics, TW-SOA have replaced FP-SOA in most applications. Consequently, TW-SOA will be simply referred as SOA hereafter.

### 2.4.1 Materials and structures for the active layer

The type of material and the structure of the active region determine the behaviour of the SOA regarding unsaturated gain, gain spectral bandwidth, central wavelength, polarization dependence, etc. The most common structures are: bulk, and quantum well [31]. In a *bulk* material all the dimensions of the active layer are significantly larger than the deBroglie wavelength, and the energy levels of the electrons and holes in the active region are continuum [31]. In *quantum well* (QW) materials, the active region has one or more dimensions (usually thickness) of the order of magnitude of the deBroglie wavelength. Single QW devices have low carrier and optical confinement and high polarization dependence; therefore, are not commonly employed. Such drawbacks are avoided by the use of multi-QW (MQW). MQW materials have a series of stacked thin active layers separated by thin barrier layers [32]. MQW devices have discrete energy density levels; therefore, the dependence with the photon energy (thus, its frequency) decreases: larger gain bandwidth is achieved [32]. MQW also present improved noise figure, higher optical gain, and higher saturation power [12]. On the other hand, bulk devices may be more interesting to non-linear applications, since these usually feature large optical confinement and phase to amplitude coupling.

SOA employing quantum dot materials (QD-SOA) are currently blooming and being intensively studied. The active layer consists on nano-size semiconductor islands spatially isolated, which exchange carriers with a wetting layer; therefore, the energy states in the active layer are discrete. QD-SOA are still under research, but it is expected that when mature they will present the following characteristics [36], [37]:

- Ultrafast gain recovery (order of the picoseconds);
- Low noise figure;
- Broadband gain;
- High saturation output power;
- High four wave mixing efficiency;
- Low threshold current;
- Low patterning effects;
- Multi wavelength conversion;
- Possibility of efficient 3R.

### 2.4.2 Semiconductor optical amplifiers with specific design

In addition to the regular SOA structure, specific design can be considered to overcome some of the SOA inherent limitations and allow particular applications.

#### Reflective semiconductor optical amplifier (R-SOA)

In a reflective SOA (R-SOA), represented in Figure 2-3, one of the facets is not coated with antireflective material. As a consequence, the optical beam is reflected in one of the ends, travelling twice through the active region.

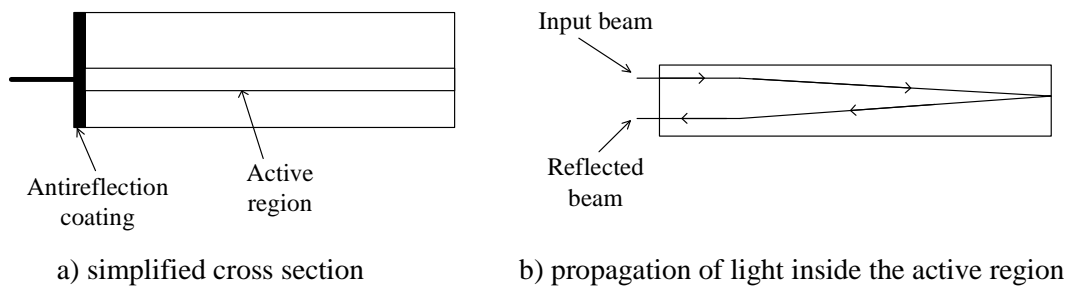


Figure 2-3. Schematic representation of a reflective SOA (R-SOA).

Due to its reflective properties, R-SOA have been proposed to integrate a wavelength division multiplexed / sub-carrier multiplexed - passive optical network (WDM/SCM-PON) that shares the same wavelength for the up and down links [38]. The

R-SOA operates simultaneously as amplifier and optical modulator, reducing the overall cost of the network [39],[40]. R-SOA and high-birefringence fiber Bragg grating (FBG) were used to generate broadband orthogonal pumps and tuneable broadband wavelength conversion [41].

#### Multi-electrode semiconductor optical amplifier (ME-SOA)

In a multi-electrode SOA (ME-SOA), schematically represented in Figure 2-4, the current bias is injected through more than one electrode. Different currents can be injected at each electrode. ME-SOA have been proposed to perform simultaneous amplification and detection [42]. ME-SOA are particularly interesting for this application since it allows the conservation of the signal DC component, and independence to temperature and bias current. ME-SOA also enable amplification, modulation, and detection in only one device [43], with reduced electrical processing. A two section SOA was used as phase modulator with intensity modulation (IM) suppression [44]. The electrical modulation signal is fed in anti-phase to the two electrodes. This combination of bias currents results in the cancellation of the overall IM, while enabling phase modulation due to the different linewidth enhancement factors of the two sections. We have proposed a similar principle to obtain independent intensity and phase modulation in a ME-SOA in [45].

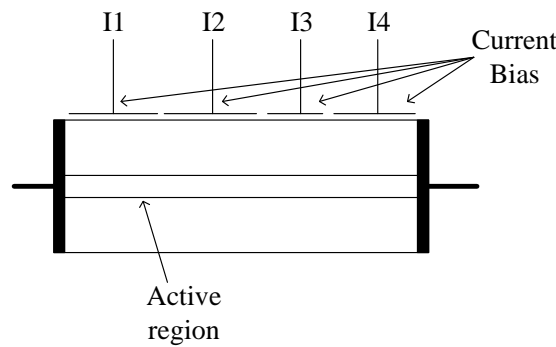


Figure 2-4. Schematic representation of a multi-electrode SOA (ME-SOA).  
I1 – I4 represent bias currents.

## 2.5 Gain and phase dynamics in SOA

Ideally an ideal amplifier should feature constant gain, regardless of the input power. However, the gain of amplifiers saturates for high power input signals, resulting in

different gain for input signals with different power values. This effect is usually called gain saturation and is represented in Figure 2-5. For low input / output powers, the amplifier delivers a high gain, usually known as *small signal gain*; as the power increases the gain is reduced. The output power at which the gain is 3 dB below the small signal gain, is known as *saturation output power*.

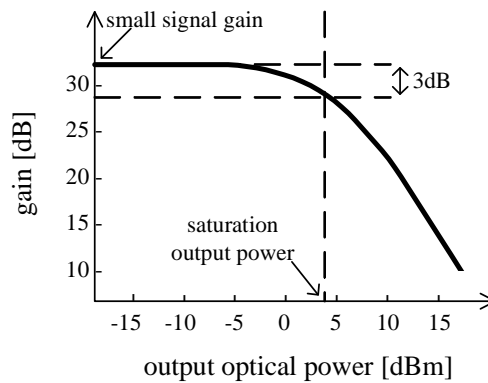


Figure 2-5. Representation of gain saturation in an optical amplifier.

In an EDFA, the gain dynamics are in the order of the milliseconds [4], whilst optical signals usually have bit periods in the order of the picoseconds. As a consequence, gain saturation occurs due to the average power of the signal being amplified, resulting in negligible inter- and intra-channel distortion. In SOA, the gain dynamics are reasonably fast: in the order of the tens of picoseconds, which is a value comparable to the pulse duration in current systems. The SOA gain saturation provokes intra and inter-channel patterning effects and newly generated frequencies, i.e. four-wave mixing (FWM). Moreover, phase modulation also occurs in the SOA due to variations of the refractive index with the input power. From the later considerations, it is evident that if a SOA is to be used as a linear amplifier, the input signal power must be carefully chosen to prevent undesired distortion effects. On the other hand, the fast gain and phase dynamics can be exploited for non-linear applications.

The gain and phase dynamics of SOA are associated to the dynamics of free carriers. The free carriers density and distribution vary due to intra-band and inter-band transitions which are represented schematically in Figure 2-6.

In inter-band transitions, carriers transfer from the conduction band to the valence band and vice versa. These transitions are determined by electrical pumping, stimulated



and spontaneous emission, non-radiative recombination, and two photons absorption (TPA) [12]. In intra-band transitions, the energy distribution of the carriers varies within the same band and is determined by: spectral hole burning (SHB), free carrier absorption (FCA), carrier heating (CH), and carrier cooling (CC) [12].

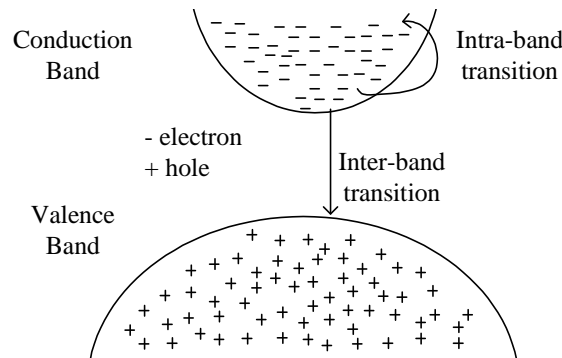


Figure 2-6. Representation of intra-band and inter-band transitions in a semiconductor.

The carrier dynamics are evident through the gain response to an ultra-short optical pulse, as represented in Figure 2-7. The incoming optical pulse stimulates carriers which have energies similar to the incoming pulse photon to recombine. This provokes a hole in the carrier distribution and is associated with SHB. The carrier density within the band is also reduced via stimulated emission. Simultaneously, TPA occurs since there is a high photon density in the active region. FCA also takes place: a free carrier absorbs a photon and moves to a higher energy level in the same band. Carrier depletion is a fast process.

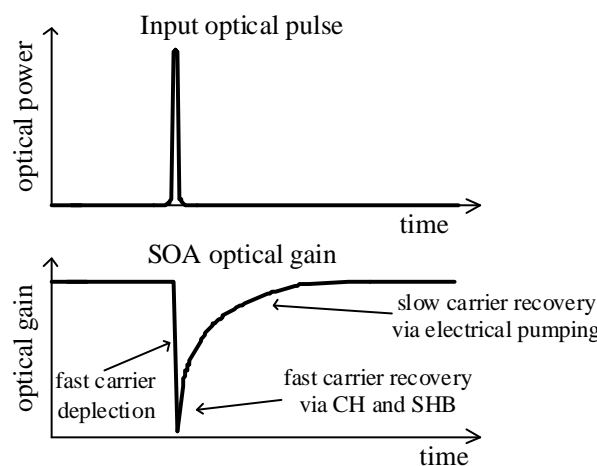


Figure 2-7. Representation of the SOA gain response to an optical pulse and associated carrier dynamics.

When the optical pulse leaves the SOA, the Fermi distribution is restored through carrier-carrier scattering; the related time constant is referred as SHB relaxation time. Although the Fermi distribution is restored, the carrier temperature has been increased due to stimulated emission, FCA and TPA. The temperature decreases via phonon emission; the related time constant is referred as CH or temperature relaxation time. These are fast intra-band processes. The original carrier level is then restored by means of electrical pumping, which is a slow process (hundreds of picoseconds). More information on carrier dynamics can be found in [12], [46], [47].

## 2.6 Modelling of signal amplification in SOA

The propagation of the electromagnetic field inside a semiconductor optical amplifier is governed by the well known wave equation [31], [48] in the frequency domain<sup>2</sup>:

$$\nabla^2 \tilde{\mathbf{E}}(w) + k_0^2 \left[ 1 + \frac{i\sigma}{\epsilon_0 w} \right] \cdot \tilde{\mathbf{E}}(w) = -\frac{k_0^2}{\epsilon_0} \tilde{\mathbf{P}}(w), \quad (2-1)$$

where  $\nabla^2$  represents the Laplacian operator,  $\epsilon_0$  is the electrical permittivity of free space,  $k_0 = w/c = 2\pi/\lambda$  is the vacuum wave number,  $c$  is the speed of light in vacuum,  $w$  and  $\lambda$  are the optical signal angular frequency and wavelength.  $\tilde{\mathbf{E}}$  is the electrical field vector of the optical field,  $\mathbf{P}$  is the polarization density arising inside the medium in response to the optical field and  $\sigma$  is the conductivity of the medium. Note that  $\tilde{\mathbf{E}}$  and  $\tilde{\mathbf{P}}$  are complex.

Under steady state conditions the response of the medium to the electric field is governed by the susceptibility  $\tilde{\chi}$ :

---

<sup>2</sup> The Fourier transform definition used throughout this work is:

$$A(w) = \frac{1}{2\pi} \int_{-\infty}^{+\infty} A(t) \cdot \exp(iwt) \cdot dt, \text{ with } t \text{ standing for time and } w \text{ for the angular frequency.}$$

$$\tilde{P}(w) = \epsilon_0 \cdot \tilde{\chi}(w) \cdot \tilde{E}(w) \quad (2-2)$$

The full deductions of the equations that rule the pulse propagation are outside the scope of this work, more details can be found in [12], [48], [49], [50]. Hereafter only results that are required for the considered model are presented.

To enable the deduction of a simple and practical equation for pulse propagation inside the SOA, it is necessary to consider some assumptions and simplifications: the amplifier is considered to be an ideal travelling-wave amplifier whose active dimensions are such that only a single waveguide mode is allowed. Assuming that the light is linearly polarized and remains as such during the propagation, the electric field inside the amplifier can be written as [48]:

$$\tilde{E}(x, y, z, t) = \hat{x} \frac{1}{2} \left\{ F(x, y) \cdot A(z, t) \cdot e^{\left[ i \left( \frac{w \cdot z}{v_g} - w \cdot t \right) \right]} \right\}, \quad (2-3)$$

where  $\hat{x}$  is the polarization unit vector,  $F(x, y)$  is the waveguide-mode distribution,  $A(z, t)$  is the slow varying envelope associated with the optical pulse,  $v_g = c/n_g$  is the group velocity,  $n_g = \bar{n} + w \cdot (d\bar{n}/dw)$  is the group index, and  $\bar{n}$  the effective mode index.

To derive the equation that governs the evolution of the pulse along the amplifier we will transform our referential in a frame moving with the pulse:

$$t' = t - \frac{z}{v_g} \quad (2-4)$$

$$z' = z \quad (2-5)$$

Without loss of continuity, and for simplicity of notation, the prime over  $t'$  and  $z'$  will be dropped hereafter. To facilitate the notation hereafter, the amplitude and phase information of the pulse are split:

$$A(z, t) = \sqrt{P(z, t)} \cdot \exp[i \cdot \Phi(z, t)], \quad (2-6)$$

With  $P(z, t)$  the pulse power, and  $\Phi(z, t)$  the pulse phase.

### 2.6.1 Gain dynamics

The signal power along the SOA is described by [13]:

$$\frac{\partial P}{\partial z} = (\Gamma \cdot g_T - \alpha_{\text{int}}) \cdot P, \quad (2-7)$$

Where  $\alpha_{\text{int}}$  is the SOA absorption coefficient caused by the internal waveguide loss,  $\Gamma$  is the confinement factor, which is described by (2-8) and describes the gain reduction due to the spreading of the optical mode beyond the active region of the SOA.

$$\Gamma = \frac{\int_{-\infty}^{\infty} \int_{-\infty}^{\infty} |F(x, y)|^2 \cdot dx \cdot dy}{\int_{-\infty}^{\infty} \int_{-\infty}^{\infty} |F(x, y)|^2 \cdot dx \cdot dy} \quad (2-8)$$

For simplicity, the confinement factor is usually assumed to be a constant. In [12] a more accurate model is presented, which includes dependence of the confinement factor with the wavelength and carrier density.

The gain coefficient  $g_T$  is also assumed to be independent of the wavelength and is given by [12] :

$$g_T = g_N + g_{\text{CH}} + g_{\text{SHB}} + g_{\text{TPA}}, \quad (2-9)$$

With  $g_N$  standing for the material gain, which reflects the contribution of inter-band processes (carrier density pulsation); and  $g_{\text{CH}}$ ,  $g_{\text{SHB}}$ , and  $g_{\text{TPA}}$  stand for the gain associated with carrier heating (CH), spectral-hole burning (SHB), and two-photon absorption (TPA), respectively.

Equation (2-7) can be simplified to:

$$P(z, t) = P_{in}(t) \cdot G(z, t), \quad (2-10)$$

With  $P_{in}(t) = P(0, t)$  the optical power at the SOA input and  $G$  the gain, given by:

$$G(z, t) = \exp\left(\int_0^z (\Gamma g_T - \alpha_{int}) \cdot dz\right) \quad (2-11)$$

### 2.6.1.1 Inter-band processes

Inter-band processes alter the carrier density,  $N$ ; however, these do not affect the carrier distribution. Variations of  $N$  are also known as carrier density pulsation (CDP). The gain of the semiconductor material is directly determined by the free carrier density. The gain associated with inter-band processes is then given by [18]:

$$g_N(t, z) = \frac{dg}{dN} \cdot (N(t, z) - N_{tr}). \quad (2-12)$$

In the previous equation,  $dg/dN$  is the differential gain coefficient, which is here assumed to be a constant;  $N$  is the free carrier density in the conduction band and, for simplicity, will be referred simply as carrier density hereafter; finally,  $N_{tr}$  is the carrier density at transparency (when  $g_N=0$ ).

The carrier density is described by [18]:

$$\frac{dN}{dt} = \frac{I}{eV} - R_{ASE} - R_{ST} - R_{REC}. \quad (2-13)$$

The first right hand term in (2-13) represents the rate of injected electrons in the SOA active layer; with  $I$  the injected current,  $q$  the electron charge, and  $V$  the active layer volume.  $R_{ASE}$  accounts for the carrier recombination, stimulated by spontaneous emitted photons and will be neglected here.  $R_{ST}$  is the stimulated recombination rate, described by:

$$R_{ST} = v_g \cdot g_T \cdot S. \quad (2-14)$$

$S$  represents the average photon density inside the active region [12], [51]:

$$S(z, t) = \frac{2\pi \cdot \Gamma \cdot L \cdot P_{in}(t)}{h \cdot V \cdot w \cdot v_g} \cdot \frac{G-1}{\ln(G)}, \quad (2-15)$$

With  $L$  the active layer length, and  $h$  the Plank constant.

The recombination of carriers not directly affected by the signal or ASE propagation, spontaneous recombination rate, is represented by  $R_{REC}$  and is given by the following expression:

$$R_{REC} = \frac{N}{\tau_s}, \quad (2-16)$$

With  $\tau_s$  the carrier lifetime, often represented by [13]:

$$\tau_s = \left( A_{NR} + B_{SP} \cdot N + C_{Auger} \cdot N^2 \right)^{-1}. \quad (2-17)$$

The coefficients in (2-17) denote non-radiative processes, spontaneous emission, and Auger recombination, respectively.  $R_{REC}$  is also often represented by  $N/\tau_s$ .

Considering (2-12) - (2-17), the material gain can be represented by the following differential equation:

$$\frac{dg_N}{dt} = -\frac{g_N}{\tau_s} - \frac{dg}{dN} \cdot \left( g_T \cdot S \cdot v_g + \frac{I}{eV} - \frac{N_{tr}}{\tau_s} \right) \quad (2-18)$$

### 2.6.1.2 Intra-band processes

Inter-band gain dynamics are the dominating gain mechanism when long pulses are used (i.e. above tens of picoseconds). However, for short optical pulses the intra-band processes become relevant in the overall gain dynamics. Intra-band processes alter the carrier distribution within the conduction band. The main intra-band processes are SHB, CH, and TPA. The differential equation for the gain associated with carrier heating,  $g_{CH}$ , is given by:

$$\frac{dg_{CH}}{dt} = -\frac{g_{CH}}{\tau_{CH}} - \frac{\epsilon_{CH}}{\tau_{CH}} \cdot g_T \cdot S, \quad (2-19)$$

Where  $\tau_{CH}$  is the CH relaxation time and  $\epsilon_{CH}$  is the CH nonlinear gain compression factor.  $\tau_{CH}$  usually ranges from hundreds of femtoseconds to few picoseconds.

For the SHB process, the related relaxation time is faster (tens of femtoseconds) therefore an approximated equation is considered [49]:

$$g_{SHB} \approx -\epsilon_{SHB} \cdot g_T \cdot S, \quad (2-20)$$

With  $\epsilon_{SHB}$  representing the SHB nonlinear gain compression factor.

The TPA process is neglected in this work since the TPA contribution is one order of magnitude smaller than the gain compression associated with CH and SHB, for sub-picosecond pulses with moderate energies [52], [12].

## 2.6.2 Phase dynamics

The gain and refractive index variations are not independent. These are linked by the Kramers-Krönig relations [53]; as a consequence, if the gain is known, the refractive index can be calculated numerically, and vice-versa. The evaluation of the exact dependence is complex; therefore, the refractive index is usually calculated through the linewidth enhancement factors<sup>3</sup>. The signal phase along the SOA can be described by [13]:

$$\Phi(t, z) = \Phi(t, 0) - \frac{\Gamma}{2} \int_0^z (\alpha_N \cdot \Delta g_N + \alpha_{CH} \cdot g_{CH} + \alpha_{SHB} \cdot g_{SHB}) dz, \quad (2-21)$$

With  $\Delta g_N = g_N(N) - g_N(N_{st})$ ,  $N_{st}$  standing for the unsaturated carrier density:

---

<sup>3</sup> The linewidth enhancement factor is also known in the literature as  $\alpha$ -factor, phase amplitude coupling factor, or Henry factor [12][54][55][48].

$$N_{ST} = \frac{I \cdot \tau_s}{e \cdot V}, \quad (2-22)$$

And  $\alpha_N$ ,  $\alpha_{CH}$  and  $\alpha_{SHB}$  are the linewidth enhancement factors for CDP, CH and SHB. The linewidth enhancement factors usually depend on  $N$ ,  $z$ ,  $t$ , on the wavelength, and on temperature; however, for simplicity these are usually treated as constants.

## 2.7 SOA simulation tool

In the previous section the equations that describe the operation of SOA have been presented. However, such equations do not allow an analytic solution. In this section the simulation model considered throughout the rest of the work is described.

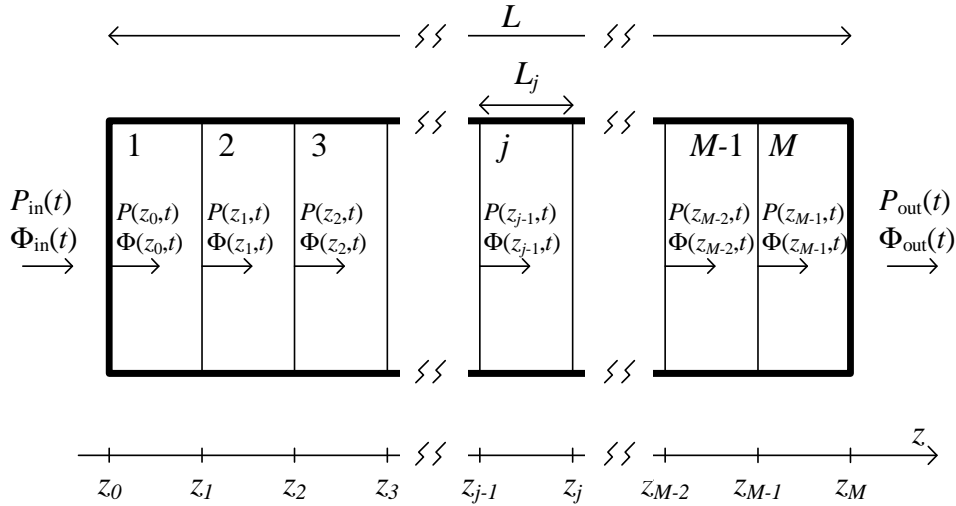


Figure 2-8. Schematic representation of the SOA active section division into  $M$  sections.

The SOA simulation model relies on dividing the SOA active section into  $M$  sections [12], [56], as illustrated in Figure 2-8. Unidirectional propagation is considered: it reduces dramatically the simulation time; furthermore, most of the experimental work done in this thesis considered unidirectional propagation. The simulations carried in this work do not consider amplified spontaneous emission noise added by the SOA, for several reasons: first, the main impairment to SOA non-linear applications is the degradation caused by SOA gain dynamics, not optical noise; second, current SOA noise figures can be



as low as 6 dB [57]; third, SOA input powers for non-linear applications are rarely below -10 dBm; by last, the impact of cascading multiple SOA based devices is not studied in this work.

The power and phase at the input of the first section are obtained from the power and phase at the input of the patch cord that connects to the SOA ( $P_{in}(t)$  and  $\Phi_{in}(t)$ ) by:

$$\begin{aligned} P(z_0, t) &= P_{in}(t) \cdot 10^{-IL_{in}/10}, \\ \Phi(z_0, t) &= \Phi_{in}(t) \end{aligned} \quad (2-23)$$

With  $IL_{in}$  the input losses (logarithmic units), determined mostly by fiber splices, coupling losses, and by the transmittance of the SOA input facet.

The power and phase at the output of the patch cord,  $P_{out}(t)$  and  $\Phi_{out}(t)$  respectively, are obtained from:

$$\begin{aligned} P_{out}(t) &= P(z_M, t) \cdot 10^{-IL_{out}/10}, \\ \Phi_{out}(t) &= \Phi(z_M, t) \end{aligned} \quad (2-24)$$

With  $IL_{out}$  the output losses (logarithmic units), determined mostly by fiber splices, coupling losses, and by the transmittance of the SOA output facet. Note that  $P(z_M, t)$  and  $\Phi(z_M, t)$  are not illustrated in Figure 2-8, but represent the power and phase at the output of section  $M$ , which is immediately before the output facet.

In the considered model all sections have similar length and the number of sections ( $M$ ) is adapted to the characteristics of the input signal (bit rate and pulse duration). In each of the  $M$  sections, the carrier density and the bias current ( $I_j$ ) are assumed to be space independent. Following the model of the section 2.6, the power and phase at the output of section  $j$  are given by:

$$\begin{aligned} P(z_j, t) &= P(z_{j-1}, t) \cdot G_j \\ \Phi(z_j, t) &= \Phi(z_{j-1}, t) - \frac{\Gamma \cdot L_j}{2} \cdot (\alpha_N \cdot \Delta g_{N,j} + \alpha_{CH} \cdot g_{CH,j} + \alpha_{SHB} \cdot g_{SHB,j}) \end{aligned} \quad (2-25)$$

With the  $j^{\text{th}}$  section gain given by:

$$G_j(t) = \exp\left[\left(\Gamma g_{T,j} - \alpha_{\text{int}}\right) \cdot L_j\right]. \quad (2-26)$$

All the components of  $g_{T,j}$  are obtained from the equations of the previous section, replacing  $L$  by  $L_j$  and  $I$  by  $I_j$ . Assuming that all sections have similar lengths,  $L_j = L/M$  and  $I_j = I/M$ . The differential equations are solved via the numeric method Runge-Kutta [58].

The simulation parameters considered in this work are detailed in Appendix II.

## 2.8 Gain-clamped semiconductor optical amplifiers

In early days of WDM systems (early 90's), SOA working in the linear regime were pointed as a promising solution to perform optical amplification. However, it was observed that severe inter-channel penalties arise from cross gain modulation. To diminish such crosstalk, a new structure was proposed by Bauer et al [59], which consisted on a laser amplifier where lasing is induced by distributed feedback (DFB). Later, a distributed Bragg reflector (DBR) scheme was also proposed [60]. These two gain clamped SOA (GC-SOA) schemes are illustrated in Figure 2-9. More recently, vertical gain clamping with DBR has also been reported [61]. However, this work will focus on longitudinal gain-clamping, since all our experimental work was developed with a DBR GC-SOA.

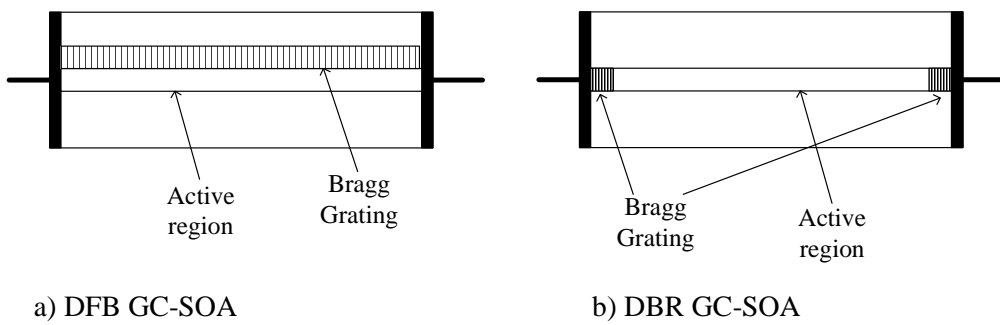


Figure 2-9. Schematic representation of a gain-clamped SOA (GC-SOA).

The principle of gain-clamping in SOA is illustrated in Figure 2-10. In a laser biased beyond the oscillation threshold, the cavity gain at the laser wavelength is clamped to a value similar to the cavity losses at that wavelength [59]. This means that, when a probe signal is injected in the GC-SOA, the power of the internal laser will vary inversely

to the probe signal power, in order to maintain a constant cavity gain. When the probe signal power exceeds a threshold value, the internal laser is shut down and the GC-SOA operates similarly to a common SOA - Figure 2-10 a). The simulated optical gain of a GC-SOA and of a common SOA are compared in Figure 2-10 b): the GC-SOA has an approximate constant gain up to higher input powers: higher saturation power is achieved at the expense of a decrease in the unsaturated gain.

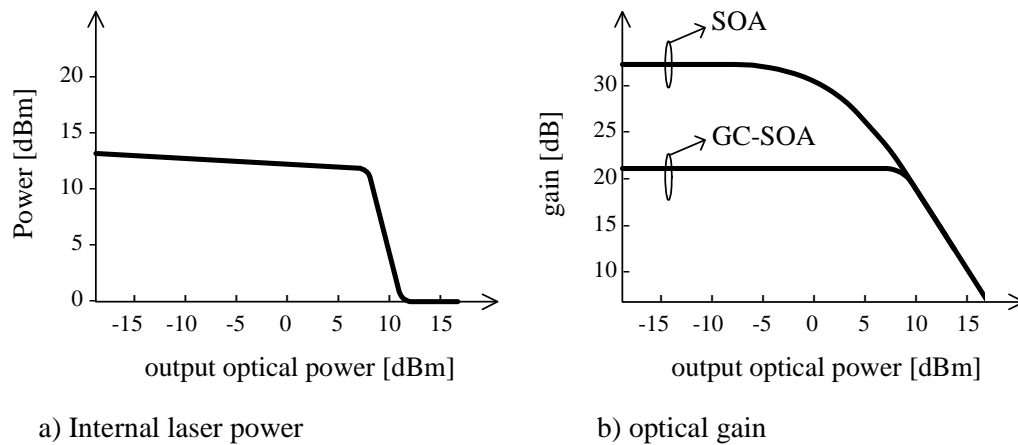


Figure 2-10. GC-SOA operation. The x axis in the graphics denote the output power at the probe signal wavelength. Scales in the graphics are for illustrative purposes only.

Since the reflectivity of the gratings is low, a considerable power of the laser leaks to the output of the SOA. This can be verified in Figure 2-11, where the output spectrum of a GC-SOA is presented in absence of input signal.

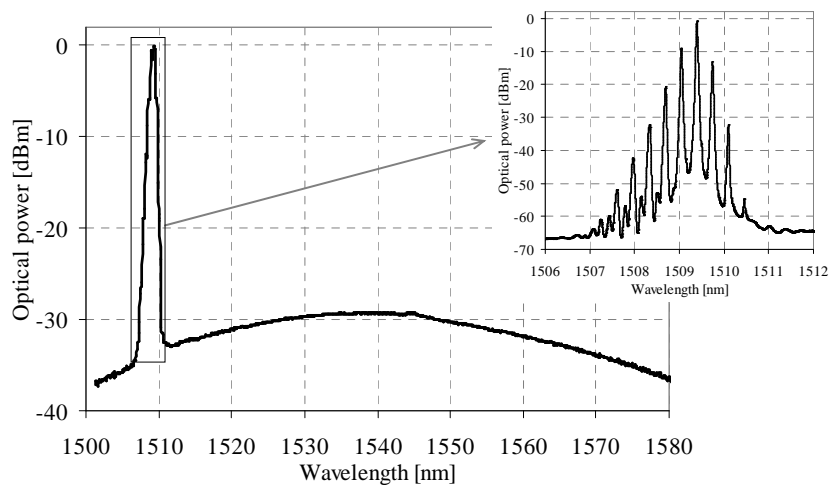


Figure 2-11. GC-SOA output spectrum in absence of input signals (resolution is 0.5 nm). Inset: zoom at wavelength of internal laser (resolution is 0.01 nm).

GC-SOA provide insensitive gain for a broader range of input powers; therefore, it became an attractive solution for in-line amplification of analogue signals: amplification of 77 channel Cable Television signals was reported in [62].

GC-SOA are also attractive devices for all-optical signal processing due to several characteristics: the internal laser leads to faster response [63]; the internal laser dynamics can be explored for specific non-linear applications [64]; and enhanced gain independence on the injection current [65]. A 2R regenerator with a “true” regeneration characteristic based on GC-SOA in an interferometric structure was proposed by Morthier et al [65]. The digital regeneration characteristic of such structure is based on linear gain (in unsaturated condition) and on very reduced gain dependence on the bias current. A wavelength converter, where the GC-SOA internal laser is directly modulated by the input optical signal, was proposed in [66], resulting in very low input power requirements. Fast optical space switches are essential elements for the deployment of WDM networks; GC-SOA have been proposed as a promising solution due to fast on-off gating, on-off ratios higher than 50 dB, and reduced inter-channel crosstalk. In [67], an 8x8 space switch based on arrays of 8 GC-SOA is experimentally reported with operation over 16x10 Gb/s WDM channels. The outstanding results are mostly due to low noise figure and very linear gain up to a high output saturation power. Patterning effects induced by common SOA have been mitigated by GC-SOA: in [68], 5000 km of fiber transmission were obtained using a GC-SOA-saturable absorber 2R regenerator, cascaded with a GC-SOA. Further transmission results report the combination of a vertical GC-SOA and distributed Raman amplification [69]; with this technique, transmission of 16x10 Gb/s amplitude modulated channels was obtained along 400 km of fiber.

## 2.9 *Applications of SOA*

In the last decades SOA have been proposed not only as low cost amplifiers, but also as a promising core component for the all-optical networks of the future. An overview of the main applications of SOA is presented in this section.

### Linear Amplifier

SOA have low cost potential due to: compatibility with monolithic integration [27], being electrically pumped, and allowing flexibility in the selection of the peak gain wavelength. Therefore, these devices have been pointed as an interesting solution to perform linear amplification, particularly in access and metropolitan networks, where the amplification performance requirements are not so strict [70][71]. Figure 2-12 illustrates a WDM network employing SOA as booster, in-line amplifier, and pre-amplifier variants.

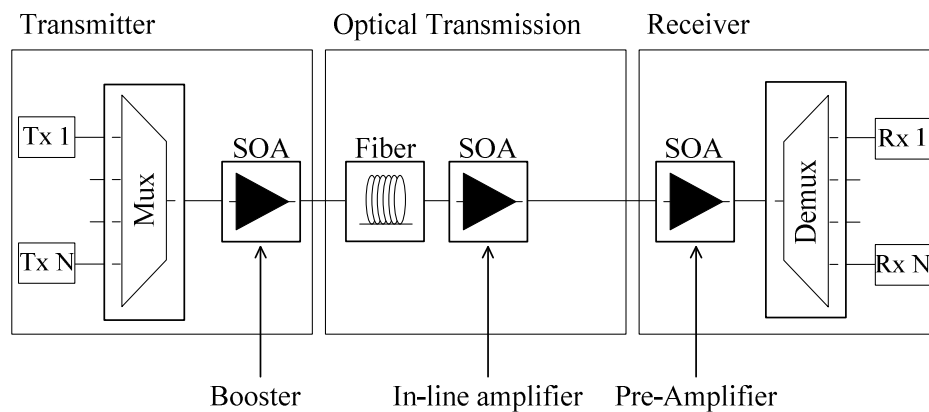


Figure 2-12. Application of SOA as linear amplifier in booster, in-line and pre-amplifier variants.

Experimental SOA based transmission tests have demonstrated 10 Gb/s single channel transmission over 550 km of standard single mode fiber, at 1300 nm [72]. Tests with WDM signals demonstrated transmission over 1050 km of eight 10 Gb/s channels at 1550 nm [73], and 640 km of sixteen 10 Gb/s channels [74]. In analogue transmission systems, such as CATV, the linearity requirements are more stringent than in the digital systems referred above; therefore, special SOA have been developed: gain-clamped SOA, which have been described in the previous section.

One of the main impairments to the use of SOA as linear amplifiers is the degradation of signals with advanced modulation formats, which carry phase information, due to cross-phase modulation at the SOA. However, in [75] we have demonstrated amplification of optical single sideband (oSSB) signals, whose sideband suppression relies on phase modulation, with reduced sideband suppression penalty, provided that the input power is controlled.

### Optical modulator and detector

SOA have been proposed as optical modulator and receiver, with particular interest in low bit rate access networks [76], [26]. SOA are particularly interesting since they perform the referred applications and simultaneously amplify the signal. These applications are illustrated in Figure 2-13.

The principle of operation of an intensity modulator based on SOA is quite simple: the power of the output amplified signal is dependent on the bias current; therefore, optical modulation is performed by modulating the bias current with the information to be transmitted. This is a low price modulator with reduced complexity; it provides gain; and also features polarization and wavelength independent operation (if the SOA is polarization insensitive and the input signal is within the gain bandwidth of the SOA). When an IM signal is being amplified in a SOA, the carrier density is modulated with the inverse of the logical information of the input signal. The carrier density variations lead to a modulation of the junction voltage, resulting in a detection process. The main disadvantage of SOA being used as modulators and detectors is that the operation is typically limited by the inter-band recombination to few GHz. ME-SOA are also promising devices for detection and modulation, as discussed in section 2.4.2.

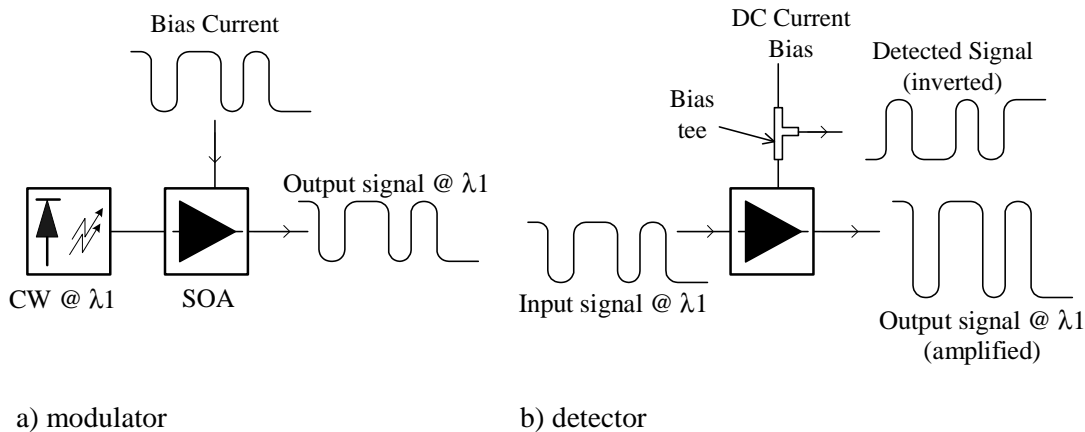


Figure 2-13. Application of SOA as modulator and detector.

### Wavelength Conversion

Wavelength converters (WC) are key elements in all-optical networks. SOA based wavelength converters usually use one of the following non-linear effects: cross gain modulation (XGM), cross phase modulation (XPM), cross polarization rotation (XPR), or

four wave mixing (FWM). All-optical wavelength converters (AOWC) based on SOA are studied in Chapter 3.

### Logic gates

Ultra fast logic operations are fundamental for the inline processing capabilities of next generation networks. Most of the network related functionalities such as add-drop multiplexing, packet synchronization, clock recovery, address recognition, and signal regeneration require logical operations, which should be performed all-optically, especially for high data rates. Several implementations of all optical logic functionalities using SOA have been presented, from the following are highlighted: XNOR, AND, NOR, and NOT functionalities achieved using a simple scheme which employs a single SOA and optical filtering [77]; several simple and complex logic functionalities are achieved via FWM in SOA for polarization shifted keying modulated signals in [78]; parallel MZI-SOA also can provide multiple logical functionalities, like XOR, NOR, OR, and AND, reported in [79].

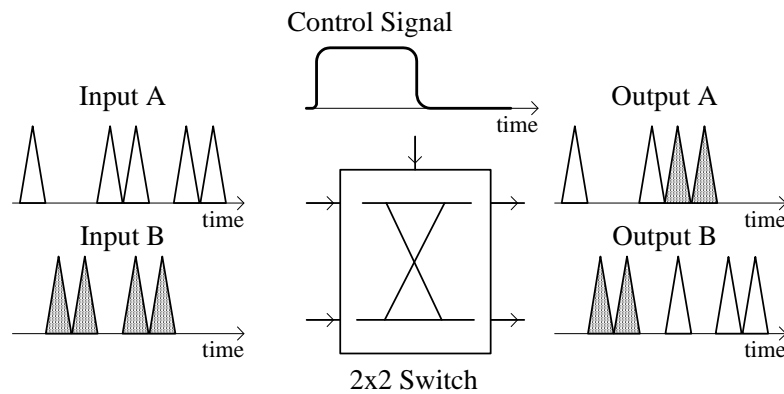


Figure 2-14. Operation of a 2x2 space switch.

All-optical routing also requires effective 2x2 space switches. Figure 2-14 demonstrates the operation of a 2x2 space switch: inputs A and B are switched either to output A or B, depending on the logic state of the control signal. 2x2 space switches can be implemented using MZI-SOA with 4 input ports [80]. Due to the difficulty in obtaining an exact  $\pi$  phase shift between the two arms and gain compression, the MZI-SOA has an inherent imperfect contrast ratio of the output ports: the input signals are not completely switched between the two output ports. Nevertheless, over 20 dB extinction ratio between

the two ports are reported in [80], by independently controlling the SOA bias currents and phase shifters of the two arms.

### Multiplexing and add-drop multiplexing

Future networks are likely to simultaneously employ WDM and optical time division multiplexing (OTDM). In the later, the lower bit rate information of several users is bit interleaved to generate a higher bit rate signal. To allow dynamic switching and routing it is essential to develop all optical demultiplexers and add-drop multiplexers.

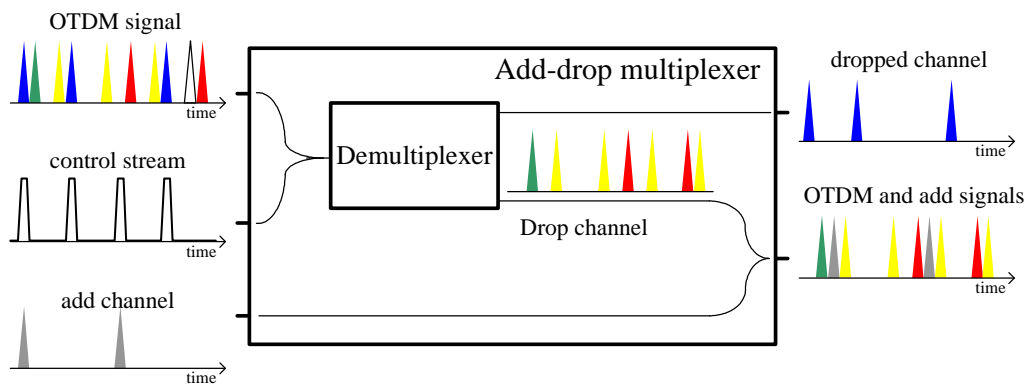


Figure 2-15. Schematic demonstration of the operation of a demultiplexer and an add-drop multiplexer. Different colours denote different sources of the OTDM signal.

Demultiplexing and add-drop multiplexing is illustrated in Figure 2-15. In a demultiplexer one of the bit interleaved channels is extracted from the higher bit rate data stream. The pulse train should be at the base data rate and in phase with the channel to extract. In an add-drop multiplexer one (or more) channel is extracted (*drop channel*) and is replaced by a new channel (*add channel*). The most promising results for demultiplexers and add-drop multiplexers based on SOA resort to interferometer XPM gates or the FWM effect. The following reported experimental achievements are worth highlighting: demultiplexing from 336 Gb/s to 10.5 Gb/s using a MZI structure in [81], and from 160 to 40 Gb/s using FWM in [82]; add-drop multiplexing from 160 to 10 Gb/s using a gain transparent UNI in [83].

### Clock Recovery and Regeneration

Clock recovery and regeneration are detailed and studied in Chapter 6.



### Pulse and modulation format conversion

Pulse Format converters are expected to be fundamental in the all-optical networks of the future, as different network scenarios require specific modulation and pulse formats [84]. Format converters are studied in-depth in Chapter 4, and pulse format converters in Chapter 5.

### Other applications

Besides the main applications described in the previous sections, SOA have also been employed in other applications, from which we highlight the following:

- Broadband light source using superluminescent light emitting diodes (SLED), which have basically the same structure as SOA [85];
- Continuous wave source, with experimental results of 50 wavelengths generation [86];
- Dispersion compensation using mid span spectral inversion through FWM [87];
- Short pulse generation, at high bit rates [88];
- Optical flip flops [89];
- Packet switches for optical packet switching (OPS) or optical burst switching (OBS) networks with contention resolution via wavelength conversion [90]; or delay of contention packets in synchronous networks [91].

## *2.10 Summary*

This chapter has presented an overview of the historical development of semiconductor optical amplifier (SOA) technology and the current-state-of the art including different materials and structures for the active layer, which determine the static and dynamic characteristics of SOA. SOA with specific design, such as reflective SOA, multi-electrode SOA, and gain-clamped SOA, have been presented as solutions for different applications.

The SOA gain and phase dynamics have been studied. The non-linear behaviour of SOA has been detailed, as it is the foundation of all-optical applications which will be studied throughout this work. The model considered for the simulation work has been presented, including intra- and inter-band effects.

A state-of-the-art in terms of the most preeminent applications of SOA in optical networks has been presented, with particular relevance for non-linear applications.

# Chapter 3

## Wavelength Conversion

### 3.1 Motivation

Wavelength converters (WC) are essential devices in wavelength division multiplexed (WDM) optical networks, as they allow wavelength reuse, dynamic routing, and avoid wavelength blocking [92][93], increasing the network throughput. Figure 3-1 demonstrates, with a simple example, how wavelength converters can reduce network wavelength blocking [94]. A uni-directional network with two available wavelengths,  $\lambda_1$  and  $\lambda_2$ , receives three traffic requests: between A and C, B and D, and C and B. If wavelength conversion is not supported, a single wavelength must be continuously utilized end to end for each traffic request. After serving connections  $A \rightarrow C$  and  $B \rightarrow D$ , the network

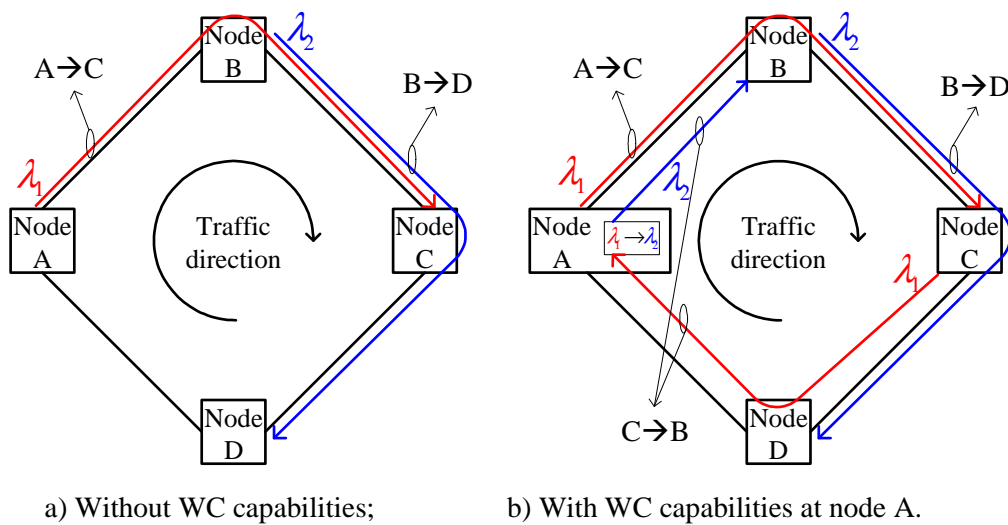


Figure 3-1: Exemplification of network capacity optimization through wavelength conversion (WC).

capacity is exhausted, as is exemplified in Figure 3-1 a). If WC capabilities are available at node A, all traffic requests can be served, as illustrated in Figure 3-1 b).

Wavelength conversion capabilities, together with pulse and modulation format conversion are also required in the interface between different hierarchies of optical networks, as discussed in more detail in Chapter 4 and Chapter 5.

A wavelength converter is a device capable to shift one input signal at wavelength  $\lambda_1$  to another wavelength  $\lambda_2$ , and is schematically illustrated in Figure 3-2. Wavelength converters can be divided in two groups [95]: optoelectronic WC (OEWc) and all-optical WC (AOWC). In OEWc the input optical signal at wavelength  $\lambda_1$  is detected, usually suffers regeneration, and is optically modulated using a laser with wavelength  $\lambda_2$ . On the other hand, in AOWC all operations are performed in the optical domain: there is no OEO conversion. OEWc have reasonable deployment in optical networks; however, these are limitative: OEWc present reduced transparency, and the costs increase with the bit rate and number of channels to be converted. Therefore AOWC have been intensively studied to avoid the so called “electronic bottleneck”.

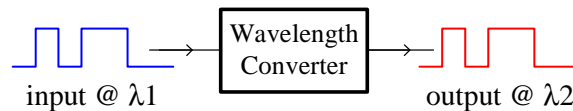


Figure 3-2. Schematic representation of a wavelength conversion.

Among the desired characteristics of a wavelength converter we highlight the following [92]:

- Bit rate independence;
- No extinction ratio degradation;
- Reduced signal to noise ratio degradation;
- Moderate input power required;
- Operation over a large input and output ranges of wavelengths;
- Operation over a large input power range;
- Low chirp;

- Simplicity;
- Polarization insensitivity.

Wavelength converters are of utmost importance since these also enable several other functionalities, such as optical logic or add-drop multiplexing of OTDM signals.

Wavelength conversion in SOA is mainly achieved through one (or more) of the following non-linear effects:

- Cross gain modulation (XGM);
- Cross phase modulation (XPM);
- Cross polarization rotation (XPR);
- Four-wave mixing (FWM).

This chapter presents a general overview of the operation principles and current state-of-the-art of SOA based wavelength converters in section 3.2. This section focuses in the four main sub-types, presented before.

In section 3.3 a technique to enhance the operation bandwidth of a XGM wavelength converter based on detuned optical filtering is proposed and studied; the detuned filter is optimized to allow conversion of the *slow SOA* device – which is usually limited to input bit rate of 2.5 Gb/s - up to 40 Gb/s. Simulation and experimental results are presented. The SOA bandwidth enhancement with detuned filtering was previously presented in [96] – [99].

A wavelength converter, suitable for return-to-zero (RZ) input signals, based on filtering of the XPM induced frequency chirp is assessed for the first time over gain-clamped SOA (GC-SOA) in section 3.4. The converter operation is experimentally validated at 2.5 Gb/s and at 10 Gb/s [100], [101].

In section 3.5 a XPM wavelength converter in MZI-SOA is experimentally characterized [102]. This characterization is the base for the results presented in section 3.6, where a 40 Gb/s 1 x 4 multi-wavelength converter is experimentally assessed and characterized [103]-[105].

## 3.2 Wavelength conversion techniques with SOA

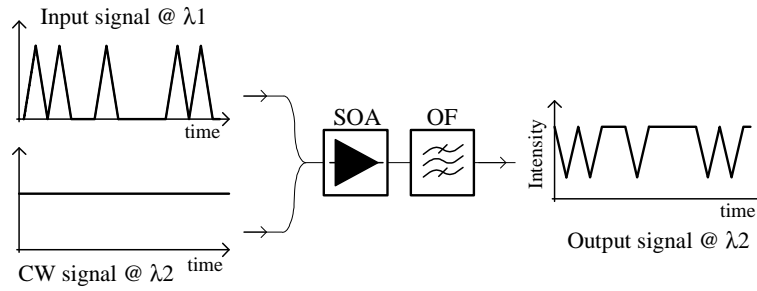
In this section, an overview is presented regarding the the main SOA-based wavelength conversion schemes. The section is organized according to the main non-linear effects: cross gain or phase modulation (XGM, XPM); cross polarization rotation (XPR); and four-wave mixing (FWM).

### 3.2.1 Cross gain modulation

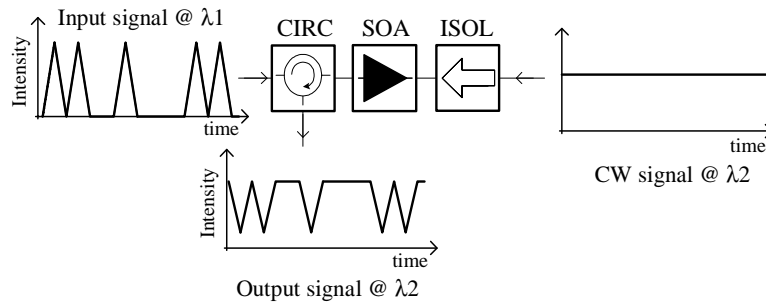
The rate of stimulated emission in SOA depends on the carrier density and distribution in the active region. When a strong optical pulse is injected in the SOA, the carrier concentration is depleted through stimulated emission, causing a decrease in the SOA gain. This effect is named *gain saturation*. This saturation affects all wavelengths within the SOA gain spectrum, since in SOA the material gain spectrum is homogeneously broadened [32].

When an intensity modulated information signal at  $\lambda_1$  and a continuous wave (CW) probe at  $\lambda_2$  are amplified simultaneously in a SOA, the gain is modulated with the inverse of the logical information carried by the information signal. Due to gain saturation effect, the CW signal intensity becomes modulated with the logical inverse of the input signal information. This simple modulation mechanism is commonly known as cross gain modulation (XGM).

As illustrated in Figure 3-3, XGM wavelength conversion in SOA can be performed in a co-propagation scheme – when the CW probe and the information signal travel in the same direction; or in a counter-propagation scheme – when the CW probe and the information signal travel in opposite directions. The counter-propagation scheme avoids the use of output optical filter, and allows conversion to the wavelength of the input signal (i.e.  $\lambda_2=\lambda_1$ ). However, the counter-propagation scheme is usually not used for operation at high bit rates, since as the transit time inside the SOA cavity approaches the order of magnitude of the bit period, the converted signal suffers amplitude distortion and temporal distortion [106] .



a) Co-propagation scheme;



b) Counter-propagation scheme.

Figure 3-3. Wavelength converter using cross gain modulation in a SOA.

Wavelength converters based on cross gain modulation in SOA are attractive because of their simplicity, high conversion efficiency, polarization independence (provided that the SOA is also polarization independent), capacity to enable conversion over a high range of input and output wavelengths, and multiple conversion at the same time [107], [108]. The main disadvantages are: small extinction ratio (because the gain is never reduced to zero); the changes in the carrier density within the SOA cause a variation in the refractive index, which will provoke a chirp in the converted signal; the conversion efficiency is dependent on the input and output wavelengths [92]; and the operation speed is limited by the slow carrier recovery times. In section 3.3 we explore a method to enhance the cross gain modulation bandwidth beyond the slow carrier recovery times, based on detuned optical filtering.

### 3.2.2 Cross phase modulation

As detailed in chapter 2.6.2, when a SOA is under gain saturation, the refractive index will change as a consequence of the gain saturation variations. The refractive index variations induce a phase change in the signals being amplified. This basic principle behind

XPM wavelength converters in SOA is illustrated in Figure 3-4. An intensity modulated (IM) information signal at  $\lambda_1$  and a CW probe signal at  $\lambda_2$  are simultaneously amplified in a SOA based scheme. If the power of the IM signal is enough to induce gain saturation, the output signal at  $\lambda_2$  is phase modulated with the input information. Since XPM affects the signal phase, and the converter should maintain the information in the intensity domain, it is then necessary to perform a phase to intensity conversion.

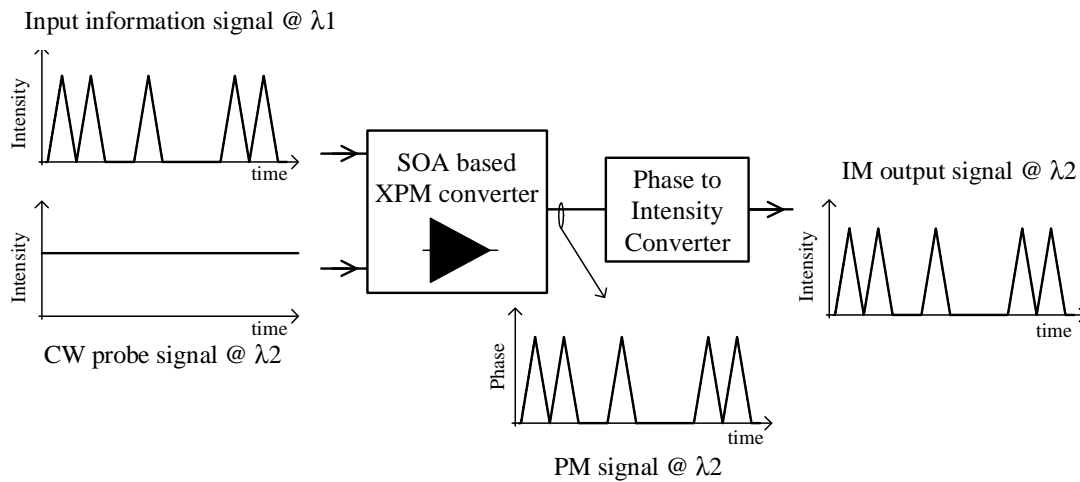


Figure 3-4: Illustration of an IM-to-IM wavelength converter based on cross-phase modulation (XPM) in SOA.

XPM based WC present significant advantages when compared to other techniques: high conversion efficiency and output extinction ratio; differential schemes can be employed to allow conversion beyond the SOA temporal response; and the output signal information is not logically inverted. XPM converted signals have narrow spectrum when compared to XGM signals, allowing transmission over higher distances of fiber [92] and higher spectral efficiency. The main disadvantage is the increase in complexity due to the additional PM to IM conversion. Moreover, it should be noted that in SOA XPM and XGM occur simultaneously, therefore the converted PM signal also presents IM distortion, which may introduce patterning effects due to the recovery time of the SOA.

### 3.2.2.1 Filter assisted XPM wavelength conversion

Figure 3-5 represents the instantaneous frequency of a probe signal at the SOA output, when a pulse is simultaneously propagated at a different wavelength. When the input signal power is at constant power level (either high or low power), the CW probe



signal wavelength remains unchanged ( $\lambda_2$ ). For the leading edged of an optical pulse the pump signal shifts to upper wavelengths – this is usually known as a red wavelength / frequency chirp. For trailing edges of the optical pulse a blue wavelength / frequency chirp occurs: the CW probe wavelength shifts to lower values.

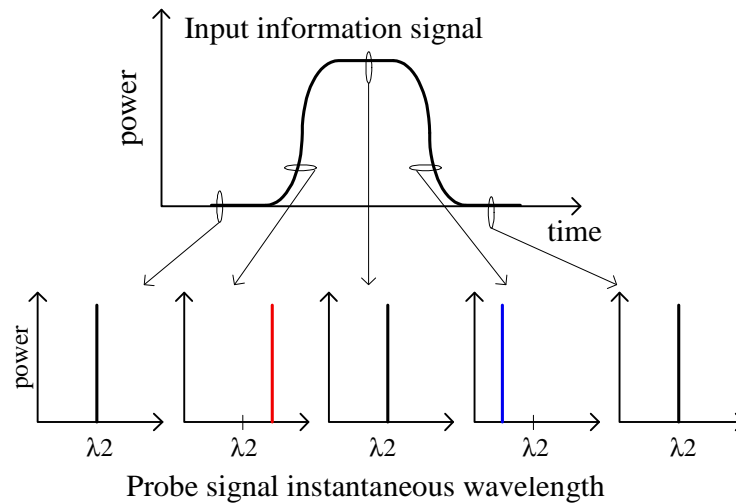


Figure 3-5: Illustration of the instantaneous frequency of the probe signal due to XPM modulation in SOA.

One very popular technique to convert the phase modulation to intensity modulation in SOA is optical filtering of the converted signal at the SOA output with a detuned filter [109], portrayed in Figure 3-6. An optical filter is detuned from the probe signal central wavelength and aligned with the blue or red part of the converted signal spectrum, retrieving an optical pulse of each leading / trailing transition of the input signal. The central wavelength of the converted signal is detuned from  $\lambda_2$  by the signal clock frequency; the discrete clock tone becomes the new optical carrier. This technique is not appropriate for NRZ signals, since for consecutive ‘1’s the NRZ signals do not have power fluctuations not causing frequency chirping.

This technique is popular for several reasons: it is simple, as the only device required, besides the SOA, is an optical filter; the output signal maintains the RZ shape; and the output extinction ratio is usually very high. Since the red chirp is associated with ultra-fast gain depletion, this converter has proved operation at ultra high bit rates such as 320 Gb/s [111]. The disadvantages of such scheme are that a very stable pump laser is required; otherwise the optical filter may provoke pulse distortion; this technique is not

appropriate for NRZ pulse format; and the converted signal may present residual distortion due to XGM.

In the literature, this technique has been demonstrated only over common SOA. In section 3.4 XPM wavelength conversion technique with PM to IM conversion through detuned optical filter is experimentally demonstrated with gain-clamped SOA devices.

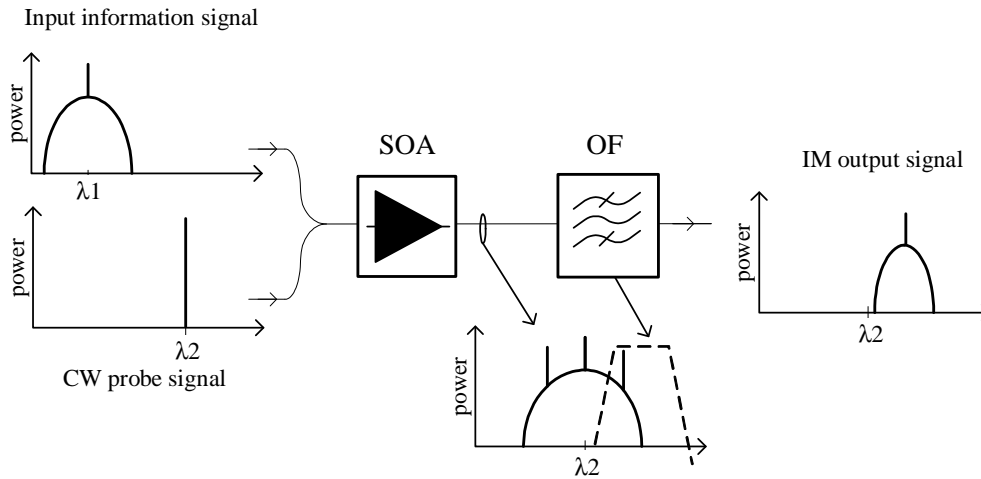


Figure 3-6: Illustration of XGM wavelength conversion by means of SOA and detuned optical filter.

### 3.2.2.2 XPM converters with standard-mode interferometric structures

Interferometric structures are widely used to obtain phase modulation to intensity modulation conversions. XPM wavelength converters based on interferometer structures can operate on standard mode or differential mode. Hereafter standard mode interferometer structures are reviewed. Differential mode structures are detailed in section 3.2.2.3.

#### Mach-Zehnder interferometer with SOA (MZI-SOA)

Figure 3-7 presents the basic scheme for a MZI-SOA wavelength converter in standard mode operation. The basic converter structure requires a local CW probe signal with optimized polarization. This signal is amplified in both the SOA of the MZI structure. In the upper SOA the input information signal is also amplified, provoking the XPM. In the lower arm the probe signal is amplified alone. In absence of information signal, the two pump replicas combine with destructive interference at the output of the MZI-SOA. When there is a pulse at the input, the phase difference between the two replicas is no longer  $\pi$

and an optical pulse is then transmitted at the probe signal wavelength. Finally, the optical filter at the output eliminates the input signal wavelength.

Although it is possible to operate interferometer structures with discrete components, great advantages outcome from monolithic integration, since it allows long term stability [92]. Other MZI-SOA structures are possible, for example, in a counter propagating scheme, the optical filter at the output is not necessary. MZI-SOA structures usually incorporate phase shifters in each arm (not represented in Figure 3-7) and independent bias current control to optimize the operation conditions.

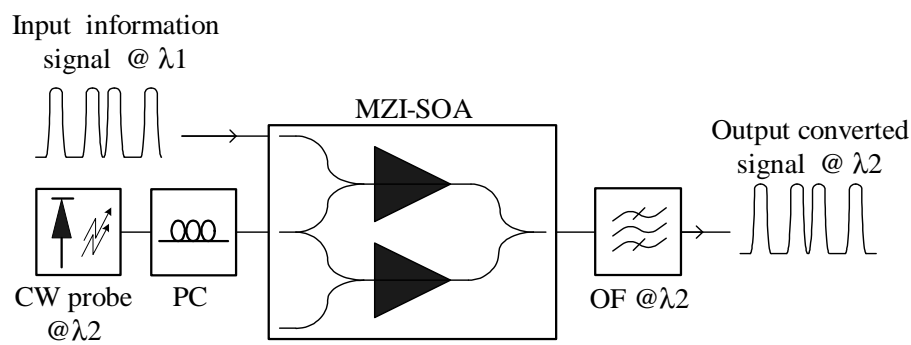


Figure 3-7: Standard mode MZI-SOA wavelength converter.

Compared to the detuned filtering technique, the standard mode MZI-SOA has the advantage that it is not necessary to have high precision optical filter. On the other hand, it is limited by the slow recovery times of SOA. Results from Nielsen et al. [112] demonstrate standard mode conversion at 40 Gb/s using SOA with ultrafast response.

#### Michelson interferometer with SOA (MI-SOA)

Michelson interferometer with SOA (MI-SOA) wavelength converter is represented in Figure 3-8. A CW probe signal is fed to the MI-SOA, where it is split and amplified in two SOA. The two SOA have reflective coefficients different from 0; therefore, a part of the CW signal wavelength is reflected back. The probe signal is then coupled and leaves the MI-SOA. In absence of light of the input signal, the two replicas of the probe signal interfere with destructive interference. For an input pulse, the phase modulation in the upper and lower SOA differ and a pulse is generated in the probe signal at the output.

MI-SOA structure has generally been abandoned in favor of the MZI-SOA, since in the former the probe signal is amplified twice in the SOA. For a typical SOA with active

length of 1 mm, the round trip time in the SOA cavity is around 25 ps, which is the bit period of a 40 Gb/s signal. For such reason, wavelength conversion in MI-SOA is limited to signals with bit period very long, when compared to the SOA round trip time. To the best of our knowledge, the maximum bit rate reported for wavelength conversion in MI-SOA is 10 Gb/s [113]. Moreover, currently there are no MI-SOA commercially available.

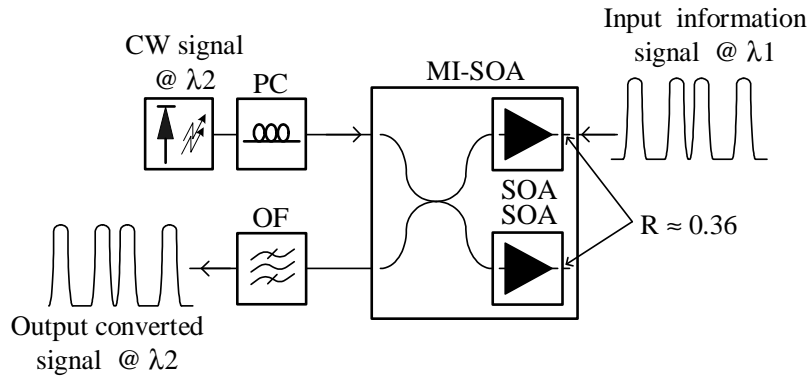


Figure 3-8: Standard mode MI-SOA wavelength converter.

### 3.2.2.3 XPM converters with differential-mode interferometric structures

Standard mode interferometric structures have been reviewed in the previous section; these are simple; however, are limited by the SOA recovery time. Differential-mode structures allow to overcome such limitation and are presented in this section. Figure 3-9 compares standard- and differential-mode interferometric structures. In the standard mode, the probe signal at  $\lambda_2$  is split in two replicas: one of the replicas suffers XPM, caused by an input pulse at  $\lambda_1$ ; whilst the second replica is not affected by the input signal (i.e. its phase remains un-modulated). At the interferometer output the two probe signal replicas interfere (i.e. are subtracted with each other). As a result, a transmission window opens due to the input pulse and the phase modulation of the first probe signal replica is converted to intensity at the output. If short optical pulses (when compared to the SOA dynamics) are converted, the output signal has a fast rise time, but the fall time is limited by the slow carrier recovery. In the differential mode, both replicas of the probe signal suffer XPM, caused by the input signal. However, the second replica has lower PM intensity and its phase modulation is delayed when compared to the first replica. At the interferometer output the transmission window is limited by the delay between the phase modulation of

the two replicas; therefore, the output signal is not limited by the SOA slow recovery time. For more information on the difference between the time dynamics of SOA during saturation and recovery, consult section 2.5. The main SOA based wavelength conversion schemes with differential operation are detailed below.

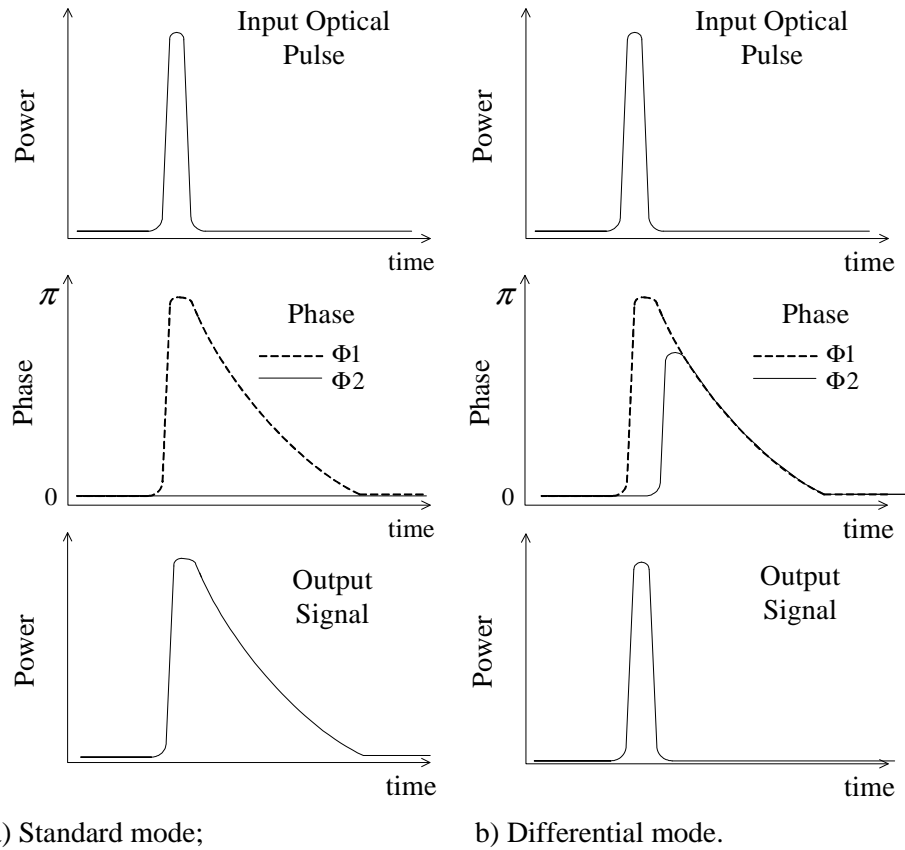


Figure 3-9: Schematic comparison between standard and differential mode XPM based on interferometer structure [13].  $\Phi 1$  and  $\Phi 2$  represent the phase of the two replicas of the probe signal.

### Differential mode MZI-SOA

The most common differential scheme is illustrated in Figure 3-10 and employs a MZI-SOA [114]. Contrary to the standard mode, where the information signal is fed only to one of the MZI-SOA arms, in the differential mode the input intensity modulated signal is split in two replicas. One of the replicas (the lower replica in Figure 3-10) suffers additional delay and attenuation when compared to the upper replica. Each replica of the probe signal suffers XPM, caused by the input signal. Since the phase modulations of the two probe signal replicas are delayed, a transmission window opens in the interferometer output and a short optical pulse is generated. This method is also known as push-pull.

The operation of this converter is not completely independent of the carrier recovery, since for high bit rates the pump signal phase does not have time to completely recover (reach  $0^\circ$ ) between consecutive bits, causing patterning effects. Nevertheless, this structure has allowed wavelength conversion up to 168 Gb/s [115].

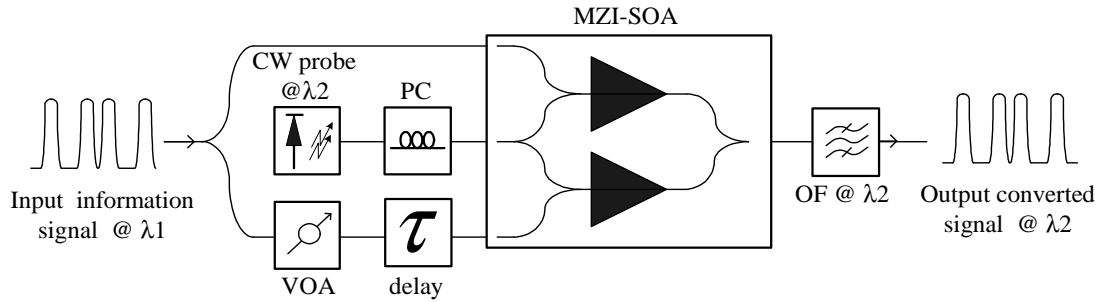


Figure 3-10: Differential mode MZI-SOA wavelength converter.

Differential mode and standard mode MZI-SOA wavelength conversion is experimentally characterized in section 3.5 at 10 Gb/s. A differential mode MZI-SOA scheme is used in section 3.6 to achieve multi-wavelength conversion at 40 Gb/s.

#### Semiconductor Laser in a Loop Mirror

The semiconductor laser in a loop mirror (SLALOM) was the first structure where the differential mode XPM was introduced [116], [117]. It is also known as non-linear optical loop mirror (NOLM), or terahertz optical asymmetric demultiplexer (TOAD) when operated as a demultiplexer.

The SLALOM is a Sagnac interferometer with a SOA placed slightly asymmetrically, with regards to the center of the loop, as represented in Figure 3-11. The CW probe signal is fed to the loop through a 3 dB coupler and split in two components that propagate through the loop in opposite directions. In absence of input signal power, both components acquire the same phase shift in the SOA and recombine with destructive interference at the coupler. In the presence of the data signal, the pump signal suffers a phase shift in the SOA. Due to the asymmetry of the placement of the SOA, a delay ( $\tau$ ) – corresponding to  $2\Delta x/c$  (where  $\Delta x$  is the difference in distance between the two paths) – between the two components of the probe signal will result in a window of constructive interference at the output. The switching window (the pulse width at the output) is defined by the SOA displacement.

This scheme originates an asymmetric switching window, since the trailing edge of the switching window is determined by the length of the SOA (since the counter clock-wise component is traveling in counter propagating relatively to the data signal), whilst the leading edge is determined by the stimulated lifetime of the carriers. This scheme is, therefore, limited to a maximum bit rate of approximately  $v_g/2L$ , where  $L$  is the length of the SOA. The SLALOM has been employed as an OTDM add drop multiplexer [118] and as wavelength converter [119].

Compared to the MZI, the SLALOM is more stable when operated in a discrete scheme, since the interfering components in the SLALOM share the same physical medium. In MZI-SOA the interferometer arms are physically separated and will have different perturbations (e.g. thermal fluctuations).

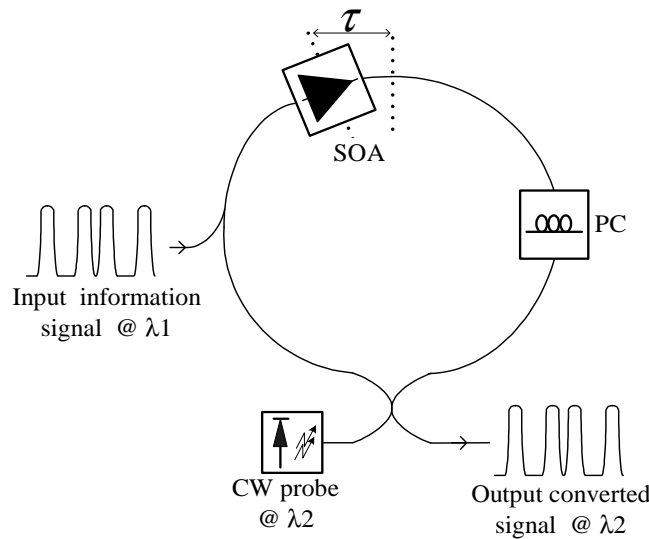


Figure 3-11: Semiconductor laser in a loop mirror (SLALOM) wavelength converter.

### Delayed-Interference Signal Converter

The delayed-interference signal converter (DISC) is one of the simplest wavelength converter schemes based on XPM in SOA. The basic scheme is represented in Figure 3-12. The information and CW probe signals are fed to a SOA and amplified simultaneously and the probe signal suffers XPM. The optical signal after the SOA is then fed to a MZI. The upper arm of the MZI has an additional delay,  $\tau$ , when compared to the lower arm. At the MZI output the two replicas are combined with destructive interference; therefore a logical

'0' is retrieved at the CW wavelength for '0' of the information signal. In presence of the data signal, the CW suffers a phase shift in the SOA. As a consequence, the two signals are recombined with constructive interference, and a transmission window, with width of  $\tau$ , is created. The phase shift is necessary to compensate the fact that with a single SOA it is not possible to ensure that  $\Phi_{\text{XPM}}(t) = \Phi_{\text{XPM}}(t+\tau)$  - where  $\Phi_{\text{XPM}}$  is the phase of the cross phase modulated signal. The DISC has been used to achieve WC at bit rates up to 640 GHz [14], [120].

The DISC, although simple, requires an MZI with delay and phase shift which must be optimized to the input signal bit rate and to the wavelength of the probe signal. This requires additional complexity and costs in case tracking of input wavelength is required.

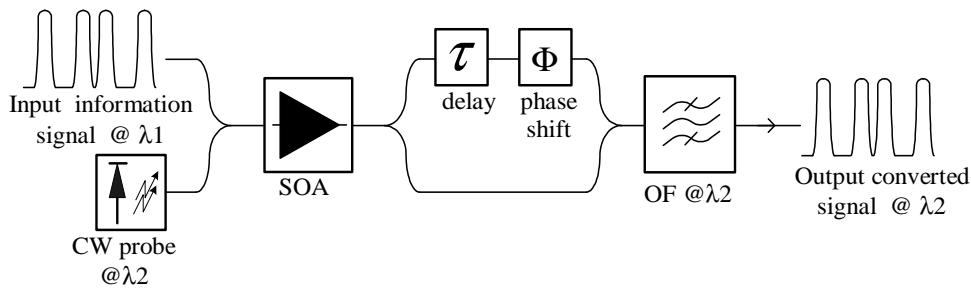


Figure 3-12: Delayed interference signal converter (DISC).

#### Comparison with fiber based interferometer structures

Highly non-linear fibers can also be used to as non-linear medium in interferometer switches. Comparing these with SOA based devices results in the following main differences:

- Due to the non-resonant nature of the fiber nonlinearity, the fiber response is not limited by recovery processes, therefore it is not necessary to employ differential schemes; and the response is independent on the repetition rate of the data signal;
- The effective nonlinearity in fiber is much lower than in SOA; therefore, high interaction lengths are required; the XPM is dependent on the state of polarization of the light signals;
- In fiber the cross-phase modulation depends on the state of polarization of the two signals [13];
- SOA have great potential for integration;



- SOA provide optical gain and usually require moderate power levels at input.

#### 3.2.2.4 Gain Transparent Operation

In all the XPM based wavelength conversion structures referred above, the probe signal also undergoes XGM non-linearity. XGM is usually undesired in schemes based on XPM, since it introduces patterning effects and degradation of the output signal. An operation mode called gain-transparent was proposed by Diez et. al.[118] to mitigate the harmful effects of the gain compression non-linearity.

In a SOA, the maximum refractive index change occurs at the wavelength where the SOA gain is maximized. Since the changes in the refractive index lead to the desired phase variations which cause XPM, the maximum gain wavelength is usually chosen to be the operating wavelength of schemes relying on such non-linear effect. For higher wavelengths (the so called gain transparent region), low gain changes are obtained; however, it is still possible to achieve significant refractive index variations. In the gain transparent operation mode, the wavelength of the data control signal is tuned to the maximum gain wavelength of the SOA, but the wavelength of the probe signal is set to the transparent region. Another advantage is the insignificant noise emission in the gain transparent region. The gain transparent operation mode has allowed interferometer schemes to operate as de-multiplexer, optical sampler and add/drop multiplexer [13]. The main disadvantages of such operation mode are that the probe signal is not amplified, and such converters are limited to out-of-band probe wavelengths.

### 3.2.3 Four-wave mixing

Optical wave-mixing results from the non-linear interactions of the optical waves present in the non-linear material, which, in the case of SOA, is the semiconductor. A full-description of four-wave mixing (FWM) fundamentals is out of the scope of this work and can be found in [121] - [125].

Figure 3-13 presents a typical FWM wavelength converter scheme. An input data signal at  $\lambda_1$  and a CW probe signal at  $\lambda_2 = \lambda_1 + \Delta$  are injected simultaneously in a SOA with the same state of polarization. The SOA carrier density and distribution are modulated

by the beating of the two waves in the active medium, which generates dynamic index and gain gratings. The interaction of the injected waves with these gratings leads to the creation of new frequency components, called the FWM components. Of particular interest is the FWM signal that is generated at frequency  $\lambda_2 + \Delta$ , usually designated *conjugate wave*, because its phase is the conjugate of the data signal.

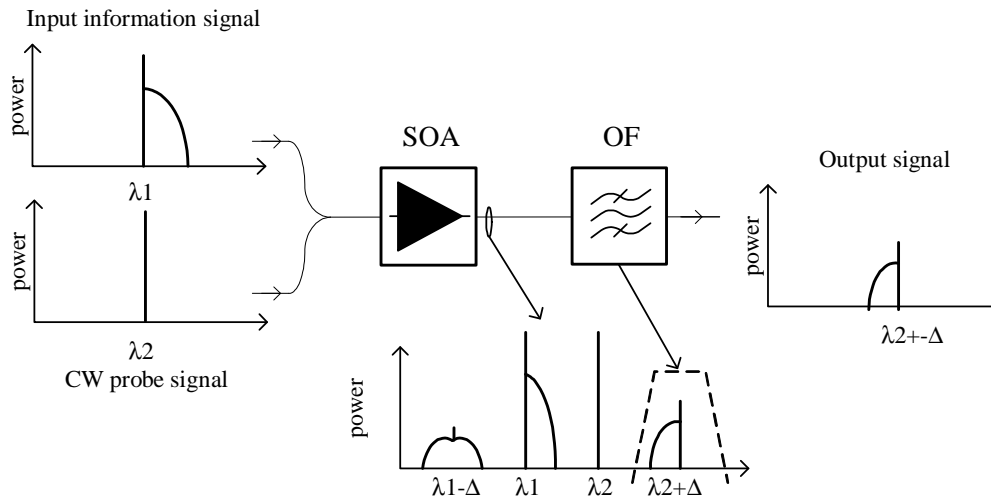


Figure 3-13: Illustration of FWM wavelength conversion in SOA.

FWM in SOA originates from both inter- and intra-band effects. For a detuning,  $\Delta$ , in the order of few tenths of GHz, FWM efficiency is high, due to the modulation of the carrier density at the beat frequency, which is an inter-band process. However, the modulation rate of the carrier density is determined by the effective carrier lifetime, as referred before. For higher detuning values, the efficiency of this mechanism declines and the intra-band dynamics will dominate. The most preeminent intra-band effects involved in FWM are those related with SHB and CH, which have very fast relaxation time, which implies ultrafast operation, allowing performance in conversion above hundreds of Gb/s [126][127]. In [128] experimental operation over 160 GHz signals is reported.

The main advantages of FWM in SOA include:

- The inherent speed of the process;
- The generated signal reproduces the input signal, being ideal for phase sensitive modulation formats;
- Low optical powers are required at the input of the device.

- FWM in SOA has an intrinsic high efficiency compared to nonlinear crystals or optical fibers, enabling shorter interaction lengths of the injected waves and decreasing the phase matching requirements;

On the other hand, the main disadvantages of FWM in SOA are [127]:

- Penalties in the OSNR due to the ASE of the SOA;
- Waveform distortion due to the gain compression of the SOA;
- The efficiency is polarization dependent;
- Lower efficiency when compared to other mechanisms (for example XGM).

### 3.2.4 Cross-Polarization Rotation

The operation of cross-polarization (XPR), or non-linear polarization switching (NPS), wavelength converters can be understood from the illustration of Figure 3-14, where a low power probe signal, with well defined polarization, is amplified in a SOA simultaneously with the input intensity modulated data signal. The gain saturation of the transversal electric (TE) mode differs from that of the transversal magnetic (TM) mode [129], [130]. Consequently, the refractive index changes of the TE and TM modes, caused by gain saturation, are also different. The output signal will then have different phase modulation in the two modes.

To exemplify the XPR operation, suppose that the probe signal is polarized with the same power at the two modes (at  $45^\circ$ ) at the SOA input, and that, in the absence of data signal light, there is no probe phase rotation between the two modes. The polarization controller (PC) and the polarization beam splitter (PBS) are adjusted to guarantee that in this condition the output power is cancelled at the probe signal wavelength. When an optical pulse and the probe are simultaneously amplified in the SOA, the state of polarization of the probe signal is changed by the SOA. If the state of polarization is rotated by  $90^\circ$ , a strong optical pulse will be transmitted at the output of the PBS. Single- and multi-wavelength conversion at 40 Gb/s was reported using the XPR effect [131]. When compared to XGM, this method has the advantage of allowing high ER; however the conversion efficiency is lower. Similarly to XGM, the applicability of this method to high bit rate signals is limited by the slow carrier density recovery.

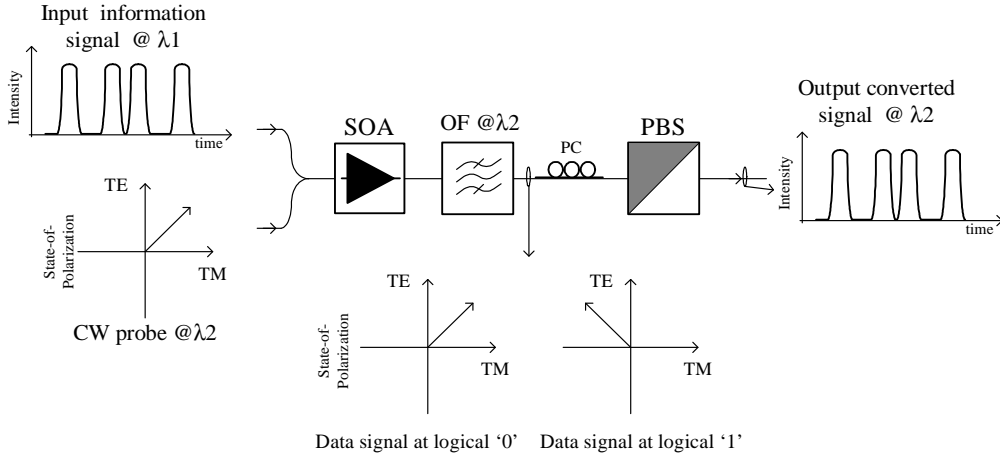


Figure 3-14: Schematic representation of the setup to perform cross-polarization (XPM) wavelength conversion and operation principle.

### 3.3 Enhancement of cross gain modulation bandwidth

Cross-gain modulation converters are limited by the slow SOA recovery times, as referred above. In this section, enhancement of the bandwidth of XGM wavelength converters is studied and detuned optical filtering is employed to allow operation beyond the gain recovery limitations.

#### 3.3.1 Decrease of the SOA effective carrier lifetime

The modulation of the carrier density ( $\Delta N$ ) for a given input photon density  $S_{in}$  at the frequency  $f_{mod}$  for a very short amplifier can be approximately described by [106]:

$$\Delta N(f) \approx g_T \cdot S_{in} \cdot v_g \cdot \frac{\tau_{eff}}{1 + j \cdot 2\pi \cdot \tau_{eff} \cdot f_{mod}}, \quad (3-1)$$

where  $v_g$  is the group velocity,  $g_T$  is the material gain and  $\tau_{eff}$  is the effective carrier lifetime, which is approximately given by [106]:

$$\frac{1}{\tau_e} \approx \frac{dR_{SN}}{dN} + \frac{dg}{dN} \cdot S_{out} \cdot v_g, \quad (3-2)$$

With  $R_{SN}$  the stimulated recombination factor,  $S_{out}$  the SOA output photon density, and  $dg/dN$  is the differential gain coefficient. From (3-1) we verify that the carrier modulation response exhibits a low pass characteristic with an optical 3dB bandwidth of:

$$BW_{3dB} \approx \frac{\sqrt{3}}{2\pi \cdot \tau_{eff}} \quad (3-3)$$

From (3-1)-(3-3), we conclude that the lower is the effective carrier lifetime, the higher is the SOA carrier modulation bandwidth. Effective carrier lifetime reduction is achieved when the output photon density and the differential gain are increased. Consequently, improvements outcome from enhancing the following parameters:

- Current injection;
- Optical input power;
- Confinement factor;
- Differential gain.

To increase the factors referred above, longer SOA have been designed [106]. However, increasing the length of the SOA also has some disadvantages: it is difficult to fabricate very long SOA with uniform cross sections of the active region; the spectral gain bandwidth of the SOA diminishes as the length of the cavity increases. Moreover, the transit time increases for long SOA; therefore, only co-propagation of the input signal and the CW can be used (since the counter-directional scheme has speed limitations, such as jitter that arises for high bit rate signals).

Increasing the SOA driving current is one of the simplest ways to reduce the SOA temporal response. Figure 3-15 presents the normalized intensity pulse response of the *fast* SOA device (consult appendix II for characteristics of the SOA devices) when the injection current is 200 mA, 300 mA and 400 mA. Increasing the injection current reduced the temporal recovery time from 10 % to 90 % from 119 ps to 78 ps and 62 ps, respectively. Nevertheless, the maximum current density in the SOA is limited, thus the current can not be increased indefinitely.

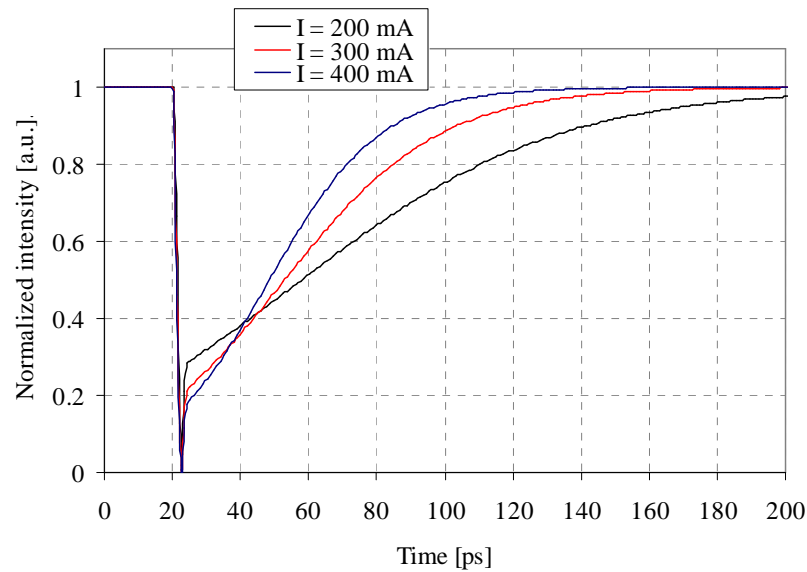


Figure 3-15: Simulated temporal response to an optical pulse with a low power probe and a high power probe at the SOA input.

The use of a holding beam was proposed [63] to increase the power level inside the SOA, enabling higher modulation speed for the carriers. Figure 3-16 presents the normalized intensity response to an optical pulse by the *fast SOA* device. When pumped by a low power signal (-20 dBm), the recovery time is around 78 ps; however, when pumped by a -5 dBm CW signal, the recovery time is reduced to 53 ps. Although it reduces the SOA temporal response, the holding beam method has the disadvantage of reducing the converted signal extinction ratio (ER).

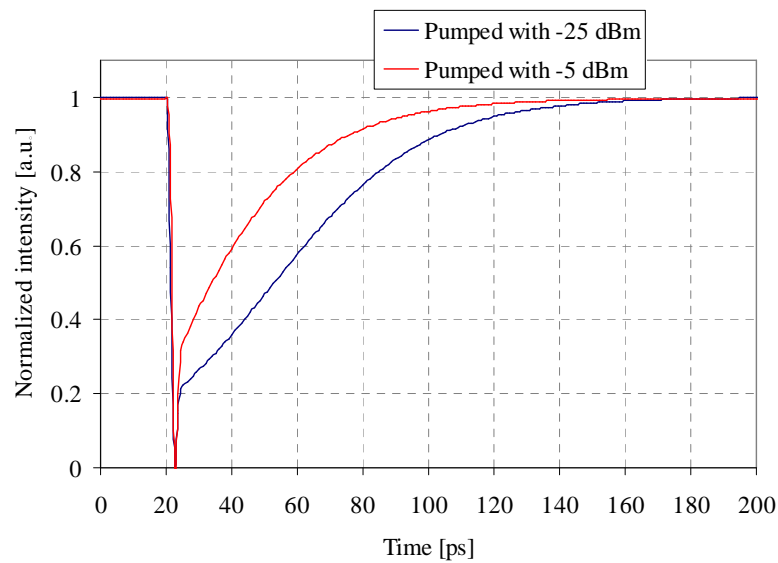


Figure 3-16: Simulated temporal response to an optical pulse with a low power probe and a high power probe at the SOA input.

### 3.3.2 XGM bandwidth enhancement by detuned filtering

We have demonstrated in the previous section that the XGM bandwidth is improved when the SOA effective carrier lifetime is reduced. Pumping the SOA with high powers or increasing the injection current are simple methods to improve the SOA response; however, pumping the SOA reduces the output signal ER, and the injection current has an upper limit, which depends on the device characteristics, but is typically below 500 mA. Employing such techniques, current state-of-the-art SOA devices are still limited to recovery times in the order of the tens of picoseconds: SOA manufacturers CIP and Amphotonix currently report recovery times around 25 ps [133], [134]. Therefore, it is important to further enhance the bandwidth of XGM in SOA to enable operation in the range of the hundreds of GHz. In this section, a simple method, based on detuned optical filtering, is proposed to enhance the XGM bandwidth beyond the SOA recovery times.

#### 3.3.2.1 Operation principle

To understand the operation principle of the XGM bandwidth enhancement via detuned optical filtering, consider Figure 3-17, which presents the simulated temporal shape and the frequency chirp shape of a XGM converted signal. The *slow SOA* device and a 10 Gb/s NRZ input information signal are considered. In this analysis, the power of the input and CW probe signals at the SOA input are -3 dBm and 0 dBm, respectively.

After the SOA, the CW probe signal is amplitude modulated with the logical inverse of the input information signal, due to cross gain modulation. However, due to the SOA limited response time, patterning effects occur, as can be verified on the intensity of the XGM signal in Figure 3-17, and inter-symbol interference (ISI) is provoked. Since the power variations of the data signal lead to variations in the refraction index, cross phase modulation occurs simultaneously with XGM in the SOA. The SOA output signal frequency chirp is also represented in Figure 3-17. A positive frequency chirp (blue chirp) happens in the transitions of '1' to '0' of the data signal and a negative chirp (red chirp) on the '0' to '1' transitions. These frequency chirps lead to a change of the instantaneous wavelength of the probe signal inside the SOA, as illustrated already in Figure 3-5.

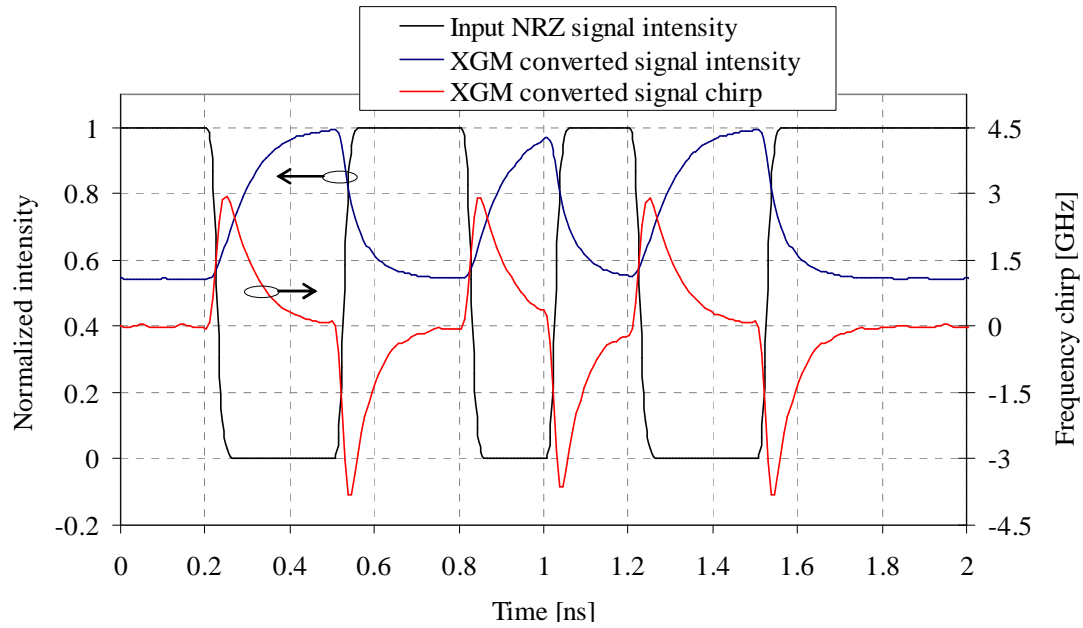


Figure 3-17: Simulated temporal characterization of cross gain modulated signal intensity and frequency chirp. The *slow SOA* device is considered..

Since the instantaneous probe signal wavelength changes with the transitions of the input signal, if the SOA output signal is filtered by a thin optical filter with positive frequency detuning from its central wavelength, a pulse is retrieved at each ‘1’ to ‘0’ transition of the input signal; similarly a pulse is obtained if at each ‘0’ to ‘1’ transitions in case the detuning is towards negative frequencies. To verify this conjecture a 3<sup>rd</sup> order Gaussian filter with -3 dB bandwidth of 10 GHz is employed. To retrieve the blue chirped part of the spectrum it is detuned by 6.5 GHz relatively to the probe signal central wavelength; to obtain the red chirped part of the spectrum the detuning is -10 GHz. Figure 3-18 presents the temporal shape of the original XGM signal and of the resultant signals after filtering with the 3<sup>rd</sup> order Gaussian filter.

Figure 3-18 demonstrates that the blue chirp filtered signal presents an optical pulse when the XGM signal is increasing its power and the red chirp filtered signal presents a pulse when the XGM signal is decreasing its power. Enhancing the power of the blue chirped part of the spectrum will lead to a stronger (faster) rising edge of the XGM signal; on the other hand, the red chirp part of the spectrum is impeding the XGM signal to return back to a low power level. Following this line of thought, faster response is expected if the blue chirped part of the spectrum is enhanced with relation to the red chirped part. Enhancement of the blue chirped part of the spectrum will be achieved hereafter using an



optical filter detuned from the probe signal central wavelength. Since the optical filter is detuned, the power of the red chirp part of the spectrum will be decreased in relation the blue chirp part.

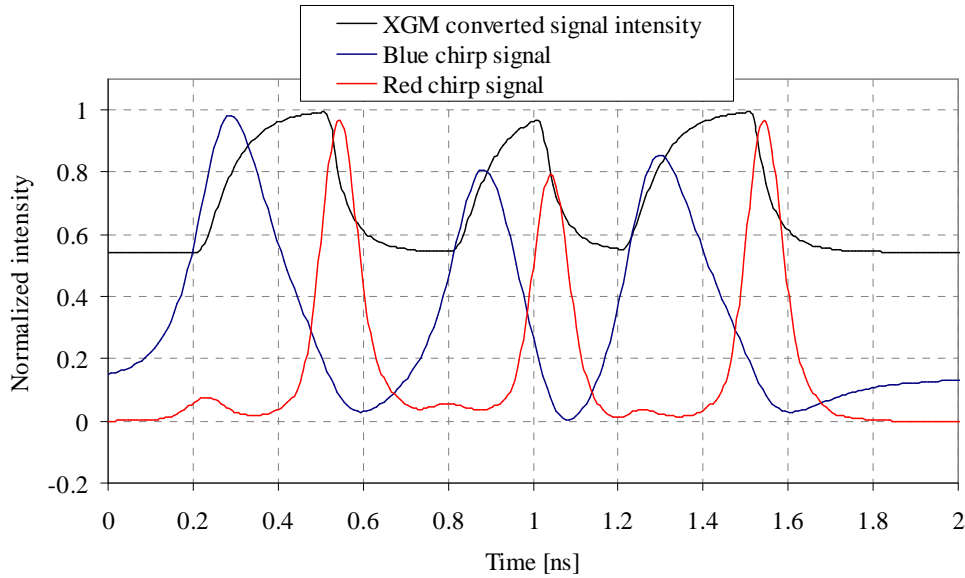


Figure 3-18: Simulated temporal intensity of the XGM signal and of the filtered blue and red chirp parts of the XGM signal spectrum, for a bit rate of 10 Gb/s.

This XGM bandwidth enhancement method relies on conversion of the phase modulation, provoked by XPM, in intensity modulation, by detuned filtering. The underlying principle can also be used to obtain RZ to RZ wavelength conversion, as detailed in section 3.2.2.1, where a detuned optical filter is used to completely isolate the red / blue part of the optical spectrum. The main difference between the two techniques is that, in the converter of section 3.2.2.1, the optical carrier and one of the sidebands of the SOA output signal are completely rejected by the detuned filter. In the XGM bandwidth enhancer the detuned optical filter only enhances the blue sideband in relation to the red sideband and there is no rejection of the optical carrier; therefore, the signal maintains the NRZ pulse format.

### 3.3.2.2 Simulation tests and filter optimization

#### 10 Gb/s results

The detuned filter bandwidth enhancer will be tested using the *slow SOA* device to assess the potential to enhance its operation bandwidth from 2.5Gb/s (its optimal

maximum bit rate) to 10 and 40 Gb/s. To characterize the performance of this method, the modified eye opening penalty (MEOP) will be considered. MEOP is used in detriment from the standard eye opening penalty (EOP) to isolate the signal penalties caused by the SOA slow response from those caused by ER variation. For more information on EOP and MEOP consult appendix III.

Figure 3-19 presents the common XGM converted signal at the SOA output when the SOA input powers of the information and probe signals are -3 and 0 dBm, respectively. The signal eye diagram presents significant closure due to the slow carrier dynamics. The XGM signal MEOP is 3.5 dB.

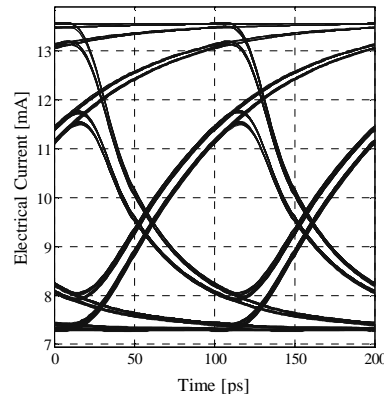


Figure 3-19: Common XGM signal eye diagram

The XGM bandwidth enhancement scheme operation principle is based on enhancing the blue chirped part of the XGM converted signal spectrum in relation to the red chirped part and to the optical carrier. First, a filter similar to that of Figure 3-20 is considered. The zero frequency refers to the central wavelength of the probe signal. The filter attenuation is zero for  $f > f_{\text{pos}}$ ;  $\text{Att}_0$  refers to the attenuation at the optical carrier frequency, and  $\text{Att}_{\text{neg}}$  refers to the attenuation at  $f_{\text{neg}}$ .

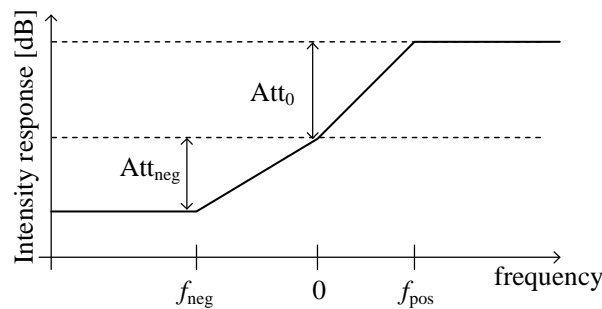


Figure 3-20: Optical filter to enhance XGM bandwidth.

It was verified that the XGM enhancement method performance is optimized when  $f_{\text{pos}}$  and  $f_{\text{neg}} \gg f_{\text{BR}}$ , with  $f_{\text{BR}}$  the frequency equal to the bit rate of the data signal. As such,  $f_{\text{pos}} = f_{\text{neg}} = 3 \cdot f_{\text{BR}}$  was considered. Figure 3-21 presents the eye closure penalty as a function of the  $\text{Att}_0$  and  $\text{Att}_{\text{neg}}$ . It can be verified from the curves of Figure 3-21 that when the filter characteristics are optimized, the converted signal MEOP can be improved to approximately 0.6 dB, which is obtained with  $\text{Att}_0 = 9$  dB and  $\text{Att}_{\text{neg}} = 7$  dB. It was verified (not represented in the figure) that if the optical filter is designed to enhance the red chirped part of the spectrum (i.e.  $\text{Att}_0$  and  $\text{Att}_{\text{neg}} < 0$ ), the output signal degrades, even when compared to standard output XGM signal (when the optical filter is centered with the probe signal wavelength).

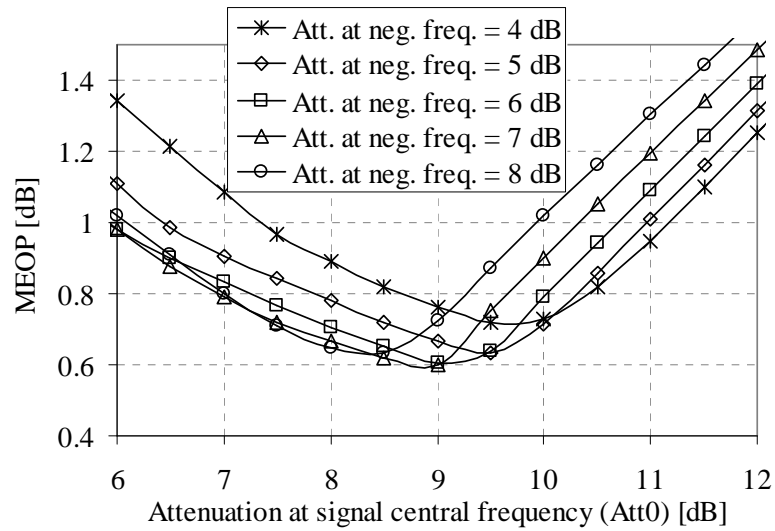
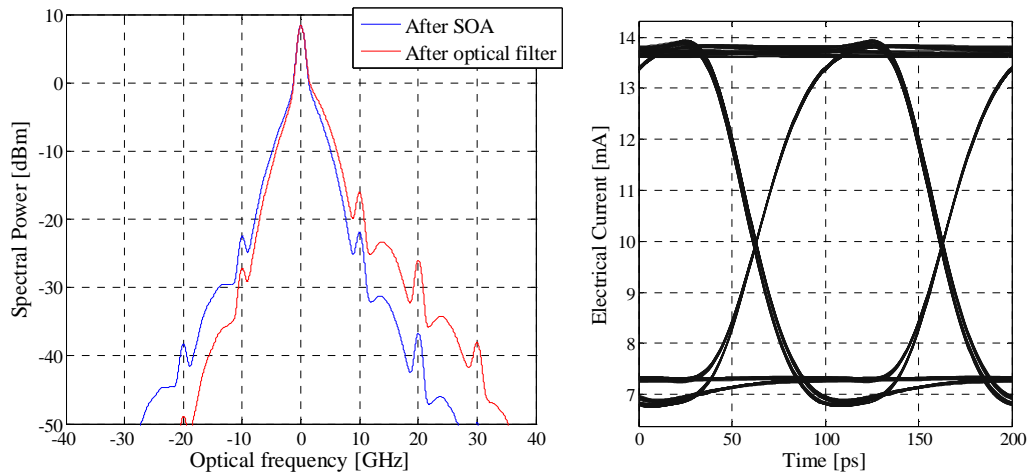


Figure 3-21: Eye closure penalty as a function of the gain at positive frequencies and attenuation at negative frequencies.

Figure 3-22 presents the optical spectra and eye diagrams of the detuned optical filter output signal. It can be verified that after the optical filter the positive (blue) frequencies are enhanced in relation to the optical carrier. On the other hand, the negative (red) frequencies are attenuated. As referred above, with this technique there is no rejection of the optical carrier. As expected, the optical filter improves both the leading and trailing edges of the optical signal when compared to the SOA output signal of Figure 3-19; as a consequence, the output eye diagram is practically undistorted.

The previous test demonstrated that with an enhancement of the blue chirped part of the spectrum relatively to the optical carrier and the red chirped part of the spectrum, the

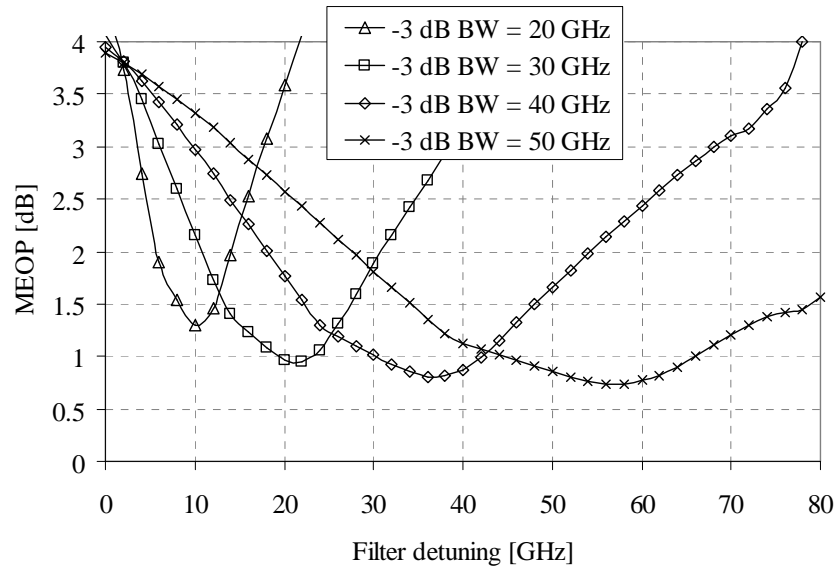
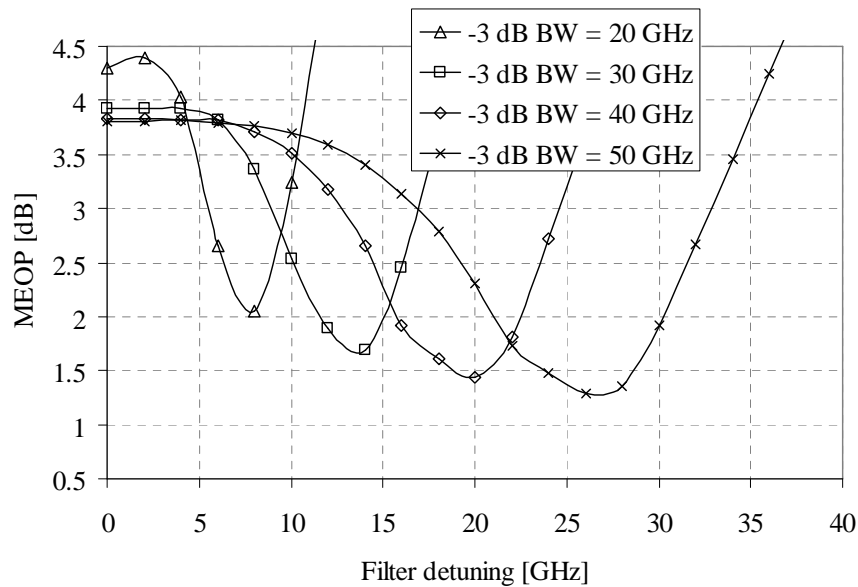


a) Optical spectra (note: the two signals are normalized to the same optical carrier power); b) Detuned filter output eye diagram.

Figure 3-22: Characterization XGM bandwidth enhancement through optical spectrum and eye diagram.  $Att_0 = 9$  dB and  $Att_{neg} = 7$  dB.

distortion caused by the slow carrier recovery is eliminated. Feasible optical filters are considered hereafter: the XGM bandwidth enhancer is tested considering Gaussian optical filters in Figure 3-23. The optical filters are detuned from the probe signal central wavelength to achieve the required enhancement of the blue chirped part of the spectrum. It can be verified that the 1<sup>st</sup> order Gaussian filter [205] with -3 dB bandwidth around 50 GHz enable an optimum MEOP of 0.75 dB, which represents only 0.15 dB penalty from the best result obtained by the filter shape of Figure 3-20. The signal attenuation due to detuned optical filtering (measured at the probe wavelength) is around 16 dB for the aforementioned case. For a filter with -3 dB bandwidth of 50 GHz, the filter central frequency can shift by  $\pm 12$  GHz while keeping the converted signal MEOP degradation below 1 dB. Gaussian filters with 2<sup>nd</sup> order present worse results than those obtained by the 1<sup>st</sup> order filter, since the out-of-band decay of 2<sup>nd</sup> order filter is too high; additionally, the sensitivity to filter detuning from optimum is also higher.

XGM wavelength converters operation performance is penalized for high output signal ER, since higher ER requires higher gain saturation, which also increases the SOA response time. The detuned filter technique is applied to SOA output signals with different ER. The ER of the converter output signal is varied by adapting the input information signal power and keeping constant the CW probe signal power at 0 dBm. Converted signal ER of 3 dB, 6 dB, 9 dB and 12 dB are enabled with input information signal powers of

a) 1<sup>st</sup> order Gaussian filterb) 2<sup>nd</sup> order Gaussian filterFigure 3-23: XGM bandwidth enhancement when 1<sup>st</sup> and 2<sup>nd</sup> order Gaussian filters are considered.

-3 dBm, 1 dBm, 4 dBm, and 7 dBm, respectively. Figure 3-24 presents the converted signal MEOP as a function of the optical filter detuning for the different ER values. As referred above, the higher is the ER, the more severe is the degradation of the XGM signal: the MEOP of the XGM signal before the detuned optical filter are 3.5 dB, 4.1 dB, 5 dB, and 6.4 dB, for ER of 3 dB, 6 dB, 9 dB, and 12 dB, respectively. Since the signal degradation increases with the ER, stronger enhancement of the blue frequencies relatively

to the red frequencies is required for higher ER. As a consequence, the filter optimum detuning increases with the converted signal ER. With optimized filter detuning, MEOP of 0.8 dB, 1.0 dB, 1.1 dB, and 1.3 dB are obtained for the set of ER under test: considerable improvement are obtained when compared to the MEOP of the common XGM signals, The main disadvantage of operating at high ER is that the optimum filter detuning increases, and so do the losses caused by it. The losses caused by the detuned filtering are 16 dB, 18.7 dB, 27 dB, and 36 dB, for ER of 3 dB, 6 dB, 9 dB, 12 dB, respectively. The losses of the whole wavelength converter, including the SOA and the filter, (measured as the power difference between the output and the SOA input information signal) are 3.2 dB, 10 dB, 24.6 dB, and 37.4 dB, for the referred ER values.

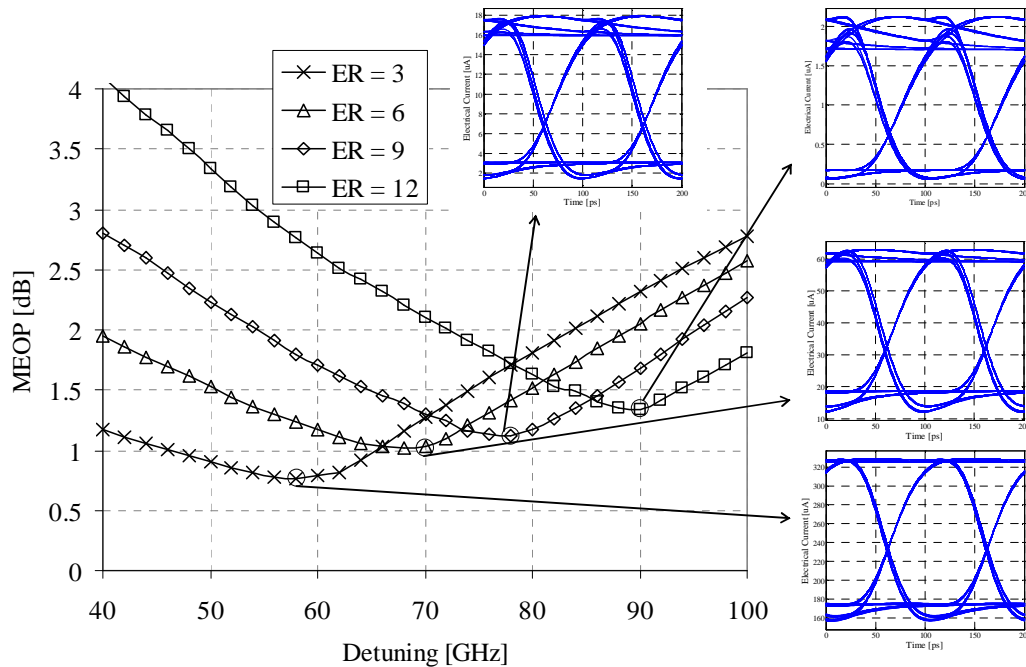


Figure 3-24: MEOP as a function of the 1<sup>st</sup> order filter detuning for different ER of the converted signal. Optical filter -3 dB BW = 50 GHz. Inset eye diagrams at optimum filter detuning.

The transmission properties in dispersive fiber are impacted by the SOA induced XPM. For comparison, the converted signal with 6 dB ER and an OOK NRZ signal with 6 dB ER, generated by a chirp-free MZM, are transmitted over dispersive fiber. The measured EOP after transmission is presented in Figure 3-25. It can be verified that the converted signal transmission properties are reduced when compared to the chirp-free OOK signal. For a maximum EOP of 3 dB, the maximum accumulated dispersion is reduced from  $\pm 1105$  ps/nm to  $\pm 765$  ps/nm.

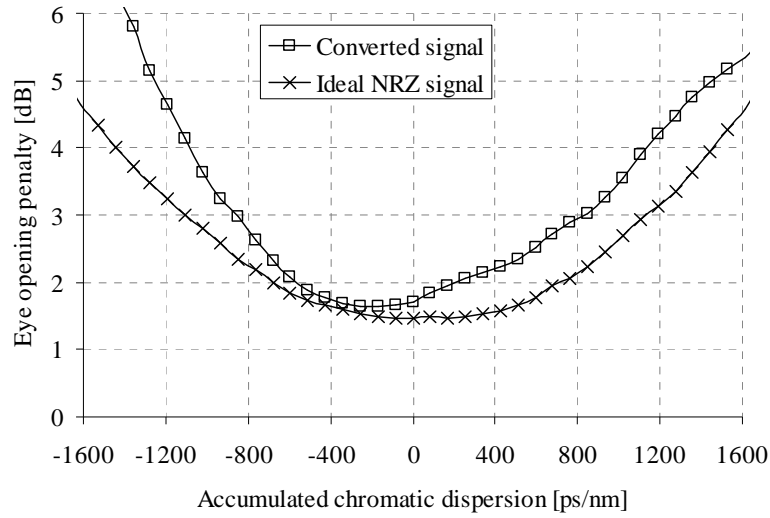
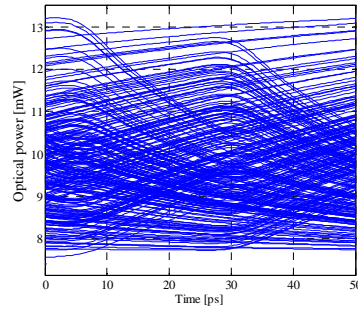


Figure 3-25: Comparison of the transmission capabilities over dispersive fiber of ideal chirp-free NRZ signal and converted signal.

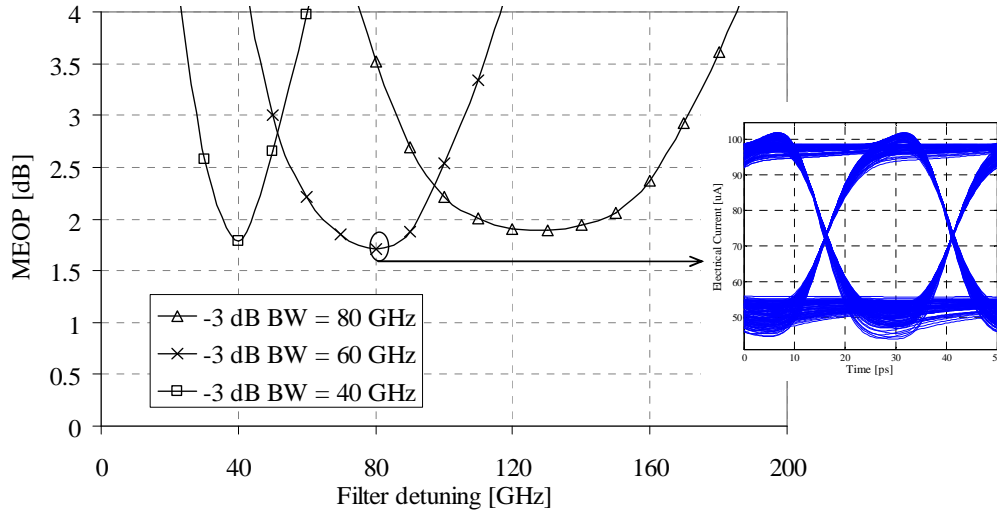
#### 40 Gb/s results

We have demonstrated above that the detuned filtering technique is able to enhance the XGM operation bandwidth of the *slow SOA* device to 10 Gb/s, since a simple 1<sup>st</sup> order Gaussian filter, detuned from the optical carrier, eliminates the distortion caused by the SOA slow response. Hereafter, the same operation principle is explored to assess the feasibility of 40 Gb/s conversion using the same *slow SOA* device.

The input information and CW probe signals powers at the SOA input are -3 dBm and 0 dBm, respectively. Under such condition, the SOA output eye diagram at the probe signal wavelength (i.e. common XGM signal) is presented in Figure 3-26 a). It can be verified that the eye diagram is completely closed due to the slow operation of the SOA. The MEOP of the detuned filter output signal is characterized in Figure 3-26 b) for different filter -3 dB bandwidth. It can be verified that the optimum filter bandwidth is around 60 GHz (1.5.BR); while for 10 Gb/s optimum operation was verified for much higher filter bandwidths (5.BR). The reason is that at 40 Gb/s the required enhancement of blue frequencies relatively to red frequencies is much higher than that at 10 Gb/s. Nevertheless, a clear and open eye diagram is obtained when the detuning is optimized. The losses due to detuned filtering are 21.1 dB for the optimum case referred above. The losses of the whole converter, including the filter and the SOA, are approximately 8.0 dB.



a) SOA output eye diagram at probe signal wavelength;



b) Converter output signal MEOP as a function of the detuning of the optical filter. Inset eye diagram for filter with -3 dB bandwidth of 60 GHz and detuning of 80 GHz.

Figure 3-26: 40 Gb/s characterization of XGM bandwidth enhancement via detuned filtering with 1<sup>st</sup> order Gaussian filters.

### 3.3.2.3 Experimental validation

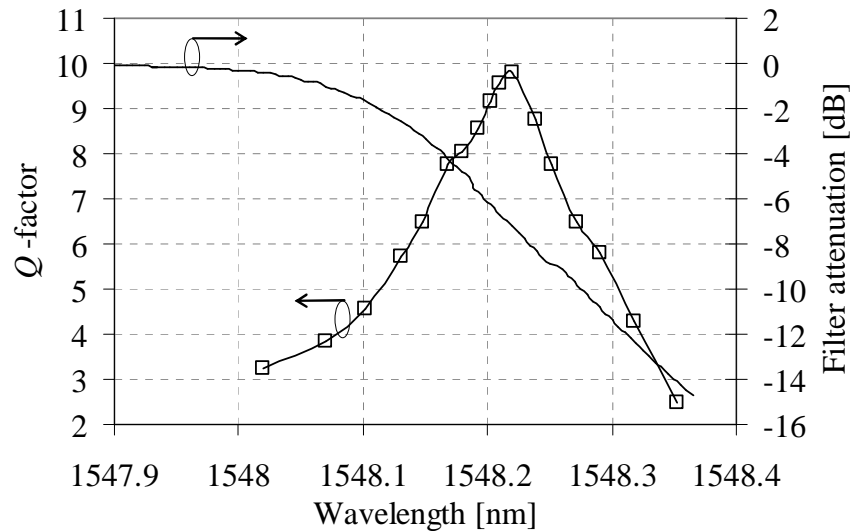
The experimental tests were performed with the *slow SOA* device, in agreement with the simulations of the previous section. The input information signal is generated by modulating an input CW signal at 1553.0 nm in a chirp free MZM. Due to experimental constraints, there was no tunable optical filter available; therefore, a WDM demultiplexer filter designed for a 200 GHz grid, is employed. This filter is approximated to a 2<sup>nd</sup> order Gaussian filter centered at 1547.61 nm, and has a -3dB bandwidth of 133 GHz and a -15 dB bandwidth of 190 GHz. Since the filter is not tunable, the detuning is performed by adapting the CW probe signal central wavelength. The signal after the detuned optical filter



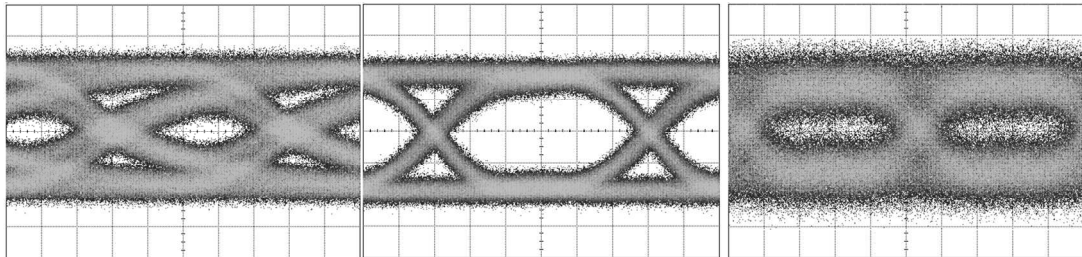
are detected in a photo-detectors with 10 GHz / 37 GHz of -3 dB bandwidth, for the 10 Gb/s / 20 and 40 Gb/s test, respectively; and the  $Q$ -factor is measured.

### 10 Gb/s results

For 10 Gb/s, the optical power measured at the SOA input is -1.8 dBm and 3.1 dBm for the input data signal and the for the CW probe, respectively. The input information signal  $Q$ -factor is 7.1. The CW probe signal wavelength is varied from 1547.60 nm to 1548.352 nm and the  $Q$ -factor of the detected signal is presented in Figure 3-27 a). For reference, the same figure also presents the attenuation of the optical filter. Figure 3-27 b) – d) presents the converted signal eye diagrams at different CW probe wavelengths.



a)  $Q$ -factor of the detected signal as a function of the CW probe signal wavelength and the attenuation of the optical filter;



b) Wavelength = 1547.61 nm; c) Wavelength = 1548.22 nm; d) Wavelength = 1548.35 nm.

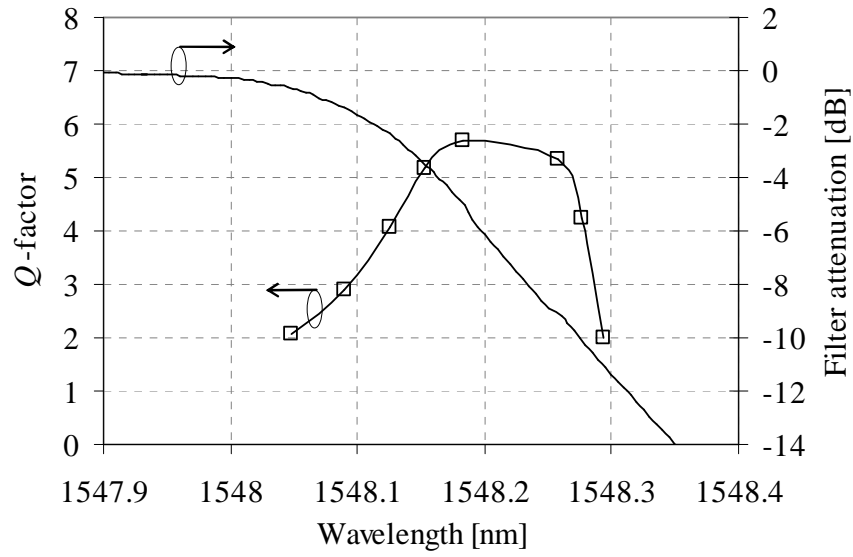
Figure 3-27: Characterization of experimental XGM bandwidth enhancement at 10 Gb/s via converted signal  $Q$ -factor - a) - and eye diagrams - b) to d).

When the CW probe wavelength is aligned with the center of the filter, the converted signal eye diagram is significantly distorted (Figure 3-27 b)), due to the intrinsic slow behavior of the SOA. This eye diagram is in agreement with the simulation results. When the probe signal wavelength is detuned from the optical filter central wavelength towards higher wavelengths, an increase in the eye opening and in the  $Q$ -factor is observed, since, in these conditions, the blue chirp part of the spectrum is being enhanced in relation to the red chirp part. The  $Q$ -factor maximum is obtained for a wavelength of 1548.22 nm. The resultant eye diagram is presented in Figure 3-27 c), which is completely open and does not present significant distortion.  $Q$ -factor improvements relatively to input are obtained for a frequency range of around 12 GHz. For higher detuning values the output signal  $Q$ -factor degrades abruptly, mostly due to the increasing attenuation of the filter, which reduces the signal to noise ratio after detection (since there is no pre-amplification), as can be verified from the eye diagram of Figure 3-27 d).

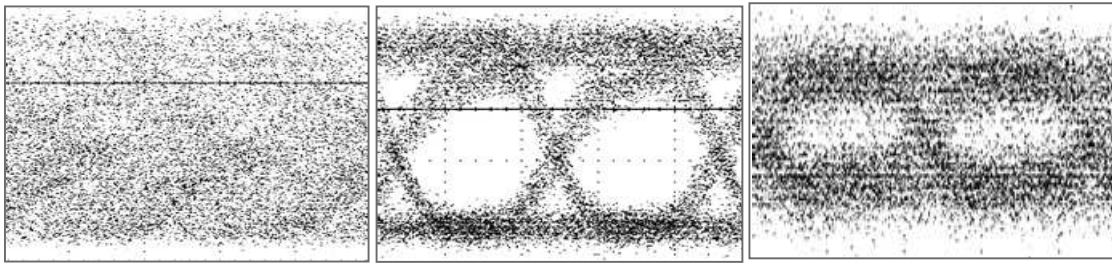
### 20 Gb/s results

For 20 Gb/s input, the optical power values, measured at the SOA input, are 1.48 dBm and 2.5 dBm for the input data signal and the for the CW probe, respectively. The input signal  $Q$ -factor is 8.8. Figure 3-28 a) presents output signal  $Q$ -factor versus detuning from the probe signal and optical filter central wavelengths.

For the standard XGM signal – when the probe is centered with the optical filter – the converted signal eye diagram is completely closed, as can be observed in Figure 3-28 b). When the probe signal is detuned from the center of the optical filter, the signal eye diagram opens and a maximum  $Q$ -factor of 5.6 is achieved. In the correspondent eye diagram depicted in Figure 3-28 b), a slow behavior is still noticed in the transitions from ‘0’ to ‘1’. This slow behavior can be overcome by using a filter with a higher decay, which would enhance more the blue chirp part of the spectrum. Similarly to the 10 Gb/s tests, the converter performance decays abruptly for higher detuning of the probe signal central wavelength from the filter center.



a)  $Q$ -factor of the detected signal and attenuation of the optical filter as a function of the CW probe signal wavelength;

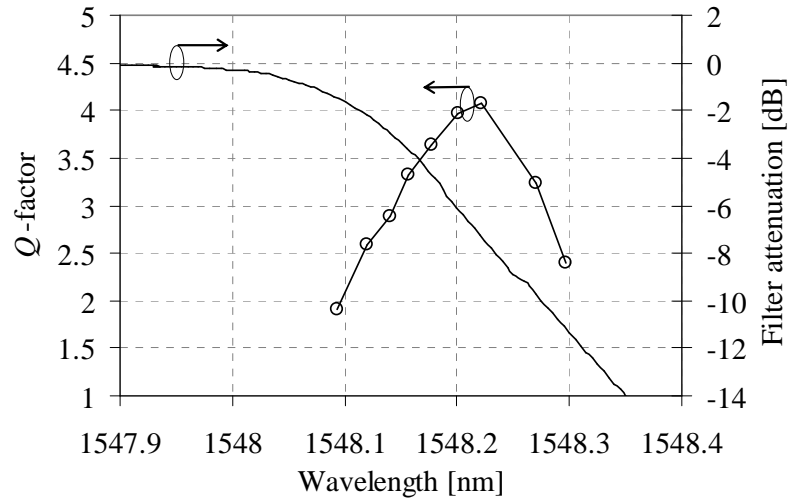


b) Wavelength = 1547.61 nm; c) Wavelength = 1548.18 nm; d) Wavelength = 1548.29 nm.

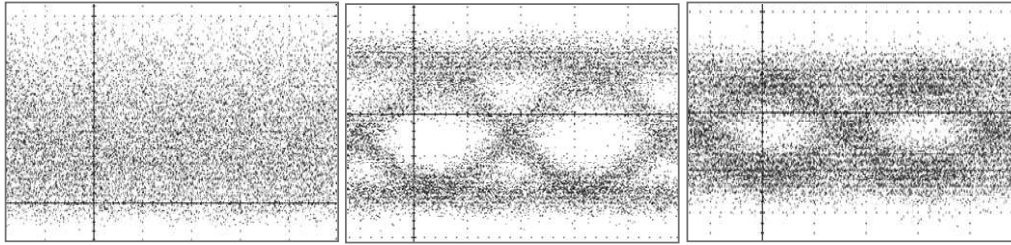
Figure 3-28: Characterization of experimental XGM bandwidth enhancement at 20 Gb/s via converted signal  $Q$ -factor - a) - and eye diagrams - b) to d).

#### 40Gb/s results

Figure 3-29 depicts the 40Gb/s results using the same *slow SOA* device, when the power values utilized are the ones considered in the 20 Gb/s test. The input signal  $Q$ -factor is 5.7. Similarly to the 20Gb/s test, the eye diagram is completely closed for the standard XGM signal, as depicted in Figure 3-29 b), due to the high recovery times of the SOA device; however, this converter still produces a considerably opened eye opening when the probe wavelength is optimized (Figure 3-29 c)), allowing a maximum  $Q$ -factor of 4.3 for the mentioned conditions.



a)  $Q$ -factor of the detected signal and attenuation of the optical filter as a function of the CW probe signal wavelength;



b) Wavelength = 1547.61 nm; c) Wavelength = 1548.22 nm; d) Wavelength = 1548.30 nm.

Figure 3-29: Characterization of experimental XGM bandwidth enhancement at 40 Gb/s via converted signal  $Q$ -factor - a) - and eye diagrams - b) to d).

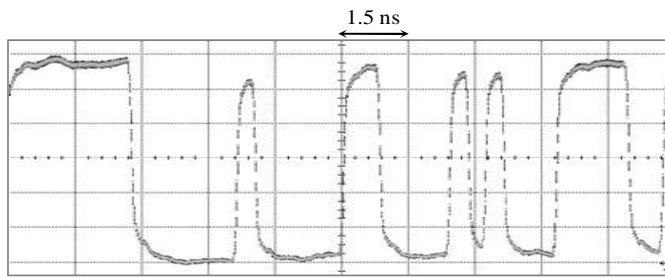
Improved experimental results are expected, particularly at 20 Gb/s and 40 Gb/s, if the optical filter is a 1<sup>st</sup> order Gaussian filter (as discussed in the previous section), and if a pre-amplified receiver is considered.

### 3.4 Filter assisted wavelength conversion in GC-SOA

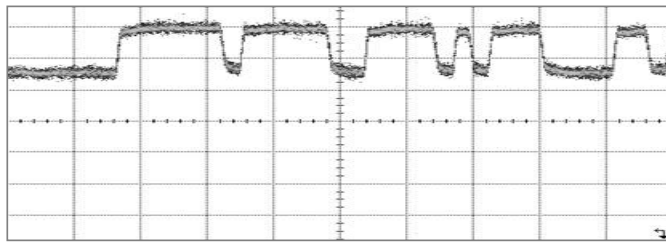
When a probe signal is amplified simultaneously in a SOA with an intensity modulated signal, XPM causes a red / blue chirping of the probe signal central frequency for the leading / trailing edges of the input signal optical pulses. In section 3.2.2.1, detuned filtering of the probe signal after the SOA was presented as a simple and effective method to convert the SOA induced phase modulation in intensity modulation. If the input information signal presents return-to-zero pulse format, detuned filtering the probe signal

at the output will retrieve a non-inverted RZ signal with high ER. As referred in section 3.2.2.1, this technique has been already demonstrated at very high bit rates. However, to the author's knowledge, all work published so far has focused on common SOA. Hereafter a gain clamped-SOA (GC-SOA) will be employed to experimentally perform wavelength conversion of RZ signals. In a GC-SOA, the blue chirp is enhanced due to the relaxation oscillations of the internal laser; therefore, higher conversion efficiency is expected when filtering the blue chirp contributions, when compared to common SOA. Moreover, GC-SOA response is inherently faster when compared to common SOA [135], [63], which is expected to allow operation at higher bit rates.

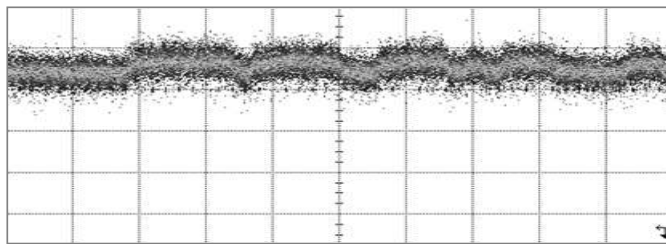
To analyze the GC-SOA response, a 2.5 Gb/s data signal and a CW probe with very low power are fed to the GC-SOA. In Figure 3-30 the GC-SOA response to the 2.5 Gb/s data signal is presented through the temporal shapes of the GC-SOA internal laser and the lower power CW probe signal. Two operating conditions are considered: low power input data signal (-12 dBm) and high power input data signal (-2 dBm). Figure 3-30 a) presents the reference input signal. The operation principle is independent on the pulse shape, therefore NRZ pulses are considered. When the input information signal presents low power, the internal laser is modulated with the inverse information of the input signal – Figure 3-30 b). This illustrates the *gain-clamping* mechanism, which retrieves an approximately constant cavity optical gain as verified by the low power probe signal Figure 3-30 c). When the input signal power increases the internal laser power will decrease and shuts down for logical '1's of the input data signal. For logical '0's of the input signal the laser turns back on; as usual in DBR lasers, relaxation oscillations are verified in the output signal [31]. Relaxation oscillations are transient effects, which are long when compared to the laser cavity loop time [136] and are due to an intrinsic resonance in the nonlinear laser system [31]. These oscillations are observed not only in the laser, but also in the carrier density (probed by the CW signal), as verified in the transitions from logical '0' to '1'. Since a blue chirp occurs for such transitions, the relaxation oscillations lead to a significant increase in the contribution of the blue chirped part of the spectrum when compared to the remainder of the spectrum. Therefore, improved results are expected when filtering the blue chirped part of the probe signal spectrum at the SOA output, when compared to common SOA.



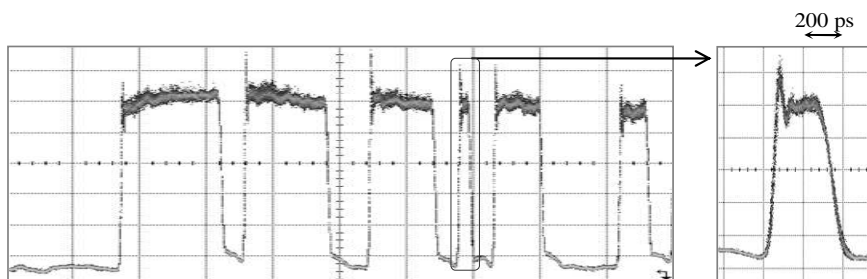
a) Input information signal;



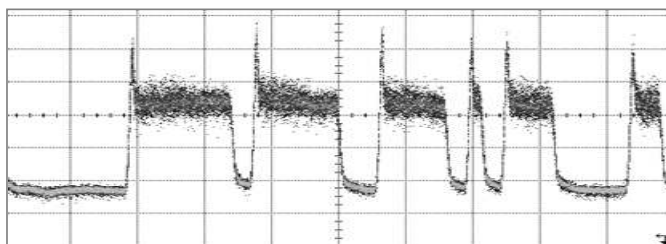
b) Laser generated by GC-SOA when input data signal power is -12.0 dBm;



c) Low power probe at GC-SOA when input data signal power is -12.0 dBm;



d) Laser generated by GC-SOA when input data signal power is -2.0 dBm;



e) Low power probe at GC-SOA when input data signal power is -2.0 dBm.

Figure 3-30: GC-SOA response to a 2.5 Gb/s input information signal.

To assess the performance of wavelength conversion via detuned filtering of the blue chirped part of the spectrum after GC-SOA, an input RZ signal with variable bit rate (2.5 Gb/s or 10 Gb/s) at 1547.30 nm is coupled to a CW probe signal at  $\lambda_2 = 1548.95$  nm. The two signals are simultaneously amplified in the GC-SOA device with driving current of 250 mA. After the GC-SOA, a detuned optical filter with -3 dB bandwidth of 15 GHz extracts the blue chirped part of the spectrum of the converted signal (i.e. the lower wavelengths). The converted signal is then detected in a pre-amplified receiver, which consists of an EDFA, an optical de-multiplexer filter with -3 dB bandwidth of 75 GHz centered with the signal, and a photo-detector.

The optical spectrum at the GC-SOA output is presented in Figure 3-31 for a 10 Gb/s input signal with 1.0 dBm and a CW probe signal with -3 dBm. The internal DBR laser generated by the GC-SOA is visible at 1509.0 nm. Besides the probe and data signals, a FWM contribution is also observed.

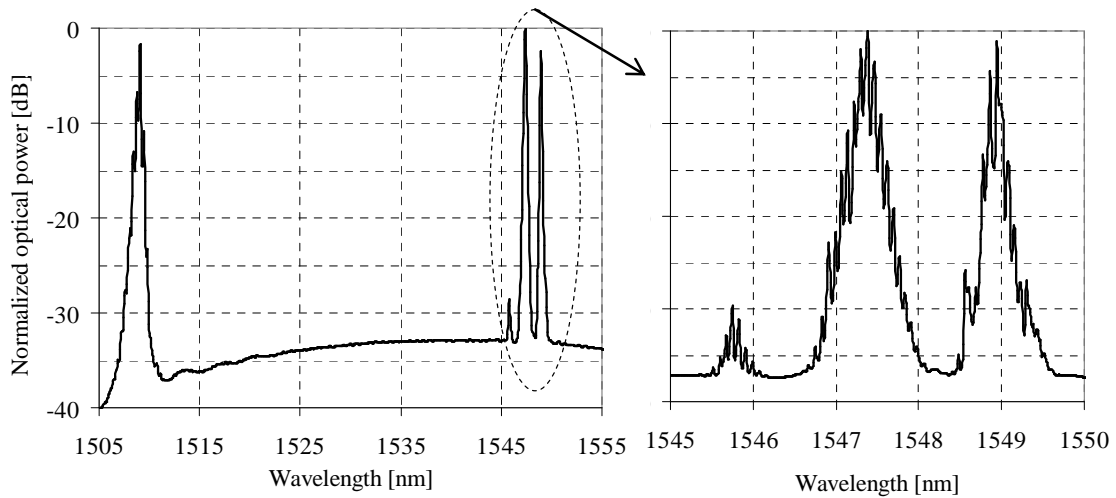
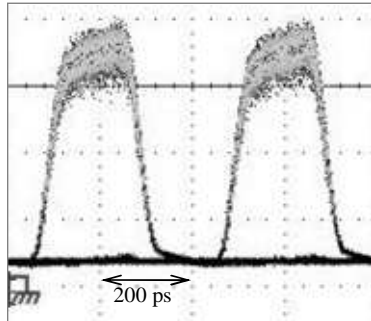


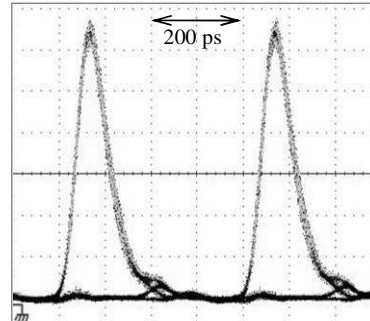
Figure 3-31: Optical spectrum at the GC-SOA output.

In Figure 3-32 the experimental eye diagrams before and after the converter are presented. The detuning of the optical filter central frequency relatively to the central wavelength of the probe signal was 14.8 GHz and 22.7 GHz for the 2.5 Gb/s and the 10 Gb/s tests, respectively. It is observed that, due to the detuned filtering, the converted signals present an increase in the ER when compared to the input signals, for both bit rates. The output signals present undistorted eye diagrams and the measured  $Q$ -factor is also improved when compared to the input, particularly for 2.5 Gb/s. A compression in the

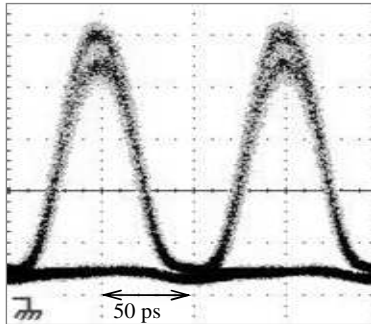
pulse width was verified at 2.5 Gb/s since the input pulse width was 117 ps and after the conversion the pulses had a width of 47 ps.



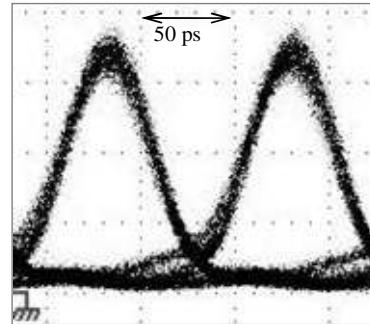
a) 2.5 Gb/s input signal eye diagram  
(ER = 12.1 dB,  $Q$ -factor = 11.5 dB);



b) 2.5 Gb/s converted signal eye diagram  
(ER = 16.8 dB,  $Q$ -factor = 14.3);



a) 10 Gb/s input signal eye diagram  
(ER = 9.0 dB,  $Q$ -factor = 10.5 dB);



b) 10 Gb/s converted signal eye diagram  
(ER = 12.1 dB,  $Q$ -factor = 10.8);

Figure 3-32: Comparison of converter input and output eye diagrams.

Figure 3-33 presents the optical spectrum of the SOA output at the probe wavelength when the input information signal bit rate is 10 Gb/s. The detuned filter transfer function and the resultant converted signal are also presented. It can be verified that the central wavelength (optical carrier) of the converted signal corresponds to the discrete spectral tone at the bit rate frequency. The resultant signal has reduced spectral occupancy and VSB characteristics.

The dependence on the optical filter position is depicted in Figure 3-34 for 2.5 Gb/s and 10 Gb/s. For both cases the output signal extinction ratio is robust to variations in the optical filter central frequency; however, the  $Q$ -factor presents reduced tolerance to filter detuning. The reduced tolerance to the filter central position can be understood with the help of Figure 3-33: the optical carrier must be eliminated by the optical filter; if there is



even a small detuning to lower frequencies, the optical carrier reappears; on the other hand, if the filter is detuned to upper frequencies, the spectral tone at the bit rate frequency, which is the central frequency of the converted signal, is eliminated.

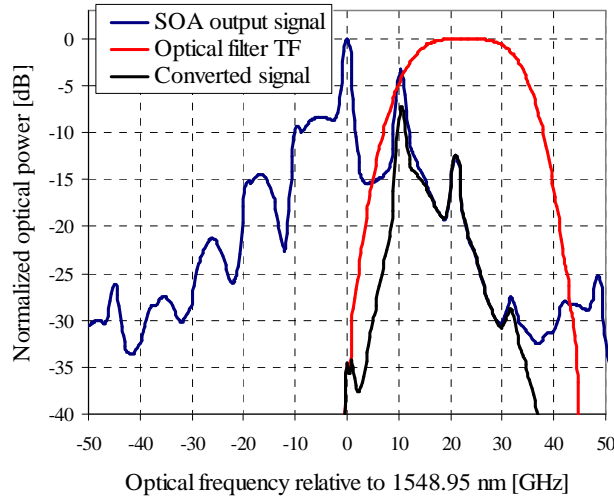
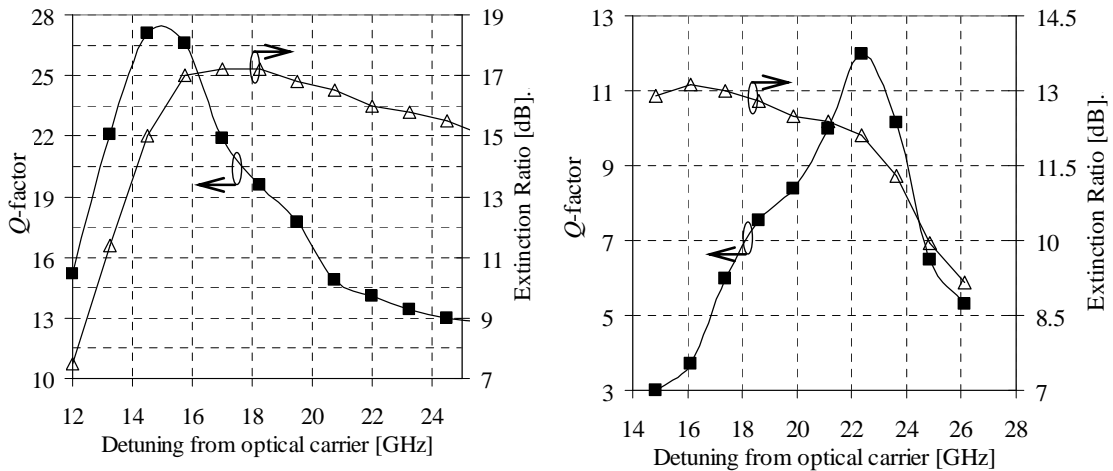


Figure 3-33: Optical spectra of: SOA output signal at pump wavelength, optical filter transfer function, and converter output signal.



a) 2.5 Gb/s input signal;

b) 10 Gb/s input signal;

Figure 3-34: Characterization of converter performance as a function of optical filter detuning.

In the previous tests filtering towards frequencies higher than the optical carrier (i.e. blue chirped part of the spectrum) has been considered. Figure 3-35 presents the converted signal eye diagram when the optical filter is detuned to optical frequencies lower than the optical carrier (i.e. red chirped part of the spectrum). The eye diagram presents

distorted due to the laser relaxation oscillations, which cause two distinct frequency chirps towards the red part of the spectrum for each bit: one just after the leading edge of the pulse and another during the trailing edge – such behavior can also be observed in the temporal shape of the probe signal, depicted in Figure 3-30 e).

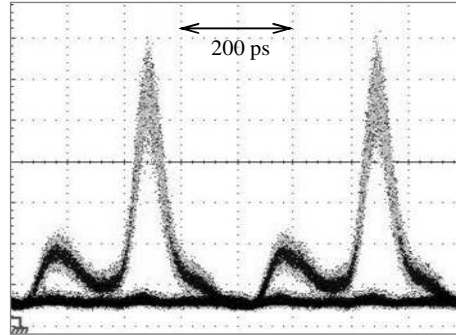


Figure 3-35: Eye diagram of 2.5 Gb/s converted signal when the red chirp is retrieved.

To effectively compare the performance of using SOA and GC-SOA for the presented wavelength conversion method, equivalent SOA and GC-SOA devices should be employed in experimental tests or an appropriate simulation model should be developed for the GC-SOA. Since equivalent devices are not available, and, within the frame period of this work, it was not possible to develop a detailed GC-SOA model for high bitrates, such comparison is not presented here. Nevertheless, the presented results demonstrate the high potential of GC-SOA for wavelength conversion of input RZ signals, when the probe signal blue chirp spectral components are extracted by a detuned filter; thus, a more thorough analysis is proposed as future work.

### *3.5 Experimental characterization of MZI-SOA based wavelength converter*

As detailed in section 3.2.2, one of the most common and effective methods to perform wavelength conversion with SOA is through the use of a MZI-SOA structure. In such structures, a probe signal suffers XPM in the SOA, caused by an input intensity modulated information signal. The interferometric structure converts the probe phase modulation in intensity modulation at the output. In this section a MZI-SOA wavelength

converter at 10 Gb/s is characterized. The impact of several parameters is assessed and studied. The purpose of such study is to provide ground basis for the operation of the 40 Gb/s multi-wavelength converter, presented in section 3.6; and also for the 2R regenerator employed in section 6.3.

The setup employed in the wavelength conversion experimental tests is depicted in Figure 3-36. Optical pulses with 2.0 ps are generated by a 10 Gpulse/s mode locked laser diode (MLLD) at 1545.0 nm, modulated with a 10Gb/s PRBS signal, with a pattern length of  $2^{31}-1$ , in a MZ modulator and fed to the differential wavelength conversion setup. The input data signal is also known as control signal. The CW probe wavelength is 1535.0 nm; this signal crosses a polarization controller to align its polarization with the SOA, due to SOA birefringence. The two signals are fed to the MZI-SOA wavelength converter in order to enable standard mode conversion, and differential mode conversion. Standard mode is achieved when the attenuation of VOA2 is equal to infinite; as a consequence, the information signal is fed only to the upper MZI-SOA arm. For differential mode operation, a variable delay and VOA control the conditions of the input signal in the lower arm. The system performance is assessed through bit error rate (BER) measurements for different optical signal to noise ratios (OSNR) at the photo detector input. To vary the OSNR, an ASE noise source is coupled to the optical signal. The -3 dB bandwidth of optical filters OF1 and OF2 is 0.85 nm, and the photo detector -3 dB bandwidth is 10 GHz.

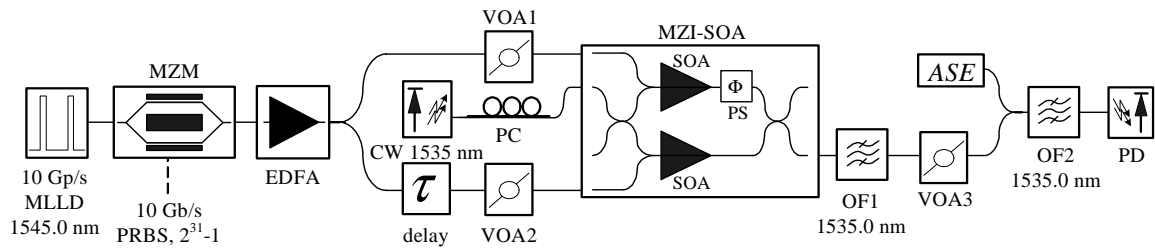


Figure 3-36: Experimental setup for XPM in SOA-MZI wavelength conversion at 10 Gb/s.

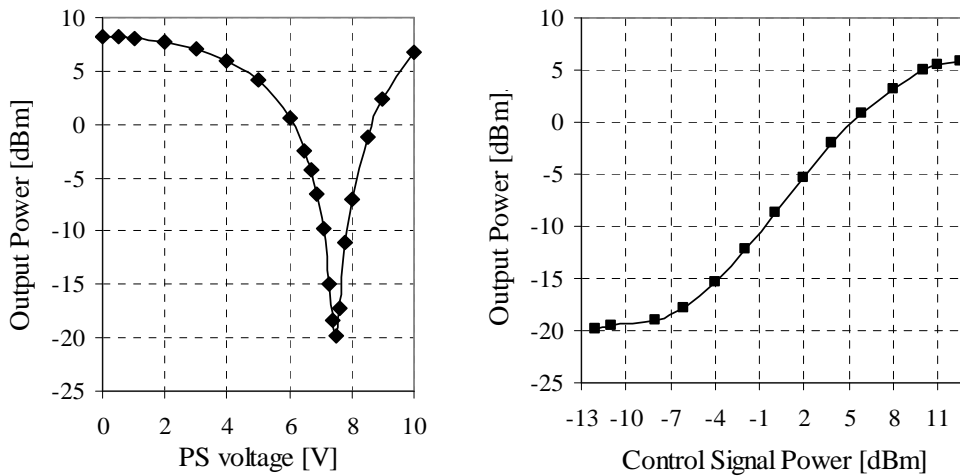
### Static characterization

In this section the XPM WC is characterized in static conditions (i.e. the input control signal is a CW) for the standard operation mode; for the differential mode it is not possible to perform any static characterization. In Figure 3-37 a) the variation of the optical power at the probe signal wavelength, measured at OF1 output, is presented when the

phase shifter voltage at the upper arm (PS) is varied. For this test the control signal is disabled and the probe signal power is 10 dBm at the MZI input. Both SOA are driven by a current of 400 mA.

When the PS voltage is set to 0 V, the phase shift suffered by the probe is similar in the two MZI arms, so the signals interfere with maximum constructive interference at the output. Increasing the voltage results in different phase shifts in the two arms; therefore, the output power is decreased; for a PS voltage of 7.5 V a phase difference of approximately  $\pi$  (maximum destructive interference) is obtained and a minimum in the output power at the probe signal wavelength is observed. For values higher than 7.5 V the phase difference between the two arms increases and the output signals interferes again with constructive interference. The maximum power contrast between the constructive and destructive interference conditions due to phase shift variation is around 28 dB.

The influence of the probe signal polarization was observed by rotating the polarization controller (PC) to obtain maximum power variations at the output. A polarization sensitivity of around 8.5 dB was verified when PS voltage is 7.5 V (destructive interference), and of 1.3 dB when PS voltage of 0 V (constructive interference).



a) Variation of phase shifter;

b) Variation of control signal power.

Figure 3-37: Output probe signal power as a function of the phase shift voltage and control signal power.

During wavelength conversion, the probe signal output power is also determined by the control signal power. In Figure 3-37 b) the probe output power is plotted for variable control signal power, fed only to the upper MZI arm, when the MZI is biased at minimum transmission (PS voltage of 7.5 V). Increasing the control signal power produces a phase shift in the SOA and the destructive interference condition is abandoned, enabling a power contrast of 25.3 dB. This extinction ratio is inferior to that obtained by phase shift tuning, because the maximum probe output power is obtained when the input signal is also at a high power level, which causes gain saturation in the SOA. The curve presented in Figure 3-37 b) also reveals the potential for 2R regeneration using MZI-SOA, as detailed in section 6.3.

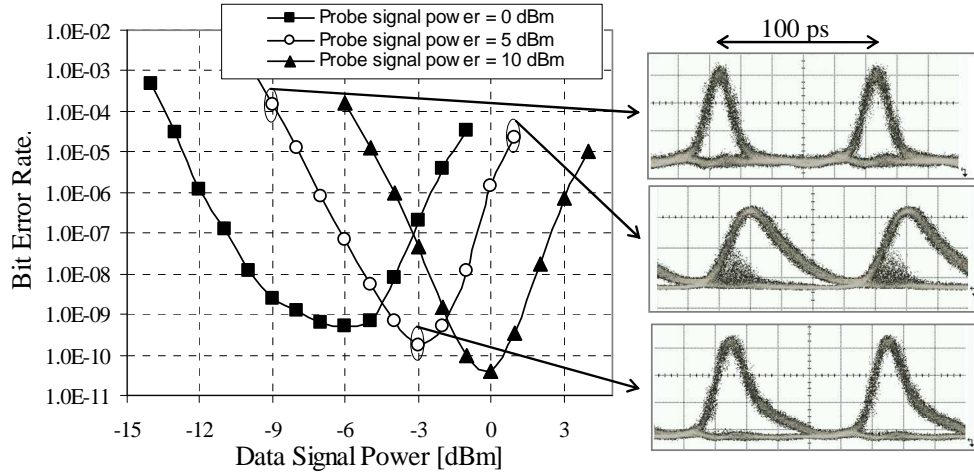
These results demonstrate the ability of MZI-SOA structures to perform wavelength conversion of intensity modulated signals. A reduction of the probe signal power is expected to increase the slope of the output power curve of Figure 3-37 b), since the SOA will be operating in condition with lower saturation.

#### Standard mode characterization

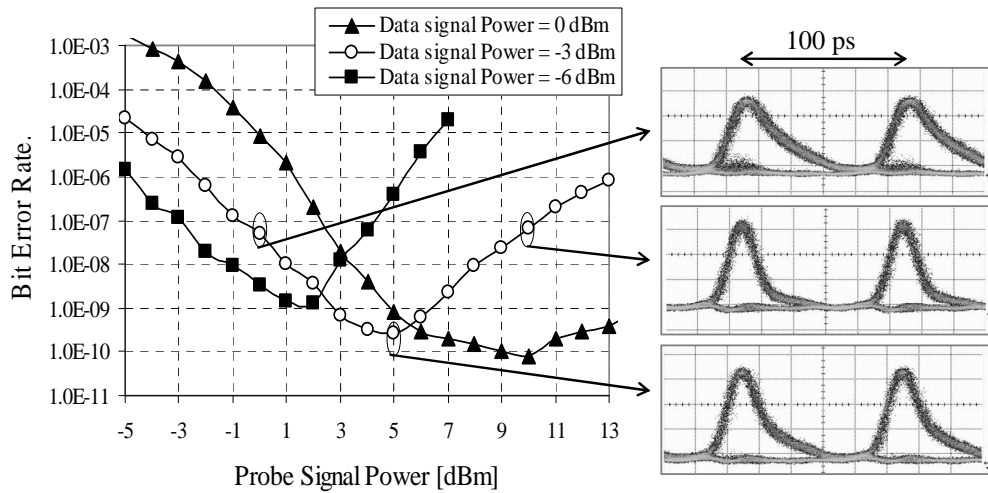
The standard mode XPM WC is characterized through BER measurements; for this purpose the OSNR at the PD input was fixed to 13.7 dB. The OSNR is measured using an inline power meter before the PD by disabling sequentially the signal or the ASE noise and measuring the power relation between the optical signal and the ASE after the optical filter (OF2). The control signal consists on the short pulse 10 Gb/s data signal. In Figure 3-38, the converted signal BER is plotted as a function of the power of the probe and of the information signal. Eye diagrams at interesting conditions are also presented; a 35 GHz optical photodiode was used for the eye diagrams.

In Figure 3-38 a) it can be verified that the input signal power for optimum BER increases for increasing probe signal power. This is because the SOA is more saturated (due to higher probe power), requiring higher data signal to obtain similar phase shifts. Similarly, for high power data signal, the optimum probe power also increases, as can be confirmed in Figure 3-38 b). For constant probe signal power, when the input data signal power is too low, the BER is penalized, since the phase shift at the output is low, and the converted signal OSNR is degraded; for very high powers of the control signal, the output

signal degrades due to severe distortion caused by the SOA extremely high gain compression.



a) Data (control) signal power variation;



b) Probe signal power variation.

Figure 3-38: Converted signal BER as a function of probe and data signals power.

Figure 3-38 b) demonstrates the converter performance improvement when the probe signal is increased (provided that the control signal power is also optimized). This improvement is due to a decrease in the SOA response time for high CW saturation [137],[63]. As a consequence, the output pulse duration is decreased. Moreover, the output OSNR is improved due to higher SOA saturation.

The previous statements can be confirmed by the eye diagrams inset Figure 3-38. When the probe signal power is high (relatively to the data signal power) the OSNR is penalized and the eye diagrams are noisier, also the pulse duration of the converted signal becomes lower and the reduced photodiode bandwidth penalizes shorter pulses. When the probe signal has low power, the converter signal presents high distortion in the logical '0'.

#### Differential mode characterization

Differential mode XPM is tested hereafter, by feeding the lower MZI arm of Figure 3-36 with a delayed and attenuated version of the data signal. The influence of the relative delay between the two arms,  $\tau$ , is evaluated in Figure 3-39. The OSNR at the PD input is fixed at 11 dB. The probe signal power is 10 dBm, the data signal power at the upper and lower arms is 1.7 dBm and -2 dBm, respectively.

As discussed in section 3.2.2.3, the converted signal pulse width is determined by the relative delay between the two arms. For very low delays, short pulses are originated; however these are penalized by the PD bandwidth of 10 GHz. As the delay increases the pulses broaden, spreading the power; as a consequence, the eye diagram opening decreases for the same average power and the BER is penalized. An optimum delay of 7 ps is obtained for the referred experimental conditions. It is also verified that the converter is more tolerant to positive delays deviations, relatively to optimum, than to negative deviations. For a PD with higher bandwidth, a lower optimum delay is expected.

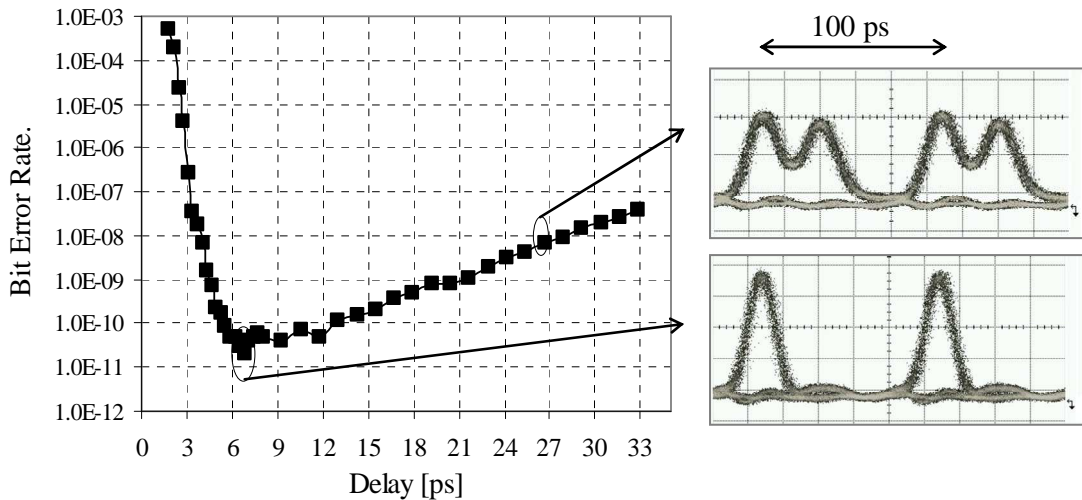


Figure 3-39: Converted signal BER as a function of the relative delay between the two arms,  $\tau$ .

The data (control) signal power at the lower SOA arm is optimized in Figure 3-40, maintaining a CW probe power of 10 dBm and a delay between the arms of 10 ps. For a fix value of power at the upper arm, the BER is penalized when the power at the lower arm is very low. Such penalty is due to the fact that when the power at the lower arm is very low, differential operation is not enabled: the XPM suffered by the probe signal in the lower SOA is very small and the converter operates similar to standard mode. For very high power levels at the lower arm, the XPM modulation suffered in the lower SOA exceeds that suffered in the upper SOA, as a consequence the output pulse tail is not eliminated, causing BER penalties. The optimum power relation between the two arms is the one that grants  $\Phi_{\text{XPM}}(t) = \Phi_{\text{XPM}}(t+\tau)$  (where  $\Phi_{\text{XPM}}$  is the phase of the cross phase modulated signal); it is observed that the optimum power at the lower arm is always 2 to 3 dB below the power at the upper arm.

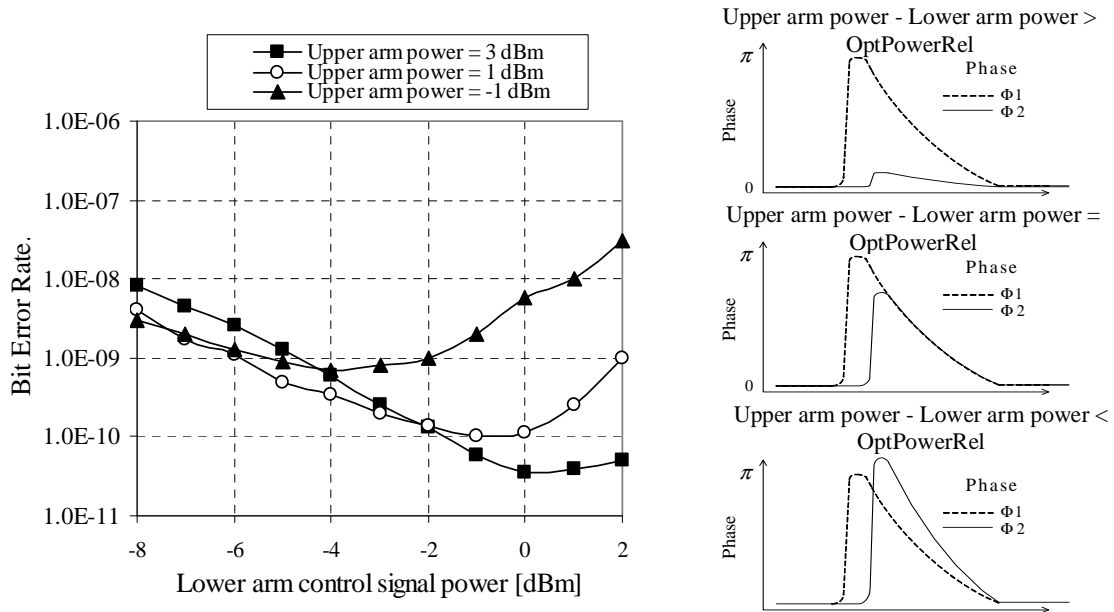


Figure 3-40: Converted signal BER as a function of the data signal power at the input of the MZI. OptPowerRel = Optimum power relation between the two arms.

#### Comparison between standard and differential modes

Figure 3-41 presents the BER curves (for different OSNR) for the input data signal and converted signals. The standard mode WC output signal is compared to the differential mode signal. In the former, probe and data powers of 10 and 0 dBm, respectively, are



employed. In the latter, the delay between arms is 10 ps, the probe power is 10 dBm and the signal power is 3 and 0 dBm for the upper and lower arms, respectively. As expected from the findings above, standard mode WC introduces a high penalty in the BER curve: for a BER of  $10^{-9}$  the required OSNR is penalized by 4 dB comparing to the input signal. Using differential mode WC improves the converted signal BER curve: a penalty lower than 1 dB is found for the same BER.

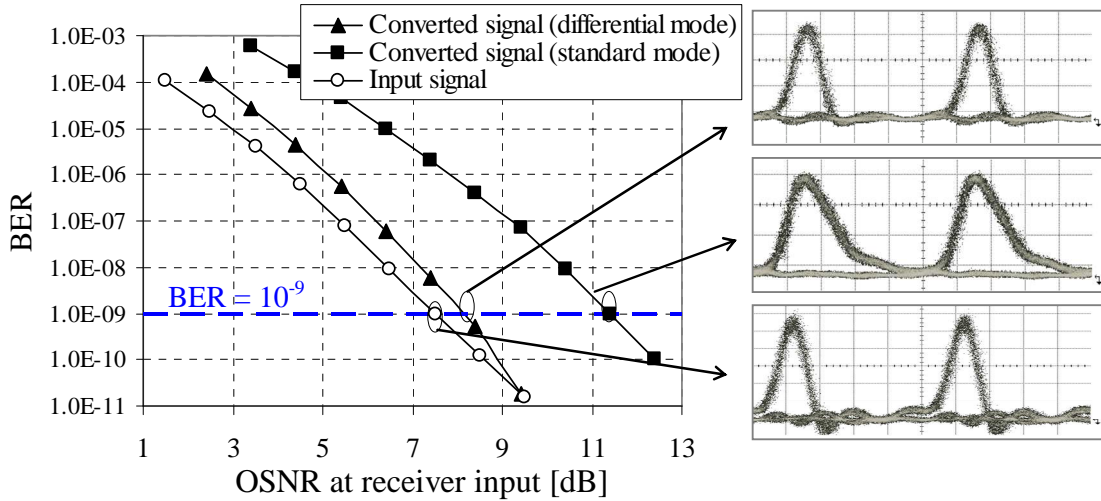


Figure 3-41: Comparison of the converted and input signals BER.

### 3.6 Multi wavelength conversion

All-optical multi-wavelength conversion (MWC), illustrated in Figure 3-42, has attracted increasing research and industry interest in the last few years. It allows all-optical wavelength multicast by simultaneously converting the input information signal wavelength to several other wavelengths. All operations are done in the optical domain, which eliminates the necessity of employing multiple optic-electronic-optic (OEO) transponders, reduces the switching system and operational cost, lowers the blocking probability, and increases the optical network transparency, efficiency and effectiveness [138]-[141]. All-optical MWC has also encouraged and facilitated several emerging applications, such as optical layer multicast [142], wavelength routing, grid networking [143], and service multi- or broadcast in access networks [105].

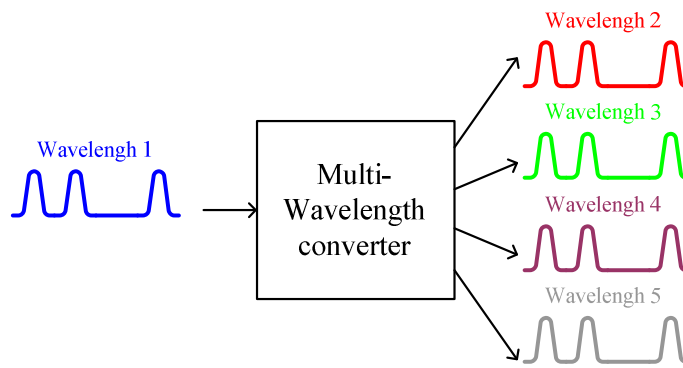


Figure 3-42: Illustration of multi-wavelength conversion.

Several solutions to achieve MWC have been proposed in recent years. The most promising results have been obtained for schemes based on FWM in SOA [142] or in optical fiber [138]; supercontinuum generation [144]; cross-phase modulation (XPM) [145]-[148]; dual-stage cross-gain modulation (XGM) [143] [149]; cross-absorption modulation (XAM) [150]; and fast nonlinear cross-polarization rotation (XPR) [151]. However, FWM is limited by its low conversion efficiency and wavelength inflexibility. XGM in double-stage semiconductor optical amplifiers is limited by SOA slow recovery. XAM suffers from the large insertion loss of the electroabsorption modulator. XPR technique is polarization sensitive, requires high input power and consequently is also penalized by the significant FWM by-products generated in the SOA. MWC based on XPM in MZI-SOA offer the widest combination of features, including [105]: high integrability, satisfactory and flat conversion efficiency, low power consumption, wide conversion bandwidth covering the SOA gain spectrum, simultaneous conversion of a considerable number of channels, wavelength flexibility, commercial product availability, compactness, supporting both RZ and non-return-to-zero (NRZ) data format, possible signal regeneration and noise suppression, and high operation speed. As discussed and demonstrated above, SOA-MZI can also be deployed with a differential scheme to operate beyond the speed limitation of the SOA devices. In this section, a 40 Gb/ MWC based on XPM in MZI-SOA operated in differential mode is experimentally assessed.

### 3.6.1 Experimental results

The setup considered in the experimental tests is shown in Figure 3-43, and is conceptually similar to that employed in the characterization of single wavelength

conversion at 10 Gb/s in section 3.5. An ultra-fast optical clock source generates 2 ps 40 GHz optical pulses at 1557.36 nm, which are modulated by a Mach-Zehnder modulator (MZM) with a PRBS signal, with a pattern length of  $2^{31}-1$ , to form the 40 Gb/s return-to-zero (RZ) optical input signal. This signal is then split to feed to the upper and lower arms of the SOA-MZI; the lower data path is delayed by 7.6 ps by a variable optical delay line (VODL); the delay was optimized to improve the output signal bit error rate. Four continuous wave (CW) probes, with wavelengths from 1547.72 to 1552.52 nm are combined using an ITU 200 GHz spaced multiplexer to feed the SOA-MZI. After MWC, the converted multicast data signals are demultiplexed and individually fed to a pre-amplified receiver. The -3 dB bandwidth of all the optical filters including the (de)multiplexers is 130 GHz. The photo detector (PD) has an electrical bandwidth of 37 GHz.

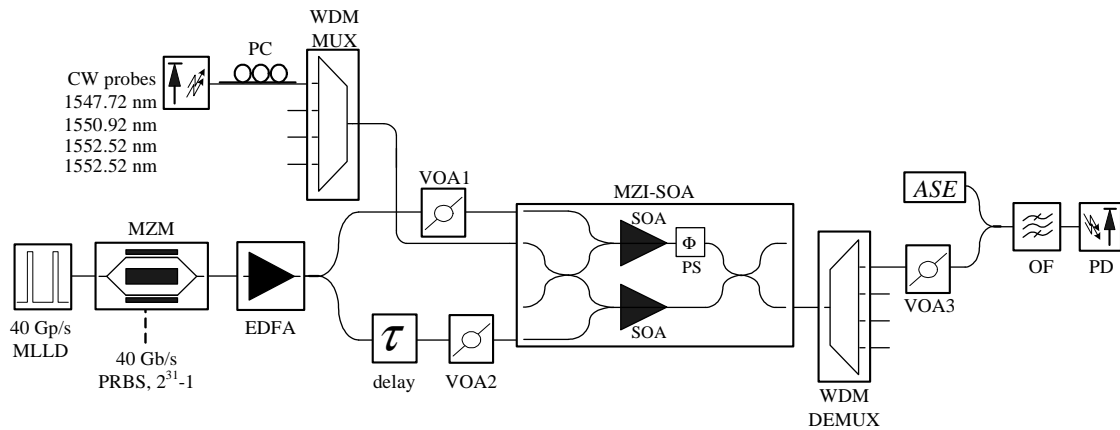
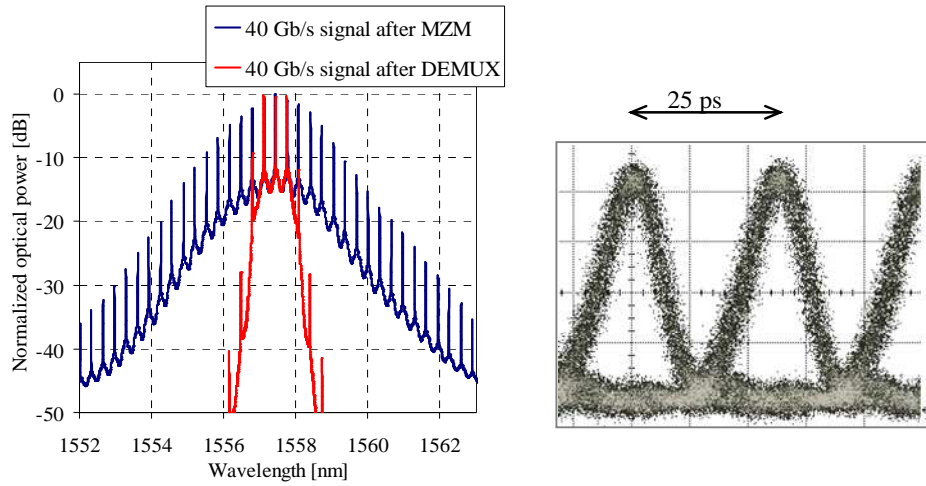


Figure 3-43: Experimental setup for 4 x 40 Gb/s all-optical multi-wavelength conversion.

The characterization of the 2 ps width input optical pulses, modulated with the 40Gb/s PRBS signal, is presented in Figure 3-44. Due to the ultra short duration of the optical pulses, the signal presents a very broad spectrum, with a spectral occupation at -15 dB of 5.5 nm. The optical spectrum of the input signal after the 130 GHz demultiplexer filter is also presented for reference. The eye diagram of the data signal is depicted in Figure 3-44: no visible differences were obtained comparing the signal before and after the demultiplexer since the photo detector used for the eye-diagram presents a -3 dB bandwidth of 35 GHz.



a) Optical spectra;

b) Eye diagram.

Figure 3-44: Characterization of the 40 Gb/s optical pulses.

In a first analysis, the converter is characterized under single-wavelength conversion (SWC). For this purpose each of the CW signals is activated while all the others are deactivated. The probe signal power is 3.2 dBm; the data signal power is 2.5 dBm for the upper arm and -9.1 dBm in the lower arm. It should be noted that the power difference of the data signal in the two arms is much superior to that optimized in section 3.5. The reason is that for the tests at 10 Gb/s of section 3.5, the relative delay of the two data signals replicas was 6 % of the bit duration, while for the 40Gb/s tests it is optimized around 30% of the pulse duration: the higher the delay between the two arms, the higher is also the optimum power difference between the two arms. The wavelength of the input data signal is 1557.36 nm. Figure 3-45 represents the optical spectra of the MZI-SOA output signal when the CW probe wavelength is 1547.72 nm; the converted signal spectrum is asymmetric around the optical carrier, due to the SOA induced chirp. Nevertheless, the eye diagram of the converted signal depicted inset Figure 3-45 is open and undistorted.

Figure 3-46 presents the output signal BER as a function of the OSNR measured at the photo-detector input for the several wavelengths of the probe signal. For each BER measurement, the signal OSNR was degraded at the photo-detector input by increasing the amplified spontaneous emission (ASE) noise level while keeping the signal power constant at -1 dBm to ensure linear operation of the electrical circuitry. To enable a BER of  $10^{-9}$ , the back to back signal requires 14.3 dB of OSNR. The converted signals required OSNR

range from 18.0 dB to 19.0 dB, which represents an average required OSNR degradation of 4.2 dB. The converted signals OSNR penalty relative to the input can be explained by the OSNR degradation of the SOA, but mostly due to the pulse broadening caused by the slow SOA gain recovery time, as it could not be completely suppressed via the differential configuration at 40 Gb/s.

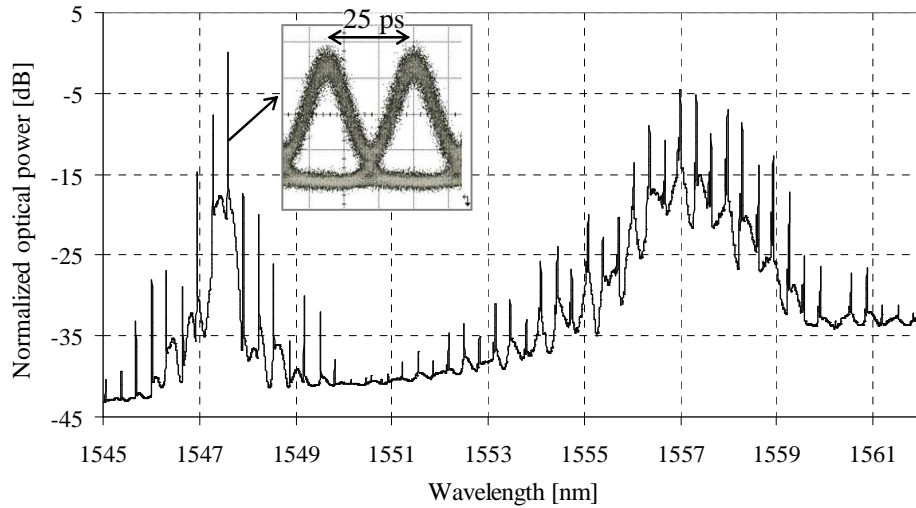


Figure 3-45: 40 Gb/s single wavelength conversion. Input data wavelength is 1557.36 nm, CW probe wavelength is 1547.72 nm. Inset: eye diagram of converted signal.

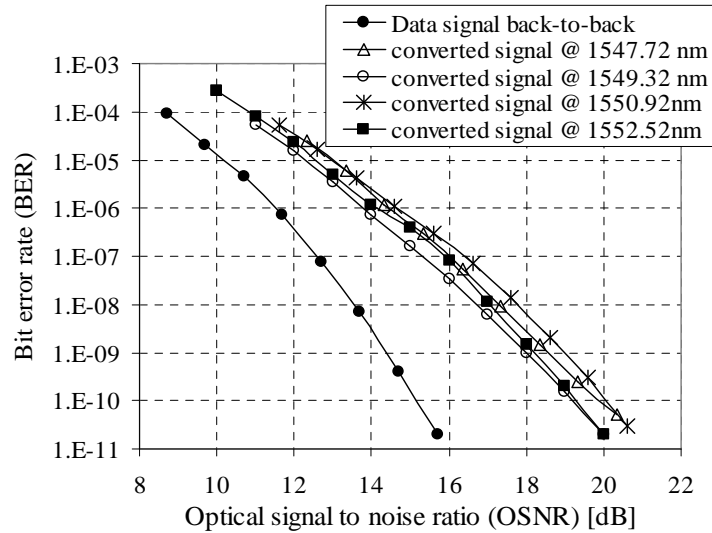


Figure 3-46: 40 Gb/s single wavelength conversion characterization through BER versus OSNR measurements.

After the initial characterization of the converter in single-wavelength operation, all four probes are activated simultaneously, and fed to the MZI-SOA. Figure 3-47 presents

the SOA output spectrum with all the MWC eye diagrams as insets. The converted signal with higher wavelength is separated by 600 GHz from the input signal wavelength. The power of the data signal is optimized as 7.3 and -3.0 dBm for the upper and lower arms of the SOA. The power of the CW probe signals was optimized to enable identical output power at the converter output for all wavelengths: 6.3, 5.7, 4.4 and 3.3 dBm for 1547.72, 1549.32, 1550.92, and 1552.52 nm, respectively. The reason why higher optical powers are required at lower wavelengths is due to the fact that the optical gain is reduced with the increase of  $|\lambda_P - \lambda_C|$  [92], where  $\lambda_P$  is the frequency of the pump and  $\lambda_C$  is the wavelength of the data control signal. Clear eye opening was obtained for all wavelengths. FWM satellites due to the SOA nonlinear effect were observed in the converter output spectrum. The oscilloscope measured an average extinction ratio (ER) of 10.16 dB for the multicast channels, with the worst being 9.68 dB.

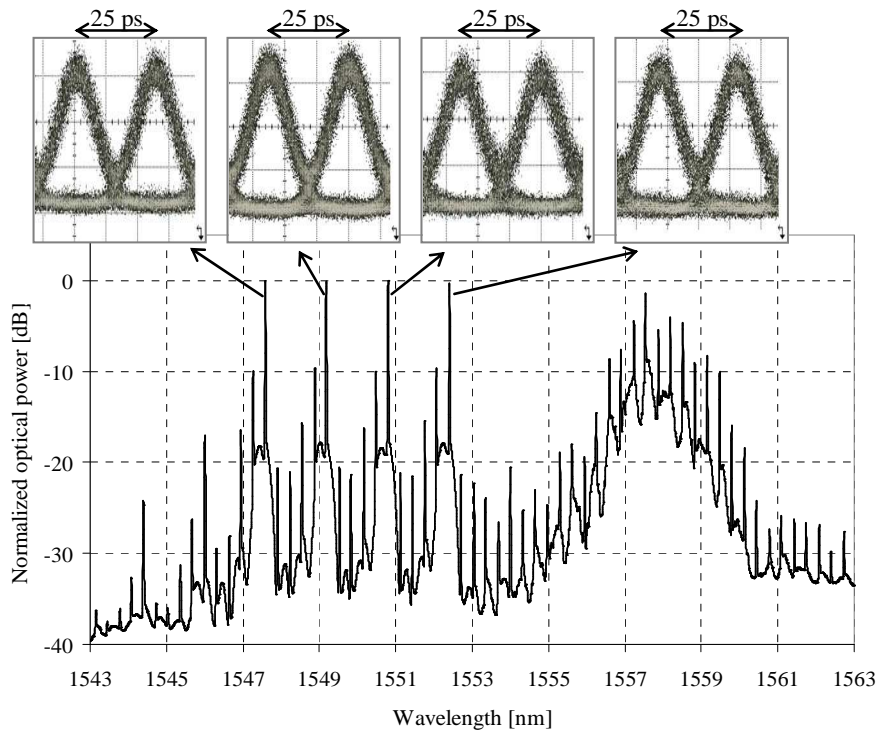


Figure 3-47: 40 Gb/s 1 to 4 multi-wavelength conversion. Input data wavelength: 1557.36 nm; CW probe wavelengths: 1547.72, 1549.32, 1550.92, and 1552.52 nm. Inset: eye diagram of converted signals.

Figure 3-48 presents BER versus OSNR characterization of all the MWC channels ( $1 \rightarrow 4$ ); as reference, characterizations of a single wavelength conversion ( $1 \rightarrow 1$ ) and of the input signal are also presented. The average OSNR penalties of the MWC channels at

BER= $10^{-9}$  ranged from 2 to 5 dB relatively to the SWC. The worse results of the outer channels can be due to the following:

- The channel at 1552.52 nm suffers crosstalk penalty from spectral broadening of the data signal. This non-linear effect is due to the high power levels in the SOA, which provoke SPM and intra-channel FWM.
- The channel at 1547.72 nm suffers from FWM by-products between the channel at 1552.52 nm and the input data signal.

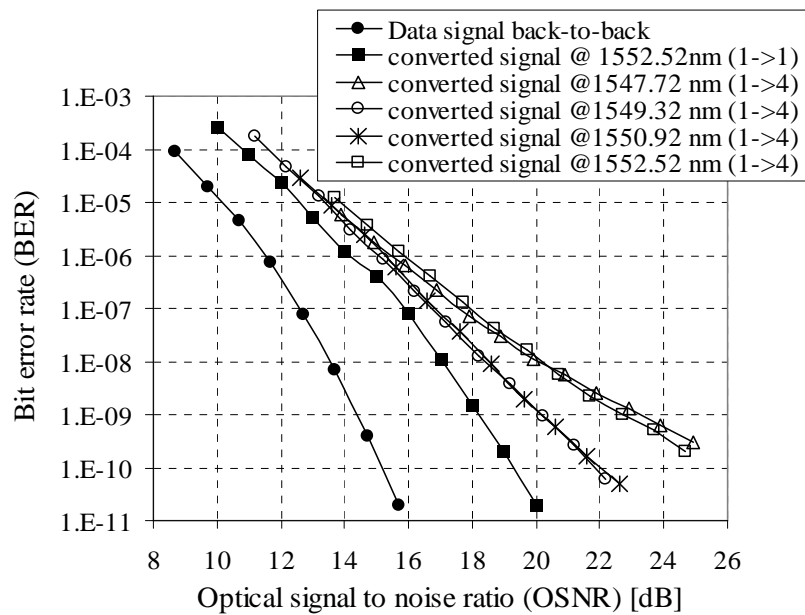


Figure 3-48: 40 Gb/s 1 to 4 multi-wavelength conversion characterization through BER versus OSNR measurements. For reference a BER curve of single wavelength conversion is also presented.

It should be noticed that in the single channel tests, characterized in Figure 3-46, the channel-dependent performance was not so evident because there were no FWM terms generated between the several CW probes, and the power levels launched in the SOA were inferior. The channel dependent performance could be mitigated if the individual CW probes power was optimized for uniform performance, as an alternative to constant output power.

The maximum number of channels can potentially be increased, as we have demonstrated in [105], where conversion to 8 wavelengths at 40 Gb/s was obtained by means of simulation. However, with experimental devices the maximum number of channels will be limited by several factors:

- The maximum power in the SOA devices (reduction of the per-channel power to accommodate more channels will result in further OSNR degradation of each channel);
- The spectral gain bandwidth of the SOA;
- Increase of the number of channels will increase the FWM products;
- Operation performance is expected to decrease for higher bit rates, and increase for lower bit rates.

### 3.7 Summary

This chapter has presented an overview of wavelength converters based on semiconductor optical amplifiers (SOA). Wavelength converters have been divided in four groups according to the main non-linear effect involved: cross gain modulation (XGM), cross phase modulation (XPM), cross polarization rotation (XPR) and four-wave mixing (FWM). The study of wavelength converters is essential in the scope of SOA-based all-optical processing not only due to its main functionality, but also because the underlying basic principles apply in other functionalities, such as: regeneration, format conversion, OTDM add-drop multiplexing, and others.

XGM based converters are usually limited by slow inter-band processes to tens or even hundreds of picoseconds. We have revised methods to enhance XGM bandwidth based on the increase of the effective carrier lifetime. Operation bandwidth via detuned optical filtering has been proposed and studied experimentally and via simulations at 10 Gb/s and 40 Gb/s. This method converts phase modulation (caused by XPM) in intensity modulation by detuned filtering. We have demonstrated that, with optimization of the optical filter, a device optimized for 2.5 Gb/s input signals can be employed in operation at least up to 40 Gb/s.

Cross-phase modulation based wavelength converters require a stage of phase to intensity conversion. Detuned filtering of the SOA output XPM converted signal is a common method to allow such conversion. In this chapter, we demonstrated for the first time the application of the detuned filtering technique to the output of a wavelength converter based on XPM in a gain-clamped SOA. Such device has the advantage of



internal lasing, which enhances the carrier recovery time. Moreover, the internal laser enhances the blue chirping of the converted signal. Operation has been demonstrated at 2.5 Gb/s, and 10 Gb/s. Phase-to-intensity conversion in a Mach-Zehnder Interferometer with SOA (MZI-SOA) is another common method to perform wavelength conversion, since it features high potential for integration and allows operation beyond the carrier dynamics bandwidth, due to differential mode operation. MZI-SOA wavelength conversion was characterized at 10 Gb/s with standard and differential mode operation. The impact of several converter parameters, such as input optical powers, polarization, or delay between the arms of the MZI, was studied. Finally, 40 Gb/s 1 to 4 multi-wavelength conversion has been experimentally demonstrated using a differential mode MZI-SOA converter. Output signals, spaced by ITU 200 GHz spacing, presented clear and open eye diagrams. Performance difference between the several channels is due to FWM terms and crosstalk from spectrally broadened input data.



# Chapter 4

## Modulation format conversion

### *4.1 Motivation*

In the last years, the study of transmitters for advanced modulation formats has been a hot topic in optical communications research and development. The use of advanced modulation formats should reduce network costs by allowing high per channel bit rate and by increasing the spectral efficiency; these advantages should come together with tolerance to chromatic dispersion, non-linear effects and other impairments of transmission and routing. Some of the most relevant modulation formats include differential binary phase shift keying (DPSK) [152]; differential quadrature phase shift keying (DQPSK)[153]; duobinary [154]; coherent-detected polarization-multiplexed quadrature phase shift keying (CP-QPSK) [155]; carrier-suppressed return-to-zero (CSRZ) [156]; and sideband suppressed signals, such as optical single sideband and optical vestigial sideband (oSSB / oVSB) [157], [158], [159].

From the previous formats, CSRZ and oSSB / oVSB have high potential for low cost networks. Sideband suppression allows an increase in the channel density of DWDM systems and improved tolerance to group velocity dispersion (GVD). Moreover, oSSB and oVSB enable the use of efficient electrical dispersion compensation (EDC) to further mitigate the effects of GVD [157]. Recent results have demonstrated the effectiveness of EDC to compensate several thousands of ps/nm of GVD per 10 Gb/s channel [160]-[163] even for optical double sideband (oDSB) signals; however, these schemes require complex and fast electrical processing. On the other hand, EDC on oSSB systems employing direct detection can be performed using simple passive dispersive lines, Butterworth filters, and

adaptive filters [157], [164], [165], [166]. Regarding CSRZ, its promising characteristics include high tolerance to non-linear transmission effects and polarization mode dispersion; moreover, when combined with tight optical filtering, CSRZ allows very high spectral efficiency without significant degradation of the RZ pulse shape [167]-[169].

All-optical converters between common oDSB and oVSB / oSSB or CSRZ are essential elements to reduce transmitter costs and in the interface between legacy networks, which still use OOK, and networks with optimized modulation formats. Figure 4-1 demonstrates the need for all-optical modulation format converters. Optical networks #1 and #2 employ the oDSB modulation format; and networks #3 and #4 utilize an advanced modulation format, such as oSSB, oVSB, or CSRZ; therefore, at the interface of the networks with different modulation formats, it is required to convert the input oDSB signals to an advanced modulation format. Moreover, all-optical format converters also allow the use of legacy oDSB transmitters for traffic locally added in networks #3 and #4, followed by format conversion; this brings a low cost potential, as the same type of optical transmitter may be employed in all the networks.

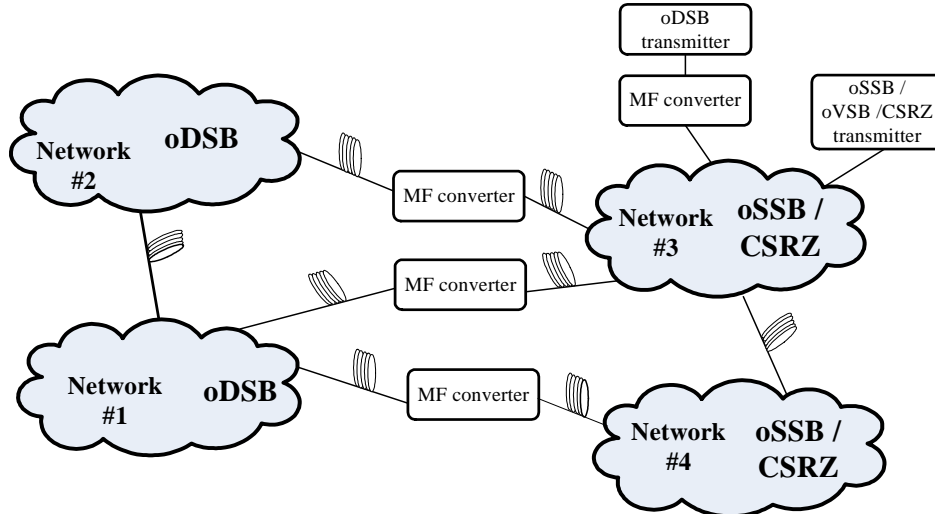


Figure 4-1: Representation of all-optical sideband suppression at the interface between networks employing oDSB and oSSB / oVSB formats; and after oDSB transmitters.

The most common all-optical sideband suppression method consists in removing part of the sideband power by detuned filtering of an optical double sideband (oDSB) signal [170], as illustrated in Figure 4-2. This is a conceptually simple method; however the sideband suppression is very dependent on the characteristics of the optical filter, such

as central wavelength, optical bandwidth and decay. Moreover, a very stable optical source is required (or tracking of the central wavelength,  $\lambda_0$ ), or information loss may occur. In [171] an all-optical scheme that employs an optical quadrature filter to obtain the Hilbert transform of the information signal is reported. However, this is a very complex method, which is wavelength dependent, requires an optical interferometer, and may present high insertion losses.

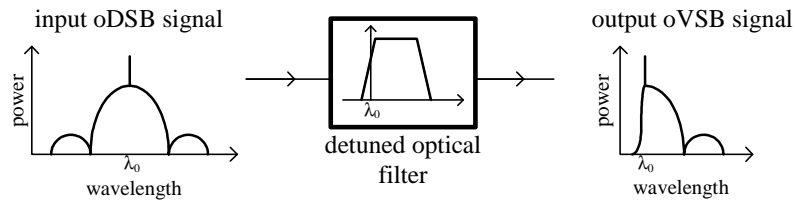


Figure 4-2. Sideband-suppression through detuned optical filtering.

All optical conversion from oDSB with NRZ or RZ pulse format to CSRZ has been achieved in a SOA based optical loop mirror [172]. However, only 10 Gb/s single channel operation has been demonstrated; moreover, this setup relies on a non-linear loop, which is inherently complex.

This chapter presents two novel all-optical format conversion schemes. The first scheme converts oDSB signals to oVSB format, based in self-phase modulation non-linearity in SOA. This scheme is, to the authors knowledge, the first all-optical sideband suppression scheme which does not require detuned optical filtering of the input signal or Hilbert transforms of the information signal. The proposed method was disclosed in [173] and experimental results have been published in [174] with operation at 10 Gb/s and in [175] at 40 Gb/s. The second novel scheme converts NRZ or RZ pulse shaped optical double sideband signals into CSRZ modulation format, based on the combination of cross gain modulation (XGM) and cross phase modulation (XPM) in SOA. This is a low cost and simple method, which presents negligible polarization dependence and high spectral bandwidth; moreover, the input signal is amplified by the SOA. This method was proposed in [176] where single- and multi-channel operation was demonstrated at 40 Gb/s.

## 4.2 Format modulation conversion from oDSB to oVSB

### 4.2.1 Introduction to optical sideband suppressed signals

The electrical field of a carrier unsuppressed optical DSB signal,  $E_{\text{oDSB}}$ , is described by:

$$E_{\text{oDSB}}(t) = 1 + z \cdot m(t), \quad (4-1)$$

Where  $m(t)$ ,  $-1 \leq m(t) \leq 1$ , is the ac coupled normalized information signal; and the modulation depth,  $z$ ,  $0 < z \leq 1$ , controls the ratio between the intensity modulation and the optical carrier. To obtain an ideal carrier unsuppressed optical SSB signal, the signal of (4-1) has to be added to the Hilbert transform of the information signal [177]:

$$E_{\text{oSSB}}(t) = 1 + z \cdot m(t) \pm j \cdot z \cdot m_H(t), \quad (4-2)$$

Where  $m_H(t)$  is the Hilbert transform of the information signal; and the signal - / + defines whether the oSSB signal has the upper / lower sideband suppressed, respectively. The Hilbert transform is ideally obtained from the information signal by a quadrature filter [178], whose transfer function is described by (With  $f$  the frequency, and  $\text{sign}(\cdot)$  the signum function):

$$H_{\text{quad.}}(f) = j \cdot \text{sign}(f), \quad (4-3)$$

Hereafter only carrier-unsuppressed optical SSB / VSB signals are considered; for generation and properties of carrier suppressed optical SSB signals, refer to [179].

Figure 4-3 compares the optical spectrum of a NRZ oDSB signal with that of an oSSB signal with suppressed lower sideband (here called oSSB – upper sideband, as only the upper sideband remains), and with an oSSB signal with suppressed upper sideband (oSSB – lower sideband). It can be verified that oSSB signals have one of the sidebands completely suppressed and the remaining sideband presents +6 dB of power in addition to the corresponding oDSB signal sideband spectrum.

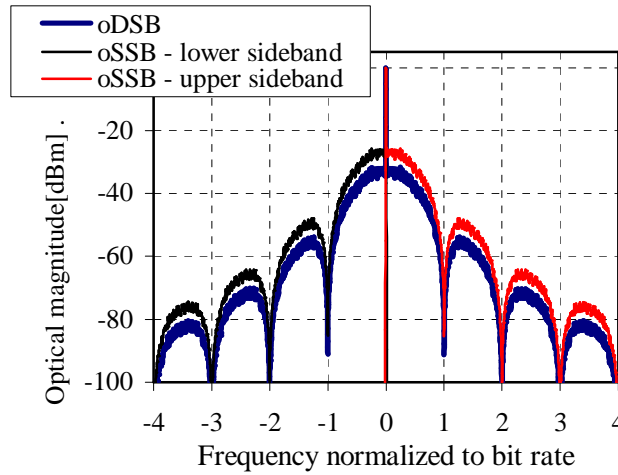


Figure 4-3. Optical spectra of ideal NRZ DSB and SSB signals.

Optical SSB signals can be detected using common direct detection. Equation (4-4) represents the electrical current after direct detection of the oSSB and oDSB signals of (4-1) and (4-2) in back-to-back situation, considering that the photo-detector bandwidth is much higher than the signal spectral occupancy. It is considered that the photo detector has a responsivity of one.

$$\begin{aligned}
 I_{\text{oDSB}}(t) &= 1 + z \cdot m(t) + z^2 \cdot m^2(t) \\
 I_{\text{oSSB}}(t) &= 1 + z \cdot m(t) + z^2 \cdot m^2(t) + z^2 \cdot m_H^2(t)
 \end{aligned}
 \tag{4-4}$$

Similarly to the result of the detection of the oDSB signal, the detection of the oSSB signal presents the data signal,  $m(t)$ , and second order distortion. However, the detected ideal oSSB signal also presents second order distortion due to the Hilbert transform of the data signal; which can be source of distortion of the detected signal.

#### 4.2.1.1 Feasible oSSB and oVSB transmitters

Several methods have been proposed to achieve optical SSB / VSB modulation. These can be divided in two groups: electro-optical methods and all-optical methods.

##### Electro-optical SSB / VSB generation

The most common electro-optical method was proposed by Sieben et al. [157] and consists in a cascade of amplitude and phase modulation. The amplitude modulation stage

is driven by the information signal, and the phase modulation stage is driven by the Hilbert transform of the signal. This method does not produce intensity distortion after direct detection due to the Hilbert transform, and can be realized using a single dual-arm MZM[157]. On the other hand, this method is not appropriate to generate carrier suppressed optical signals.

A dual-MZM, which consists in a Mach-Zehnder structure with MZM embedded in each arm can also be employed to generate SSB signals [179]. One of the MZM is driven by the information signal and the other by its Hilbert transform. This method is more appropriate to generate carrier suppressed oSSB signals; however, it produces distortion after detection, due the Hilbert transform of the signal, particularly when used with information signals with NRZ pulse shape, or RZ with high FWHM.

Fonseca et al. [180] have proposed a converter to the oSSB format where the incoming oDSB signal is split in two copies. One of the copies is detected and suffers electrical processing. The second copy is phase modulated with the processed electrical signal, to generate an oSSB signal. The advantage of this method is that it is wavelength independent and allows high sideband suppressions. On the other hand, it requires photo-detection and electrical processing.

#### All-optical SSB / VSB generation

All-optical filtering is the simplest method to convert an optical DSB signal to oSSB / oVSB [170]. This method, illustrated in Figure 4-2, is very limited by the characteristics of the optical filter, such as decay and out-of band attenuation. Moreover, high stability between the optical source and the optical filter is required.

Transversal optical filters can also be used to convert oDSB signals to the oSSB format [171]. However, this method is also based in the transfer function of an optical filter, and has similar disadvantages as the detuned filtering method.

#### 4.2.1.2 Transmission of oSSB signals over dispersive fiber

The propagation of a single channel over silica optical fibers, which are only weakly non-linear, can be described by the non-linear Schrödinger equation, which is



considered accurate to describe the evolution of optical pulses as short as 1 ps [11]:

$$\frac{dE}{dz} + \beta_1 \frac{dE}{dt} + \frac{i}{2} \beta_2 \frac{d^2 E}{dt^2} - \frac{i}{6} \beta_3 \frac{d^3 E}{dt^3} + \frac{\alpha}{2} E = i\gamma |E|^2 E, \quad (4-5)$$

Where  $E$  is the electrical field of the optical signal,  $\beta_1 = v_g^{-1}$ , with  $v_g$  the group velocity;  $\beta_2$  and  $\beta_3$  account for fiber dispersion, and  $\gamma$  is the non-linear parameter.

Considering that  $\beta_3$  is negligible in the signal bandwidth, that  $\gamma|E|^2$  is insignificant when compared to the remaining terms, and that we transform our referential in a frame moving with the pulse; the pulse propagation can be simply described by the following transfer function in the frequency domain, where attenuation was also neglected, since it can be compensated by in-line amplification:

$$H_{\text{fiber}}(f) = \exp\left(\frac{-i\omega^2 \beta_2 L}{2}\right). \quad (4-6)$$

The dispersive fiber transfer function can also be represented considering the well know dispersion parameter,  $D = -2\pi c \beta_2 / \lambda^2$ :

$$H_{\text{fiber}}(f) = \exp\left(\frac{i\pi D L \lambda^2 f^2}{c}\right). \quad (4-7)$$

From previous equation results that signals with higher spectral occupancy suffer more degradation with chromatic dispersion. Since SSB signals have approximately half the spectral occupancy of DSB signals, enhanced transmission reach is obtained [157].

#### 4.2.1.3 Electrical dispersion compensation

The enhanced tolerance of oSSB signals to chromatic dispersion is an important asset; however, even in metro networks, an optical signal can travel several hundreds of kilometers. Dispersion compensation in the optical domain is a widely used technique in such networks. However, such modules are expensive, introduce additional latency, and usually there is still a reasonable amount of uncompensated dispersion due to non-ideal

match of the fiber and DCM dispersions (for example due to non equal dispersion slope of DCM and optical transmission fiber).

Figure 4-4 illustrates the effect of direct detection in optical DSB and oSSB signals. For oDSB signals, the positive and negative sidebands overlap after direct detection. As a consequence, the phase modulation caused by the optical fiber dispersion is scrambled after detection. This effect is known as spectral back-folding, and makes impossible to use simple linear filters for dispersion compensation. For oSSB signals one of the spectral sidebands is suppressed; as a consequence, there is no spectral back-folding after detection and simple electrical dispersion compensation is enabled after direct detection [164] or before modulation [177].

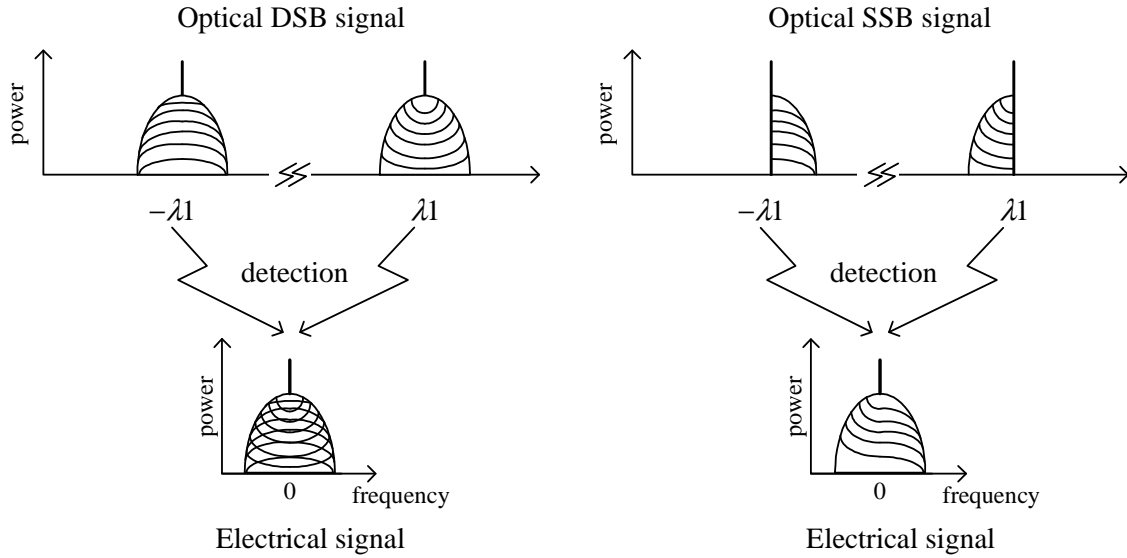


Figure 4-4: illustration of direct detection in optical DSB and oSSB signals.

The ideal filter to compensate the chromatic dispersion accumulated by the propagation of oSSB signals in optical fiber is described by the transfer function presented in (4-8) [157]; where the - / + and +/- refer to upper and lower sideband signals, respectively.

$$H_{\text{EDC}}(f) = \begin{cases} \exp\left(\mp \frac{i\pi DL\lambda^2 f^2}{c}\right), & f \geq 0 \\ \exp\left(\pm \frac{i\pi DL\lambda^2 f^2}{c}\right), & f < 0 \end{cases} \quad (4-8)$$

Figure 4-5 presents the response of the ideal electrical dispersion compensation filter for optical SSB signals of equation (4-8); considering transmission over 100 km of standard single mode fiber (SSMF) ( $D = 17$  ps/nm/km at 1550.0 nm). This filter has a flat intensity response and a quadratic phase response. As demonstrated in previous works, approximations of this transfer function can be obtained through simple passive filters like microstrip lines or Butterworth filters, or through adaptive filters [157], [164], [165], [166], with results similar to the theoretical filter of (4-8).

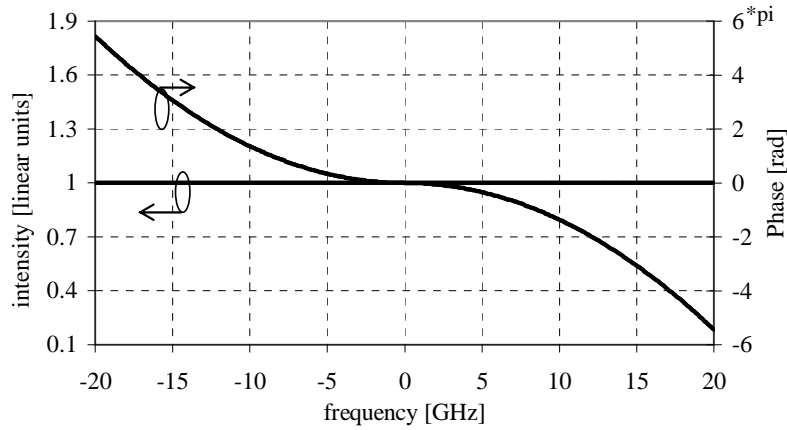


Figure 4-5: Phase and intensity response of the ideal electrical dispersion compensation filter for optical SSB signals, for 100 km of SSMF.

#### 4.2.2 All-optical generation of VSB signals with SOA

The start point for this analysis is an optical SSB signal, generated through the method proposed by Sieben et al. [157]. This method, illustrated in Figure 4-6, can be understood as a cascade of amplitude modulation (AM) and phase modulation (PM). The AM stage is driven by the electrical data signal and at its output the optical signal is a common optical DSB signal; the PM is driven by the electrical Hilbert transform of the data signal and converts the optical DSB signal into the oSSB format.

An example of the temporal evolution of the Hilbert transform of the data signal is illustrated in Figure 4-7 for a bit period of 100 ps (equivalent to 10 Gb/s). The Hilbert transform signal presents negative or positive peaks for negative or positive bit transitions of the data signal, respectively. We have demonstrated in [181] and [182] that the Hilbert transform signal can be approximated by a low-pass filtered derivative of the data signal

with acceptable sideband suppression results. Figure 4-7 presents also the frequency chirp of a lower-sideband (in the frequency domain) optical SSB signal,  $\Delta f(t)$ , defined as:

$$\Delta f(t) = -\frac{1}{2\pi} \cdot \frac{d[\phi(t)]}{dt}, \quad (4-9)$$

Where  $\phi(t)$  stands for the phase modulation. As it can be observed in Figure 4-7, the SSB signal presents a positive/negative chirp peak prior to the leading/tailing edge of the pulses, while afterwards it presents a negative/positive chirp peak.

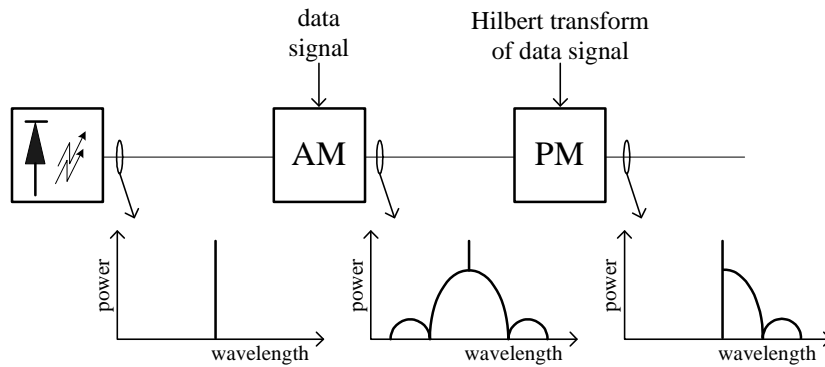


Figure 4-6: Generation of SSB signals through cascade of AM and PM [157]

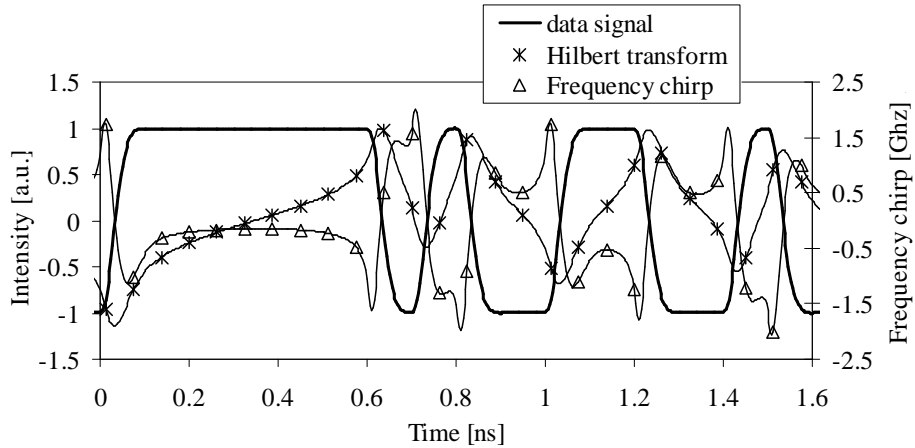


Figure 4-7: Data signal and correspondent Hilbert transform for 10 Gb/s.

The converter proposed in this work replaces the phase modulator stage of Figure 4-6 by a SOA, where the phase modulation is achieved through self phase modulation non-linear effect in the SOA. It is a well know effect [110] that, due to SPM, bit transitions lead to chirp peaks in the amplified signal. As a consequence, the signal after the SOA presents

negative / positive chirp peaks after the leading / tailing edges of the input pulses. Comparing to the oSSB signal generated according to the method described above, the chirp peaks before the bit transitions are not present in the signal after the SOA.

#### 4.2.2.1 Impact of non-ideal phase modulation in sideband suppression

In the previous section we have compared the chirp of an oSSB signal with that of a signal after a SOA: in both cases there are negative / positive chirp peaks after the leading / tailing edges of the input pulses; however, in oSSB signals there are also chirp peaks before the bit transitions. In this section, the impact of the lack of chirp peaks prior to bit transitions in the suppression of a sideband is assessed, in order to understand the potential of SPM in SOA to suppress one of the signal sidebands.

The chirp of the oSSB signal was altered through simulations: the chirp before bit transitions was removed. Figure 4-8 compares the chirp of the optical SSB signal generated after [157], and the manipulated chirp.

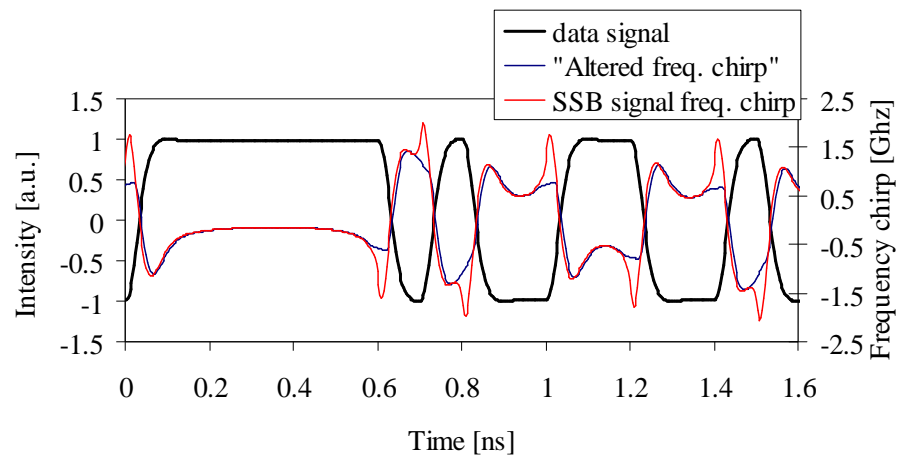


Figure 4-8: Comparison of frequency chirp in an oSSB signal generated after [157], and the chirp curve manipulated to eliminate chirp prior to bit transitions.

Figure 4-9 compares the optical spectrum of the SSB signal generated after [157] with the spectrum of the signal obtained with the manipulated chirp; the optical DSB spectrum is also presented for comparison. The ER of the plotted optical signals is 6 dB, value which maximizes the transmission reach in optical SSB systems [183], [157]. The oSSB signal depicted in Figure 4-9 presents a sideband suppression ratio of around 25.5 dB. When the first chirp peak is filtered out, the SSR is reduced to around 18.2 dB.

This result demonstrates that there is still a reasonable suppression of one of the sidebands, when the first chirp moment is filtered out.

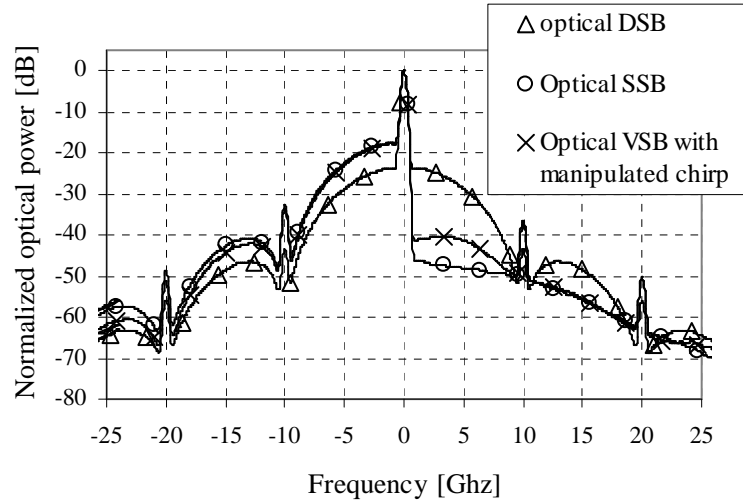


Figure 4-9: Optical spectra of oDSB signal, oSSB signal, and VSB signal with manipulated chirp.

The transmission capabilities of the vestigial sideband signal, obtained by removal of the chirp contributions prior to transitions, are compared with those of the oSSB signal in Figure 4-10: the eye opening penalty (EOP) (consult appendix III for definition of EOP) is assessed after (linear) transmission over dispersive fiber, modeled with equation (4-7), with  $D = 17$  ps/nm/km (similar to SSMF at 1550.0 nm). The optical DSB signal presents the highest degradation of EOP with the increase of transmission distance. The oSSB signal and the modified chirp signal present improved results when compared to the oDSB; additionally, the signal with modified chirp presents negligible increase in the EOP when compared to the oSSB signal. EDC is applied to both the oSSB and the modified signal, using the ideal transfer function of (4-8). It can be observed that EDC is effective also on the modified signal, since transmission over 500 km is enabled with an EOP of around 6 dB; while the SSB signal achieves that same distance with a penalty only 0.7 dB inferior.

The results presented in this section demonstrate that the lack of the chirp contribution prior to bit transitions does not affect significantly the sideband suppression. Moreover, small EOP degradation is obtained by the VSB signal with manipulated chirp, in comparison with oSSB, after transmission over dispersive fiber, in systems with and without EDC.

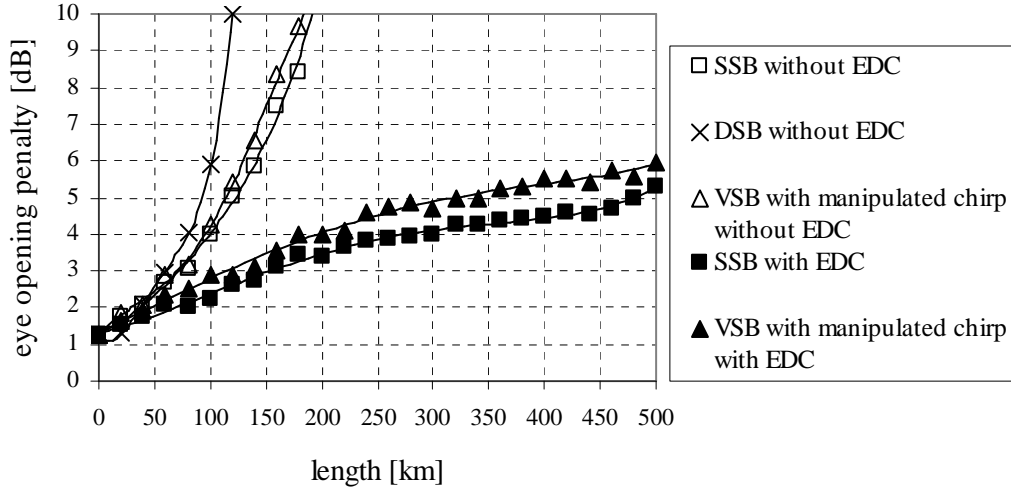


Figure 4-10: Comparison of the transmission capabilities of oDSB signal, oSSB signal, and VSB signal with manipulated chirp.

#### 4.2.2.2 SOA based converter operation principle

The operation principle of the all-optical oDSB to oVSB converter proposed in this work is based on temporal frequency chirp,  $\Delta f_{\text{SOA}}(t)$ , induced during amplification of an intensity modulated signal (IM) in a SOA [48]. Frequency chirp originates from SPM in SOA. The chirp after the SOA is represented in Figure 4-11 for a bit rate of 10 Gb/s; the SOA was modeled to fit the behavior of the device used in the experimental tests. For more details on the SOA model parameters, see Appendix II. The chirp of an oSSB signal generated with the method described in [157] is also depicted in Figure 4-11 for reference. These two signals have similar chirp curves for stand alone ‘1’ and ‘0’ of the data. For sequences of consecutive ‘1’ or ‘0’, the main difference between the two signals is that oSSB presents a positive/negative chirp peak prior to the leading / trailing edge of the pulses, and a negative / positive chirp peak after such edge; whilst the signal after the SOA only presents the negative / positive chirp peak after the leading/trailing edge of the pulses. The chirp after the SOA presents strong similarities to the modified chirp analyzed in the previous section, where it was demonstrated that reasonable suppression of a sideband can be achieved without the chirp peak prior to the bit transitions. Since the sideband suppression can never be complete using the modified chirp, the terminology Vestigial Sideband (VSB) is used hereafter. Since the SOA phase to gain coupling factor is positive, this method only enables suppression of the upper sideband.

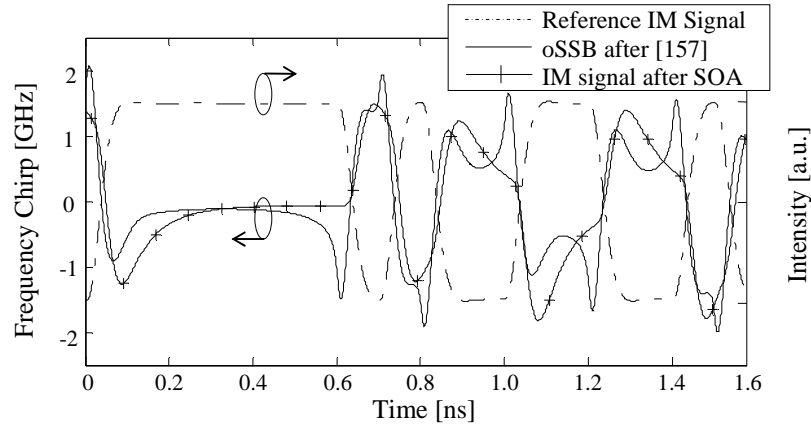


Figure 4-11: Data IM signal; frequency chirp of the IM signal after SOA amplification, and after oSSB generation with the method described in [157].

The use of the modified chirp has been employed to convert a radio-frequency (RF) signal to the SSB format [184]. However, direct application of this technique to broadband information signals causes significant amplitude distortion due to the occurrence of self gain modulation (SGM) simultaneously with SPM in SOA. Such distortion can be observed in Figure 4-12, which compares the 10 Gb/s signal at the SOA input with the SOA output signal, when the SOA is saturates with an input power of -8 dBm.

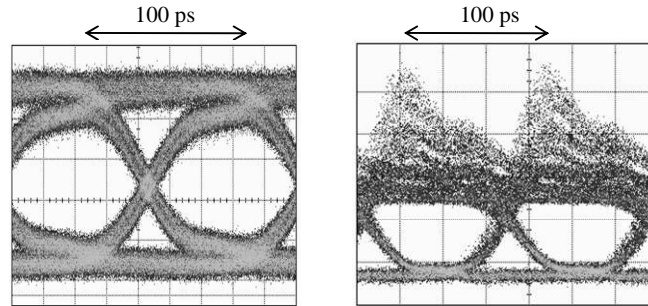


Figure 4-12: SOA input optical DSB signal (left); signal after SOA (right).

To minimize the power distortion caused by SGM effect, it is proposed in this work to couple the input data signal at  $\lambda_1$ , to a CW probe, at  $\lambda_2 \neq \lambda_1$ , at the SOA input. The conceptual converter setup is presented in Figure 4-13. The CW probe saturates the SOA and decreases the device response time[63]; therefore, higher frequency chirp is obtained for lower gain and phase variations. As a consequence, the proposed setup can operate with high bit rate broadband signals, achieving substantial sideband suppression with reduced intensity distortion. At the SOA output the two signals are present – due to XPM and XGM



the output WC probe presents residual IM and PM –, therefore an optical filter is used to remove the CW probe.

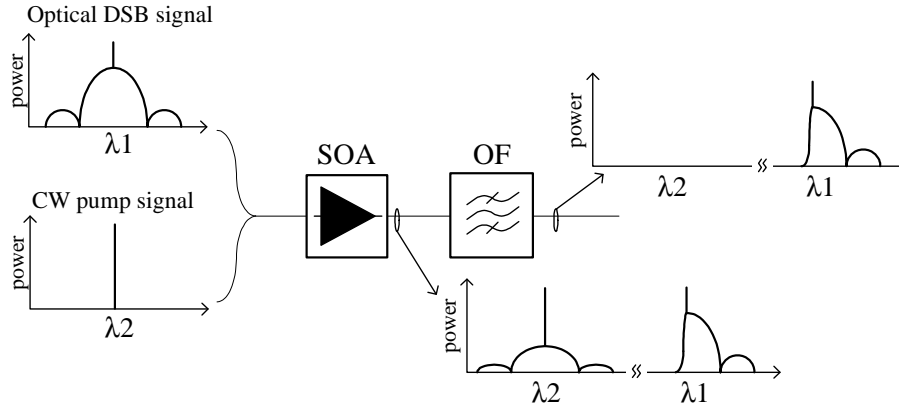


Figure 4-13: Proposed SOA based converter between oDSB and oVSB formats.

### 4.2.3 Converter operation assessment

In this section the operation of the optical DSB to oVSB converter is experimentally demonstrated at 10 Gb/s and 40 Gb/s. The setup of Figure 4-14 is used to test the performance of the converter. An optical DSB signal at  $\lambda_1$  is generated by driving a dual-arm chirp-free MZM with the information signal at the bit rate under test (10 Gb/s or 40 Gb/s). This signal is coupled with a CW probe at  $\lambda_2$ . Due to the polarization dependence of the SOA employed for the 10 Gb/s tests, the polarization of such signals is optimized; the SOA employed in the 40 Gb/s tests had only residual polarization dependency and polarization adjustment is not necessary. At the SOA output the CW probe signal is filtered out by optical filter OF1; it is important to stress that the transfer function of the optical filters do not influence the sideband suppression of the data signal. Transmission over optical fiber can be done to test the transmission properties of the VSB signal. The signal is then detected in a pre-amplified receiver, which consists of an Erbium doped fiber amplifier, an optical filter with -3 dB of 130 GHz, and a photodiode receiver with -3 dB of 10 GHz and 37 GHz for the 10 Gb/s and 40 Gb/s tests. The performance of the converter is analyzed measuring the sideband suppression ratio. The SSR is experimentally measured with an optical spectrum analyzer (OSA) with a 0.01 nm resolution (RES). Since the SGM effect can cause amplitude degradation,  $Q$ -factor and BER measurements are also presented.

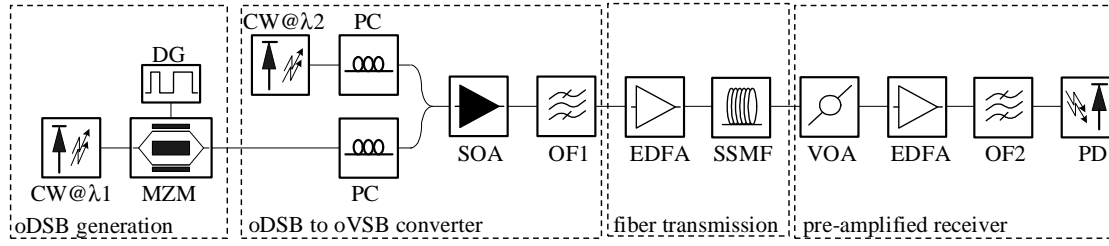


Figure 4-14: Experimental setup to assess the performance of the optical DSB to oVSB format converter.

#### 4.2.3.1 Results at 10 Gb/s

For the 10 Gb/s tests, an IM oDSB signal with a pattern length of  $2^{11}-1$  bits is considered. The wavelengths of the data signal and CW probe are 1552.38 nm and 1550.8 nm, respectively. The employed SOA is the *slow* device (consult Appendix III for characteristics of the SOA devices utilized throughout this work.). A notch rejection filter, realized through FGB, is employed to remove the CW probe signal at the output of the SOA; the notch filter, OF1, is centered at  $\lambda_2$ , and has a -3 dB bandwidth of 0.73 nm.

Figure 4-15 a) depicts the optical spectra of the optical DSB signal before the SOA and of the converted optical VSB signal; the correspondent eye diagrams are presented in Figure 4-15.b) and c), respectively. The extinction ratio (ER) of the input signal is 6 dB in order to optimize the optical VSB signal transmission over fiber [157], [183]. From Figure 4-15 a), a considerable part of the spectral power is moved to the lower sideband (in the frequency domain); the SSR in this case is 15.7 dB.

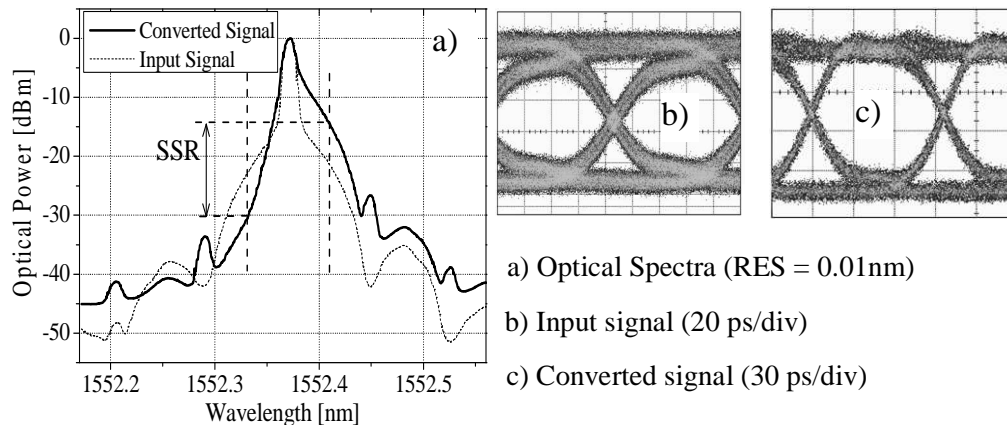


Figure 4-15: Optical spectra and eye diagrams of the input and converted signal, when the SOA input power of the optical DSB signal and CW probe are -0.4 and 1.9 dBm, respectively.

The oVSB signal eye diagram depicted in Figure 4-15 c) evidences an improvement in the eye opening, comparing to the input oDSB, presented in Figure 4-15 b). This improvement results simultaneously from the reshaping caused by the SOA response, which decreases the signal rise time [48]; and the SOA gain compression that, for the referred input power conditions, reduces the variance of the logical '1' [185].

Tolerance to power variations of data signal and CW probe signal

The operation of the proposed setup relies on SPM non-linear effect, which is dependent on the input signal power. The influence of the power of the data signal and of the CW probe signal on the converter performance is analyzed. Figure 4-16 presents the SSR and  $Q$ -factor of the converted oVSB signal for two scenarios: in the first, the CW probe signal is disabled, and the data signal is amplified in the SOA; in the second, the probe power is 1.9 dBm and both signals are amplified in the SOA. The input signal  $Q$ -factor is 6.5.

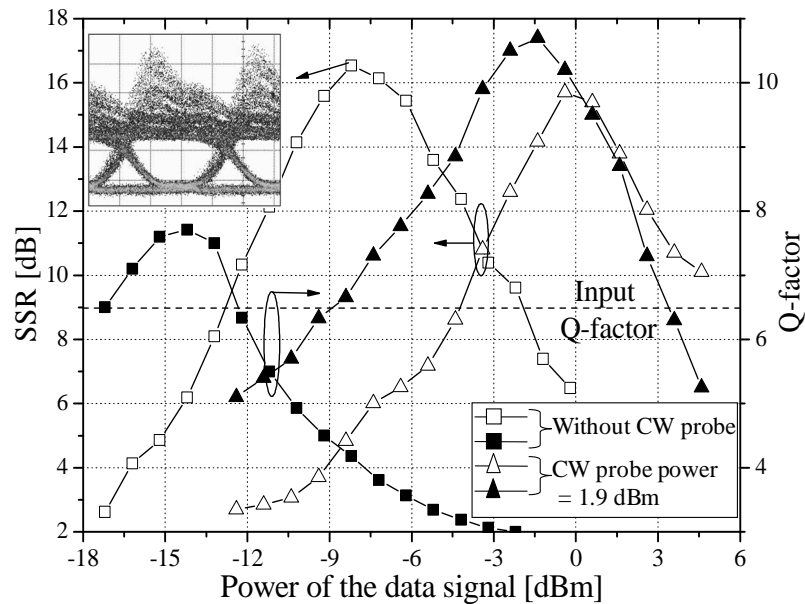


Figure 4-16: SSR and  $Q$ -factor as a function of the data signal power at the SOA input. Inset: eye diagram for data signal power of -8.2 dBm and disabled CW probe.

When the probe signal is disabled, a low  $Q$ -factor, 4.2, is retrieved for the power value of the data signal that enables the highest SSR. Under such condition, the SOA optical gain varies 4 dB between the two logical levels of the data signal (measured in

continuous wave conditions) resulting in high SGM and eye diagram distortion, which can be observed inset Figure 4-15. Similarly, a low SSR, 6.2 dB, is obtained with the input signal power is tuned for maximum output  $Q$ -factor.

As discussed above, enabling the CW probe signal results in faster SOA response; therefore, lower gain variations are required for the same amount of chirp, and the SGM induced distortion is reduced. By optimizing the probe power, an optimum operation point can be reached, where the input data signal power that leads to the maximum SSR also enables the maximum  $Q$ -factor. Considering a CW probe power of 1.9 dBm a maximum SSR of 15.7 dB is retrieved, for data signal power of -0.4 dBm. In this condition, the SOA optical gain only varies 1.4 dB between the two logical levels of the data signal, so the SGM effect does not affect negatively the eye diagram. Furthermore, gain saturation leads to improvements in the data eye diagram [185], and a  $Q$ -factor of 10.2 is retrieved. Under these conditions, the oVSB optical spectrum and eye diagram are presented in Figure 4-15.a) and c). Considering a minimum SSR requirement of 13 dB to assure the VSB characteristic, and a minimum  $Q$ -factor of 6.5 for the oVSB signal, the power of the input data signal can vary between -1.9 and 1.7 dBm, while keeping the probe signal power constant.

If the probe signal power is adapted to the input signal power, higher operation range is expected. Higher data signal power leads to the increase of the frequency chirping above the optimum level. To compensate, the probe signal power should also be increased to drive the SOA further in saturation. Similarly, for lower data signal powers, the probe signal power should also decrease to reduce the SOA saturation. Figure 4-17 presents a characterization of the converted oVSB signal SSR and  $Q$ -factor as a function of data signal and the CW probe powers.

Figure 4-17 demonstrates that SSR above 13.0 dB can be achieved simultaneously with an output  $Q$ -factor higher than the input (6.5), for a range of signal input power higher than 13 dB (from -9.2 dBm to 4 dBm), provided that the probe power is optimized. The probe signal is required to change from -16 dBm to 5.8 dBm to allow the referred operation range, Such results demonstrate the potential for the converter operation in a meshed network, where optical power values may assume arbitrary values, depending for example on wavelength, fiber type and fiber length, and other factors.

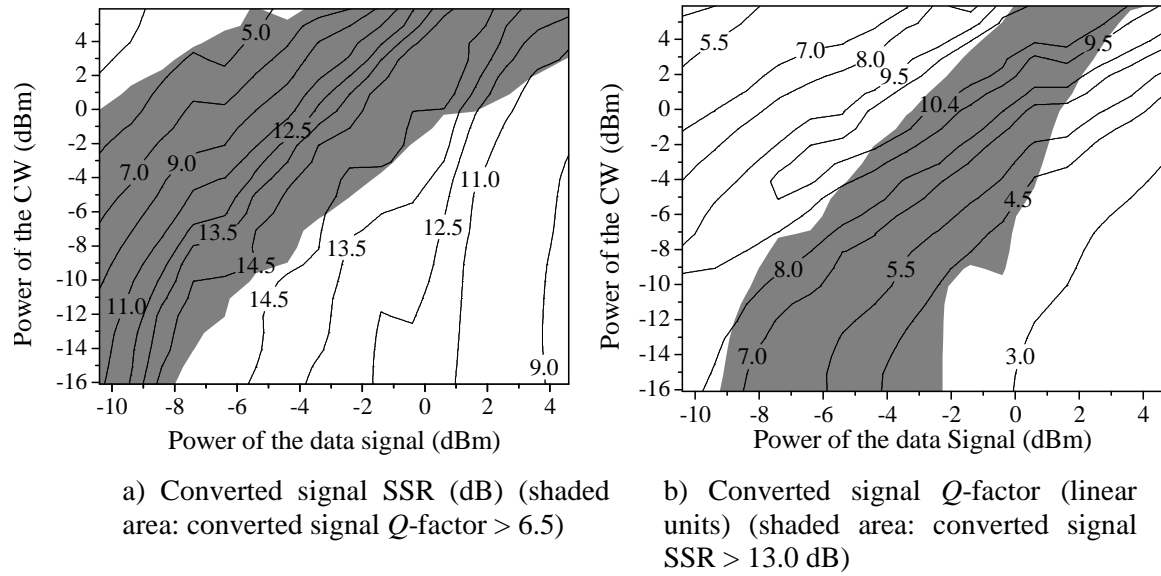


Figure 4-17: Converted signal characterization as a function of the power of the input data signal and of the CW probe.

#### Input signal extinction ratio

The impact of the input signal extinction ratio on the converter operation is studied in this section. For such purpose, the ER of the signal to be converted is varied by actuating the voltage swing of the electrical signals driving the MZM; the maximum ER obtained with the experimental MZM is 8.3 dB. The characterization of the converter output signal is presented in Figure 4-18, where the signal SSR and  $Q$ -factor are depicted. The input signal and CW probe powers are kept constant at -8 dBm and 2.5 dBm, respectively.

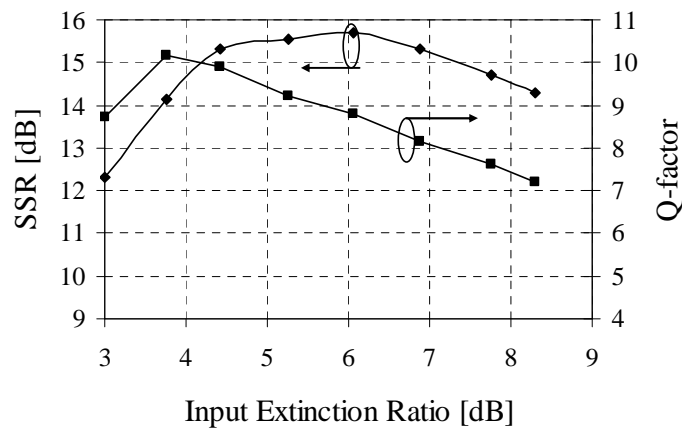


Figure 4-18: Characterization of the converted signal SSR and  $Q$ -factor as a function of the input signal ER.

The converted signal SSR is above 13.0 dB for provided that the input ER is higher 3.5 dB. The converted signal  $Q$ -factor is above the input  $Q$ -factor, which is 6.5 for all tested ER. The decrease in  $Q$ -factor observed for high ER is due to penalty from SGM effect, which has a higher impact for higher input power variations between the two logical levels. The  $Q$ -factor degradation could be compensated by adapting the probe power separately for each ER. Nevertheless, these results demonstrate wide ER operation range.

#### Input signal wavelength

The proposed setup is expected to depend on the input wavelength, since the SOA gain is not constant with the wavelength: it has a -3 dB gain bandwidth of 41 nm. Figure 4-19 shows the variations in the  $Q$ -factor and SSR for different data signal wavelengths. The power conditions are maintained in all the measurements of Figure 4-19, and the CW probe wavelength was set to 1550.8 nm. The data signal wavelength is varied from 1531 nm to 1569 nm, excluding 3 nm around the probe wavelength, due to the use of the FBG notch. An SSR higher than 13 dB is observed for data signal wavelengths ranging from 1537.3 nm to 1563.3 nm (26 nm). For this range the measured  $Q$ -factor is always above 8.5. The operation range can be increased optimizing the power levels at the SOA input for each wavelength or using a SOA with wider gain bandwidth.

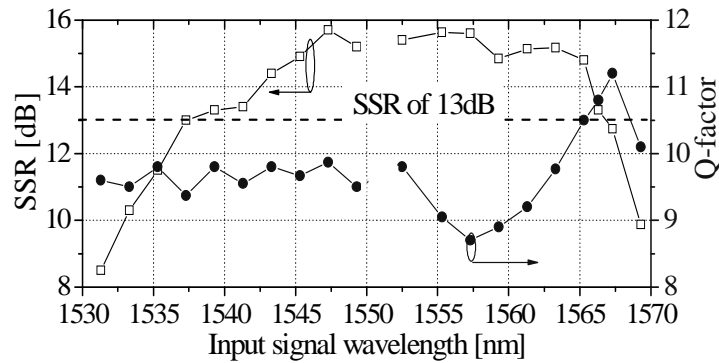


Figure 4-19: Impact of the signal wavelength on the output SSR and  $Q$ -factor.

#### Transmission tests

One of the most interesting features of sideband suppressed signals is its robustness to chromatic dispersion. The original oDSB and the oVSB signals at 1552.38 nm are transmitted over fiber with positive dispersion ( $D+$ ) (SSMF); the measured receiver sensitivity for a bit error rate (BER) of  $10^{-9}$  is plotted in Figure 4-20 as a function of the

accumulated dispersion. The optical power at the fiber input is kept below 0 dBm, to ensure that non-linear effects are insignificant. For chirp free signals, such as the oDSB signal used throughout this work, transmission over positive and negative dispersion results in identical penalties; to verify the impact of the chirp induced by the SOA, the oVSB signal was also transmitted over fiber with negative dispersion (D-) (dispersion compensation fiber).

The oDSB signal presents a 4.0 dB penalty in the receiver sensitivity for 1360 ps/nm of accumulated positive dispersion (equivalent to 80 km of standard single mode fiber (SSMF)), relatively to back-to-back. On the other hand, the oVSB is penalized by only 1.1 dB for 1360 ps/nm of D+ and the transmission distance can be further extended to 2720 ps/nm (160 km of SSMF) with only 5.3 dB of penalty, demonstrating the enhanced tolerance of oVSB to chromatic dispersion. The transmission results and inset eye diagrams are in agreement with those of another setup to generate oSSB signals [157]. Transmission of the oVSB signal over accumulated negative dispersion also demonstrates enhanced tolerance compared to oDSB, since -2720 ps/nm of dispersion result in a penalty of 8.2 dB. Small difference between transmission over positive and negative dispersion are due to SOA induced phase modulation. Improved results are expected if electrical dispersion compensation is used after the receiver [157].

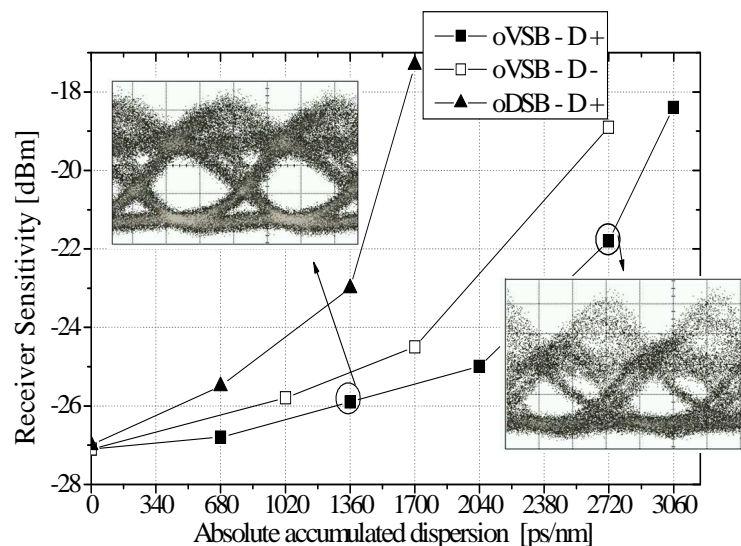


Figure 4-20: Receiver sensitivity for the oDSB and oVSB signals. Insets: oVSB signal diagrams after 1360 and 2720 ps/nm of accumulated positive dispersion.

### Electrical dispersion compensation after direct detection

An important characteristic of sideband suppressed signals is their aptitude to electrical dispersion compensation using very simple dispersive lines. In this section, the sideband suppressed signal generated with SOA is transmitted and detected, and then filtered with an ideal dispersion compensation filter.

Due to the unavailability in our facilities of an electrical dispersive filter appropriate to compensate dispersion on a lower sideband signal at 10 Gb/s, the tests of this section are performed through simulations. Figure 4-21 compares the eye diagram of an oSSB signal generated with the method of [157] when an ER of 6 dB is considered (a), and of a VSB signal generated by SPM in a SOA (b). As previously noted, the detection of the oSSB signal generated by the method of [157] does not present any amplitude distortion due to the Hilbert transform. On the other hand, the signal generated by the method presented in this work presents some amplitude distortion after detection. Nevertheless, the simulated sideband suppressed signal of Figure 4-21 still presents an open eye diagram, which can be employed in transmission over fiber.

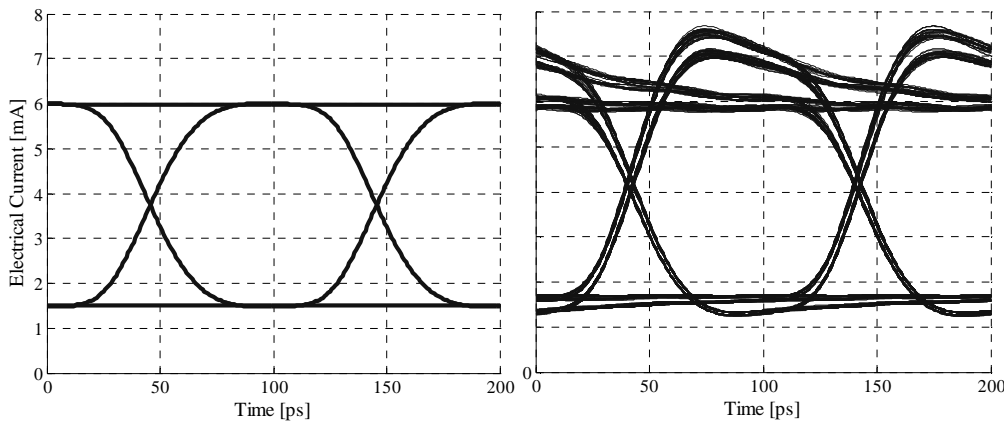


Figure 4-21: Detected eye diagrams of ideal oSSB signal [157] with 6dB ER (left), and oVSB signal generated with SOA (right).

The optical spectra of the optical SSB signal after [157] and of the oVSB signal are compared in Figure 4-22. The oSSB signal presents a SSR of approximately 29.0 dB, whereas the oVSB signal SSR is around 15.5 dB. This result is in agreement with the experimental results of the previous section.



Figure 4-23 compares the eye diagrams of the oSSB signal and the sideband suppressed signal after transmission over 160 km when EDC is not used – (a) and (b), respectively –, and when ideal EDC, realized by equation (4-8), is considered – (c) and (d), respectively. Before EDC, both eye diagrams present significant opening, due to accumulated dispersion. When EDC is applied, the oSSB signal presents an eye diagram with reduced distortion, proving the effectiveness of EDC. The oVSB, resulting from conversion in SOA, also presents eye diagram improvements when EDC is considered, but it demonstrates considerably higher distortion than the oSSB signal, arising from non-ideal sideband suppression in the SOA.

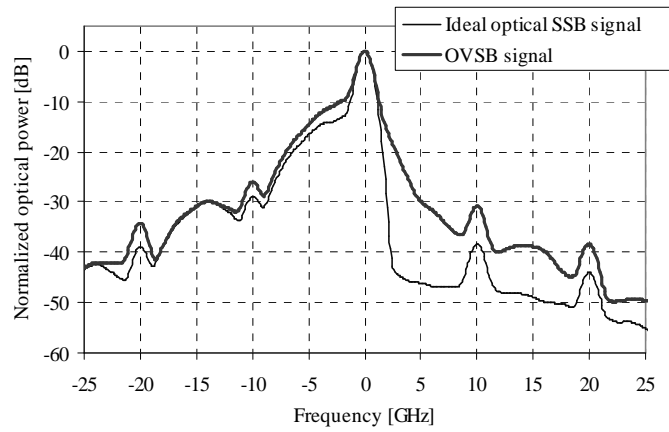


Figure 4-22: Optical spectra of the oSSB signal generated after [157] and of the oVSB signal generated with SPM in SOA.

In [186] and [187] it was demonstrated that a composed electrical dispersion compensation filter, realized by the cascade of a dispersion compensation device with non-ideal transfer function – a microstrip line – and a transversal filter, obtains results comparable to the ideal dispersion compensation filter of equation (4-8). In this work the ideal dispersion compensation filter is cascaded with a transversal filter to improve the transmission results of the sideband suppressed signal. Note that microstrip lines can not be considered, since these can only compensate for dispersion of upper sideband signals (in the frequency domain). The composed filter is presented in Figure 4-24. The input electrical signal is first equalized in the ideal dispersion compensation filter. The resultant signal is fed to a transversal filter with 7 taps. In the transversal filter, the input signal is split in seven replicas. The replicas suffer consecutive delays of  $\tau$ , are amplified with gain  $a_i$  and are added at the filter output. The delay between taps,  $\tau$ , is 50 ps. The gain of each tap,  $a_i$ , is optimized to improve the signal eye opening with a modified simplex algorithm,

known as Nelder-Mead method [188]. The number of taps is chosen as a compromise between convergence time and obtained improvements in the output signal.

The modified simplex method uses the general concept of *simplex*. In geometry, a simplex generalizes the concept of a triangle to  $N$  dimensions. The modified simplex method creates an  $N$  dimension object where each dimension represents one of the optimization variables (the filter coefficients in this specific case). In each step, the method modifies the object shape in size in order to converge to a minimum of the function to optimize (EOP in this case). The modified simplex algorithm is simple to implement and allows fast initial convergence. Moreover, it is robust as it allows discontinuities. The main disadvantages are that it may converge to local minimums, and its convergence pace slows close to the minimum. In depth description of the simplex algorithm can be found in [188].

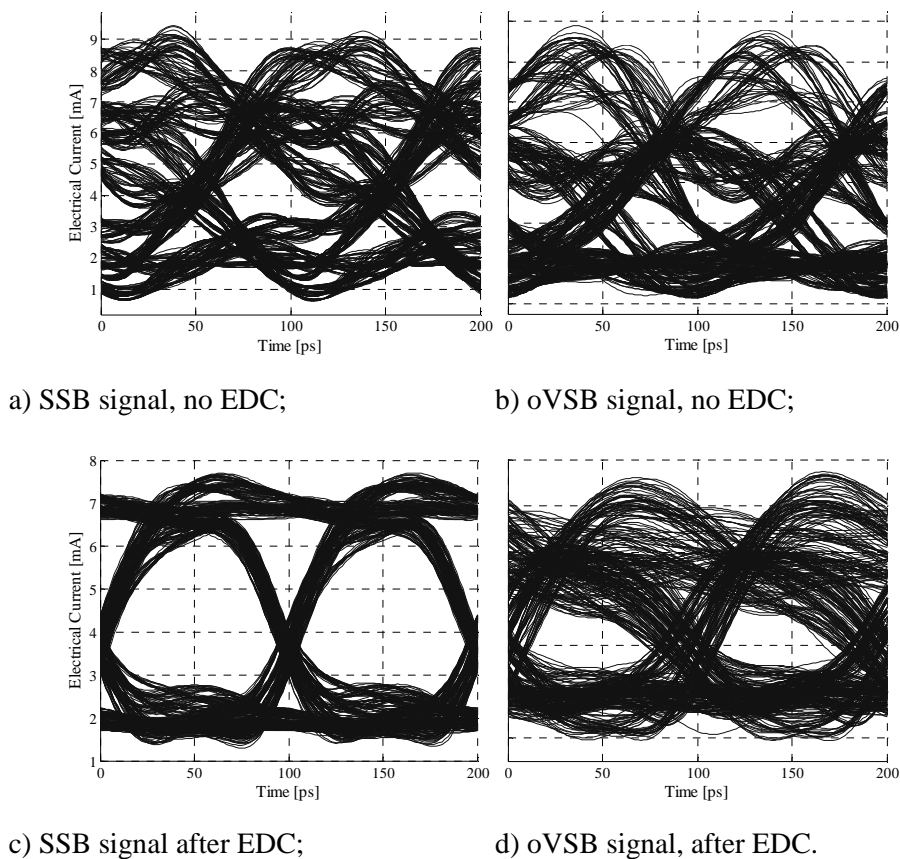


Figure 4-23: Eye diagrams after transmission over 160 km of SSB signal and of the oVSB signal after conversion in SOA. Two scenarios considered: no EDC and EDC via ideal filter.

Figure 4-25 compares the eye opening penalty as a function of the transmission distance for optical DSB, optical SSB with and without ideal EDC, and the sideband

suppressed signal with and without the composed EDC of Figure 4-24. If a maximum EOP of 6 dB is allowed, optical DSB is limited to 100km of transmission, according to the results of Figure 4-25. Optical SSB and the sideband suppressed signals increase this distance to 140 km without any EDC. When the composed EDC filter is employed, the maximum transmission distance for the oVSB signal is doubled to 280 km. This represents nearly the triple of the transmission distance of the oDSB signal. Optical SSB signal and ideal filter allows transmission over distance higher than 500 km. The inset in Figure 4-25 presents the eye diagram of the oVSB signal when the composed EDC is considered, which presents considerable improvements when compared to the signal obtained with only the ideal EDC filter depicted in Figure 4-23 d).

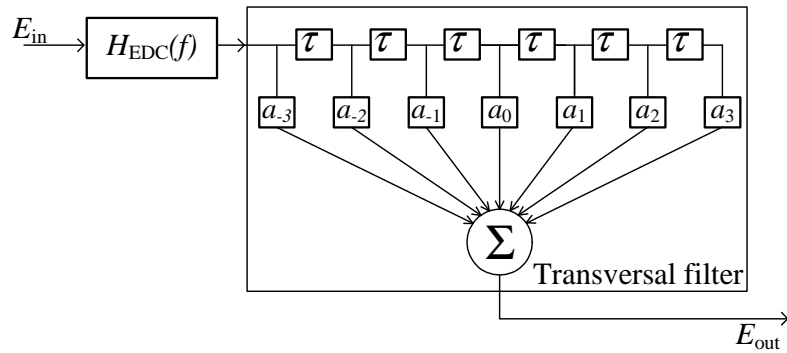


Figure 4-24: Composed filter to compensate dispersion of the sideband suppressed signal. First stage consists on the ideal filter of equation (4-8), and second stage is an adaptive filter with 7 taps.

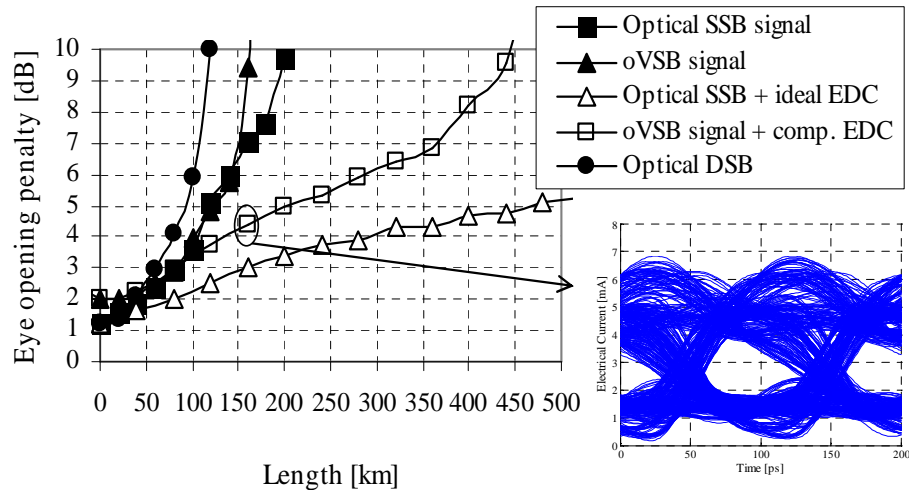


Figure 4-25: Comparison of the transmission capabilities of oDSB signal, oSSB signal with and without ideal EDC, and oVSB signal without and with composed EDC. Inset: eye diagram of the oVSB signal after 160 km and composed EDC.

#### 4.2.3.2 Results at 40 Gb/s

In the previous section we have experimentally demonstrated conversion of a 10 Gb/s oDSB signal to the oVSB format with SOA. In this section the same operation principle is exploited to obtain conversion at 40 Gb/s. First, the *slow* SOA device (the same considered in the 10 Gb/s tests) is employed; afterwards the *fast* SOA is considered. Back-to-back and transmission tests are performed.

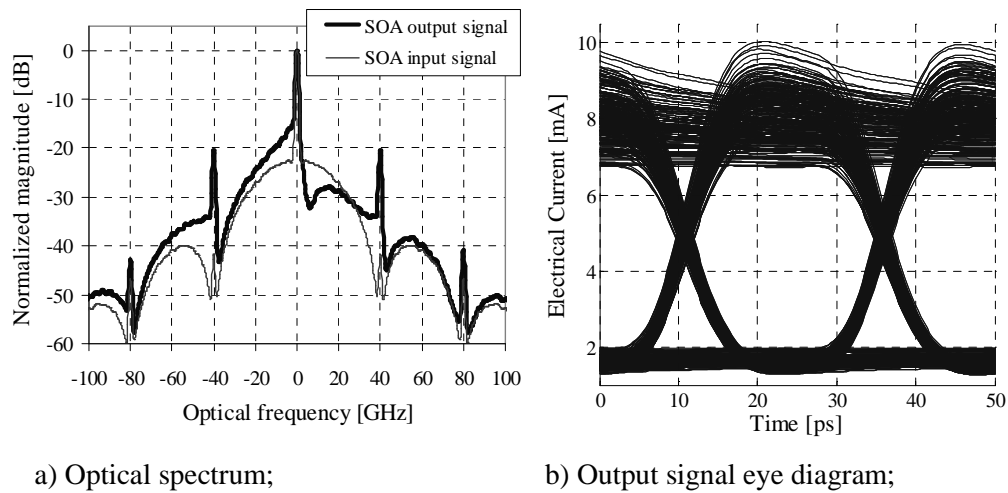
##### Performance with slow SOA device

The process underneath suppression of sideband power of oDSB signals proposed here is based on the SPM induced by SOA. However, such non-linear process is limited by the SOA carrier lifetime. If the carrier lifetime is short in comparison to the bit period duration, the SPM process will be too fast and no power suppression will occur in the frequencies near to the optical carrier. On the other hand, if the carrier lifetime is too large in comparison to the bit period duration, frequencies distant from the optical carrier will suffer insufficient power suppression.

To illustrate the affirmation above for the case where a too slow device is employed (larger carrier lifetime), it is attempted to suppress a sideband of a 40 Gb/s signal with the *slow* device (employed in section 4.2.3.1 to perform conversion at 10 Gb/s). The optical powers of the CW probe and of the data signal are 2 dBm and 0 dBm, respectively. These values are approximately the optimum power values obtained in the previous section for conversion at 10 Gb/s. The resultant output optical spectrum and eye diagram are illustrated in Figure 4-26 where it can be observed that reasonable sideband suppression is obtained close to the optical carrier; however, for higher frequencies the sideband suppression mechanism is not efficient.

It was observed in the section 3.3 that one of the techniques to improve the SOA carrier recovery time is to increase the power of the signals at its input. Figure 4-27 represents the SSR and EOP as a function of CW probe signal power at the SOA input, for different input signal power values. The converter input signal presents an EOP around 1.2 dB, corresponding to ER of 6 dB.

Considering a minimum acceptable SSR of 13 dB, the EOP of the output signal is 5.6 dB, 5.0 dB for data signal power of 5 dBm, and 10 dBm, respectively (for 0 dBm, of input power, SSR of 13 dB is not obtained within the probe power range under test). Such EOP values represent a significant degradation of the data signal when compared to the input; therefore, we may conclude that for acceptable power levels in the SOA (below 10 dBm) it is not possible to obtain acceptable sideband suppression at 40 Gb/s with the *slow* device employed for the 10 Gb/s tests.



a) Optical spectrum;

b) Output signal eye diagram;

Figure 4-26: Simulation of sideband suppression at 40 Gb/s with the device used for 10 Gb/s.

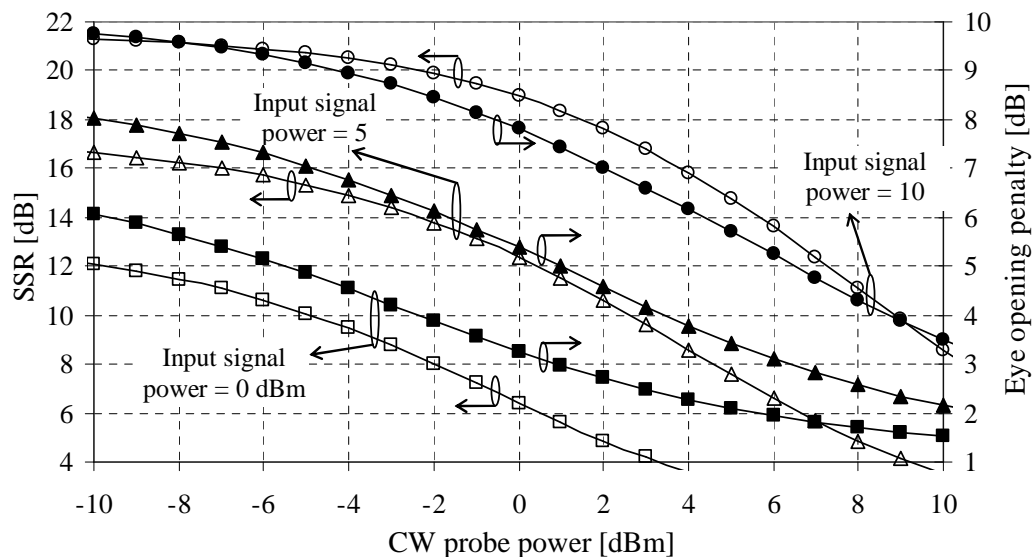


Figure 4-27: SSR and EOP the 40 Gb/s oVSB signal converted in the device used for 10 b/s, as a function of the power of the input signals.

### Back-to-back performance and sideband suppression with fast SOA device

The setup of Figure 4-14 is employed to experimentally test the converter operation at 40 Gb/s. For such purpose a 40 Gb/s data generator is employed, originating an intensity modulated oDSB signal with a pattern length of  $2^{11}-1$  bits. The *fast* SOA device is operated with 400 mA.

Figure 4-28 presents the experimental optical spectrum of the input oDSB signal, and of the converted oVSB signal. The converted signal presents the vestigial sideband characteristic spectrum, as significant power suppression of the signal upper sideband is observed; the measured SSR is 13.5 dB. Regarding the eye diagram, some distortion is observed in the converted signal, particularly in the transitions from '0's to '1's: this distortion is due to self-gain non-linearity. This effect is more preminent in the experimental results of 40 Gb/s than in the 10 Gb/s results, due to the particular shape of the eye diagram of the input oDSB signal employed at 10 Gb/s; nevertheless, the converted signal eye diagram depicted in Figure 4-28 resembles the converted signal eye diagram of the 10 Gb/s simulations of Figure 4-21 b).

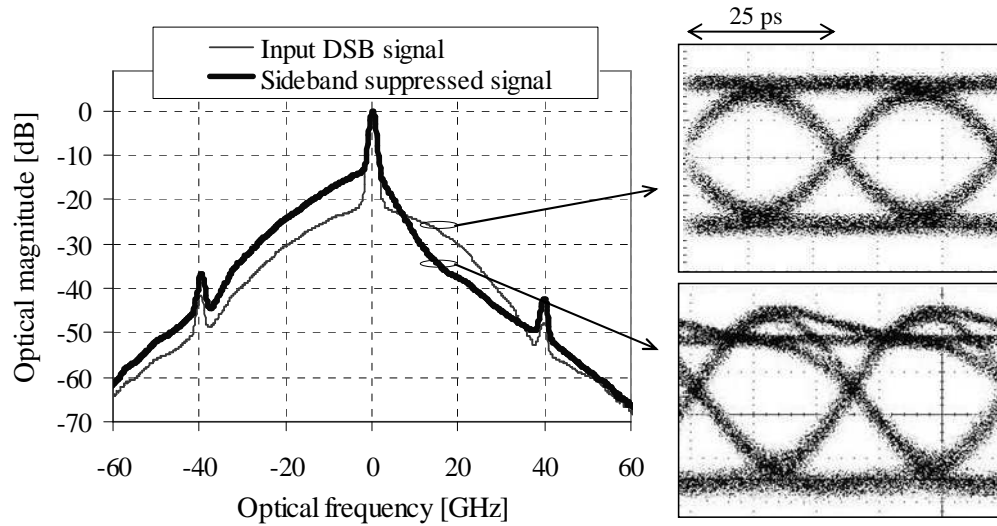


Figure 4-28: Experimental optical spectra of oVSB converter input and output signals. Inset: input signal eye diagram and converted signal eye diagram.

In addition to the SSR, bit error rate measurements are performed to evaluate the intensity of the distortion introduced by the SGM. Figure 4-29 presents the BER and SSR of the oVSB converted signal, as a function of the optical power of the oDSB data signal at the SOA input; the CW probe power is kept constant at 0.5 dBm. The optical power at the

input of the receiver EDFA was chosen to grant  $\text{BER}=10^{-9}$  for the input oDSB data signal when the oDSB generator was characterized in back-to-back.

Figure 4-29 shows that with constant probe signal power, the converter enables SSR values above 13 dB for input data signal power ranging from -2 dBm to 3 dBm, enabling a 5 dB variation of the signal power; the maximum SSR obtained is 14.5 dB, corresponding to a data input power of 0 dBm. It can be verified that there is a BER degradation when compared to input, which is due to OSNR degradation in the SOA and to distortion induced by SGM. Moreover, the degradation verified in the BER curve with the increase of the input data power is due to the eye distortion provoked by the SGM; such distortion increases with the data signal power, as can be verified from the inset eye diagrams. For the power range that allows higher SSR the BER is around  $3.5 \cdot 10^{-4}$ ; which represents a degradation of 4.5 orders of magnitude, when compared to the input signal.

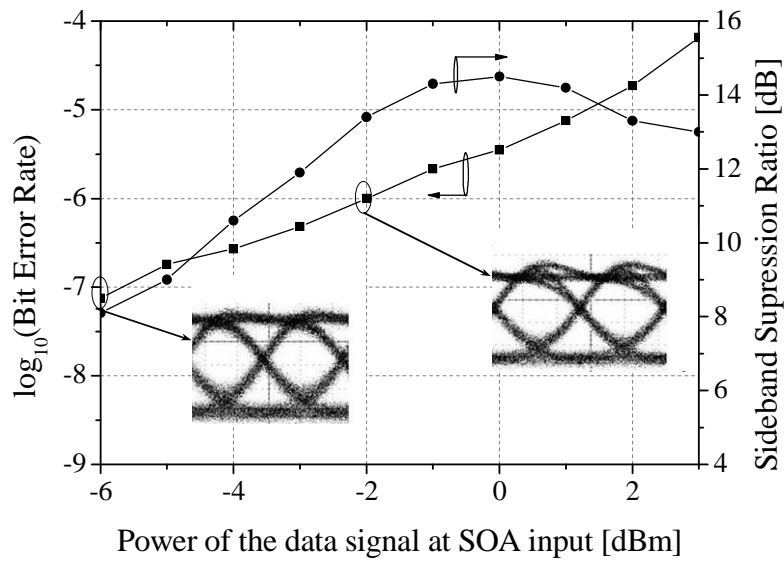


Figure 4-29: BER and SSR of the converted oVSB signal, as a function of the data signal power at the SOA input for constant probe power of 0.5 dBm. Inset: eye diagrams for input signal power of -6 dBm and -2 dBm.

### Transmission results

Experimental tests of previous section showed that the 40 Gb/s converter output signal presents penalties in the BER in back-to-back condition. Here, the resilience to chromatic dispersion accumulation is assessed. For such purpose, different lengths of standard single mode fibre (SSMF) are introduced in the transmission link after the oVSB

converter, as illustrated in the setup depicted in Figure 4-14. The oVSB signal power at the SSMF input is below 5 dBm, guaranteeing negligible impact from the nonlinear transmission effects. The power levels of the data signal and the CW probe at the SOA input are -2.0 dB, and 0.4 dBm; such power levels are chosen from Figure 4-29, as a compromise between SSR and BER degradation. Figure 4-30 presents BER curves for oDSB and oVSB signals for different accumulated fiber dispersion values, as a function of the optical receiver input power. The back-to-back receiver required input power for a BER of  $10^{-9}$  is 2.4 dB higher for oVSB than for oDSB; which is in agreement with the conclusions of Figure 4-29. However, after 102 ps/nm, the BER curve of the oVSB signal presents an improvement of 2.2 dB compared to back-to-back, due to the chirp introduced in the sideband suppression process using the SOA. The power penalty for a BER of  $10^{-9}$ , verified by the oVSB signal after 170 ps/nm, is 9 dB, when compared to the back-to-back oDSB signal. Overall, the results of Figure 4-30 demonstrate that the oVSB signal extends the maximum transmission distance when compared to original oDSB signal: whilst oVSB reaches 170 ps/nm (10 km of SSMF) without BER floor, whilst the oDSB signal already presents a BER floor after 102 ps/nm of accumulated dispersion (6 km).

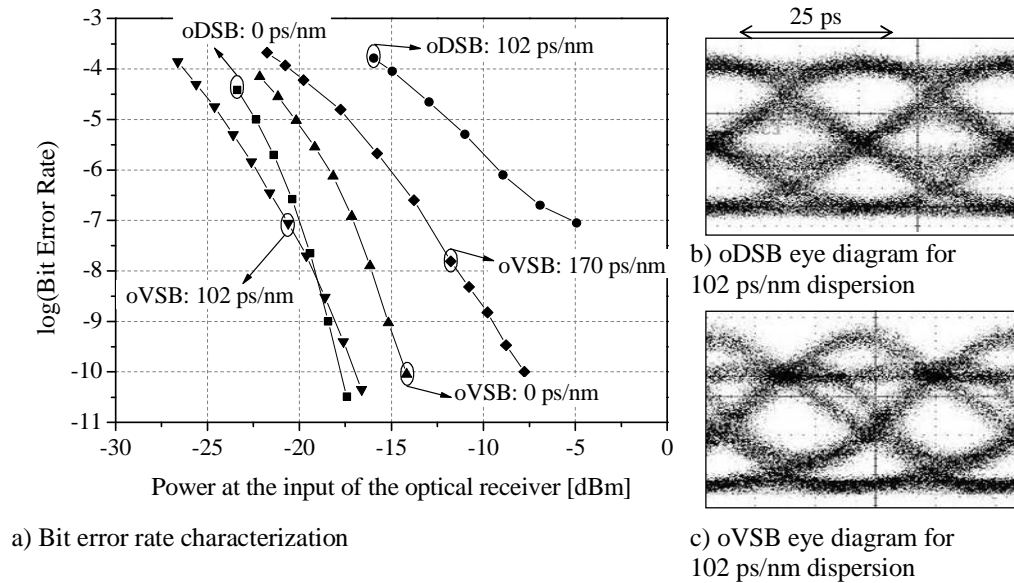


Figure 4-30: BER as a function of the optical receiver input power for different fibre dispersion values.

As detailed previously, self-homodyne detection of optical DSB signals introduces the so called *spectral back-folding*, which prevents from the use of simple methods to perform EDC. On the other hand, signals with a sideband suppressed, suffer reduced



spectral back-folding after self-homodyne detection; therefore, oVSB signals allow the use of efficient EDC at the receiver side. Hereafter experimental 40 Gb/s EDC, implemented using a transversal filter (TF) with 5 taps and tap delay of 18 ps [189], is employed after self-homodyne detection. The degrees of freedom in the TF are the gain of each tap, which can be independently optimized to minimize the BER. Due to experimental constraints, there is no automatized feedback loop available; therefore, tap gain optimization is done manually. Figure 4-31 presents BER as a function of the optical receiver input power for different fiber dispersion values, using the TF at the receiver side.

The use of the TF, allows significant improvements in back-to-back. This occurs because the TF optimizes the receiver bandwidth, reducing the total noise; moreover, the TF compensates for the inter-symbol interference introduced by the SGM of the SOA. Additionally, the TF also extends the allowed CD range from 170 ps/nm to 238 ps/nm for oVSB. A penalty of 10 dB in the received power for a BER of  $10^{-9}$  is observed after 238 ps/nm of accumulated dispersion (14 km of SSMF) using the TF. This result demonstrates the potential of the proposed method, especially when combined with adaptive EDC.

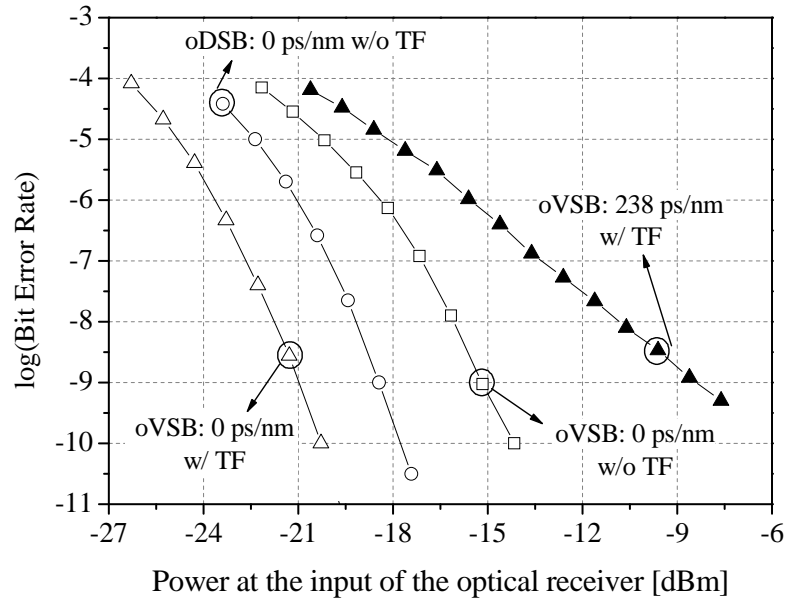


Figure 4-31: BER as a function of the optical receiver input power for oVSB and an adaptive transversal filter (TF), for different accumulated dispersions

We have proposed and experimentally demonstrated ODSB to oVSB conversion in a simple SOA-based scheme. This converter is resilient to input signal variations, such as power, wavelength or extinction ratio. Moreover, we demonstrated promising fiber

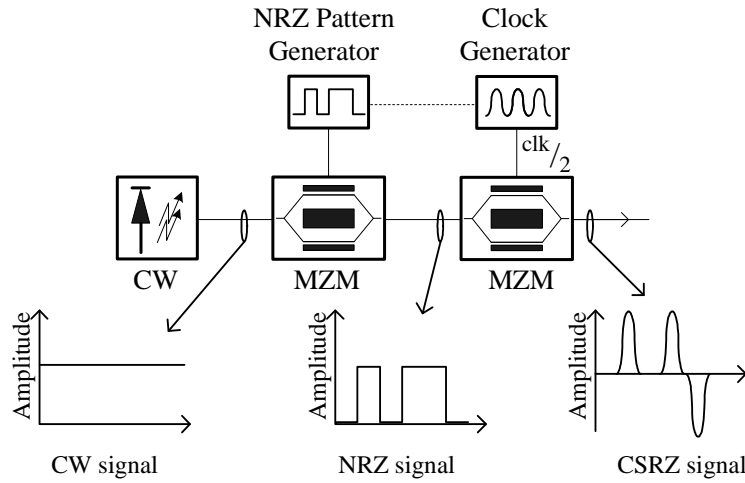
transmission results without any optical dispersion compensation devices. Since this thesis is developed in an industrial environment, 10 Gb/s and 40 Gb/s stand-alone prototypes have been developed. These are reported in detail in appendix IV.

### 4.3 *On-off keying to CSRZ converter*

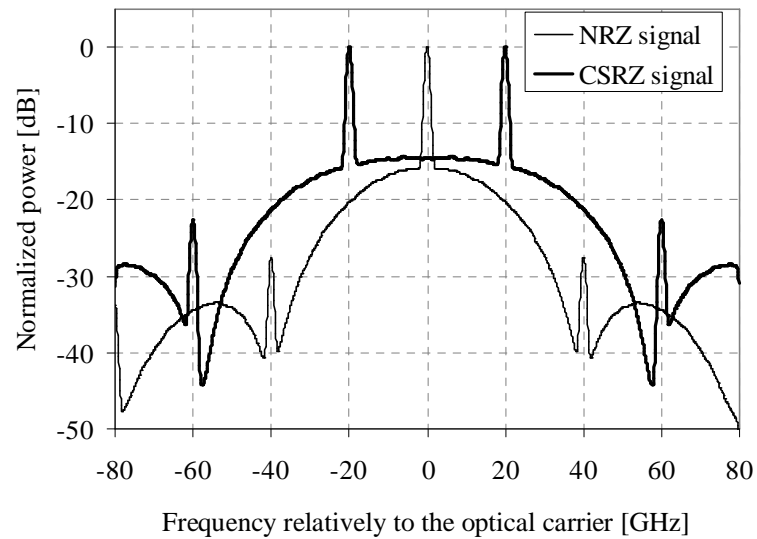
#### 4.3.1 Operation Principle

In this section a converter from on-off keying (OOK) to carrier suppressed return-to-zero (CSRZ) signaling, based on cross-gain and cross-phase modulation in SOA, is proposed. For comparison, Figure 4-32 a) presents the conventional CSRZ modulator scheme [167]. A continuous wave (CW) signal is first modulated at a MZM, biased at quadrature, fed by an electrical NRZ signal. The MZM output signal is common optical OOK NRZ signal with double sideband modulation. The optical NRZ signal is then modulated in a second MZM; this modulator is biased at minimum transmission and driven by a clock signal, at half the repetition rate of the data signal. At the output of the second MZM, the optical signal intensity presents an RZ shape; however, consecutive the phase of consecutive bits is shifted of  $\pi$ . Since this method requires the use of two cascaded MZM devices, it presents several drawbacks: high insertion loss (IL), polarization dependence (since MZM are polarization dependent), an electrical clock generator is required, and is not cost effective.

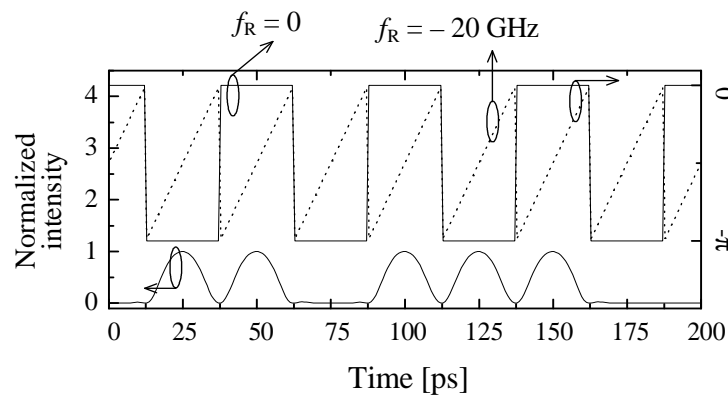
Figure 4-32 b) compares the CSRZ signal optical spectrum at the output of the CSRZ modulator scheme, and the optical spectrum of the NRZ optical signal at the output of the first MZM, for a bit rate of 40 Gb/s. The NRZ signal has one optical carrier at the center of the spectrum; on the other hand, the CSRZ signal has two optical carriers with equal intensity, separated by  $\pm 20$  GHz from the center of the spectrum. The central frequency of the CSRZ spectrum, which corresponds to frequency 0 in Figure 4-32 b), coincides with the frequency of the continuous wave input signal and with the optical carrier of the NRZ signal.



a) CSRZ modulator structure employing two MZM;



b) Optical spectra of intermediate NRZ signal and CSRZ signal at output;



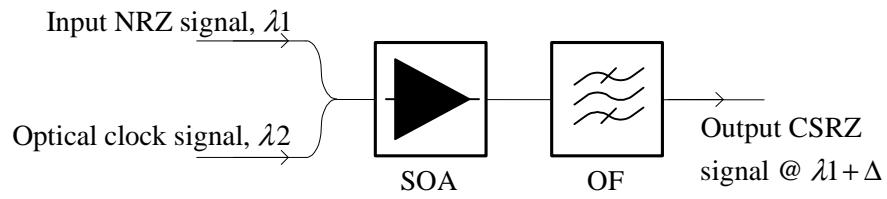
c) Temporal intensity and phase of CSRZ signal.

Figure 4-32: CSRZ signal generation via the conventional technique [167]. Optical spectra and temporal shapes for 40 Gb/s.

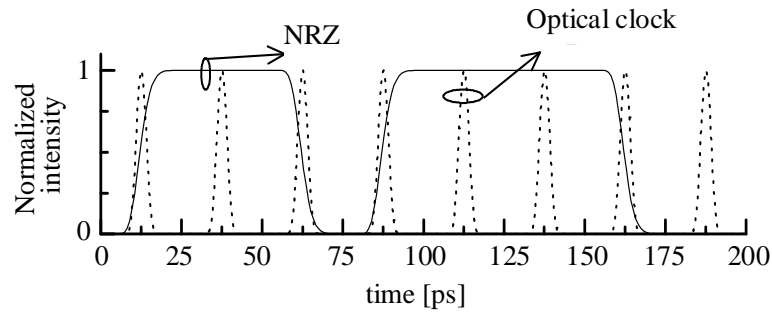
The temporal intensity and phase of the CSRZ signal are depicted in Figure 4-32 c). As mentioned above, the CSRZ signal intensity is similar to that of a common RZ signal. The optical signal phase is analyzed considering a low pass equivalent of the optical signal, where a reference frequency ( $f_R$ ), relative to the input CW signal central frequency, is considered. To obtain the optical signal phase at an arbitrary reference frequency,  $f_R$ , the signal time domain phase obtained when the reference is the input CW central frequency ( $f_R = 0$ ) should be added to  $\exp(-j.2\pi.t.f_R)$ , where  $t$  represents time. When  $f_R$  corresponds to the central frequency of the CSRZ signal (0 GHz in Figure 4-32 b)), constant phase is observed within the bit period, and  $\pi$  phase shifts occur between adjacent bits. Such  $\pi$  phase shifts contribute to the absence of optical carrier of the CSRZ signal. To facilitate the comprehension of the proposed converter, based on SOA, the signal phase is also analyzed considering  $f_R$  detuned from the CSRZ central frequency towards negative frequencies by half the signal bit rate ( $f_R = -20$  GHz in Figure 4-32 c). For such reference frequency, linear phase with slope equal to  $f_{BR}\pi$  ( $f_{BR}$  is a frequency equivalent to the bit rate) is observed within the bit period, and  $\pi$  phase shifts occur between consecutive bits. We will demonstrate hereafter that similar phase evolution can be obtained due to self-phase modulation in a SOA.

The proposed all-optical NRZ to CSRZ converter based on XGM and XPM in SOA is presented in Figure 4-33 a): an input optical OOK signal (here an NRZ signal is considered), at  $\lambda_1$ , is coupled to an optical probe clock signal at  $\lambda_2$ , with repetition rate equal to the signal bit rate. The two signals are then simultaneously amplified in a SOA. The optical clock can be obtained from a clock recovery circuit, not represented in the figure for simplicity. The power of each optical signal incoming the SOA is optimized so that the SOA non-linear effects are dominated by the optical clock signal.

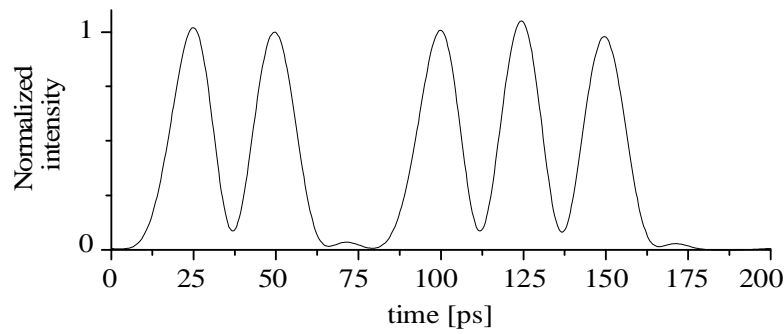
Figure 4-33 b) represents the intensities of the signals at  $\lambda_1$  and  $\lambda_2$  at the SOA input (to improve visualization, the intensities are normalized to their peak values). To guarantee correct operation of the proposed converter, the clock signal pulses must be aligned with the bit transitions of the NRZ signal. As referred above, the SOA non-linearities are dominated by the optical clock signal. The SOA gain is therefore depleted due to the clock pulses: due to XGM non-linear effect, the intensity shape of the input NRZ signal is carved into a RZ-like shape. The clock signal at the SOA output is removed by an optical filter.



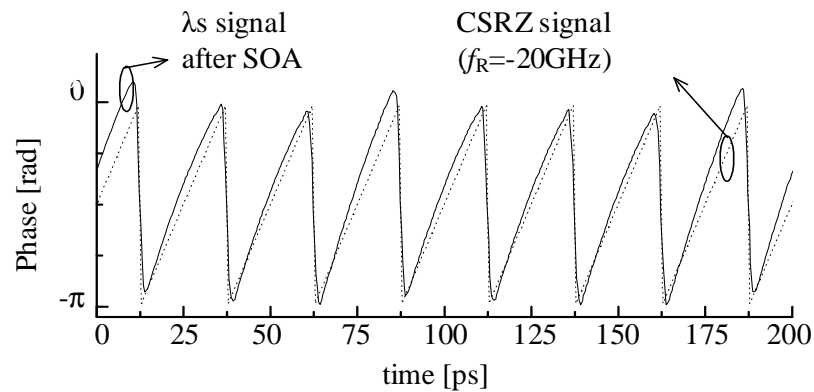
a) Conceptual setup;



b) Temporal intensity of input signals;



c) Temporal intensity of output signal;



d) Phase of output signal and comparison with CSRZ signal.

Figure 4-33: Proposed on-off keying (OOK) to carrier suppressed return-to-zero (CSRZ) converter based on cross-gain and cross-phase modulation (XGM and XPM) in SOA.

The signal intensity after OF, obtained by means of simulation, is illustrated in Figure 4-33 c), confirming the return-to-zero shape. The gain saturation, caused by the clock signal pulses, also leads to cross-phase modulation, which provokes periodic variations in the information signal phase. The phase of the information signal after the SOA is presented in Figure 4-33 d) (considering  $f_R$  correspondent to the input NRZ carrier frequency): when a clock signal pulse enters the SOA, a fast phase decrease is observed (caused by fast carrier depletion); when the optical pulse leaves the SOA, the phase slowly recovers to the initial value (the phase recovery is mostly determined by slower inter-band processes). The power of the clock signal at the SOA input is adjusted to achieve approximately  $\pi$  phase shifts between adjacent bits. The common CSRZ signal phase is also depicted in Figure 4-33 d) considering  $f_R = -20$  GHz, which presents strong similarities with the phase of the information signal after SOA. From the SOA output signal intensity and phase of Figure 4-33 d), we conclude that the input OOK NRZ signal is converted to the CSRZ format, with detuning of central frequency by 20 GHz ( $f_{BR}/2$ ).

The principle of operation of the proposed converter supports conversion of multiple input NRZ signals. For such purpose it is necessary to ensure that the power of the input signals is kept at a low level, so that the non-linear effects are still dominated by the clock signal. Moreover, all the input NRZ channels must have the same baseline bit rate, and the bit transitions of all input signals must be temporally aligned with the clock signal pulses. These conditions may be granted without complexity, for example in multicast applications, where all the input NRZ signals have the same origin. Although the principle of operation has been presented for NRZ signaling, the proposed converter is not limited to NRZ signals: conversion of OOK RZ input signals is also supported.

## 4.3.2 40 Gb/s simulation tests

### 4.3.2.1 CSRZ generation with SOA

The 40 Gb/s conversion is performed using the *fast* SOA device. The input information signal is a NRZ signal with infinite extinction ratio; -5 dBm optical power, measured at the SOA input; and central wavelength of 1548.0 nm. The clock signal is composed by optical pulses with 3 ps full width at half maximum (FWHM), intensity

Gaussian shape, and 2.0 dBm power at 1561.0 nm. The optical filter at the SOA output (OF in Figure 4-33 a)) is a 3<sup>rd</sup> order Gaussian filter detuned from the NRZ wavelength by 40 GHz and -3 dB bandwidth of 90 GHz. The impact of the optical filter bandwidth is studied in section 4.3.2.2.

Figure 4-34 a) depicts the optical spectra at the SOA input and output. Similarly to a CSRZ signal, the SOA output signal has two optical carriers with approximately the same power, separated by a frequency equal to the bit rate (40 GHz in this case). Comparing to the SOA input, the tone at the central wavelength is maintained, but the tone at 40 GHz is enhanced by the SOA non-linear behavior. Additionally, the SOA also enhances the tones at -40 GHz, -80 GHz, etc. This enhancement of the red tones is due to the ultra-fast carrier depletion. After the optical filter these tones are removed and the output spectrum is similar to the conventional CSRZ spectrum, presented in Figure 4-32 b). The converted signal eye diagram, presented in Figure 4-34 b), is open, undistorted and presents RZ pulse format.

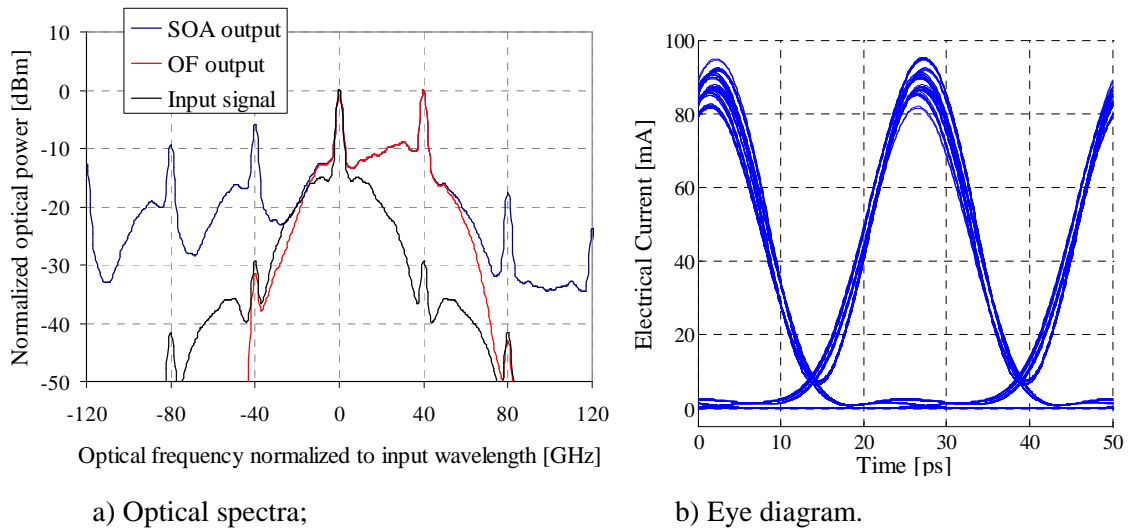


Figure 4-34: Optical spectra of the signals at SOA input, SOA output, and OF output; and signal eye diagram at OF output. (OF: optical filter at SOA output)

The phase of the NRZ to CSRZ converter output signal is presented in Figure 4-35, considering  $f_R = +20$  GHz, and compared to the phase of a the CSRZ signal generated by the conventional method. For this comparison, the optical carriers of the SOA output signal are tuned to the carriers of the CSRZ signal generated by the conventional method. Similarly to the CSRZ signal, it can be verified that in each bit there is a phase shift of

approximately  $\pi$  (i.e. polarity inversion). Nevertheless, this method does not generate an ideal CSRZ signal, since the output phase is only an approximation to the ideal CSRZ phase evolution.

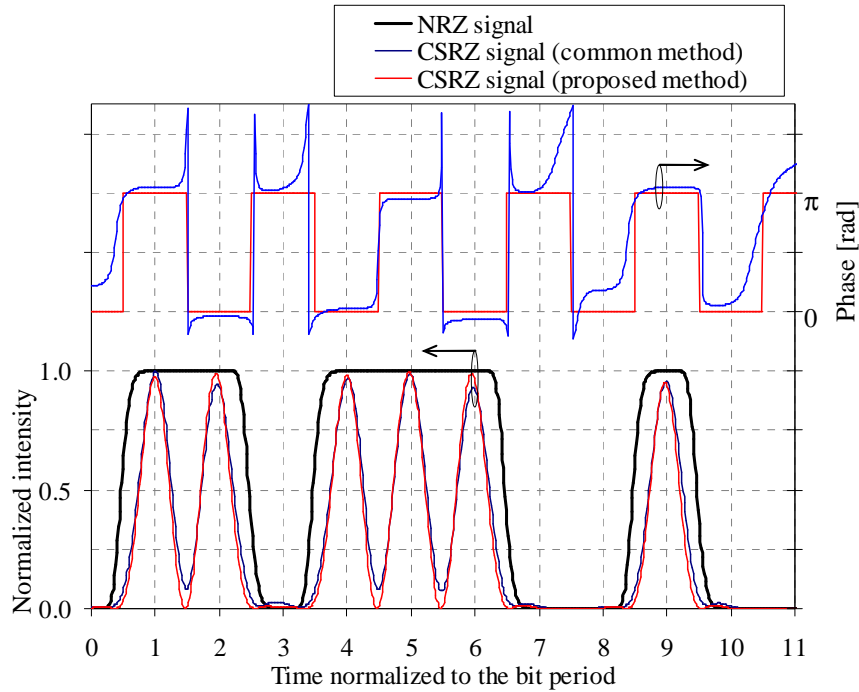


Figure 4-35: Comparison of temporal intensity and phase shapes for the converter output signal and CSRZ signal generated with common method. NRZ signal envelope is presented for reference.

One of the methods to verify if an optical signal is a CSRZ consists in feeding it to a delay-add interferometer. The interferometer input signal is split in two replicas; the two replicas suffer a delay of a bit period relative to each other and are added at the interferometer output. Considering a set of consecutive CSRZ pulses at the input, the interferometer retrieves an optical pulse at the beginning of the pulse sequence; all consecutive pulses cancel mutually due to the relative phase shifts of  $\pi$ ; finally, after the last pulse of the input signal, another pulse is retrieved. Figure 4-36 presents the delay-add interferometer output when it is fed by the conventional CSRZ signal and by the proposed converter output signal. The signal generated by the proposed converter behaves as expected: a high power optical pulse is retrieved at the beginning of a pulse train and another after the pulse train. Due to the non-ideal phase of the converter, low power satellite pulses are also retrieved. Nevertheless, such satellite pulses are 12 dB below the pulses power when there is constructive interference.



From the spectrum and intensity shape of Figure 4-35 and from the delay-add interferometer output of Figure 4-36, we conclude that the proposed method is able to effectively convert an input OOK NRZ signal to the CSRZ format.

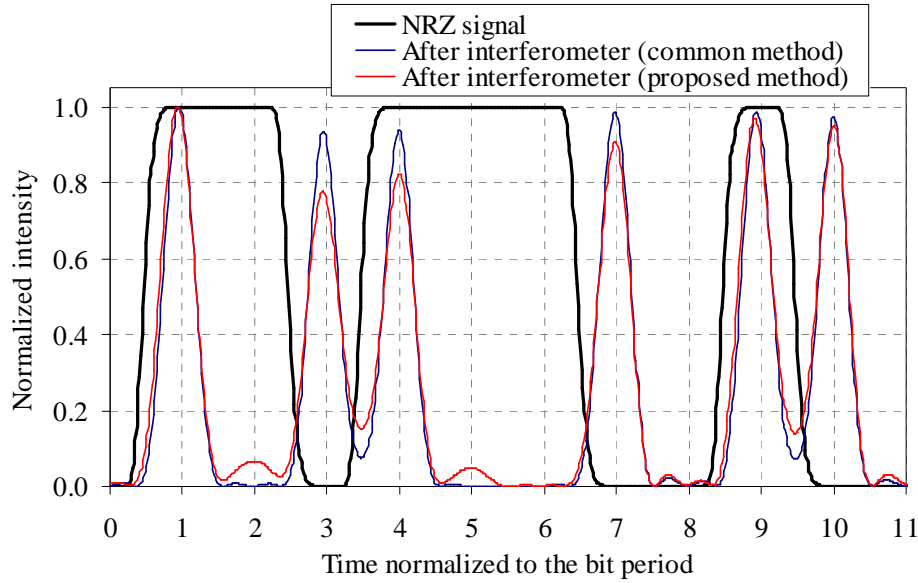
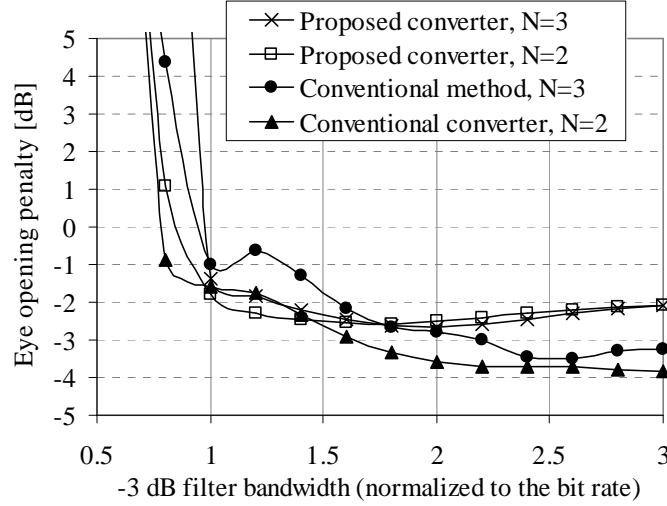


Figure 4-36: Temporal shapes at the output of a delay-add interferometer, when it is fed by the conventional CSRZ signal and by the CSRZ signal generated by the proposed method. NRZ signal envelope is presented for reference.

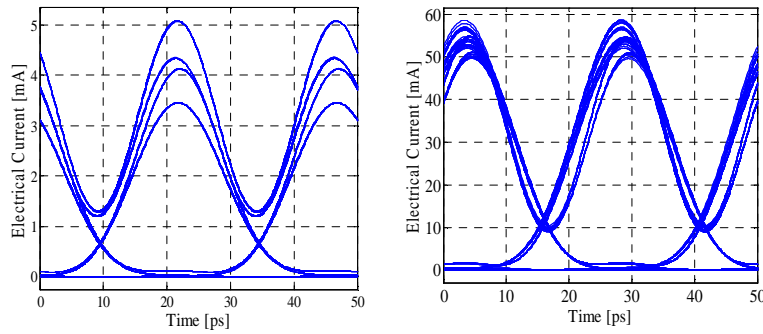
#### 4.3.2.2 Comparison with common transmitter

One of the key benefits of CSRZ signals, when compared to common RZ is high tolerance to tight optical filtering: since two consecutive bits have opposite phase, CSRZ signals are more tolerant to inter-symbol interference caused by tight filtering. Figure 4-37 a) presents the simulated EOP, as a function of the optical bandwidth of an optical filter placed at the transmitter output for the proposed and conventional converters. A photo detector with 40 GHz -3 dB bandwidth is considered. The considered optical filters are Gaussian of second and third order. The presented results evidence that for high bandwidths (superior to  $1.5 \times \text{Bit Rate}$  for 2<sup>nd</sup> order filters, and  $2 \times \text{Bit Rate}$  for 3<sup>rd</sup> order filters), the conventional transmitter EOP excels the proposed transmitter, due to residual SOA amplitude distortion. However, for lower bandwidths the signal originated by the proposed converter presents similar or even lower distortion than the common transmitter. The eye diagrams of Figure 4-37 b) and c) present the filtered signals for 2<sup>nd</sup> order filter

with bandwidth of  $1.2 \times \text{Bit Rate}$ : the signal generated by the proposed converter presents lower distortion than the signal generated by the conventional transmitter.



a) Characterization via EOP;



b) Eye diagram of filtered CSRZ signal generated by conventional method.;

c) Eye diagram of filtered CSRZ signal generated by the proposed method.

Figure 4-37: CSRZ signal tolerance to tight optical filtering.  $N$  denotes the order of the Gaussian filter. Eye diagrams represent detected signal for 2<sup>nd</sup> order filter with -3 dB bandwidth of  $1.2 \times \text{Bit Rate}$ .

Another important characteristic of CSRZ is the enhanced tolerance to non-linear effects. Figure 4-38 presents a simple comparison of the robustness to non-linearities of the signal generated by the proposed converter, and the signal generated with the conventional method. The optical CSRZ signals are filtered by a 3<sup>rd</sup> order Gaussian filter with -3 dB bandwidth of 90 GHz and are transmitted over SSMF fiber with  $D$  of 17 ps/nm, attenuation coefficient of 0.2 dB/km and non-linear refractive index of  $2.6 \times 10^{-20}$ . The signals under test are transmitted over 5 and 10 spans of 70 km of SSMF. After each span the chromatic dispersion and transmission losses are perfectly compensated. No noise is considered in

these tests. Since the chromatic dispersion is perfectly compensated, it is observed that for very low powers the calculated EOP after transmission is similar to back-to-back: the conventional transmitter presents better EOP. For increasing power, the proposed and common transmitter present similar evolutions, with the proposed converter slightly excelling. The superior results of the proposed transmitter are most likely due to higher pulse width (56% of FWHM), when compared to the conventional method (45% of FWHM).

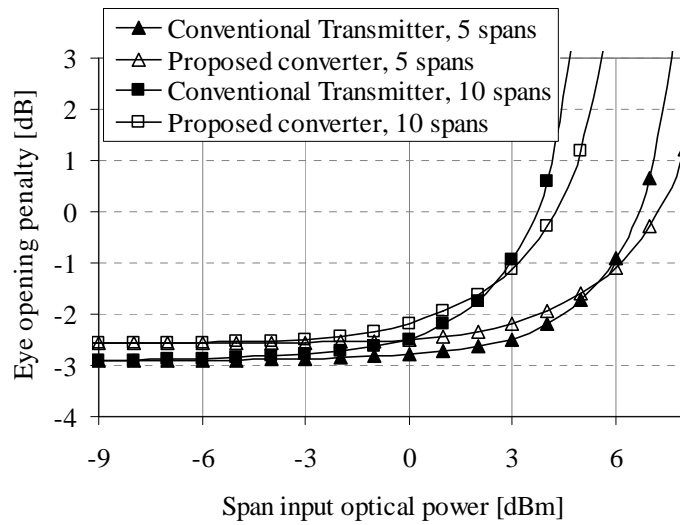


Figure 4-38: CSRZ signals degradation with non-linear transmission.

Since the SOA induces chirping, caused by SPM and XGM, it is also necessary to compare the tolerance to chromatic dispersion accumulation of the CSRZ signal obtained with SOA with the conventional CSRZ signal. Figure 4-39 plots the eye opening penalty of the signals generated by the proposed and common transmitter as a function of dispersion accumulation. For such tests the non-linear effects and attenuation of the fiber are disregarded and only the effect of  $\beta_2$  is considered. The CSRZ signal generated by the proposed method presents enhanced tolerance to negative dispersion, when compared to positive dispersion, due to SOA induced chirping. Nevertheless, similarly to the non-linear transmission tests, the proposed converter presents enhanced chromatic dispersion tolerance, due to higher pulse widths.

The results presented in this section have demonstrated that the CSRZ signal presents similar tolerance to tight filtering, when compared to the conventional transmitter. Moreover, slightly improved tolerance to non-linear effects and accumulated dispersion are

obtained; mostly due to higher pulse width, when compared to the conventional transmitter.

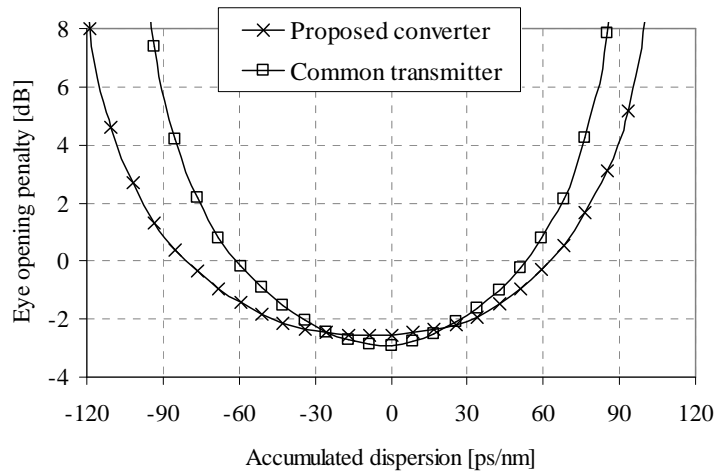


Figure 4-39: CSRZ signals degradation with accumulated chromatic dispersion.

#### 4.3.2.3 NRZ to CSRZ converter robustness to input signal variations

We have demonstrated in the previous section that under optimized conditions, feeding a SOA with a data signal and an optical clock, a CSRZ signal is obtained. Although the phase of the resultant optical signal does not present a perfect match with the ideal CSRZ signal phase, the converted signal presents similar advantages for optical network applications when compared to a CSRZ signal obtained through the conventional method: tolerance to tight optical filtering, to non-linear effects, to the accumulation of chromatic dispersion. In this section, the converter robustness to variations in the input signal is assessed via simulations at 40 Gb/s. Such tests allow further understanding of the true potential of the proposed converter application in a real network.

For practical application in a network, the converter should operate over a wide range of input power values. Figure 4-40 presents the imbalance between the two CSRZ signal optical carriers, as a function of the input and clock signal powers. The imbalance is measured as the absolute value of the power difference between the two spectral tones at  $\pm 20$  GHz of the CSRZ spectrum. The results demonstrate that optimum performance over a wide range of input powers is possible, provided that the clock signal power is adapted accordingly. For the modeled device characteristics, the optimum clock signal power is approximately equal to the input power added by 7 dB. Figure 4-40 also presents

in grey the range where the output EOP is below -2.0 dB; it is observable that the grey area overlaps with the area where minimum power difference between the two carriers is achieved. For constant input power, the clock signal power may vary by approximately  $\pm 0.75$  dB relatively to the optimum value while keeping the power difference between the two carriers below 1 dB. On the other side, similar power variation is allowed for the input signal, when the clock signal power is constant.

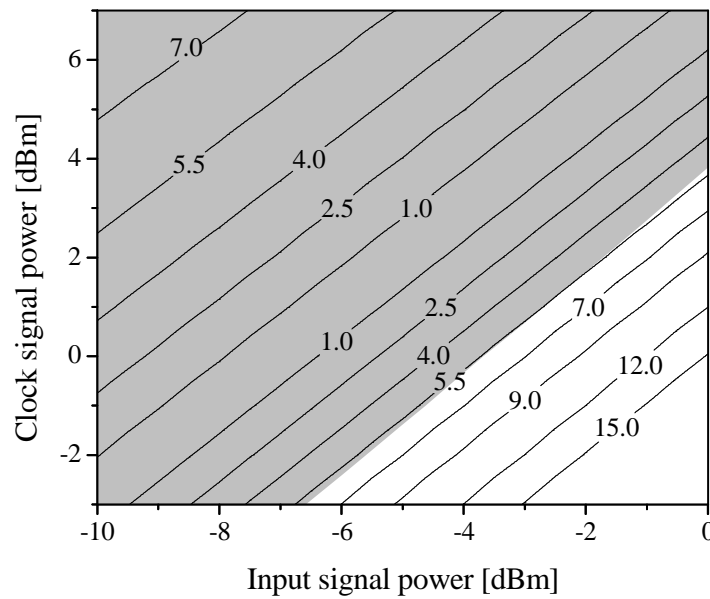


Figure 4-40: Absolute value (in dB) of the power difference between the two CSRZ signal optical carriers as a function of input and clock signal powers. Grey area denotes the operation range where the signal EOP is below -2.0 dB.

The impact of the clock signal pulse width is analyzed in Figure 4-41, which plots the power difference between the two optical carriers of the converted CSRZ signal, for varying clock signal power and different FWHM values. The input NRZ signal power is constant at -5 dBm and the SOA output signal is filtered by a 3<sup>rd</sup> order Gaussian filter with 90 GHz of -3 dB bandwidth. It is verified that for higher FWHM, higher power is required to achieve the same frequency chirping; therefore, with the increase of the FWHM, the optimum clock power increases. For FWHM = 0.4, the ideal condition (the two carriers having the same power) is never achieved. The EOP for clock FWHM of 0.1, 0.2, and 0.3 was measured at target power difference between the optical carriers, 0 dB, and is 2.8 dB, 3.1 dB, and 3.2 dB, respectively. As a conclusion, the optimum clock signal FWHM is a

compromise between converted signal EOP and necessary power at SOA input. Moreover, very short optical pulses are also more complex to generate.

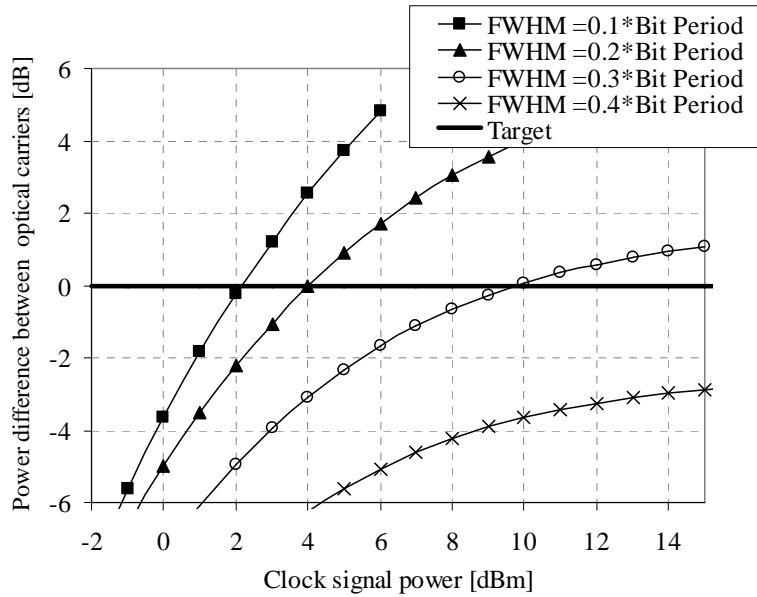
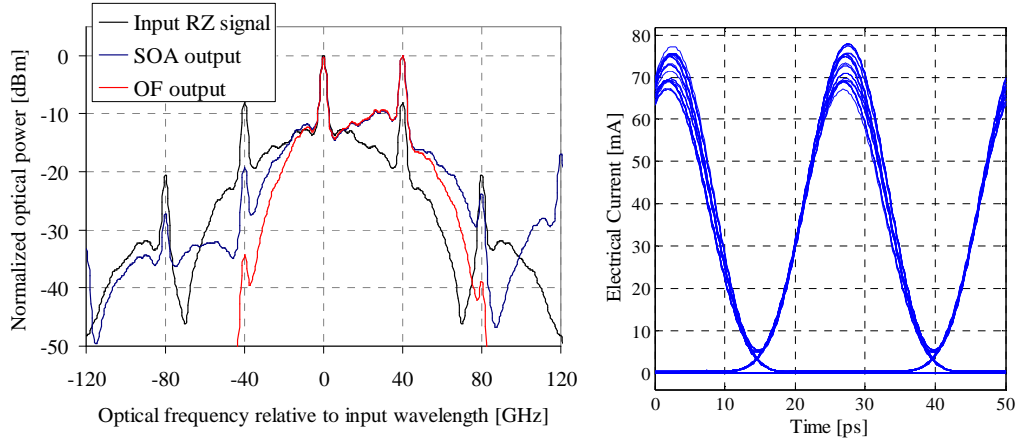


Figure 4-41: Power difference between the two CSRZ signal optical carriers (power of the spectral tone at +20 GHz, relative to the center of the spectrum, subtracted by the power of the spectral tone at -20 GHz), as a function of the clock signal power, for different clock signal full width at half maximum (FWHM). Horizontal line represents the power difference target of 0 dB.

As referred above, the proposed method is also appropriate for OOK RZ input signals. The converter operation with input OOK RZ signals is assessed in Figure 4-42. The RZ signal is generated using two cascaded MZM. In the first stage, a CW signal is first modulated in a MZM biased at quadrature and driven by an NRZ electrical signal. The resultant optical signal is fed to the second MZM, which is biased at quadrature and driven by a electrical clock signal, which oscillates at the signal bit rate frequency. The resultant RZ signal has an approximate FWHM of  $0.5 * \text{Bit Period}$ . The RZ signal is then fed to the SOA-based converter with -5 dBm input power; the optimum clock signal power is now 4.5 dBm. Figure 4-42 a) presents the converted signal spectrum, which also presents carrier suppressed characteristics. The red chirped part of the spectrum presents lower power than in the NRZ spectrum of Figure 4-34. This part of the spectrum is mostly generated by red frequency chirping originated by the leading edge of the clock signal pulses. For the RZ signal case, the optical clock pulses leading edge is temporally aligned to the RZ signal ditch between two pulses. As a consequence the red chirping occurs in an instant where the

RZ signal has no (or very low) power. The resultant eye diagram of Figure 4-42 b) is clear and undistorted (EOP of -3.3 dB).



a) Optical spectra of SOA input, SOA output, and converter output signals;      b) Converter output signal eye diagram;

Figure 4-42: RZ to CSRZ conversion (OF: 3<sup>rd</sup> order Gaussian optical filter at SOA output with -3 dB bandwidth of 90 GHz).

The results of this section have demonstrated that the proposed converter is fit for arbitrary input powers, provided that the clock signal power is adjusted accordingly. The ideal clock signal FWHM is a compromise between the output signal EOP and the required clock power. Finally, we have demonstrated that the proposed converter setup is also appropriate for input OOK RZ signals.

### 4.3.3 40 Gb/s single- and multi-channel experimental validation

The 40 Gb/s setup, considered in the experimental tests, is represented in Figure 4-43. Single- and multi-channel operations are experimentally assessed. In single channel operation, an NRZ signal at  $\lambda_{S1} = 1547.72$  nm is fed to the converter. In multi-channel operation two configurations are tested: conversion of two independent NRZ signals at  $\lambda_{S1}$  and at  $\lambda_{S2} = 1549.32$  nm with different binary information (dual conversion) but temporally aligned; and a configuration for multi-cast applications, where four ITU 200 GHz grid wavelengths ( $\lambda_{S1}$ ,  $\lambda_{S2}$ ,  $\lambda_{S3} = 1550.92$  nm, and  $\lambda_{S4} = 1552.52$  nm) with similar binary information are converted simultaneously to CSRZ (quadruple conversion). In all cases, the NRZ signals are obtained by driving a MZM with 40 Gb/s signal with a pattern length of  $2^{31}-1$  bit. The input data signals are coupled to a 40 Gb/s optical clock signal at

1562.23 nm with 2 ps pulses, generated by a mode locked laser diode (MLLD). The optical pulses are aligned with the data signal bit transitions by a variable delay line (VDL). The signals are amplified in the *fast* SOA device. Low SOA polarization dependency ( $\approx 0.5$  dB) avoids the use of polarization controllers. The signal after the SOA is filtered at OF1, which isolates the wavelength under analysis and reduces its spectral occupancy. OF1 is a tunable optical filter with intensity response approximated to a 3<sup>rd</sup> order Gaussian and -3 dB bandwidth of 91.2 GHz. The signals are detected in a pre-amplified receiver, composed by an optical filter (OF2) with 130 GHz optical bandwidth centered with the wavelength of the signal under analysis, and a photo-detector (PD) with a -3 dB cut-off frequency of 37 GHz. The signals are characterized via bit error rate measurements, as a function of the optical signal to noise ratio at the photo-detector input. The OSNR is adjusted by adding optical noise with variable power and maintaining the signal power constant at 0 dBm.

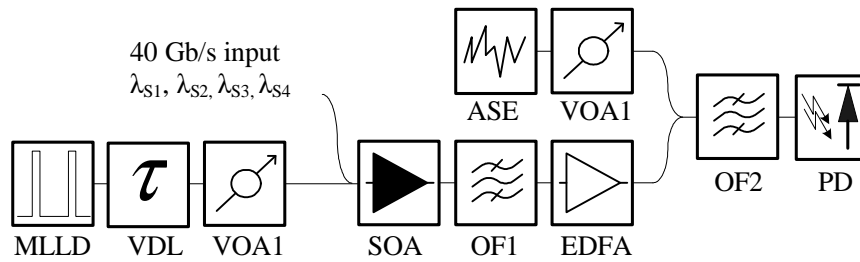


Figure 4-43: 40 Gb/s format converter setup for experimental tests.

Single channel conversion is characterized in Figure 4-44. Optical spectrum and eye diagram of the NRZ signal at the SOA input are depicted in Figure 4-44 a). Figure 4-44 b) depicts the optical spectrum of the  $\lambda_{s1}$  signal at the SOA output when the optical pulse train is amplified simultaneously with the NRZ signal. The optical pulse train power is adjusted to 8 dBm: this value was found to optimize the CSRZ shape at output. The NRZ signal power is adjusted to -4 dBm, which is the maximum level at which the non-linear effects are still dominated by the clock signal. In this situation, the heavily saturated SOA induces conversion to the CSRZ format, as described in the previous section. The spectral shape of the signal at the SOA output is similar to that obtained in the simulation tests; the spectrum presents identical power of the two main spectral tones (difference of 0.17 dB), as expected for a CSRZ signal. OF1 is centered with the output CSRZ signal central wavelength: detuned from  $\lambda_{s1}$  by 20 GHz. The resultant signal presents reduced spectral occupancy and a RZ shaped open eye diagram with negligible distortion, as can be verified



by the spectrum and the inset eye diagram in Figure 4-44 b). Comparing to the simulation tests, the experimental results require higher clock signal power; such difference is due to the fact that the simulation model ignores wavelength dependency, since the input wavelength is much lower than the clock signal wavelength, lower conversion efficiency is observed experimentally [92].

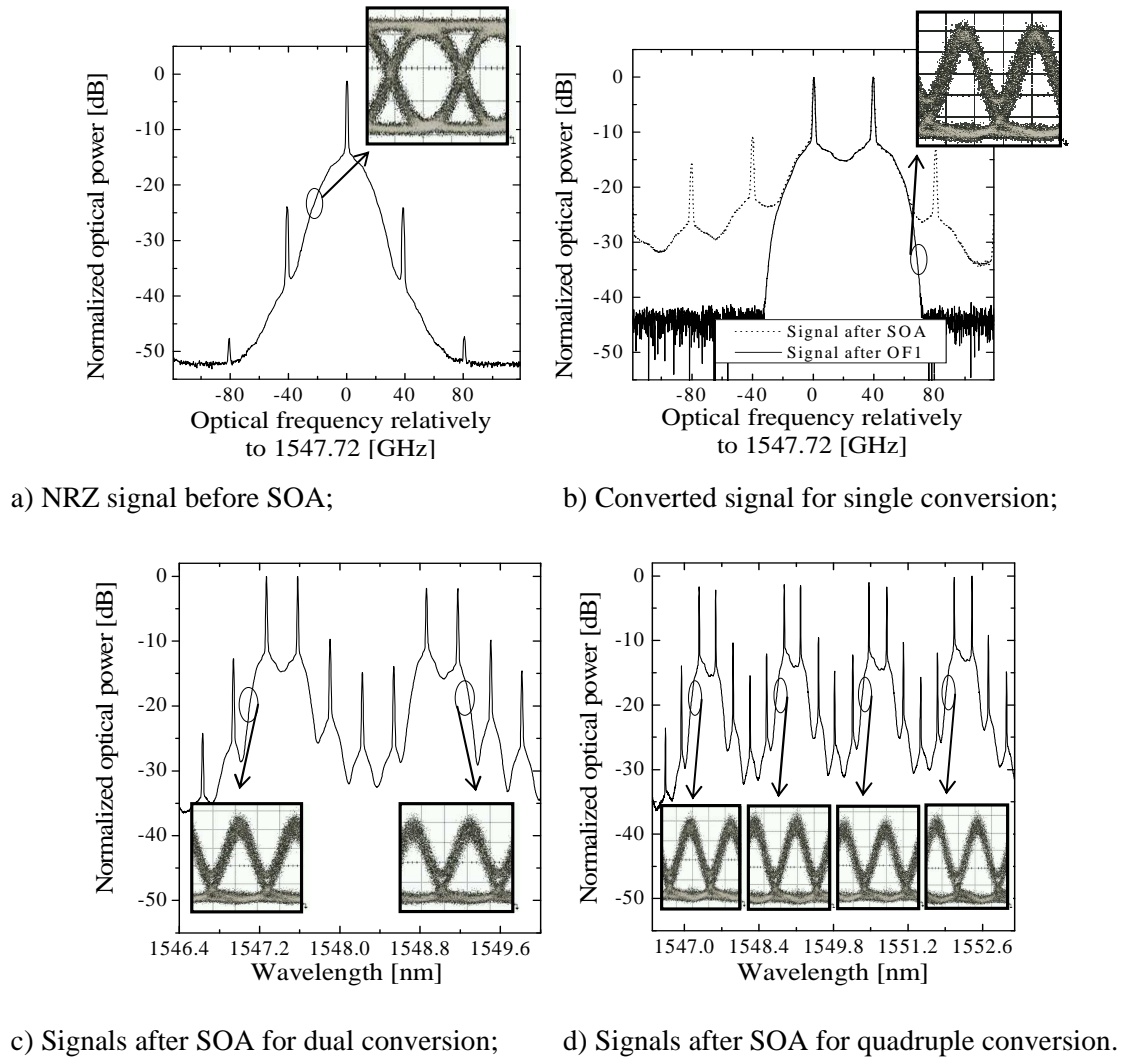


Figure 4-44: Optical spectra and eye diagrams (10 ps/div).

Dual and quadruple conversions are achieved by feeding the SOA with 8 dBm clock signal power. All input wavelengths are temporally aligned with the clock signal. The input signals total power is maintained approximately constant when the channel count increases, by reducing the power per channel. For dual configuration  $\lambda_{S1}$  and  $\lambda_{S2}$  NRZ signals with powers of -6.9 and -7.1 dBm are fed to the SOA; whereas for quadruple configuration, the powers of  $\lambda_{S1}$ ,  $\lambda_{S2}$ ,  $\lambda_{S3}$ , and  $\lambda_{S4}$  are -9.8, -10.0, -10.1, -10.2 dBm. The

clock signal power is kept constant at 8 dBm in all tests. The multi-input conversion results are presented in Figure 4-44 c) and d). All signals present identical power of the two main spectral tones at the converter output. The inset eye diagrams are obtained detuning OF1 by 20 GHz from  $\lambda_{Si}$  (similarly to the single channel test). Clear and open eye diagrams are obtained in both tests for all wavelengths.

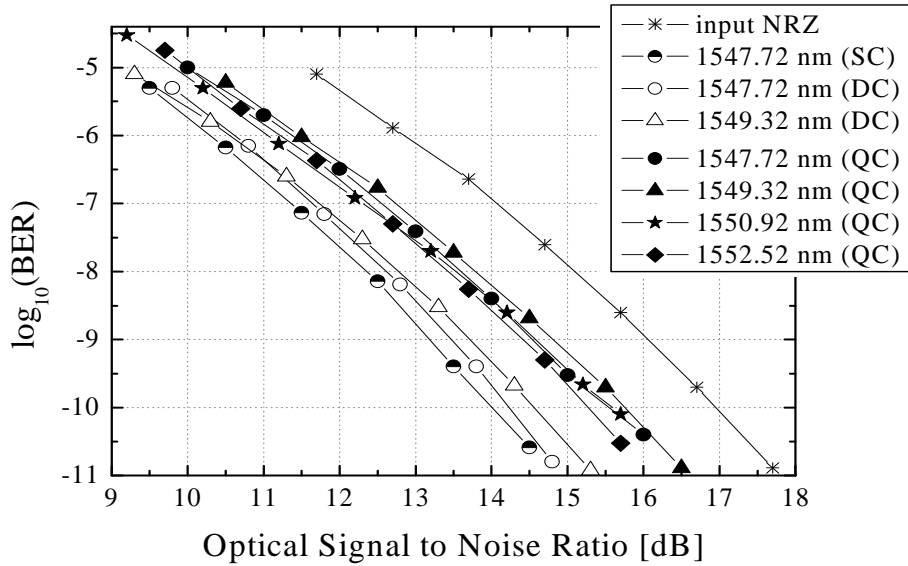


Figure 4-45: BER characterization versus OSNR (SC, DC, and QC – single, dual, and quadruple conversion).

The converter performance is characterized in Figure 4-45 in terms of BER as a function of the OSNR. The input NRZ signal requires 16.1 dB OSNR for a BER of  $10^{-9}$  ( $OSNR_{req}$ ). When single input is considered, a converted signal with 13.1 dB  $OSNR_{req}$  is obtained. The lower OSNR requirement of RZ signals is commonly observed, since these require lower power than NRZ for the same vertical eye opening. Considering two input channels, the output signals  $OSNR_{req}$  is 13.4 and 13.7 dB (0.6 dB of maximum penalty relatively to the single input test). When four channels are converted, the output  $OSNR_{req}$  ranges from 14.4 to 14.6 dB, representing a maximum penalty of 1.5 dB compared to the single input converted signal. From such results, it is expected that the maximum number of simultaneously converted channels can be further increased; the limiting factors will probably be the SOA induced noise, since the per-channel power is reduced by a factor of 3 dB every time the channel count is doubled; inter-channel non-linearities in the SOA (such as XGM, XPM or FWM) are not expected to be a dominant factor, since the non-linear effects are dominated by the high power optical clock signal.

## 4.4 Summary

This chapter has focused on all-optical format modulation converters. Such schemes are especially required at the interfaces of optical networks with use different modulation formats. Two novel format modulation conversion schemes have been proposed. The first converts optical double sideband (oDSB) signals to the optical vestigial sideband (oVSB) format. To the authors knowledge this is the first all-optical method that does not depend on optical filtering and does not require Hilbert transforms of the information signal. The second converts on-off keying signals to the carrier suppressed return to zero (CSRZ) format with operation for both NRZ and RZ input signals.

The oDSB to oVSB converter operation is based on the frequency chirp generated by the self-phase modulation (SPM) nonlinearity in a semiconductor optical amplifier (SOA). An additional CW signal is introduced to minimize the self-gain modulation (SGM) distortion, improving the converted signal quality. The converter has been experimentally assessed at 10 Gb/s with sideband suppression ratio (SSR) above 15 dB and an improved  $Q$ -factor, due to the resultant gain compression effect on the SOA. Using a faster device, 40 Gb/s operation has also been experimentally achieved with SSR results above 14 dB.

Enhanced tolerance to chromatic dispersion accumulation, when compared to oDSB has been verified with and without electrical dispersion compensation (EDC). At 10 Gb/s experimental transmission was possible over 160km of SSMF (2720 ps/nm of dispersion), while the oDSB signal allowed only 80 km (1360 ps/nm). By simulation the use of EDC was assessed with transmission up to 280 km without any optical dispersion compensation. At 40 Gb/s extended dispersion tolerance has also been verified: without optical or electrical dispersion compensation, transmission over 170 ps/nm (10 km of SSMF) has been allowed, while oDSB allows only 102 ps/nm (6 km). Using only EDC at the receiver side, implemented by an adjustable transversal filter, fiber dispersions up to 238 ps/nm (14 km) have been experimentally tolerated.

Format conversion from OOK to RZ with modulation format conversion to carrier suppressed (CS) was proposed in a simple scheme where XGM and XPM interact in a

SOA. The converter operation was compared to the conventional CSRZ transmitter via 40 Gb/s simulations: tight filtering penalty similar to the common transmitter was verified; improved tolerance to chromatic dispersion accumulation was obtained by the proposed transmitter; and also enhanced tolerance to fiber non-linear effects. The converter is able to operate with both NRZ and RZ input signals. Single- and multi-channel operation up to four channels has been experimentally assessed at 40 Gb/s. Carrier suppressed spectrum and clear RZ eye diagrams have been obtained at the converter output for all input configurations. For all input channel counts, the converted signal present improved required OSNR, when compared to the input NRZ signal. We expect that the channel count can still be further increased without major degradation of the output signal quality. To our knowledge, this is the first 40 Gb/s all-optical multi-channel demonstration of a OOK to CSRZ converter.

# Chapter 5

## Pulse format conversions between RZ and NRZ

### 5.1 Motivation

Wavelength division multiplexing (WDM) and optical time division multiplexing (OTDM) technologies respond to the bandwidth demand increase, motivated by the data exchange growth. In transport networks, several channels are aggregated using OTDM, through the bit interleaving technique. Return-to-zero (RZ) pulse format is usually preferred in such networks due to superior tolerance to polarization mode dispersion, inter-symbol interference, and nonlinear effects. On the other hand, non-return-to-zero (NRZ) is commonly employed on lower bit rate access networks, as these require pulse formats with improved spectral efficiency and enhanced jitter and dispersion tolerance [190]. As

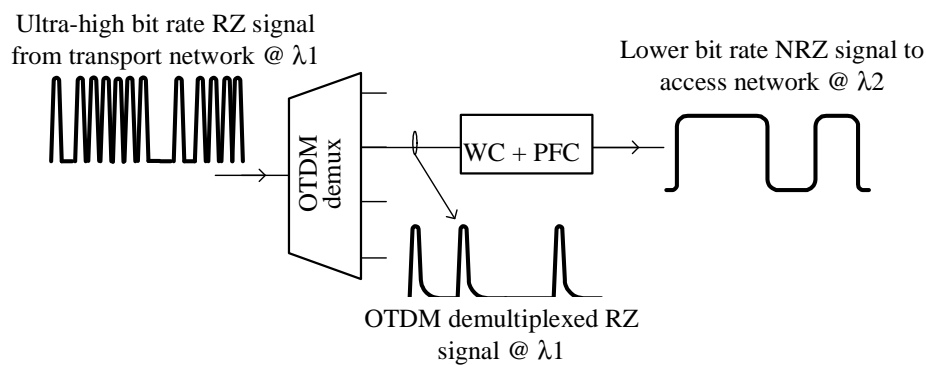


Figure 5-1: Illustration of pulse and wavelength conversion functionalities required in the interface between transport and access networks.

illustrated in Figure 5-1, in the interface between transport and access networks, all-optical OTDM de-multiplexers, wavelength converters, and format converters are required to enable a transparent inter-connectivity between the two networks [190]. In the reverse direction the inverse functionalities are required.

Promising results for de-multiplexers and add-drop multiplexers have been reviewed already in section 2.9. Wavelength conversion is also thoroughly investigated in Chapter 3. NRZ-to-RZ format conversion can be simply obtained by replacing the probe signal in the SOA based wavelength converters of Chapter 3 by a pulsed clock signal [191] - [193]. Such functionalities have also been reported using highly non-linear optical fibers [194]. On the other hand, optical RZ-to-NRZ pulse format conversion is a more complex functionality.

Current implementations of all optical converters between RZ and NRZ include: a scheme which uses XGM and WDM to TDM conversion [190]; a SOA based non-linear optical loop mirror (NOLM) [195]; a Fabry-Perot laser with injection locking scheme [196]; a scheme in which the red and the blue chirped parts of the spectrum of a XGM and XPM signal suffer different delays after which are recombined [110]; a scheme using XPM in a SOA Mach-Zehnder interferometer (MZI) structure and a pulse duplicator [197]; a SOA based Michelson interferometer (MI) [198]; and finally, a method based on FWM in SOA [199]. From these methods, only the scheme which is based on MI has been demonstrated at 40 Gb/s; however, MI-SOA is not a commercially available structure.

In this chapter we propose and experimentally demonstrate two solutions to obtain wavelength and simultaneous pulse format conversion from RZ to NRZ. In section 5.2 a scheme is investigated, where amplification in SOA and detuned optical filtering are combined to reach wavelength and simultaneous RZ-to-NRZ format conversion at bit rates up to 40 Gb/s [200]. A second novel method is presented in section 5.3 [64][201]; the setup consists in two stages: in the first, the input RZ signal modulates the internal laser of a gain clamped SOA (GC-SOA); in the second stage, this signal is wavelength converted using XGM in a common SOA. Both proposed methods are simple, since these do not require interferometric schemes or non-linear loops; and retrieve a non-inverted converted signal. Moreover, in the scheme based on GC-SOA the output signal wavelength can match the input one if required.

## 5.2 *RZ to NRZ converter with SOA and detuned filtering*

Detuned optical filtering can be used for several applications, as mentioned already in this work: oVSB generation [170], enhancement of the modulation bandwidth in SOA [202], or isolation of either the red or blue chirped part of the spectrum of a XGM converted signal to obtain RZ to RZ wavelength conversion [110]. In this section we investigate format and simultaneous wavelength conversion based on XGM and detuned filtering. Experimental results according to this method have been presented in [203]; however, to the author's knowledge, the operation principle has not yet been investigated, the filter shape has not been optimized and only 10 Gb/s results have been presented.

Pulse format conversion from RZ to NRZ based on detuned optical filtering only is first presented in section 5.2.1; in section 5.2.2 a XGM stage is added to the setup to reduce the insertion losses, allow input wavelength independence and enable wavelength conversion.

### 5.2.1 Pulse format conversion based only on detuned filtering

#### 5.2.1.1 Operation principle

In this section the principle of operation of the RZ to NRZ converter based on detuned optical filtering is presented and demonstrated by means of simulation. The principle of operation is bit rate (BR) independent, provided that the characteristics of the optical filter are dimensioned according to a scale factor dependent on the bit rate.

The proposed scheme to convert RZ to NRZ signals is depicted in Figure 5-2. An input RZ signal at  $\lambda_1$  is fed to a detuned optical filter. If the filter spectral response is optimized, its output signal is converted to the NRZ pulse format. The spectral tone at the clock signal, typical of RZ signals, becomes the central wavelength of the converted NRZ signal. In absence of phase modulation, the RZ optical spectrum is symmetrical relatively to the optical carrier; therefore, the optical filter can either be detuned for positive or for negative wavelengths. For simplicity, the study presented hereafter considers always that the optical is detuned towards negative wavelengths (positive frequencies).

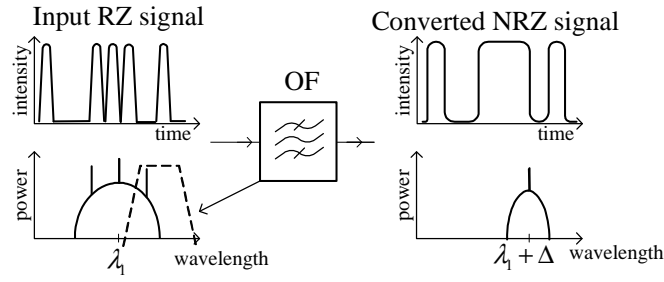


Figure 5-2: RZ-to-NRZ signal conversion based on detuned optical filtering

Figure 5-3 illustrates the optical spectra of NRZ and RZ signals. The NRZ signal central frequency is detuned by a frequency equal to the bit rate. The RZ pulses have a raised cosine shape [204] with a roll-off factor of 0.5, a full width at half maximum (FWHM) of a quarter of the bit period (BP). The NRZ signal was generated as rectangular pulses and limited by a 3<sup>rd</sup> order Bessel filter with a cut-off frequency of 0.8·BR.

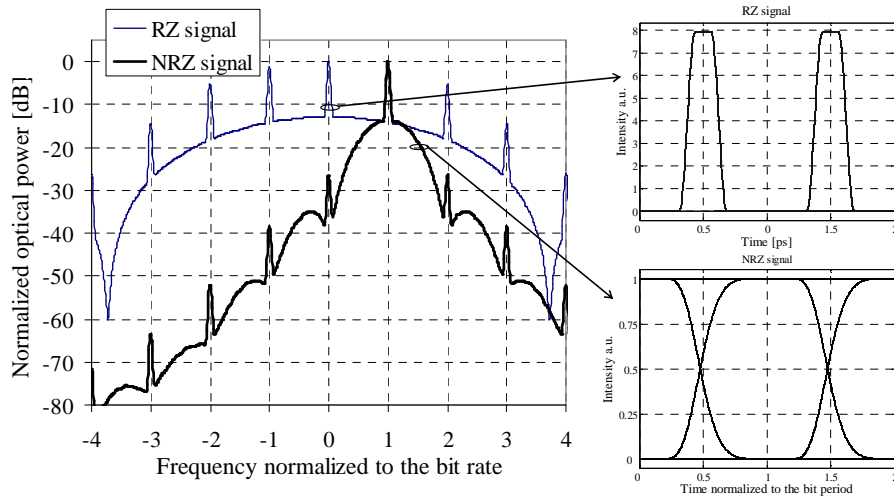


Figure 5-3: RZ and NRZ optical spectra. NRZ signal is detuned by a frequency equal to the bit rate.

The transfer function of the ideal optical filter to convert a RZ signal to the NRZ format,  $H_{RZ-NRZ}(f)$  format is given by equations (5-1) and (5-2):

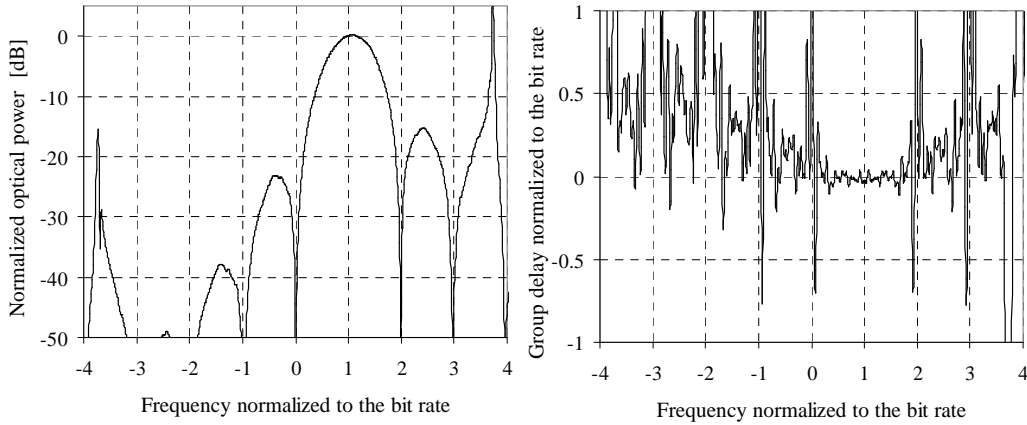
$$|H_{RZ-NRZ}(f)| = \left| \frac{S_{NRZ}(f + \Delta_f)}{S_{RZ}(f)} \right|, \quad (5-1)$$

$$\tau_H(f) = -\frac{1}{2\pi} \cdot \frac{\partial[\Phi_H(f)]}{\partial f} = -\frac{1}{2\pi} \cdot \frac{\partial[\Phi_{NRZ}(f + \Delta_f) - \Phi_{RZ}(f)]}{\partial f}, \quad (5-2)$$



Where  $|H_{RZ-NRZ}(f)|$  and  $\tau_H(f)$  stand for the filter spectral intensity response and group delay, respectively.  $\Phi$  stands for the phase, and  $S$  stands for spectral power density.

In Figure 5-4 the intensity and the group delay of the ideal optical filter for format conversion are depicted. Regarding the intensity response of the filter, several lobes are observed. However, considering the RZ and NRZ spectra of Figure 5-3, it can be observed that only the lobe centered at  $1 \cdot \text{BR}$  has significant influence, since the other lobes are centered in frequencies where the resulting NRZ signal has low spectral power. Regarding the group delay of the ideal filter, in the frequency range of most interest ( $0 - 2 \cdot \text{BR}$ ), correspondent to the main lobe, variations lower than  $\pm 0.1 \cdot \text{bit period}$  are required. From the considerations above, if the main lobe is considered the most important part of the filter spectrum, the results anticipate that an optical filter with linear phase response can be employed. The intensity response of such optical filter is also simple to obtain by feasible filters, since there are no discontinuities in the band of interest.



a) Intensity response;

b) Group delay.

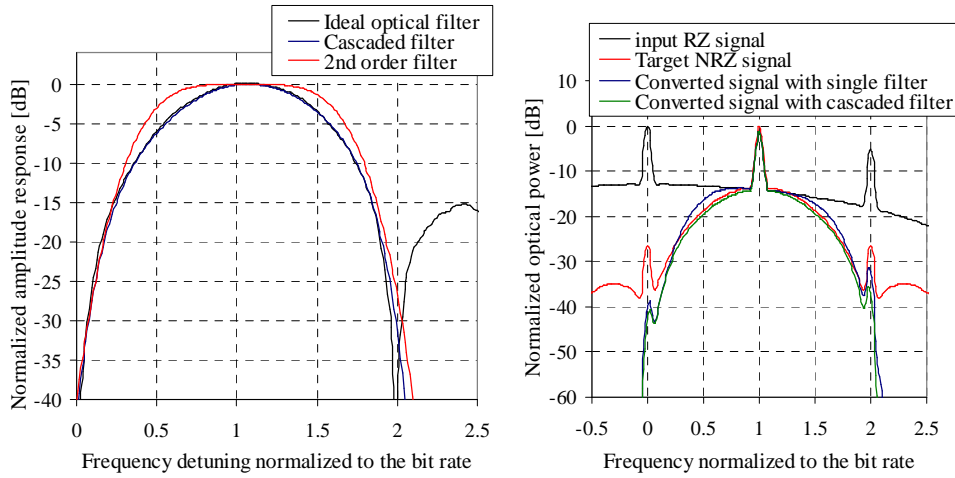
Figure 5-4: Simulated ideal filter response to convert RZ-to-NRZ pulse format,  $H_{RZ-NRZ}(f)$ .

### 5.2.1.2 Simulation results

In the simulation tests, Gaussian shaped optical filters will be considered, due to their similarity to available experimental optical filters and to potential for simple implementation. The transfer function of a Gaussian filter is described by the following expression [205]:

$$H_{\text{Gauss}}(f) = \exp \left[ -\ln(\sqrt{2}) \cdot \left( \frac{2 \cdot (f - f_c)}{\Delta f_{3\text{dB}}} \right)^{2N} \right], \quad (5-3)$$

where  $f_c$  is the center frequency of the optical filter,  $\Delta f_{3\text{dB}}$  is the -3 dB optical bandwidth and  $N$  represents the filter order. The group delay of the Gaussian filters is constant, which should not be impairment since the ideal filter required small variations in the group delay in the band of interest.



a) Optical amplitude response of filters;    b) Optical spectra.

Figure 5-5: Comparison of ideal filter spectral response with one 2<sup>nd</sup> order Gaussian filter, and with a cascade filter composed by a 1<sup>st</sup> and 4<sup>th</sup> order Gaussian filters.

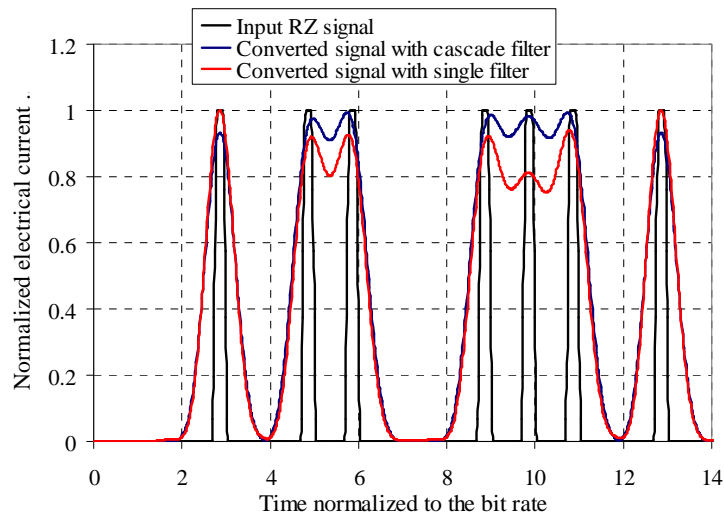
Two filtering configurations are considered, and their spectral response is compared in Figure 5-5 a) with the spectral response of the ideal filter. The characteristics of such configurations have been optimized to allow highest similarity with the ideal filter intensity transfer function of Figure 5-4:

- The first filtering configuration consists in a single 2<sup>nd</sup> order Gaussian filter with a -3 dB bandwidth of 1.1\*BR and a detuning of 1.05\*BR.
- The second configuration consists in a cascade of a 1<sup>st</sup> and a 4<sup>th</sup> order Gaussian filters. The -3 dB bandwidth of the 1<sup>st</sup> and 4<sup>th</sup> order filters were 0.8\*BR and 1.6\*BR, respectively; the detuning relatively to the optical carrier was 1.05\*BR for both filters.

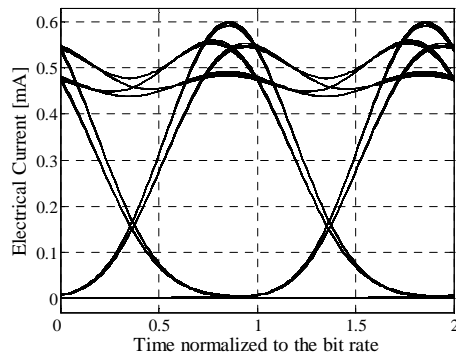
The single filter configuration is simpler; however, the spectral response diverges from that of the ideal filter. The cascaded filter presents an excellent match with the ideal filter for the main lobe. The spectra of the converted signals are compared with the target NRZ signal in Figure 5-5 b); as expected, the cascade filter enables a better approximation to the target spectrum, particularly near the optical carrier. However, both filtered signals present low-pass characteristics; since both optical filtering configurations only allow transmission of the main spectral lobe, there is a low-pass filtering effect in both output signals. The insertion losses of the filtering-based format converter are 6.3 dB for the single filter and 6.7 dB for the cascade filter case. Such high losses are due to the fact that the NRZ signal optical carrier is effectively a spectral tone at clock frequency of the RZ signal; and such component presents much lower power when compared to the original optical carrier.

The signals after the filter-based converters are compared in Figure 5-6 in terms of eye diagram and temporal evolution. Both signals present NRZ signal shapes and open eye diagrams. As expected, both signals present high rise and fall times when compared to the target NRZ signal (inset Figure 5-3), due to the low pass filtering effect. The signal after the cascade filter presents improved eye opening and reduced distortion, when compared to the signal after the single filter. The ER of the converted signals is very high (ideally infinite). This is related to the fact that the power ratio of the spectral component at the clock tone and the adjacent spectral tones in a RZ signal is similar to that of the optical carrier and adjacent tones in a NRZ signal with infinite ER. As will be verified later in this section, the converted signal still presents very high ER even when the input signal has low ER.

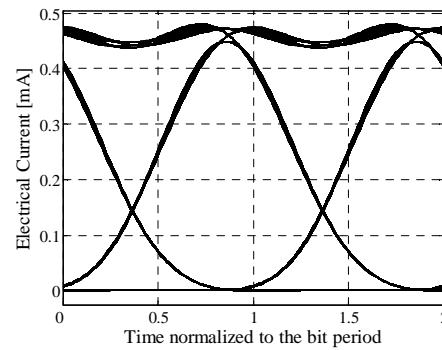
To allow operation over arbitrary pulse rates of the transport network, the converter should ideally be independent on the pulse duration of the input signal. However, the spectral shape of the RZ signal is dependent on pulse duration. Figure 5-7 characterizes the optical spectrum of the RZ signal for different FWHM: for small FWHM the RZ spectrum is very broad, while for higher FWHM, the spectral occupancy is reduced. Moreover the RZ signal presents spectral notches which become closer to the optical carrier when the FWHM increases and affect the spectrum of the converted signal.



a) Temporal evolution (current is normalized);



b) Eye diagram with single filter;



c) Eye diagram with cascaded filter.

Figure 5-6: Comparison of temporal evolution and eye diagrams of converted signals when the single and cascaded filter configurations are employed.

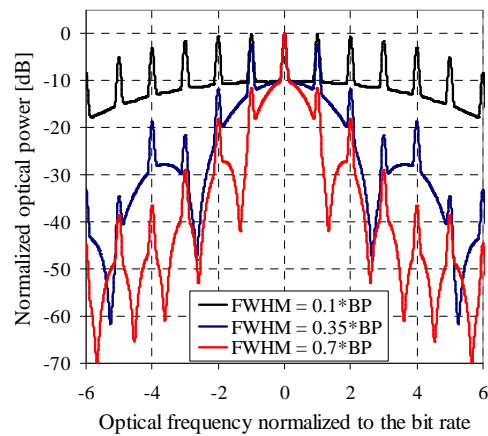


Figure 5-7: RZ signal optical spectrum for variable FWHM.

To characterize the converter resilience to the input pulse width, Figure 5-8 depicts the eye opening penalty (EOP) (consult appendix III for definition of EOP) and the insertion power losses as a function of the input RZ signal FWHM. The filters were kept constant throughout the test.

For low FWHM the input signal spectral occupancy increases, spreading the power over a wider spectrum. As a consequence, the insertion losses of the converter are high under such conditions. On the other hand, for high FWHM the RZ signal spectral power is concentrated closer to the optical carrier, reducing the power of the clock signal tone, which also leads to an increase of the losses. The EOP shows reduced variation for FWHM between  $0.1 \cdot BR$  and  $0.5 \cdot BR$  and  $0.6 \cdot BR$  for the single and cascaded configurations, respectively. For higher FWHM, the notch observed in the RZ signal spectrum (Figure 5-7) causes severe eye diagram degradation. Nevertheless, input signals with high FWHM ( $>0.5 \cdot BR$ ) are not an interesting use case, since the typical signals to be used as input of the proposed converter are demultiplexed signals from a high bit rate transport network, which consist in short optical pulses.

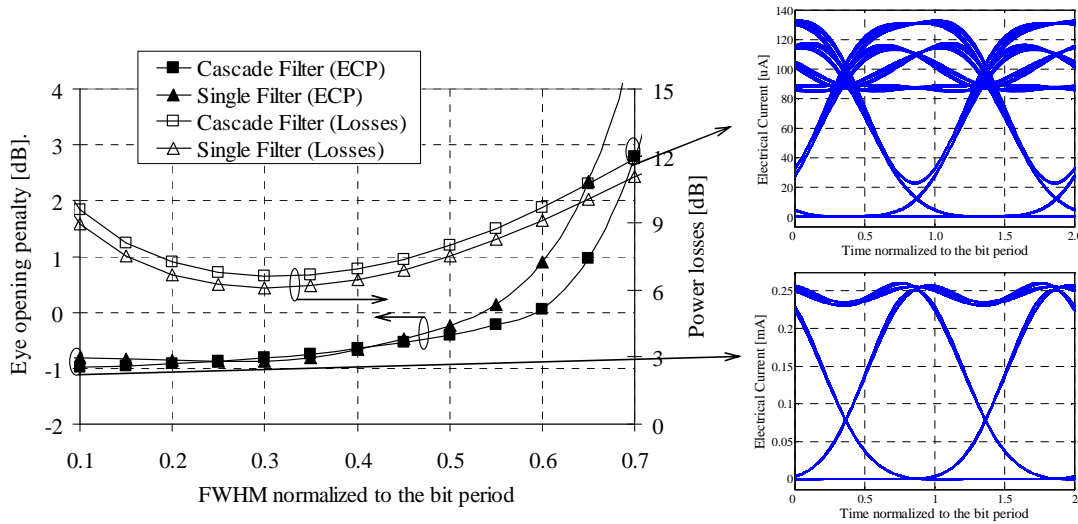
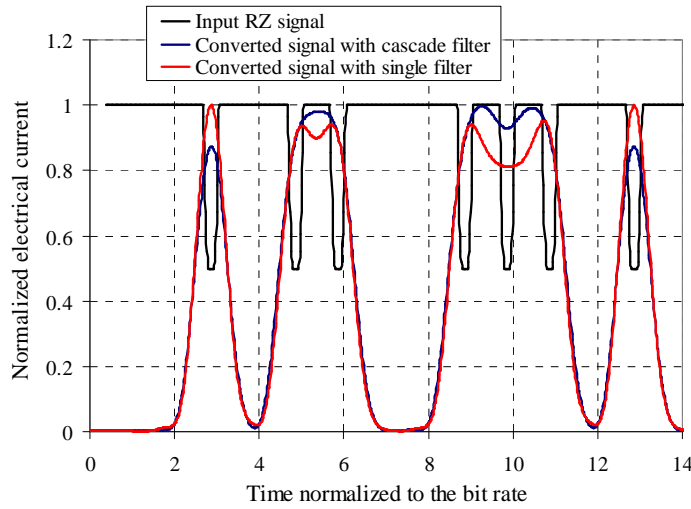


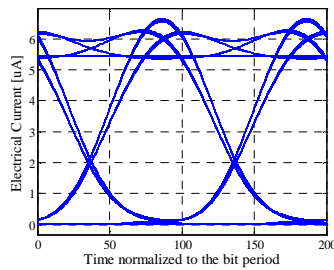
Figure 5-8: Characterization of converter performance over variable input pulse width. Inset: eye diagrams of converted signal for the cascaded filter configuration when input FWHM =  $0.1 \cdot BR$  and  $0.7 \cdot BR$ .

The conceptual principle of the RZ-to-NRZ conversion based on detuned optical filtering is to be applied to the XGM signal after a SOA, which has inverted polarity and low ER. Therefore it is essential that the conversion principle is independent on the input

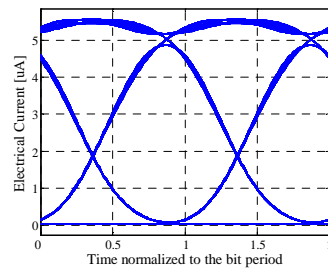
signal polarity and ER. The ER and polarity of an OOK signal are determined by the intensity and phase of the optical carrier, respectively: with the exception of the optical carrier, the entire RZ signal spectrum is independent of its polarity and ER. The proposed method nearly removes the original optical carrier, and the resultant NRZ signal is centered around the spectral tone at the clock frequency, which is not affected by the original RZ signal polarity or ER; therefore, independent operation over a wide range of ER and absolute independence on the signal polarity is expected.



a) Temporal shapes;



b) Output eye diagram when a single filter is used;



c) Output eye diagram when a filter cascade filter is used.

Figure 5-9: Converted signal when at the input RZ signal has inverted polarity and 3 dB of ER.

The filter-based format converter is characterized in Figure 5-9 with an input inverted RZ signal with low ER (3dB). It can be observed that the output NRZ signal is inverted in relation to the input RZ signal; however, it is non-inverted in relation to the original logical information. Moreover, the ER of the converted signal is not affected by

the input ER. Negligible impact from the input signal ER and polarity is observed in the converted signals eye diagrams. The EOP was measured for a range of input signal ER between 3 dB and 50 dB and less than 0.1 dB variations was obtained.

The RZ-to-NRZ converter with detuned filter has demonstrated promising results: undistorted eye diagram regardless of input signal extinction ratio, independence of input signal polarity, and high tolerance to input FWHM. However, it has high insertion losses and is dependent of the input signal wavelength, which would require wavelength tracking in realistic network scenarios.

### 5.2.2 Pulse format and wavelength conversion based on SOA and detuned filtering

The previous section demonstrated detuned optical filtering as a simple and effective method to convert RZ signals to the NRZ format. Such method is robust to the input signal FWHM, ER and polarity. Moreover, it is scalable to any bit rate, provided that the optical filter bandwidth is adjusted accordingly. However, it is highly dependent on the input signal wavelength, which would require wavelength tracking of the input signal wavelength; has high losses; and does not feature wavelength conversion.

In this section we propose the use of the detuned filtering method on the signal resulting from XGM wavelength conversion of an input RZ signal. Several advantages are foreseen when combining XGM and detuned filtering:

- No wavelength tracking is necessary, since the filtering is done over a locally generated laser;
- The high filtering losses can be mitigated by the SOA gain;
- The converter features wavelength conversion;
- The converter output signal is not logically inverted and presents high ER (unlike the typical XGM converted signal);

- Higher operation speed is expected due to the detuned filtering technique, according to the results from section 3.2.2.1;
- The overall operation principle is simple and uses low cost components.

### 5.2.2.1 Operation principle

The principle of operation of the RZ to NRZ and wavelength converter, based on wavelength conversion in SOA and detuned optical filtering, is presented in Figure 5-10. An input RZ signal at  $\lambda_1$  and a continuous wave (CW) at  $\lambda_2$  are simultaneously amplified in a SOA. At the SOA output, the signal at  $\lambda_2$  is intensity modulated due to XGM. Such signal is logically inverted; has reduced extinction ratio; and presents patterning effects due to the SOA slow gain response. This signal is then fed to a detuned optical filter with optimized transfer function. The detuned filter will retrieve at the output a non-inverted NRZ signal with high ER, as demonstrated in the previous section.

Cross phase modulation (XPM) occurs in the SOA simultaneously with XGM; hence, the signal at  $\lambda_2$  presents phase modulation in addition to amplitude modulation. As a consequence, the signal at  $\lambda_2$  is shifted towards the red and blue wavelengths for the rising and falling edges of the  $\lambda_1$  input signal, respectively. Detuned filtering of the SOA output signal at  $\lambda_2$  will induce phase-to-intensity conversions. It is then expected that the detuned filtering will exploit fast frequency chirping to enhance the converted signal quality, together with the format conversion. Detuned filtering of the SOA output signal has been presented in Chapter 3 as a common technique to obtain wavelength conversion of RZ signals with bit rates beyond the SOA gain response; however, without pulse format conversion.

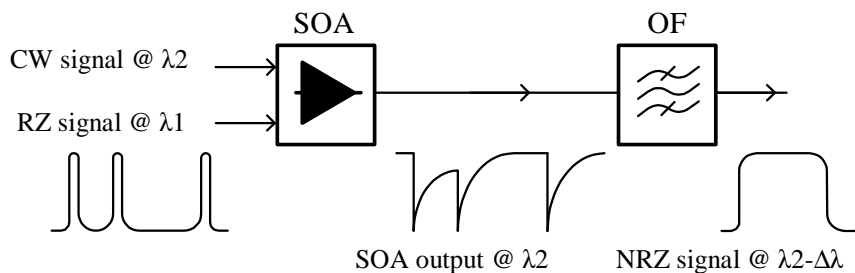


Figure 5-10: RZ-to-NRZ signal conversion based on detuned optical filtering.

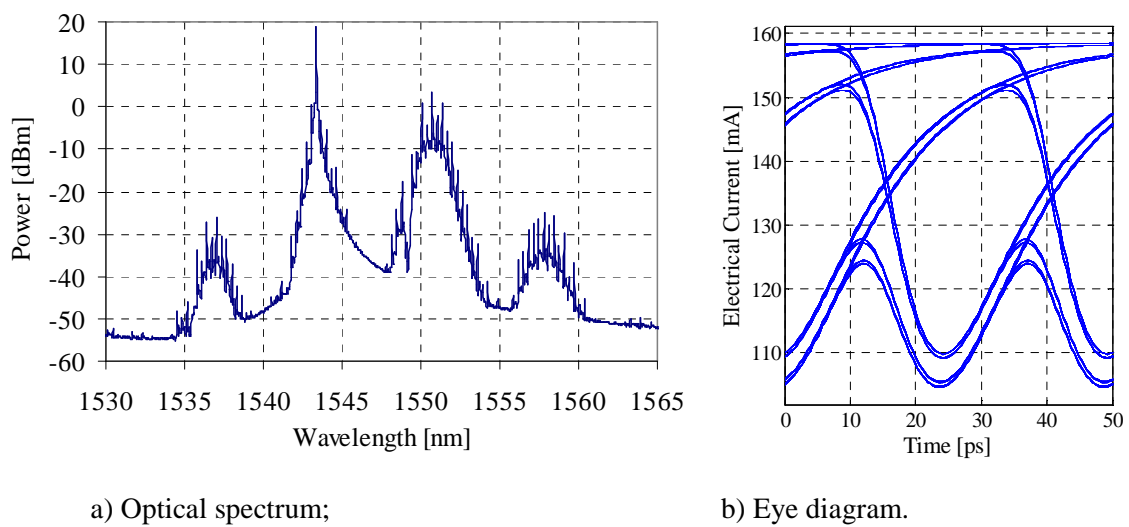


### 5.2.2.2 Simulation tests and optimization

As previously referred, one of the main applications for format converters is in all-optical interfaces between transport and access networks. At such interfaces, the  $N$  time multiplexed channels of an ultra-fast OTDM signal are separated using a  $1 \times N$  time demultiplexer, and converted to the NRZ format. Afterwards, each signal is routed to the correspondent access network. Hereafter, a 40 Gb/s RZ signal with 3 ps pulses is fed to the format converter. Due to its FWHM, this signal can represent one of the 4 time demultiplexed signals obtained from a 160 Gb/s OTDM signal delivered from a transport network.

#### 40 Gb/s conversion with fast SOA device

Figure 5-11 a) presents the simulated SOA output spectrum when the input signal presents 3 ps FWHM, with -5 dBm power, and wavelength of 1550.7 nm; and the CW probe signal power is 3 dBm and wavelength is 1543.4 nm. The SOA considered in these simulations was the *fast* SOA device (consult appendix II for more details). The SOA output signal at the probe wavelength (common XGM signal) is presented in Figure 5-11 b). This signal was obtained after a broad optical filter centered with the probe wavelength. The signal is inverted, has low ER and presents eye opening distortion due to the SOA slow response.



a) Optical spectrum;

b) Eye diagram.

Figure 5-11: SOA output spectrum, and eye diagram at the probe signal wavelength after SOA when a broad optical filter is used.

Figure 5-12 illustrates the optical spectrum of the SOA output signal around the probe signal wavelength in more detail. The spectrum of a 40 Gb/s NRZ signal with infinite extinction ratio is also depicted. The NRZ signal carrier is detuned from the probe signal by a frequency equal to the bit rate ( $\Delta\lambda$ ), to match the wavelength of its optical carrier with the discrete spectral tone at the clock frequency of the probe signal. The transfer function of the ideal filter to convert the SOA output signal to the NRZ format is obtained dividing the NRZ signal spectrum by that of the SOA output signal at the probe wavelength. The ideal optical filter spectral amplitude response is also depicted in Figure 5-12. In the frequency range of the NRZ main spectral lobe (between 0 and 80 GHz), the filter response does not present significant discontinuities. This result is consistent with that obtained in the previous section for an undistorted RZ input signal. The phase response of the ideal filter is not presented since it presents negligible group delay variations in the frequency range of interest, similarly to the converter of the previous section.

The ideal optical filter intensity response can be approximated by feasible filters in the frequency range of interest, due to the reduced group delay variations and well behaved intensity response. Gaussian optical filters presented promising results in the previous section; therefore such filters will be also considered also hereafter.

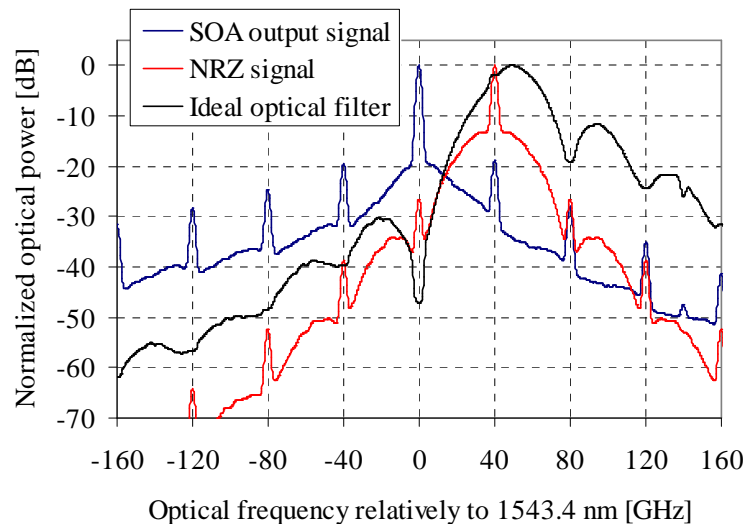


Figure 5-12: Optical spectra of: SOA output at the probe signal wavelength; NRZ signal with infinite ER detuned from the probe wavelength by 40 GHz; and ideal optical filter to convert the SOA output to NRZ pulse format.

Two filtering configurations are considered and their characteristics are optimized in order to allow maximum approximation with the ideal filter: a single first order Gaussian filter with -3 dB bandwidth of 25 GHz and detuning of 51 GHz relatively to the probe signal central wavelength; and a cascade of a first and a second order Gaussian filters with -3 dB bandwidths of 30 GHz and 57 GHz and detunings of 55 GHz and 39 GHz, respectively. The intensity transfer functions of the two filtering configurations are compared in Figure 5-13 with the response of the ideal filter. Both filtering configurations present a good agreement with the ideal filter curve for the main lobe frequencies.

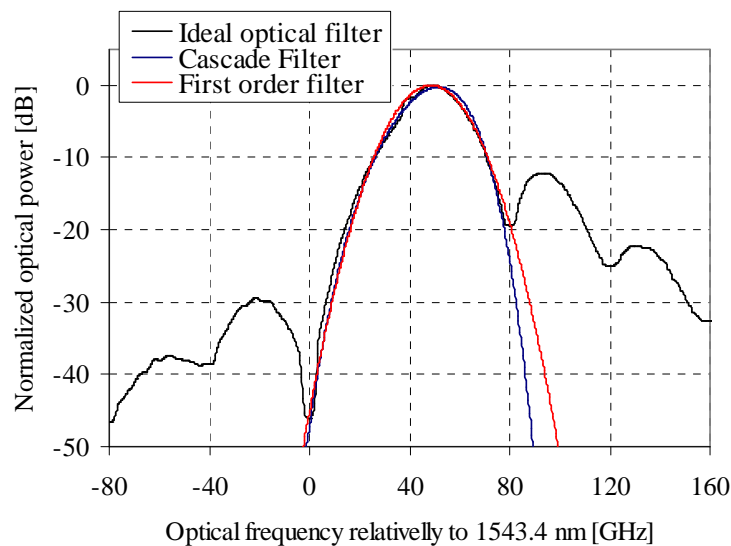
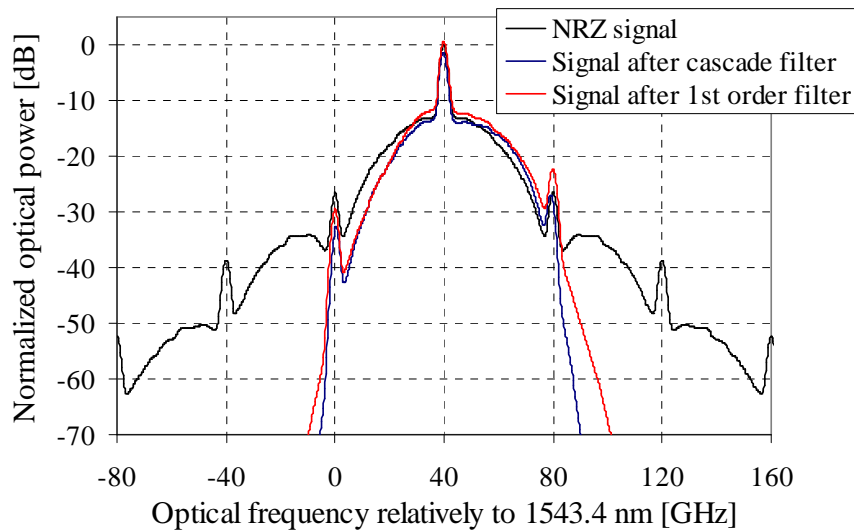


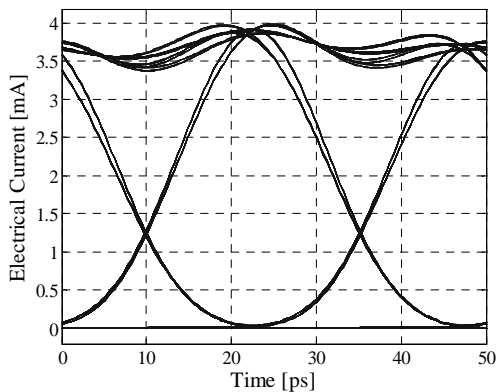
Figure 5-13: Intensity response of ideal filter to convert the SOA output signal to the NRZ format, and approximation by a cascade of filters, and by a single first order Gaussian filter.

Figure 5-14 a) compares the optical spectrum of the converted signals after SOA and detuned filtering with the spectrum of NRZ signal with infinite ER. The spectra are reasonably approximated for the main spectral lobe; for higher frequencies, the converted signals have complete spectral suppression due to the filtering. Figure 5-14 b) and c) present the converted signals eye diagrams. The signal after the cascade filter presents an open and undistorted eye diagram. Comparing to an ideal NRZ signal, the converted signals have high rise and fall times due to the low-pass filtering effect. The single filter provides insufficient suppression of the optical tone at 80 GHz (as can be verified in the optical spectrum), and as a consequence the resultant signal presents an oscillation in the logical '1' level. Both signals present very high extinction ratio. Comparing the converted

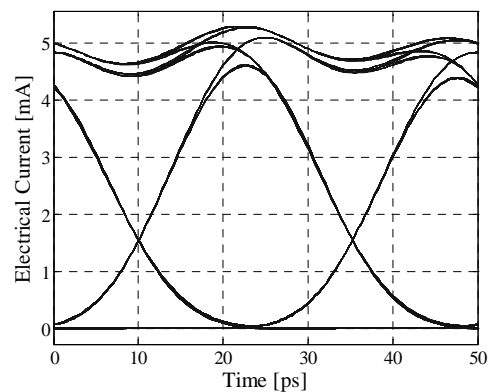
signals eye diagrams to the converted signal obtained when a broad filter tuned with the probe wavelength is used (Figure 5-11 b)), demonstrates that the proposed scheme not only performs format conversion, but also improves the SOA temporal response. Both configurations feature optical gain, since the SOA amplifies the signals, and the information is converted to the higher power probe. With the single filter, the output signal optical power is 3.4 dB, corresponding to 8.4 dB of gain relatively to the input RZ signal; with the cascade filter a gain of 7.3 dB was obtained.



a) Optical spectra of NRZ signal, and signals after SOA and detuned filtering with single filter, and cascade configuration;



b) Output eye diagram for cascade filter configuration;



c) Output eye diagram for single filter configuration.

Figure 5-14: Optical spectra and eye diagrams of converted signals after SOA and detuned filtering for single and cascade filtering configurations.

The impact of detuning of the probe signal wavelength relatively to the optical filter is assessed in Figure 5-15, by means of output signal eye opening penalty and converter gain. For negative detuning, the optical gain of the configuration increases; however, the optical tone at the probe signal carrier causes distortion in the eye diagram and penalties in the EOP (as can be verified from the upper inset). For positive detuning the optical tone at 80 GHz becomes preponderant, which also causes distortion in the converted signal (although the EOP is not necessarily degraded): the output signal becomes shaped as an RZ (lower inset); moreover, positive detuning reduces the gain of the optical converter. Nevertheless, around  $\pm 4$  GHz of filter detuning are allowed with a variation of the converter gain below 1.5 dB and with EOP below 0 dB.

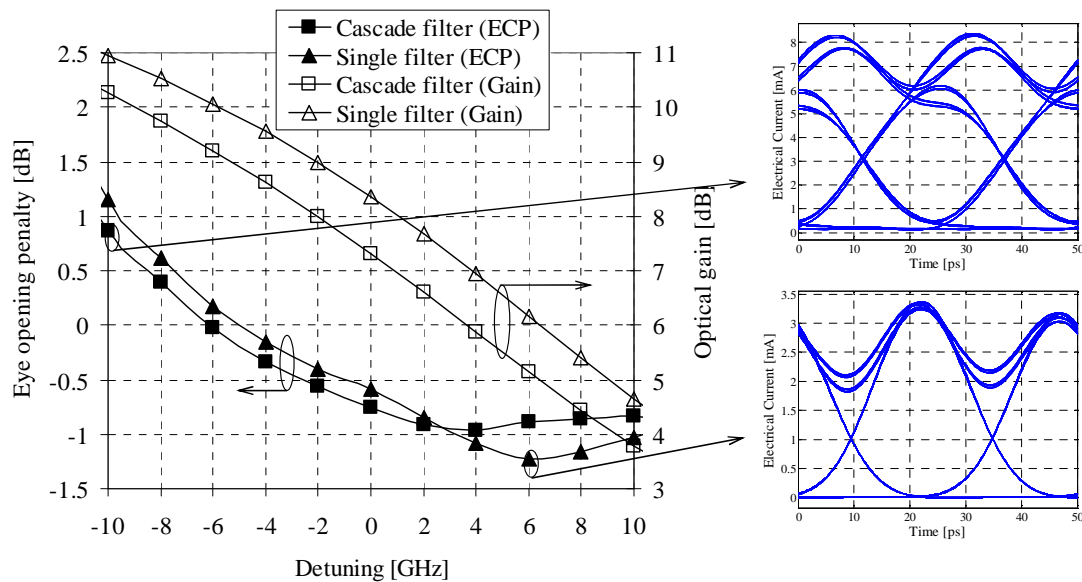


Figure 5-15: Impact of detuning of the probe signal central wavelength relatively to the optical filters. Inset eye diagrams of the converted signals for: cascade filter structure with detuning of -10 GHz; and single filter with detuning of 6 GHz.

The input signal pulse width may vary, for example due to tight optical filtering of the signal to convert or due to accumulated chromatic dispersion. Therefore, it is important that the converter is tolerant to such pulse width variations. Figure 5-16 characterizes the dependence of the converter performance on the input pulse width. Since the optical filters were designed for input FWHM of 3 ps, EOP penalties arise for both filtering configurations when the converter input signal presents higher FWHM. The optical gain is also penalized for higher pulse widths since under such circumstances the converted signal spectrum has lower power in the side lobes. Nevertheless, input pulse widths up to 7 ps or

9 ps are tolerated without penalizing the converted signal EOP above 0 dB, for the cascade and single filter configurations, respectively.

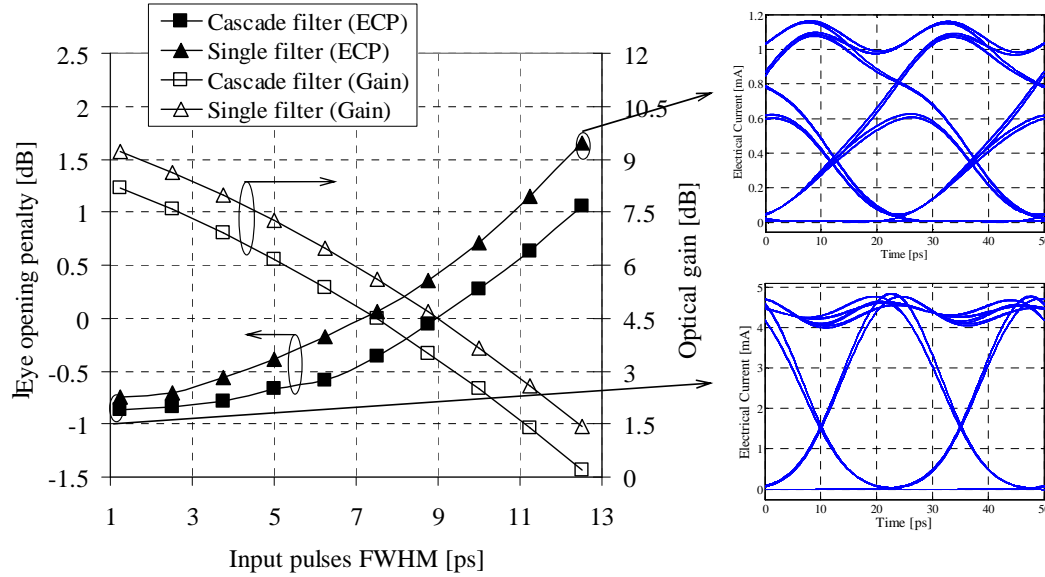


Figure 5-16: Impact of input signal pulse width. Inset eye diagrams of the converted signals for: cascade filter structure and FWHM of 1.5 ps, and single filter and FWHM of 12.5 ps.

The powers of the input data signal and of the CW probe impact the converter performance. For constant probe signal power, variation of the input signal power leads to changes in the modulation of the SOA carrier density and, as a consequence, in the amount of XGM and XPM suffered by the probe signal. Similarly, for constant input signal power, changes in the probe signal power affect the level of SOA gain saturation, which also impacts the amount of XGM and XPM. Changes in the gain and phase modulation suffered by the probe signal lead to different output spectral shape: different optical filter transfer function is then required. Figure 5-17 characterizes the converted signal EOP as a function of the input and probe signal powers for the single and cascaded filter configurations. Both filtering structures show high tolerance to input signal power variations, provided that the probe signal power is adapted accordingly. When the probe signal power is adapted to optimize the converted signal EOP, the power of the converted signal is also kept approximately constant. For example, when the input signal power varies from -14 dBm to -2 dBm and the probe power is optimized to maximize the EOP, it was verified that the output power varies less than 1 dB.

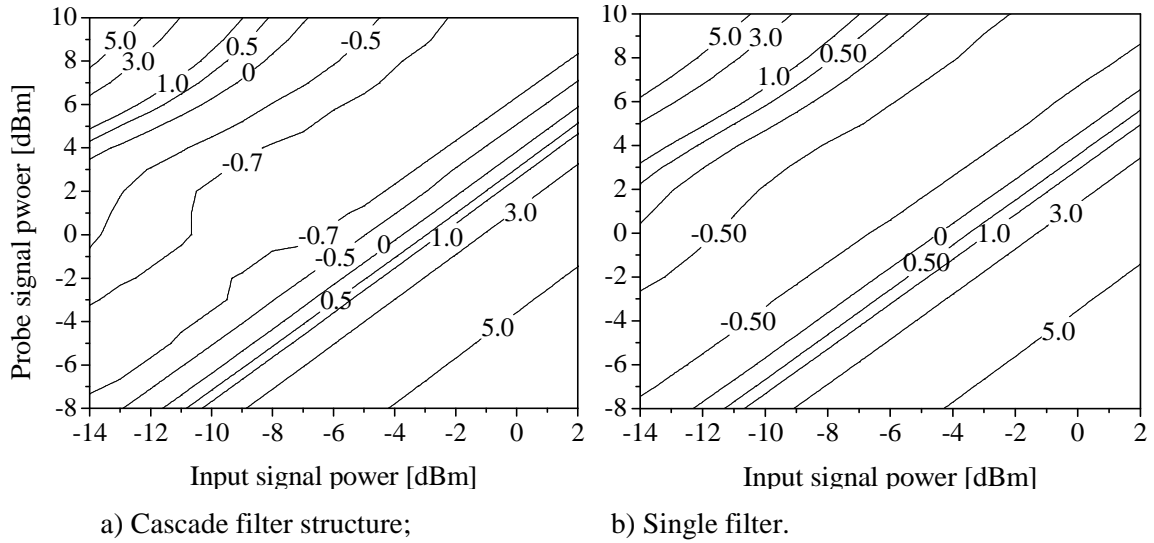
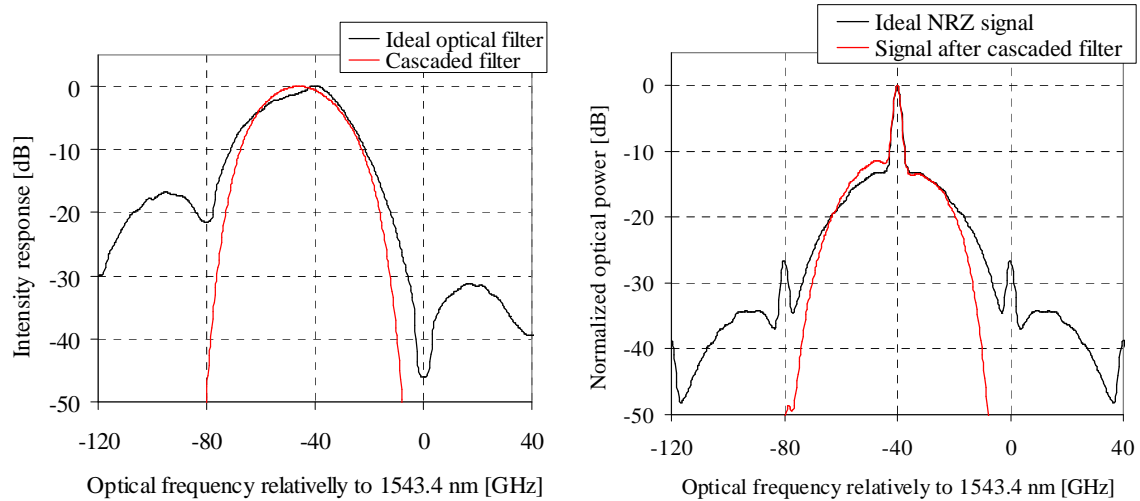


Figure 5-17: Converted signal EOP as a function of input and probe signals power.

It was referred in the previous section that the detuned optical filter can be applied both to the positive (blue) and negative (red) parts of the optical spectrum, when its input RZ signal is unchirped; however the SOA output signal presents chirp due to XPM. To verify if it is possible to perform format conversion using also the red chirped part of the spectrum, the ideal filter transfer function was derived for such condition. Figure 5-18 a) presents the intensity response of the ideal filter, detuned towards the negative frequencies. A reasonable approximation has been found by a cascade of a first order and a third order Gaussian filters. The -3 dB bandwidths of the first and third order filters are 27 GHz and 67 GHz, respectively; and the detunings relatively to the probe signal central wavelength are -46 GHz and -43.5 GHz. Figure 5-18 b) presents the converter output spectrum under such conditions, and compares it to the ideal optical NRZ signal spectrum. The optical gain of this configuration is 7.7 dB.

Figure 5-19 a) presents the eye diagram of the converted signal after the cascaded filter when applied over the red part of the SOA output signal spectrum. Severe signal distortion is observed in such eye diagram when compared to the converted signal when using the blue part of the spectrum, which is depicted in Figure 5-14 a). The amplitude distortion is due to the strong and fast red chirp occurring in the leading edge of the input optical pulses; this chirp translates in the overshoot observed in the '0' to '1' transitions of the output signal in Figure 5-19 a). To eliminate such distortion, it would be necessary to consider an optical filter with non-constant group delay. To confirm such assumption, the

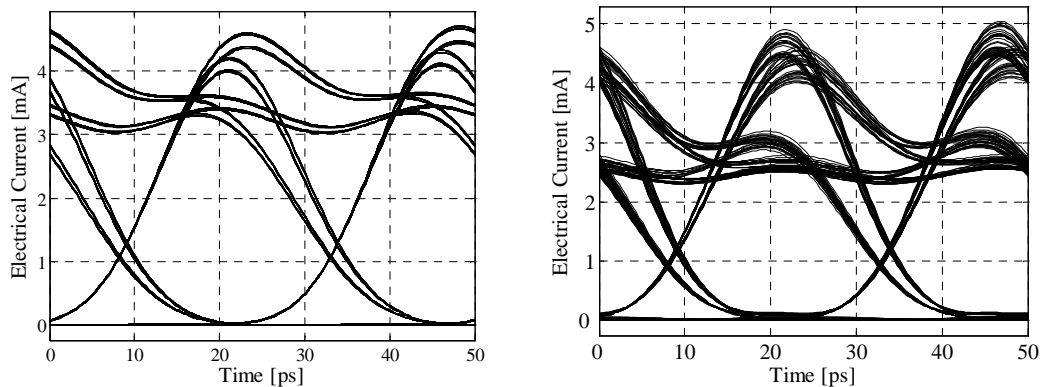
ideal filter of Figure 5-18 a) has been applied to the SOA output signal: an ideal NRZ signal is obtained when both intensity and phase response of the filter are considered (not presented in any figure); when only the intensity response of the filter is employed (the group delay is a constant), the distorted signal of Figure 5-19 b) is obtained. Therefore, we may conclude that the blue part of the spectrum is more appropriate for RZ-to-NRZ conversion than the red part of the spectrum.



a) Ideal and approximated filter transfer function;

b) Optical spectra of ideal NRZ signal, and converted signal with approximated filter.

Figure 5-18: RZ to NRZ conversion by filtering the “red” part of the spectrum (negative frequencies) of the signal after the SOA.



a) Approximated filter by cascade of Gaussian filters;

b) Ideal filter with only intensity response (group delay is constant).

Figure 5-19: Obtained signal after detuned filtering of the converted signal spectrum red frequencies.



40 Gb/s conversion with slow SOA device

We have previously demonstrated RZ to NRZ conversion at 40 Gbit/s using the *fast* SOA device, with recovery times of approximately 80 ps. The detuned filtering not only enabled conversion to the NRZ format, but also reduced the patterning effects due to the SOA slow response. Hereafter, the potential of this method for overcoming the gain recovery limitations is investigated by using the *slow* SOA device, with recovery times of around 380 ps.

The input signal FWHM is 3 ps, similarly to the previous tests. It was verified that, for optimum performance, higher probe signal power is required when compared to the test with the *fast* device, for constant input signal power. Therefore, the input signal power is -3 dB, and the probe signal power is 9 dBm. Higher probe power requirements are due to the fact that the SOA response improves for higher saturation.

Figure 5-20 a) compares the *slow* SOA output spectrum at the probe signal wavelength with the equivalent spectrum when the *fast* SOA is employed. The slower response of the SOA acts like a low pass filter in the converted signal (consult section 3.3 for more details), as can be verified from the optical spectrum of the converted signal when the slow SOA is used. The spectral tone at the clock frequency, which will be the NRZ signal central tone, presents power approximately 19 dB lower for the slow SOA. A broad optical filter, centered with the probe signal wavelength, is used to extract the common XGM signal. The resultant eye diagram is represented in Figure 5-20 b): due to the slow SOA response the converted signal eye diagram is completely closed.

The spectral intensity response of the ideal filter to convert to NRZ format, when the *slow* SOA is used, is compared in Figure 5-21 a) to the ideal filter response for the fast SOA. The two filter responses are similar in the main lobe, with the exception that the slow SOA requires a much higher attenuation at the central wavelength of the probe signal. The higher attenuation relates to the lower modulation depth obtained from the slower SOA. The ideal filter is approximated by cascading a first and a third order Gaussian filters with -3 dB bandwidths of 27 GHz and 64 GHz, respectively; and detunings of 48 GHz and 45 GHz. Figure 5-21 b) presents the converted signal eye diagram, which presents very high ER and complete suppression of the distortion that was present at the SOA output

(Figure 5-20 b)). Unlike the *fast* SOA configuration, which features optical gain, the slow SOA converter scheme presents 12 dB insertion losses. This result proves that the detuned filter provides conversion beyond the SOA modulation bandwidth; however, in such condition the converter is penalized by a reduction of the output signal power.

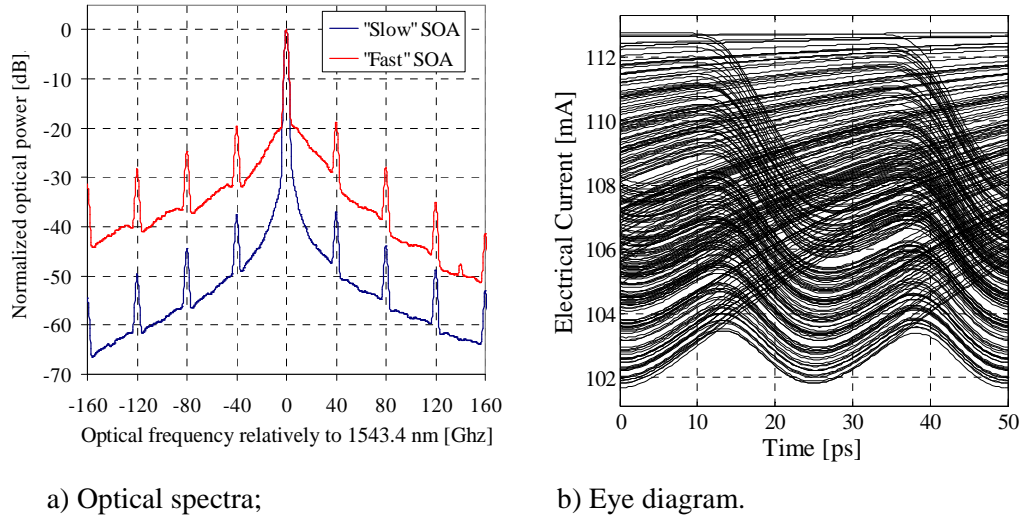


Figure 5-20: SOA output spectra, and eye diagram at the probe signal wavelength when a broad optical filter is used.

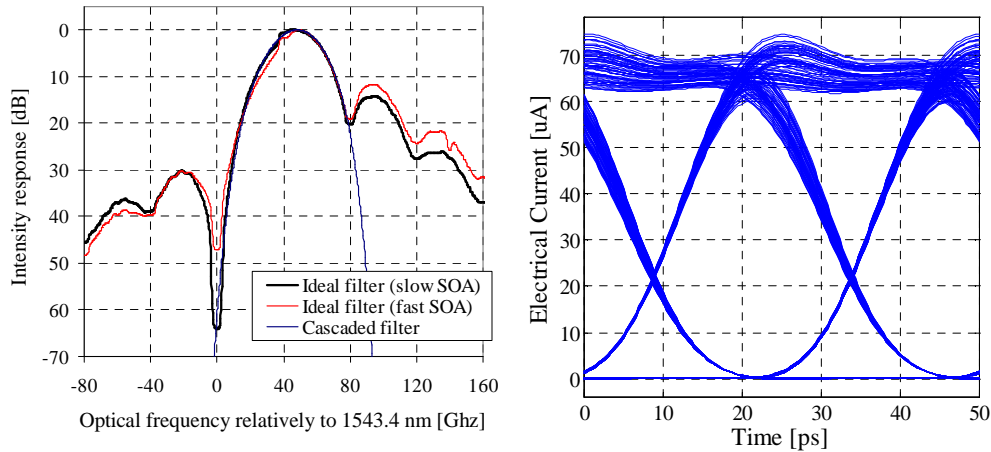


Figure 5-21: Spectral response of filters for conversion of SOA output signal to NRZ format, and eye diagram considering a cascade of Gaussian filters.

The simulation results of this section demonstrate the great potential of the configuration with SOA and detuned filter for simultaneous wavelength and format

conversion. Using the fast SOA device the scheme presents optical gain and an undistorted output signal was obtained at 40 Gb/s. Independence of the input signal FWHM was demonstrated and tolerance to a high input power range is enabled, provided that the probe signal power is adapted accordingly. With the same method the slow device was also capable to convert an input 40 Gb/s RZ signal to the NRZ format with negligible distortion. The main drawback of using the slow device are the high insertion losses, due to lower carrier modulation at high bit rates.

### 5.2.2.3 Experimental validation

#### 40 Gb/s conversion with fast SOA device

The converter is experimentally tested at 40 Gb/s using the experimental setup depicted in Figure 5-22. The input RZ signal at  $\lambda_1 = 1549.9$  nm is obtained by modulating the output of an ultra-fast optical clock (UOC), which generates 3 ps optical pulses, in a MZM. The optical RZ signal spectrum and eye diagram are depicted in Figure 5-23. The RZ signal is coupled with a continuous wave (CW) at  $\lambda_2 = 1552.52$  nm and amplified in a SOA. The *fast* SOA is considered for this test. The power of the RZ and probe signals at the SOA input are adjusted to -2.0 dBm and 5.0 dBm, respectively. After the SOA, the signal is filtered by optical filters OF1 and OF2; such cascade of filters is employed to obtain an approximation of the ideal filter, as described in the previous section. Transmission of the converter output signal over SSMF is carried to assess its dispersion tolerance. The resultant signal is detected at a pre-amplified receiver, where OF3 is used to reduce the amplified spontaneous emission (ASE) noise spectral bandwidth. The -3 dB bandwidth (BW) of OF3 and the photo-detector are 130 and 37 GHz, respectively.

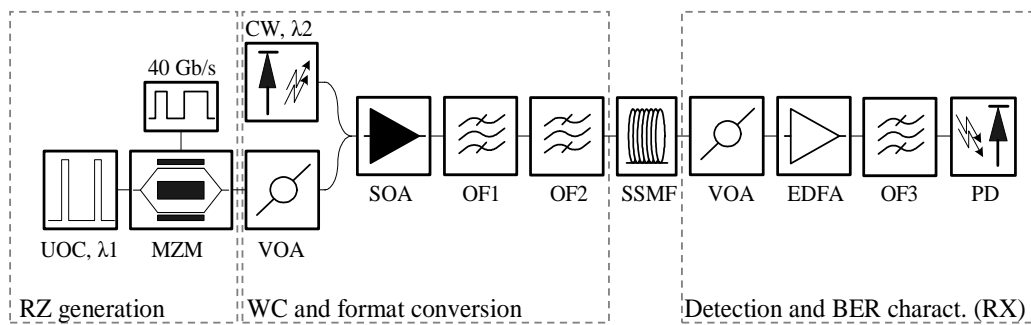


Figure 5-22: Wavelength and RZ to NRZ converter setup.

Figure 5-24 presents the optical spectrum at the SOA output and the XGM signal eye diagram, retrieved at the SOA output when a broad optical filter is considered. The XGM signal was obtained after a broad optical filter, tuned with the probe signal wavelength. The eye diagram presents reduced ER (2.4 dB), and patterning effects due to the SOA slow gain response. The experimental eye diagram and optical spectrum present similarities with those obtained via the 40 Gb/s simulation tests presented in previous section (Figure 5-11).

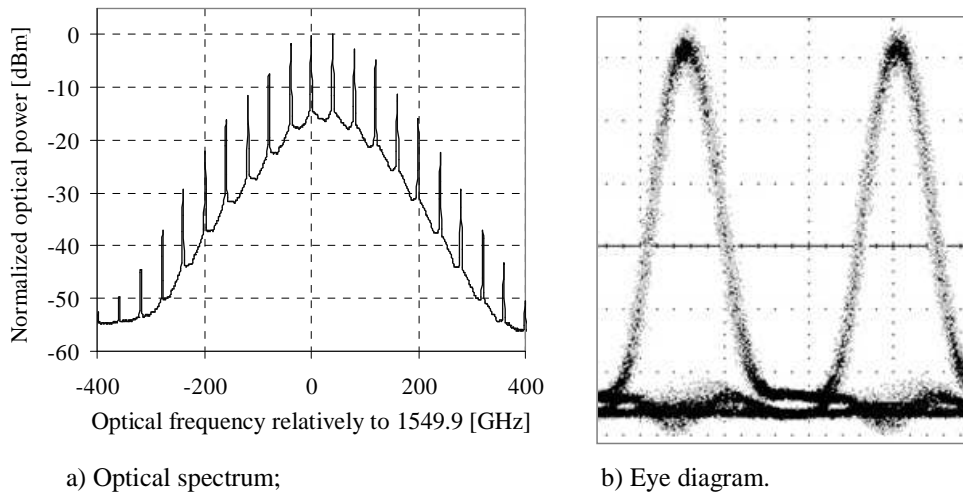


Figure 5-23: Optical RZ signal with 3 ps optical pulses. Eye diagram obtained with a 65 GHz photo detector.

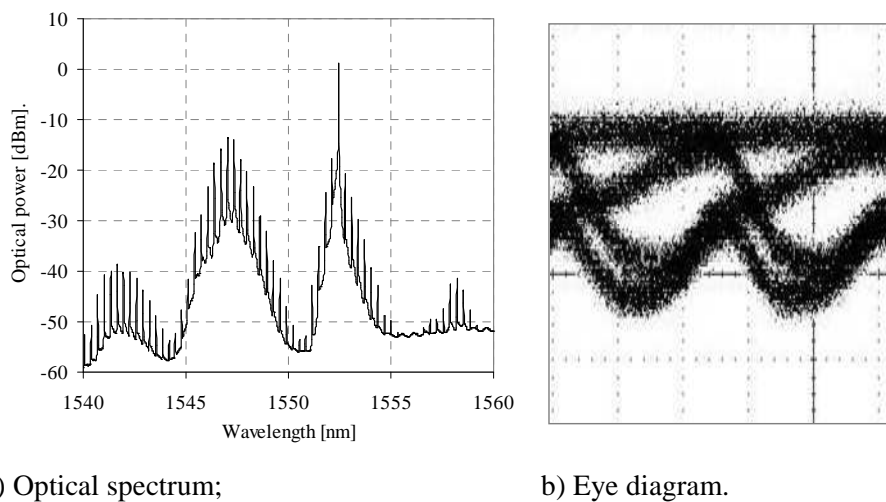


Figure 5-24: SOA output spectrum; and SOA output eye diagram when a broad optical filter tuned with the probe signal wavelength is used.

Figure 5-25 presents a detailed view of the probe signal optical spectrum, and the spectrum of an NRZ signal with infinite ER. From these two spectra, the intensity spectral

response ideal filter to convert the SOA output to the NRZ format is obtained and represented also in Figure 5-25. For comparison, the ideal conversion filter obtained via simulations (originally presented in Figure 5-12) is also represented. An excellent match of the two filters is observed in the main lobe.

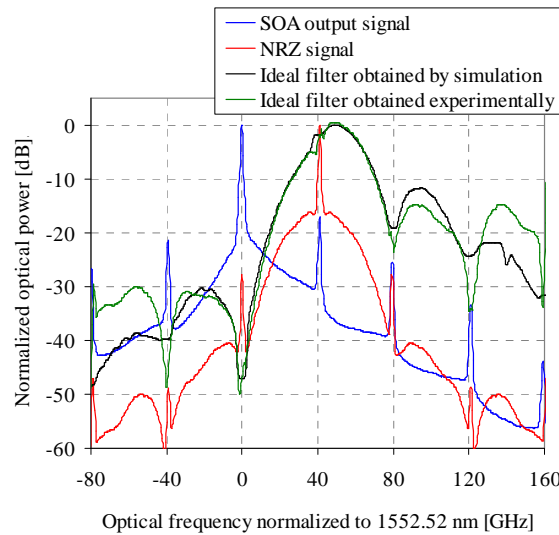


Figure 5-25: Optical spectra of: experimental SOA output at probe signal wavelength, NRZ signal with infinite ER detuned from the probe wavelength by 40 GHz; and ideal optical filters to convert the SOA output to NRZ pulse format obtained by simulations in section 5.2.2.2 and obtained from the SOA experimental output spectrum.

Figure 5-26 presents the intensity transfer function of the filter that enables ideal conversion to the NRZ format, obtained from the experimental SOA output spectrum. Due to our experimental constraints, it was not possible to achieve an optimal approximation, as that obtained in the simulation results. Two cascaded filters are considered: OF1 and OF2, which can be approximated by 1<sup>st</sup> and 3<sup>rd</sup> order Gaussian shaped characteristics, with -3 dB bandwidth of 42 and 37.5 GHz, respectively. OF1 and OF2 have tunable central frequencies, which are optimized considering the ideal filter optical spectral response, and the output NRZ signal eye diagram. Optimum detuning of 61 GHz and 45.5 GHz relatively to the probe signal central wavelength were found for OF1 and OF2, respectively. Under such conditions, the measured spectral intensity responses of OF1 and OF2 are depicted in Figure 5-26; also the resultant intensity response of the cascade of the two filters; and the ideal filter response are illustrated. Comparing the responses of the ideal filter and the experimental cascade filter, a reasonable approximation is observed from 25 to 68 GHz, with intensity response difference lower than 3 dB.

Figure 5-27 a) and b) presents the converted signal optical spectrum and eye diagram. The signal eye diagram is open and has negligible distortion; moreover, this signal features high ER (12.1 dB). The signal slow rise and fall times (approximately 17 ps), are due to the high decay of the experimental filter cascade for frequencies between 0 and 25 GHz and from 68 to 80 GHz, when compared to the ideal filter.

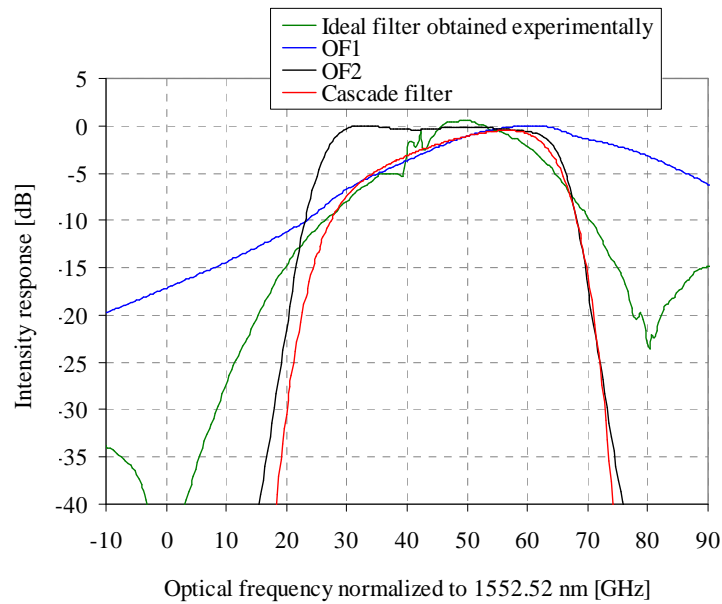
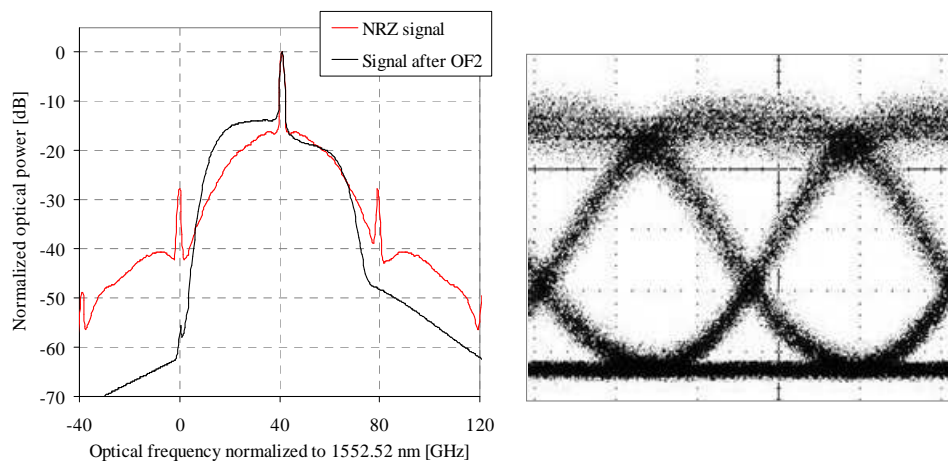


Figure 5-26: Ideal and experimental optical filters spectral intensity response.

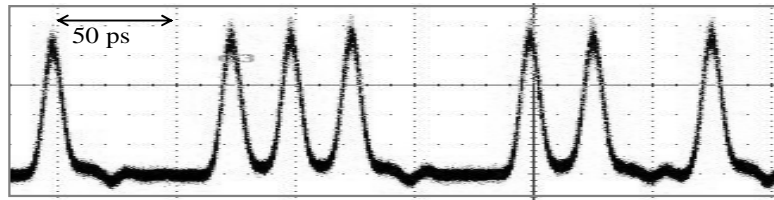


a) Optical spectra;

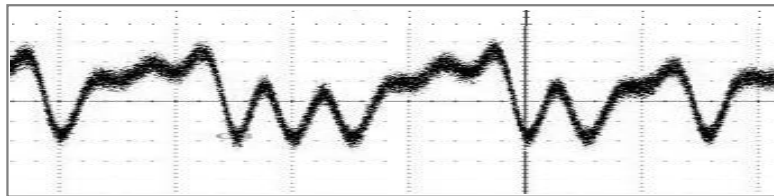
b) Eye diagram.

Figure 5-27: Comparison of ideal NRZ signal optical spectrum and spectrum obtained after the experimental filter cascade; and experimental eye diagram at converter output.

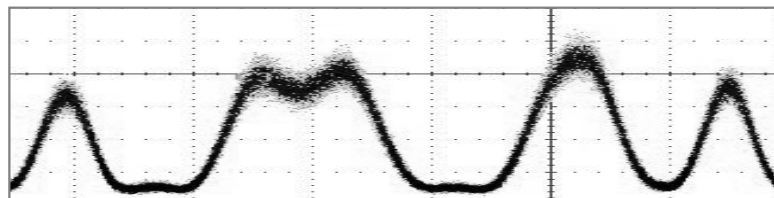
Figure 5-28 compares the temporal shapes of the input RZ signal with the signals obtained after the SOA when a broad optical filter extracts the probe wavelength (XGM signal), and after the filter cascade. It is visible that the information carried by the signal after the SOA is logically inverted relative to the input signal data, and presents strong patterning effects due to the SOA slow carrier recovery. However, the filter output signal is no longer inverted and overcomes the signal degradation caused by slow carrier dynamics.



a) RZ input signal;



b) Signal after SOA at the probe wavelength (XGM signal);



c) NRZ signal after detuned optical filtering.

Figure 5-28: Experimental temporal shapes of input RZ signal, XGM signal and signal after the cascaded filter.

The converter performance is characterized in Figure 5-29 for different central frequencies of OF1 and OF2, by means of bit error ratio (BER) measurements. The power at the input of the pre-amplifier receiver was kept fixed at -26.9 dBm. A bit pattern length of  $2^{11}-1$  is used for the BER tests. First, the central frequency of OF2 is detuned from 45.5 GHz relatively to the probe signal wavelength and OF1 central frequency is varied. More than 35 GHz of OF1 central frequency variation are allowed for the BER to rise from  $10^{-10}$  to  $10^{-9}$ . The BER demonstrated less tolerance to OF2 central frequency deviations from the optimum value, due to its higher out of band decay: with OF1 tuned at 61 GHz, the

allowed variation of OF2 central frequency is only around 7 GHz for the same BER degradation.

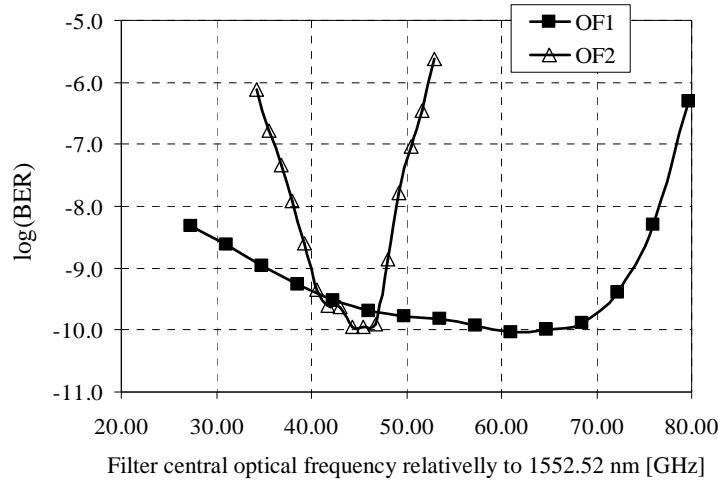


Figure 5-29: Characterization of converter performance as a function of OF1 and OF2 central optical frequency.

The influence of the filter shape was assessed by replacing the cascaded filters with only one of the filters. Considering only OF1 (the 1<sup>st</sup> order Gaussian shaped filter), the spectral component at the probe signal wavelength is not sufficiently rejected, and a signal with distorted shape and closed eye diagram is observed. On the other hand, considering only OF2 (the 3<sup>rd</sup> order Gaussian shaped filter) detuned from 45 GHz from the probe signal central frequency, the NRZ eye diagram of Figure 5-30 is retrieved at the output. Although presenting an open eye diagram, this signal presents significant eye opening penalty, since OF2 diverges from the ideal filter response. In this case, a 2.5 dB power penalty at the pre-amplified receiver is obtained in back-to-back for a BER of  $10^{-9}$ , when compared to the cascade of the two filters. Therefore, the cascade of the two filters is required to obtain proper converter performance, considering our experimental constraints. Nevertheless, the ideal filter may be approximated by a custom designed single device, using fiber Bragg grating technology, for example.

The converter performance is characterized in Figure 5-31 for different transmission distances, by means of bit error ratio (BER) measurements, as a function of the pre-amplified receiver input power. The converted NRZ signal in back-to-back presents a penalty in the required optical power for a BER of  $10^{-9}$  of approximately 1 dB, compared to the input RZ signal. Such a power penalty is commonly observed even when comparing



ideal NRZ and RZ signals, due to a higher vertical eye diagram opening of RZ for the same optical power.

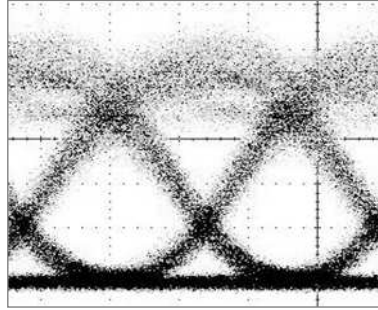


Figure 5-30: Obtained eye diagram when only OF2 is utilized at the SOA output.

Since SOA induce phase modulation in the converted signal through XPM non-linearity, it is important to verify the converted signal ability to be transmitted over dispersive optical fiber. The converted signal is transmitted over 4 km and 6 km of SSMF (68 ps/nm and 102 ps/nm, respectively) to characterize its tolerance to accumulated chromatic dispersion. The optical power penalty for a BER of  $10^{-9}$ , after such distances, is 0.7 and 3.3 dB, respectively, when compared to the NRZ signal in back-to-back. These penalties are in agreement with the results of section 4.2.3.2 for conventional on-off keying (OOK) format, demonstrating that the SOA induced phase modulation does not impact the dispersion tolerance of the converted signal.

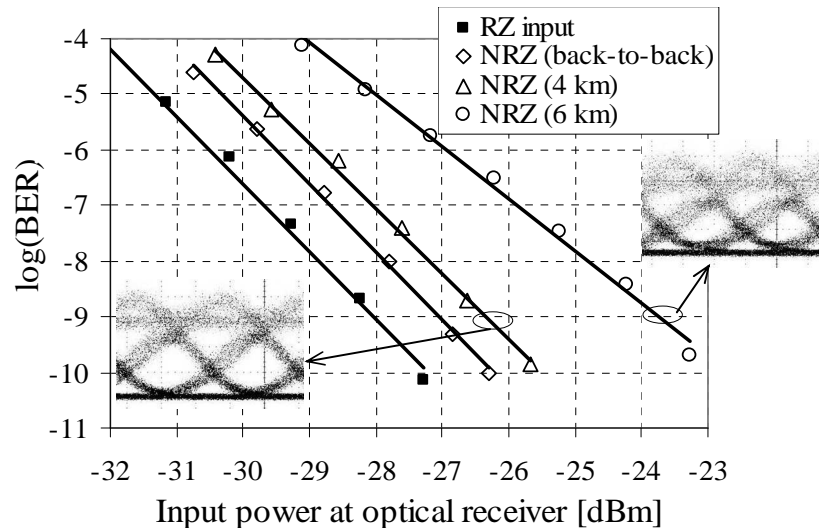
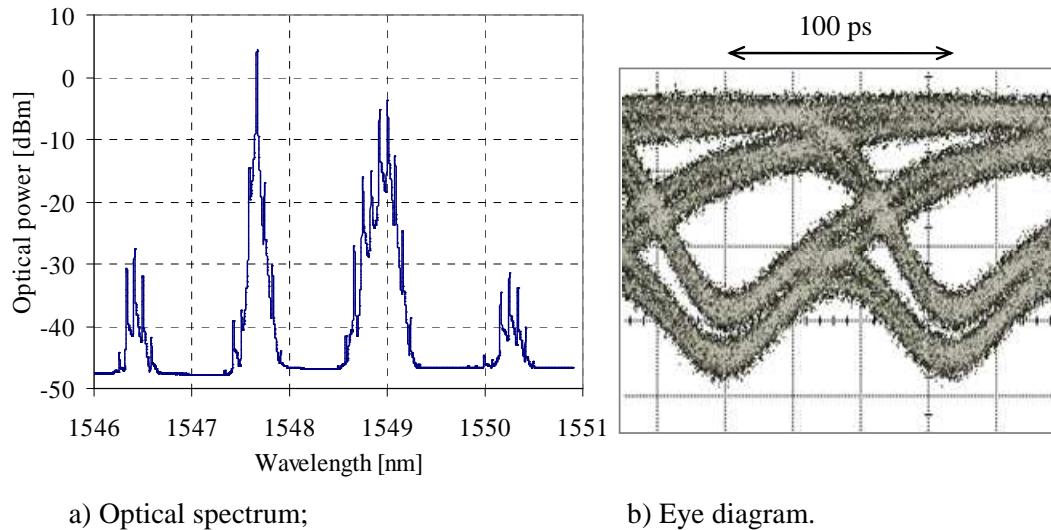


Figure 5-31: BER as a function of the pre-amplified receiver input power. Insets: eye diagrams of the converted NRZ signal after 4 and 6 km of SSMF transmission.

### 10 Gb/s conversion with slow SOA device

The experimental 10 Gb/s RZ signal has a FWHM of about 60% of the bit period, a  $Q$ -factor of 10.1, and an ER of 8.4 dB. The power of the data signal at the SOA input is -5.6 dBm and the CW probe power is 2.3 dBm. The data signal wavelength is 1548.8 nm and the CW wavelength is 1547.55 nm. The detuned optical spectral intensity response is approximated by a 2<sup>nd</sup> order Gaussian filter with a -3dB bandwidth of 13.5 GHz. The *slow* SOA device is employed in the 10 Gb/s tests.

In Figure 5-32 the optical spectrum after the SOA is presented, as well as the eye diagram of the converted signal when a broadband optical filter tuned with the probe signal is employed. The signal eye diagram presents patterning effects due to the SOA recovery time.



a) Optical spectrum;

b) Eye diagram.

Figure 5-32: Optical spectrum after the SOA, and eye diagram of the XGM converted signal.

Figure 5-33 presents the converted signal measured  $Q$ -factor as a function of the detuning relative to the probe signal wavelength. For a detuning of 14.2 GHz from the input CW probe signal optical carrier, a non inverted NRZ signal with undistorted eye diagram is obtained. The converted signal presents an improved  $Q$ -factor of 9.4, and extinction ratio of 10.3 dB. It can also be verified that the slow response of the SOA is not noticed in the detected eye diagram, similarly to the 40 Gb/s tests.

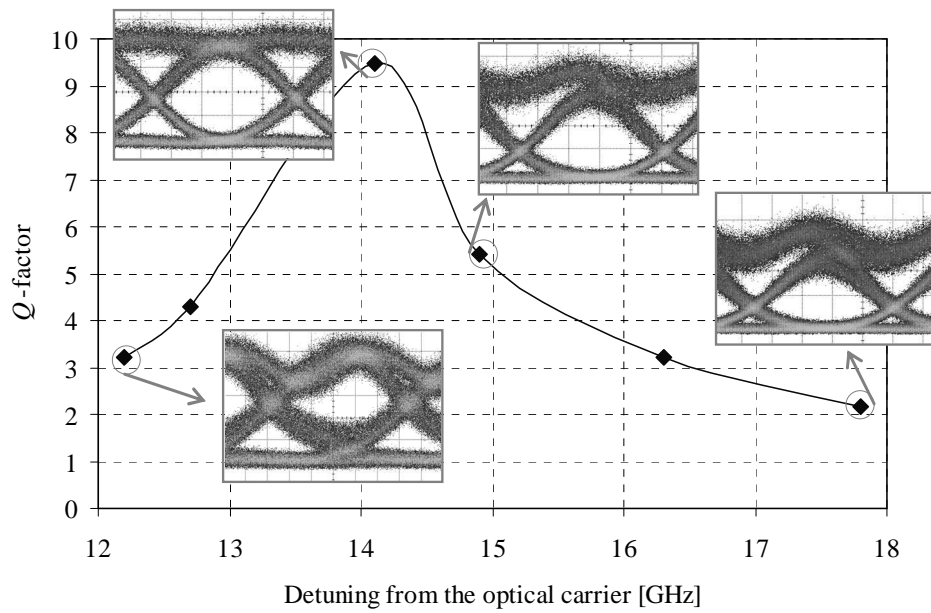


Figure 5-33: Q-factor as a function of the detuning of the optical filter; the insets show the eye diagrams for selected values of detuning.

### 5.3 RZ to NRZ pulse converter with GC-SOA

#### 5.3.1 Operation principle

As detailed in section 2.8, GC-SOA are similar to a common SOA where lasing is induced by a distributed Bragg reflector (DBR). In absence of input signal, the internal laser power is constant at a level determined by the cavity losses. When an optical pulse is injected into the GC-SOA the internal laser power decreases in order to obtain a constant cavity gain. However, if the input power is high enough, the carriers are depleted below the lasing threshold, the laser turns ‘off’ and the GC-SOA acts as a common saturated SOA. When the input power level decreases and the carrier density at the excited state becomes sufficient to provide the necessary gain, the internal laser turns ‘on’ again. In Figure 5-5-34 the GC-SOA carrier density and the internal laser power temporal evolutions are represented when two consecutive optical pulses are injected, considering a pulse spacing ( $T_P$ ) close to the maximum modulation rate of the GC-SOA internal laser. Two situations are considered:

- When a *low power* pulse train is injected (Figure 5-5-34. a), the carrier density falls below the lasing threshold (i.e. the laser is extinct). When the pulse leaves the SOA, the carrier recovery time to the lasing threshold level ( $T_{\text{OFF-ON}}$ ) is lower than  $T_P$ , and the laser turns back on before the next pulse. In this condition all the transitions of the input signal are tracked by the laser: it is modulated with the inverse of the input signal logical information.
- In case of a *high power* pulse train (Figure 5-5-34. b), the laser is also extinct when an optical pulse enters the GC-SOA. The difference from the *low power* pulses is that the amplifier is driven into deeper saturation (i.e. the carrier density is further reduced) and  $T_{\text{OFF-ON}}$  is higher than  $T_P$ . As a consequence, the laser remains ‘off’ during two consecutive pulses. In this condition, the internal laser is NRZ modulated with the inverted equivalent of the input signal logical information.

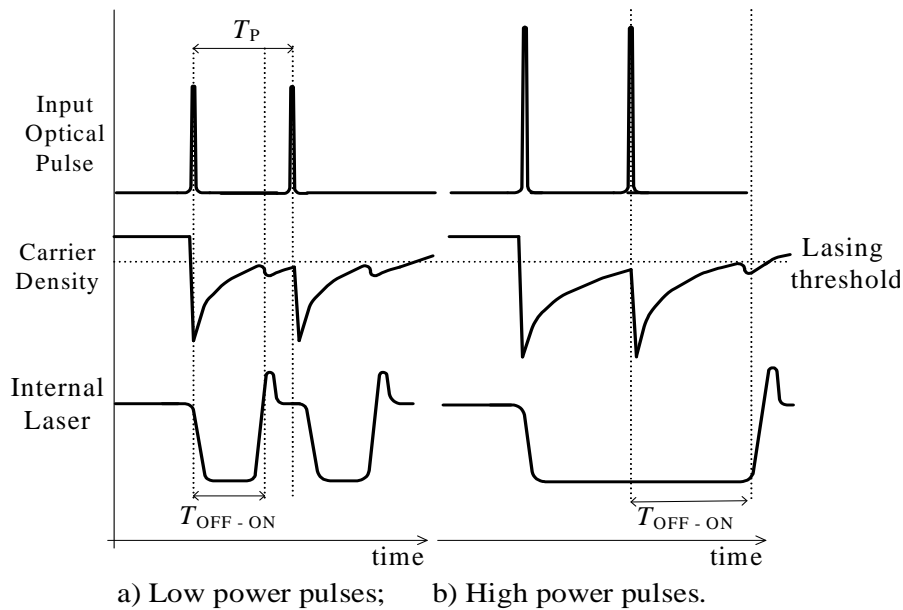


Figure 5-5-34: Schematic representation of the variations in the GC-SOA carrier density and in the internal laser intensity, when low and high power pulses are injected.

As illustrated, if the power of the RZ pulses signal is chosen so that  $T_{\text{OFF-ON}}$  is slightly higher than  $T_P$ , the GC-SOA internal laser is modulated with the inverse of the input signal logical information and with NRZ format. This laser is generated inside the

GC-SOA, but due to the limited reflectivity of the GC-SOA facets and gratings, it is available at the GC-SOA output. Such signal results from modulating a laser near its maximum rate; therefore significant distortion is observed. An additional stage, consisting of a XGM wavelength converter in a common SOA will be cascaded to overcome this impairment, due to the low pass effect characteristic of XGM. The resultant scheme is non-inverting; moreover, the output signal wavelength may be the same as the input or it can be converted to any arbitrary wavelength within the SOA working range.

### 5.3.2 10 Gb/s experimental results

The setup of Figure 5-35 is used to obtain format conversion based on modulating the GC-SOA internal laser and XGM in a common SOA. The input 10 Gb/s optical pulses at  $\lambda_1$  of 1547.3 nm have variable FWHM of 5 ps or 40 ps. This signal is amplified in the GC-SOA and modulates the internal laser at  $\lambda_{\text{DBR}} = 1509.5$  nm. As referred above, the internal laser is modulated with the inverse of the input signal logical information and NRZ pulse format. Due to the limited reflectivity of the GC-SOA gratings, the internal laser is available at the output; this signal is then amplified and filtered to remove the input wavelength and optical noise (OF1 is centered at  $\lambda_{\text{DBR}}$ ). The resulting signal is then fed to a XGM stage, which removes part of the incoming distortion and allows for flexible output wavelength. In the tested scheme, the CW probe wavelength is the same as the original RZ signal,  $\lambda_1$ . At the SOA output, an optical filter removes  $\lambda_{\text{DBR}}$  (OF2 is centered at  $\lambda_1$ ). The fast SOA device is employed in this test. Optical filters OF1 and OF2 have -3 dB bandwidth of 0.4 and 0.46 nm, respectively. The converted signal is detected in a pre-amplified receiver, which consists in an EDFA, an optical filter with -3 dB bandwidth of 1.27 nm (OF3 is centered at  $\lambda_1$ ), and a photo detector (PD) with 10 GHz bandwidth.

In a first analysis, the photo detector is placed at the output of OF1 to observe the amplitude dynamics of the modulation suffered by the GC-SOA internal laser. In Figure 5-36 b)-d) the time domain curves of this laser are presented for several RZ signal input powers; the input signal is also depicted in Figure 5-36 a). For this characterization the input signal FWHM is 5 ps. Figure 5-36 b) presents the laser temporal shape for low power pulses (-16.7 dBm); in this case the laser is intensity modulated with the inverse of the

input signal logical information. Since the carrier density never falls beneath the lasing threshold, the laser never turns ‘off’ and its modulation follows all the input signal transitions with reduced extinction ratio. For an input power of -9 dBm, the temporal shape of the GC-SOA laser is presented in Figure 5-36 c): the laser modulation speed is insufficient to follow all the transitions; therefore, the laser turns ‘off’ when an optical pulse enters the GC-SOA and remains in the ‘off’ state until the next logical ‘0’. In this condition, the input information is converted to the NRZ shape. Further increasing the input power drives the GC-SOA into deeper saturation - where stand alone ‘0’s are lost, as depicted in Figure 5-36 d) for an input power of 0 dBm.

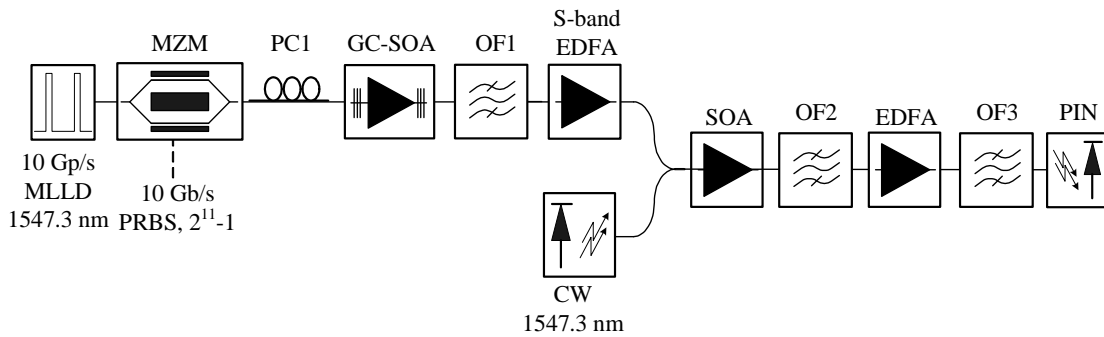
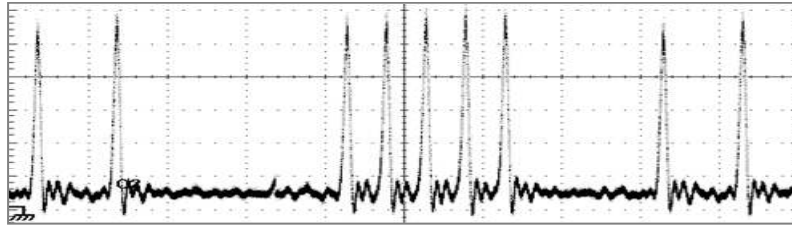


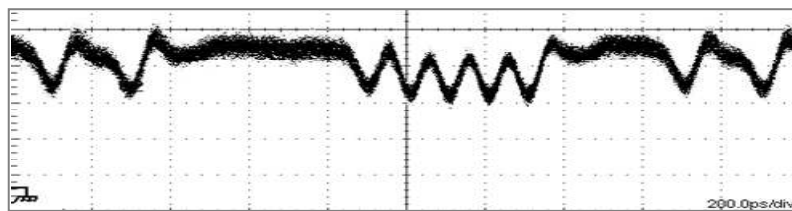
Figure 5-35: Setup to perform non-inverting format and wavelength conversion.  
Inset: Optical spectra after GC-SOA and after SOA.

We have verified that the signal of Figure 5-36 c) is converted to NRZ format and presents high extinction ratio (ER); however, it is limited by the GC-SOA characteristics. First, the reflection band of the internal gratings is broad; therefore, the internal laser has several modes, reducing its suitability for fiber transmission. Second, this signal presents distortion due to the relaxation oscillations that occur when the laser turns ‘on’. Third, the output signal presents inversion of the logical information; and its wavelength is predetermined to the wavelength of the internal grating of the GC-SOA. A XGM stage in a common SOA is added to overcome such drawbacks. In the XGM stage, a CW probe signal is amplitude modulated, allowing the converter to present wavelength conversion capabilities to an arbitrary wavelength (different from  $\lambda_{\text{DBR}}$ ). Since the XGM stage is inverting, the converter output signal will be non-inverted in relation to the input RZ signal. Furthermore, the resulting signal presents less distortion than the GC-SOA modulated laser, due to the SOA gain compression effect and the low-pass effect of the XGM effect. In Figure 5-36 e), the temporal shape of the signal after the XGM stage (after

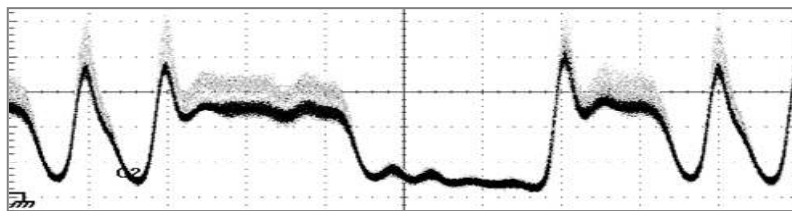
OF2) is depicted for -9 dBm input power. As discussed above, the resulting signal is non-inverted in relation to the input RZ signal, and most of the amplitude distortion observed in the modulated laser (of Figure 5-36c)) has been removed.



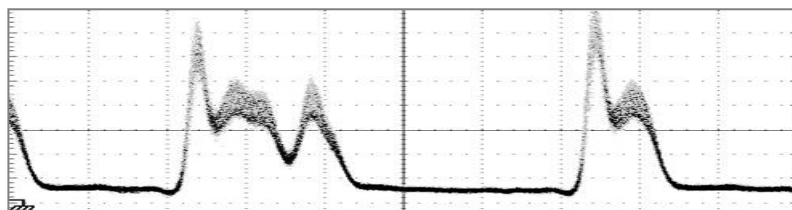
a) input signal



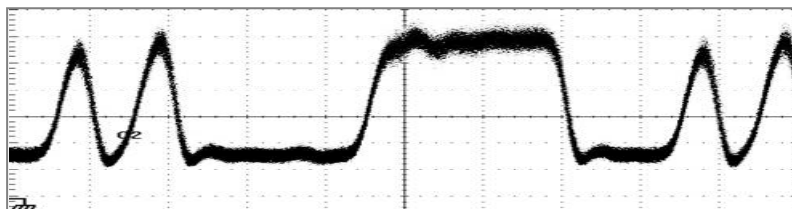
b) laser generated by the GC-SOA for input powers of -16.7 dBm;



c) laser generated by the GC-SOA for input powers of -9 dBm;



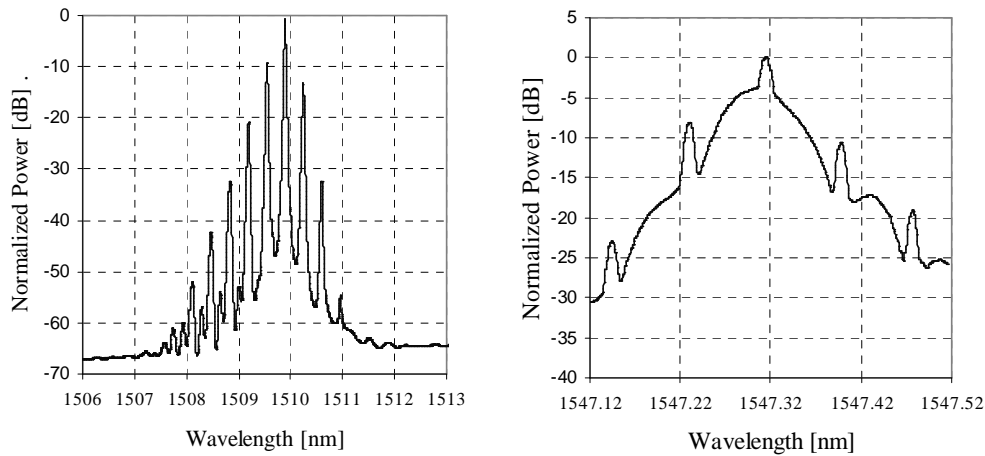
d) laser generated by the GC-SOA for input powers of 0.0 dBm;



e) Output signal after the XGM stage for an input power of -9 dBm.

Figure 5-36: RZ to NRZ format converter characterization via temporal shapes of input pulses, GC-SOA internal laser and XGM output signal.

The optical spectra after the GC-SOA and SOA are presented in Figure 5-37. It can be verified that after the GC-SOA the spectrum of the optical signal is very broad, since the converted signal consists in the GC-SOA generated laser. After the second stage such signal is converted to a local wavelength, and the output spectrum is now similar to a common NRZ signal, with some residual chirping, visible from the unbalance of the red and blue parts of the optical spectrum. Such unbalance is due to XPM non-linearity.



a) After first conversion stage;

b) After second conversion stage;

Figure 5-37: Optical spectra of the signals after the first conversion stage (in GC-SOA) and after the second conversion stage (in common SOA).

The converter operation is investigated using RZ pulses with FWHM of 5 ps and 40 ps; for the former case the RZ signal input power is -9 dBm and for the latter the input power is -10 dBm. The eye diagrams of the input RZ and the converter output NRZ signals are illustrated in Figure 5-38. From the converted signals eye diagrams, it is noticeable that the converter retrieves open and undistorted eye diagrams in both cases. The output signal ER in both cases is around 6 dB. The jitter in the falling edges of the output signal is higher than in the rising edges; such jitter is caused by the turn ‘on’ of the GC-SOA internal laser.

We have verified that GC-SOA input power can vary by  $\pm 1.5$  dBm without significant performance degradation. For lower optical powers, the output signal format becomes RZ; and for higher optical powers, two stand alone ‘0’ are lost. The impact of the GC-SOA driving current was also verified: the tests presented above considered a driving current of 200 mA; when this value falls below 150 mA, the internal laser  $T_{\text{OFF-ON}}$  increases and the output signal does not follow all the logical transitions.



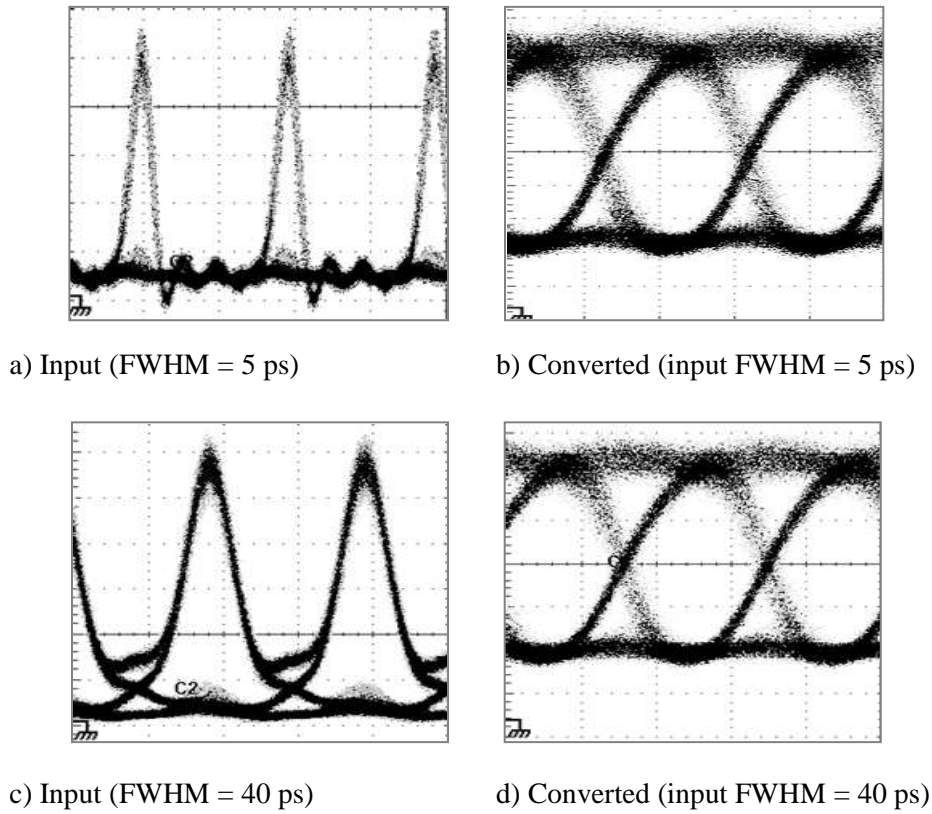


Figure 5-38: Eye diagrams of the input and converted signals.

To assess the impact of the CW probe signal wavelength, it was set to 1530 nm retrieving a converted signal ER of 7.5 dB, and to 1560 nm, retrieving an ER of 4.8 dB. Improved ER is expected if a GC-SOA with internal laser wavelength closer to the SOA central wavelength is used, and if down conversion is performed at the SOA [206] (conversion to lower wavelengths).

The eye diagrams presented in Figure 5-38 were obtained when the GC-SOA and SOA input signals are polarized for the maximum amplifiers gain. Polarizing these signals orthogonally originates a small decrease in the output signal ER (less than 0.6 dB), since the employed SOA and GC-SOA present low polarization dependence, of less than 0.5 dB.

The system BER is measured for the RZ input signals and for the corresponding converted NRZ signals, as a function of the optical power at the pre-amplified receiver input. The results are presented in Figure 5-39. A  $2^{11}-1$  sequence is utilized due to 3R and BER equipments limitations; nevertheless, when the sequence length is increased to  $2^{31}-1$ , there is no visible eye diagram penalization.

The 5 ps RZ signal is penalized by 6 dB for a BER of  $10^{-9}$ , comparing to the 40 ps signal. This penalty is due to the low bandwidth of the photo detector, which was used to simulate the lower bandwidth of an access network receiver: as result, part of the spectral energy of the short pulses is lost. The two output NRZ signals BER curves are similar, with a difference of less than 0.8 dB; such similarity demonstrates the converter robustness to the input pulse width. For a BER of  $10^{-9}$ , the converted signal presents a power penalty of 2.5 dB relatively to the 5 ps pulses, and of approximately 8.5 dB for the 40 ps RZ signal. Since the retrieved NRZ signals present open eye diagrams, as depicted in Figure 5-38, these penalties are mostly caused by two factors. First, the converted signal reduced ER; second, because RZ signals usually feature improved sensitivity when compared to NRZ, due to higher vertical eye opening for the same optical power.

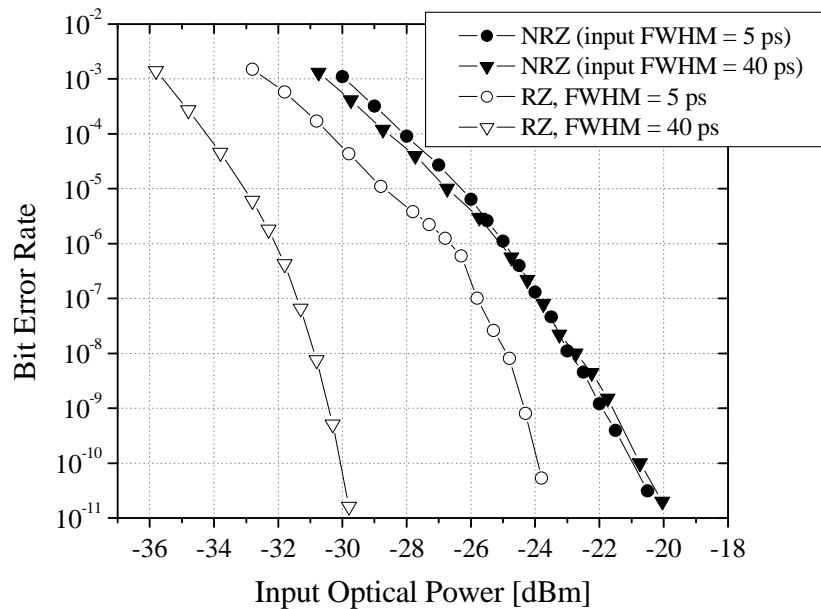


Figure 5-39: BER measurements of the input RZ and converted NRZ signals.

In this section we have proposed and experimentally demonstrated a 10 Gb/s converter from RZ to NRZ pulse format. The converter is non-inverting and features wavelength conversion. The converter delivers an open and undistorted eye diagram, mostly limited by an ER of 6 dB. The output signal ER can be increased if the GC-SOA is designed so that the internal laser wavelength is higher, so that down-conversion is performed in the SOA. Optionally the XGM modulation can be replaced by XPM, which typically allows high output ER.

## 5.4 Summary

Return-to-zero (RZ) to non-return-to-zero (NRZ) pulse format conversions are key elements in the interfaces between high bit rate transport networks and access networks. For full functionality, these should allow conversion of short optical RZ pulses and feature wavelength conversion. In this chapter we proposed and experimentally demonstrated two schemes to obtain such conversion.

The first method employs cross-gain modulation (XGM) in semiconductor optical amplifier (SOA) and detuned optical filter and was assessed via simulations and experimental tests. The ideal optical filter shape was investigated, and approximated experimentally cascading two filters. NRZ signals have been obtained at 10 Gb/s and at 40 Gb/s. The converted signal presents high ER and undistorted eye pattern. At 40 Gb/s the converter input pulses had 3 ps full width at half maximum, demonstrating the potential for support of 160 Gb/s networks. By appropriate filter design, we have demonstrated 40 Gb/s pulse format conversion using the *slow* SOA device. We have verified that the converter is robust to input signal power variations, provided that the probe signal power is adjusted accordingly. For constant optical filter shape, optimized for 3 ps optical pulses, the input signal FWHM can vary between 1 ps and 8 ps without EOP increasing above 1.5 dB. The converted NRZ signal presents similar tolerance to chromatic dispersion, when compared to conventional OOK, demonstrating that its transmission capabilities are not prejudiced by SOA induced chirp.

The second proposed scheme is based on two stages. In the first stage the internal laser of a gain-clamped SOA is intensity modulated by the input signal; due to the laser dynamics, the output signal presents NRZ pulse format and high ER. The second stage consists in a XGM stage in a common SOA; this stage allows flexibility of the output wavelength and removes some of the distortion of the GC-SOA laser. The resultant signal is non-inverted and features eventual wavelength conversion. The operation of the converter was experimentally demonstrated at 10 Gb/s, where 5 ps and 40 ps pulses were successfully converted to the NRZ format, revealing robustness to the pulse width. Open and undistorted eye diagrams were obtained and error free operation was verified.



# Chapter 6

## Optical regeneration

### 6.1 *Motivation*

With the outcome of the EDFA and dispersion compensation techniques, transmission of optical signals over hundreds or thousands of kilometers became possible without intermediate OEO regenerators. The increasing demand for optical bandwidth has lead to the development of WDM systems and to the increase of the per channel bit rate. In parallel to the explosion of per channel bit rates and transmission distances, optical systems are also evolving from simple transmission systems to a higher level of complexity, where switching and signal processing is supported by the optical layer. By eliminating the *electronic bottleneck*, all-optical signal transmission and processing are expected to enable the next generation of optical networks, by dramatically reducing costs, energy consumption, and increasing the network throughput.

The increase of the per-channel bit rate usually leads to a reduction of the signal tolerance to optical impairments. Such optical impairments are mostly originated from propagation and from signal processing. Propagation degrades the optical signal due to various distortion sources; such as: uncompensated chromatic dispersion, polarization-mode dispersion, non-linear effects, or noise accumulation. Optical signal processing degrades the signals by tight optical filtering; crosstalk in photonic-cross connects; polarization dependent losses (PDL) of components; and by imperfect optical functionalities, like wavelength or format conversion. Usually, signal distortion is divided in two main categories [207]: amplitude distortion, and temporal distortion. *Amplitude*

*distortion* degrades the contrast between logical ‘1’ and ‘0’; while *temporal distortion* refers to temporal fluctuations between optical pulses (also known as phase timing jitter).

Signal degradation in optical systems is typically overcome by adding regeneration stages at periodic transmission distance intervals. The most common type of regeneration consists in detecting the optical signal, recovering it in the electrical domain and re-transmitting it. However, this technique suffers from the general disadvantages of OEO signal processing. On the other hand, all-optical regenerators are expected to overcome the drawbacks of OEO converters and are considered essential elements for fully-functional optical networks; however, all-optical regeneration at high bit rates is still a research topic.

Regeneration can be divided in the three main functionalities of Figure 6-1: re-amplification, re-shaping, and re-timing. The simplest functionality is *re-amplification* (or 1R), which consists in simple optical amplification. A device which also provides *re-shaping* in addition to *re-amplification* is known as 2R. *Re-shaping* consists in increasing the contrast between the two logical levels; which improves the required optical signal to noise ratio (OSNR) for a specific bit error rate (BER) level. Finally, 2R is combined with *re-timing*, to create a full 3R. Re-timing refers to the reduction of the signal jitter.

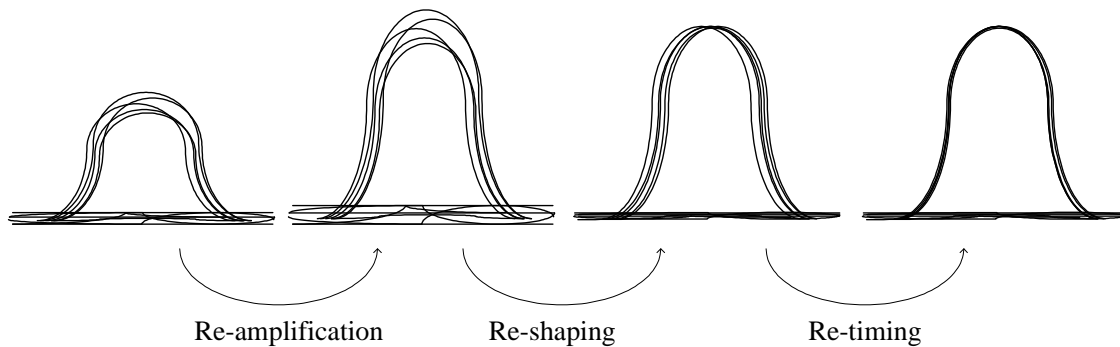


Figure 6-1: illustration of the basic regeneration functionalities applied to an RZ signal eye diagram.

Section 6.2 reviews the state-of-the-art in all-optical regeneration using SOA based devices. Section 6.3 reports for the first time to the author’s knowledge regeneration of coherent optical code division multiple access (OCDMA) signals with distortion provoked by multiple access interference (MAI). The regeneration scheme is based on a Mach-Zehnder interferometer exploiting cross phase modulation in semiconductor optical amplifiers. Experimental regeneration of an 8 Chip 10 Gb/s OCDMA signal is

demonstrated with improvements in the required optical signal to noise ratio and elimination of bit error rate floor. This work has been presented in [208] and in [209]. Section 6.4 presents a novel scheme based on Gain-clamped SOA, which has been assessed with 2.5 Gb/s input signal and reported in [200].

## 6.2 All-optical regeneration techniques in SOA

Figure 6-2 depicts the basic all-optical 3R scheme [210]-[212]. The input signal is split in two replicas; one of the replicas feeds a clock recovery sub-system, which produces stable optical pulses with reduced jitter. The second input signal replica is then used to control a non-linear gate, which encodes the logical information in the optical clock signal. Usually 3R features also wavelength conversion, as the output signal wavelength is the same of the clock signal. This scheme only supports on-off keying input signals. The two main building blocks of Figure 6-2 are revised hereafter.

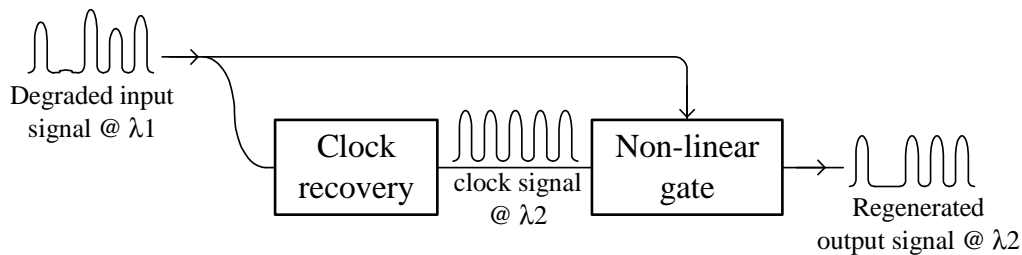


Figure 6-2: Common all-optical 3R scheme.

### 6.2.1 Non-linear gate

In an optical regenerator, the non-linear gate is responsible for the *re-shaping* functionality. Therefore, non-linear gates are employed in 2R and in 3R. Figure 6-3 illustrates the conceptual transfer function of such non-linear gate [213]. The input signal is improved in two distinct manners. First, signal improvement is achieved through an increase of the ER; obtained by the steep slope of the transfer function between the logical '0' and '1' of the input signal. Second, fluctuations in logical '0' and '1' levels are reduced by the approximately constant output power over input logical '1' and '0'. Such re-shaping functionality is similar to that performed in electronic decision circuits, present in most

opto-electronic regenerators. The main drawback of the decision circuit like transfer of Figure 6-3 is that input amplitude noise is converted in output timing jitter [213]; therefore, in 2R regeneration there is a trade-off between amplitude regeneration and output jitter degradation.

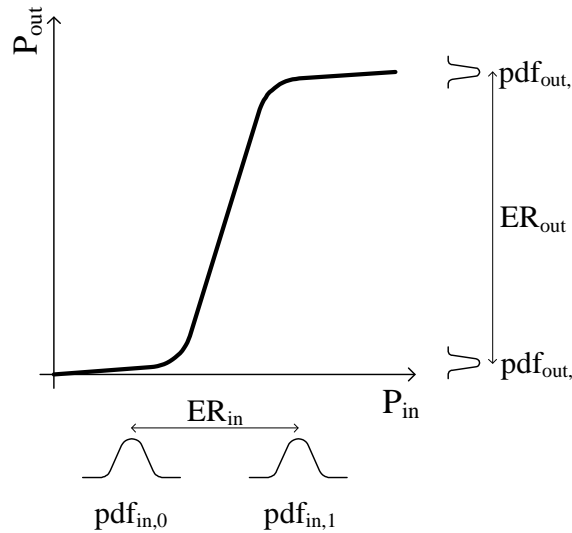


Figure 6-3: Transfer function of non-linear gate.  $P_{in}$  and  $P_{out}$ : input and output power;  $pdf_i$ : probability density function;  $ER_{in}$  and  $ER_{out}$ : input and output extinction ratio.

Optical 2R and 3R regenerators with non-linear gates such as the one illustrated in Figure 6-3 do not necessarily allow recovering from errors in the input signal: the input BER is not improved. Therefore, 2R and 3R should be periodically employed over the signal transmission line to decrease the error accumulation with further transmission.

Optical re-shaping requires a scheme to provide the non-linear transfer function depicted in Figure 6-3. SOA can be employed to achieve such purpose through one of two means: directly using the SOA non-linear intensity transfer function, which arises from carrier density modulation; and recurring to the non-linear transfer function of a scheme employing SOA. SOA-based non-linear gates are usually divided in two groups: pass-through, and wavelength-conversion, as depicted in Figure 6-4 [214]. In pass-through schemes, the input signal is self-modulated at the SOA-based regenerator; as a consequence, the output and input signal wavelengths are the same. Pass-through regenerators can only perform 2R. In wavelength-conversion schemes, the input signal at  $\lambda_1$  is fed to the non-linear gate together with a CW signal or an optical clock signal (CLK)



at  $\lambda_2$ . The non-linear transfer function is applied from the input signal at  $\lambda_1$  to a local wavelength,  $\lambda_2$ . The input signal is also known as *control-signal*. Such non-linear gates are appropriate for both 2R (when the signal at  $\lambda_2$  is a CW) or 3R (when the signal at  $\lambda_2$  is an optical clock).

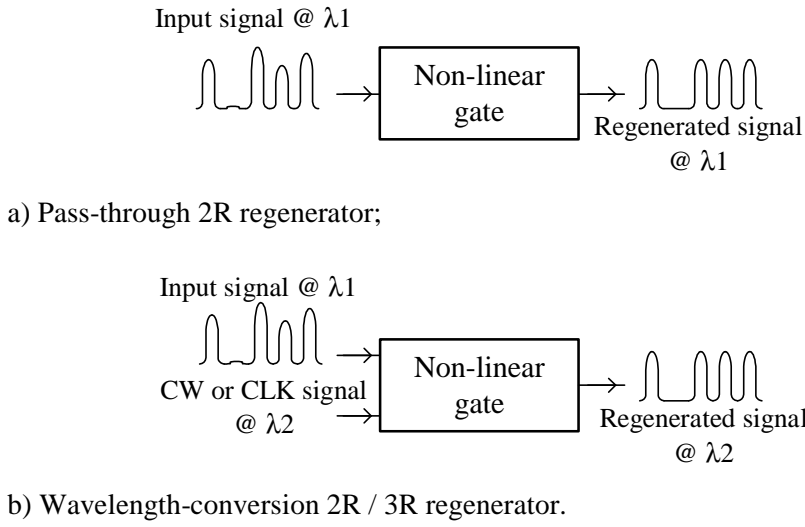


Figure 6-4: Use of non-linear gates in pass-through and wavelength-conversion schemes.

One of the most common regeneration schemes with SOA is based on MZI-SOA devices, which is a wavelength-conversion scheme. This basic regeneration scheme is similar to the wavelength conversion scheme of Figure 3-7, when standard operation is considered, or to that of Figure 3-10, when differential operation is employed. To understand the principle behind regeneration in MZI-SOA structures, consider the conceptual schematic of Figure 6-5, which depicts an interferometer with a non-linear medium in one of the arms. The input signal at  $\lambda_1$  is the control signal of the non-linear medium and the CW signal at  $\lambda_2$  is the local probe wavelength. Considering that the non-linear medium response to a control signal is a phase modulation of the probe signal:

$$E_{probe,out} = E_{probe,in} \cdot \exp[j \cdot (\alpha \cdot P_{ctl} + \Phi)], \quad (6-1)$$

Where  $E_{probe,out}$  and  $E_{probe,in}$  are the electrical fields of the input and output optical signals,  $P_{ctl}$  is the power of the control (information) signal, and  $\alpha$  and  $\Phi$  are constants. The interferometer output power is then given by:

$$P_{probe,out} = \frac{P_{probe,in}}{4} \cdot (1 + \cos(\alpha \cdot P_{ctl} + \Phi)), \quad (6-2)$$

Where  $P_{probe,in}$  is the CW signal input power, and  $P_{probe,out}$  is the output power at the CW signal wavelength.

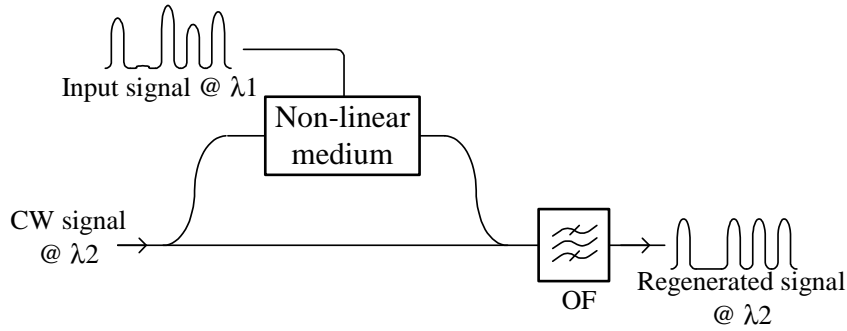


Figure 6-5: optical 2R regeneration via interferometric schemes

Figure 6-6 exemplifies the static power transfer function of an interferometric gate, similar to Figure 6-5, when parameters  $\alpha$  and  $\Phi$  are optimized to obtain optimum regeneration characteristics. It can be verified that such transfer function reshapes the input signal, since for logical '0' and '1' the input power can vary by  $\pm 10\%$  around the nominal logical level and the output power only varies by  $\pm 2.5\%$ . Cascading two of these interferometric gates results in further improvements of the 2R characteristics: with two gates the input signal power at each logical level can vary by  $\pm 15\%$  with only  $\pm 2.5\%$  of output power variation.

With the aforementioned simple example, we have illustrated the potential for signal regeneration of interferometric structures with phase modulation in one of the arms. MZI-SOA are excellent candidates to implement non-linear gates with regeneration, and have been experimentally demonstrated in scheme with single MZI-SOA [215] and with cascade MZI-SOA [216], where 4000 km of optical transmission are enabled. MZI-SOA can also be used in pass-through configurations, provided that the parameters of the system are optimized, as demonstrated in [217]. A similar operation principle has been presented with GC-SOA [218].

Optical regeneration has been achieved in other SOA-based schemes, such as a method which employs SOA birefringence in pass-through and wavelength conversion

schemes [219], [220]; the use of cross-gain compression (XGC), where the SOA is fed with the signal to regenerate and a second signal which is the logical complement of the input signal [221]; a pass-through method where a saturable absorber, which regenerates the logical ‘0’, and a SOA, which regenerates the logical ‘1’, are cascaded [222]; a scheme where a highly non-linear fiber and a SOA with a delay interferometer enable transmission of 40 Gb/s signals over 1.000.000 km[223]; and a scheme where parameters of FWM in SOA are optimized to enable reshaping [224].

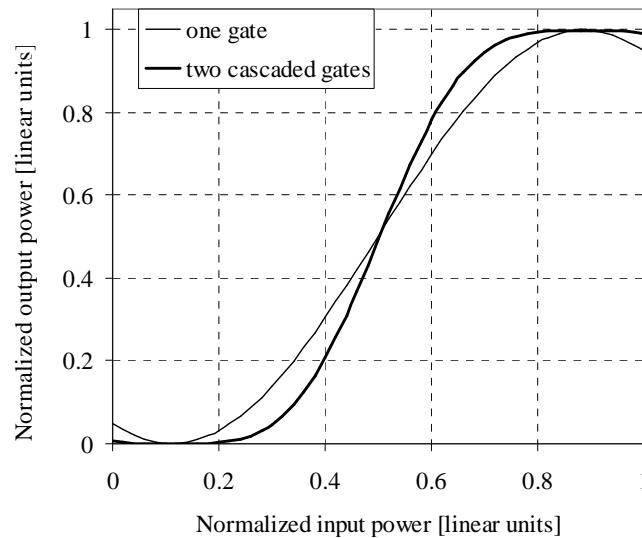


Figure 6-6: Characteristic of non-linear gate similar to Figure 6-5, when the signal passes by one gate, and by two cascaded gates.

## 6.2.2 Clock recovery

Clock recovery is a key element to achieve 3R as it performs the *re-timing* functionality. One approach for the clock-recovery subsystem is to use electro-optical schemes; the other is to use an all-optical scheme. All-optical 3R can employ electro-optical schemes to achieve clock-recovery without losing the *all-optical* label [207]. All-optical 3R allows some electronic processing, provided that such processing is narrow-band, as is clock recovery. Several electro-optical schemes have been proposed with operation at high bit rates [225], [226]. However, electro-optical schemes have higher power consumption and costs; therefore, all-optical clock recovery is generally preferred.

One simple method to recover the clock signal is presented in Figure 6-7 [227]. The clock-recovery consists in a first stage, where the information signal is wavelength

converted in an MZI-SOA. The converted signal is filtered with a Fabry-Perot filter (FPF), which extracts the clock components of the converted signal. The power of the pulses at the FPF filter output fades exponentially for consecutive '0' of the input signal. Therefore, a second MZI-SOA wavelength conversion stage is used to equalize the power of the optical pulses. The first wavelength conversion stage could potentially be omitted; however, since the FPF central frequency must be tuned with the input wavelength, wavelength tracking would be required.

The clock recovery scheme based on MZM-SOA with FPF has great potential due to its simplicity, and very fast clock acquisition time, which is very useful in packet or burst applications, for example.

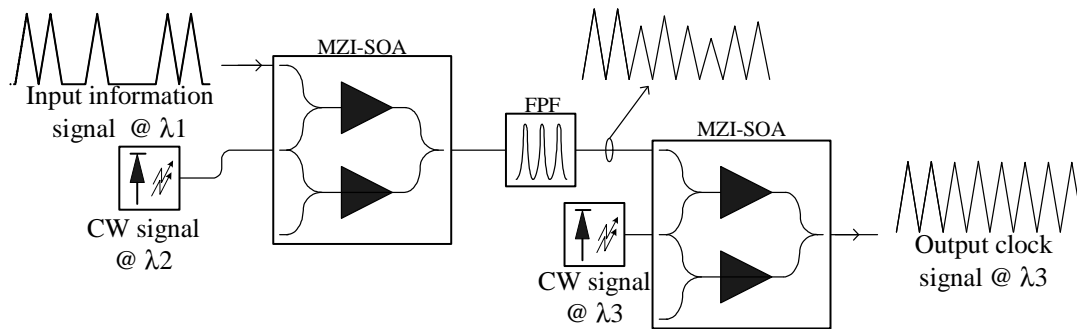


Figure 6-7: Clock recovery circuit using MZI-SOA and Fabry-Perot filter.

Other all-optical SOA based schemes to extract optical clock include: the use of a FPF and a single SOA [228]; a technique where a phase-comparator based on FWM in SOA is employed [229]; in [230], SPM in SOA and a detuned optical filter are used to convert a NRZ signal into a pseudo-RZ signal and allow clock recovery of input NRZ signals; and in [231], a pulse format independent principle is presented, based on a SOA and a FPF to extract and enhance the clock components of an input signal, and a self-pulsating DFB laser to recover the clock signal.

### 6.3 2R Regeneration of OCDMA with MZI-SOA

Wavelength and time division multiplexing (WDM, TDM) have been found as interesting solutions for the increasing demand for bandwidth in metro and wide-area networks. However, for local area networks (LAN), optical code division multiple access

(OCDMA) is a very attractive and common solution due to its promising features [232]. These include [233]:

- Full asynchronous transmission;
- Low latency access;
- Soft capacity on demand;
- Protocol transparency;
- Simplified network control;
- Increased flexibility of QoS control;
- Robust information security.

Several different OCDMA implementations have been proposed; these can be roughly classified according to the operation principle as incoherent and coherent OCDMA [233]. The *coherent* OCDMA technique has received growing attention due to the overall superior performance over incoherent OCDMA and improvements on compact and reliable encoder/decoders, such as spatial light phase modulator (SLPM), super-structured fiber Bragg grating (SSFBG), and planar lightwave circuit (PLC) [234]-[236]. PLC encoder and decoder are illustrated in Figure 6-8. An optical pulse arrives to the converter and is split in  $N$  replicas, each delayed by a multiple of  $\tau$ . The replicas suffer a phase shift,  $\theta_i$ , of 0 or  $\pi$  and are coupled again. At the encoder output, a pulse train is present with positive or negative amplitude. The decoder performs the inverse function: a strong optical pulse is transmitted when the code of the encoder and decoder match.

The maximum number of active users in an OCDMA network is usually limited by multiple access interference (MAI) noise [234]. MAI is illustrated in Figure 6-9: three signals are fed to an OCDMA decoder: a signal which matches the decoder sequence, a signal which is orthogonal with the decoded sequence, and a third signal which is not matched nor orthogonal. In the first case a strong pulse is retrieved at the decoded output. For the orthogonal signal, no MAI is created since no pulse is generated after the decoder. However, for the last signal a low power optical pulse is generated, which creates MAI.

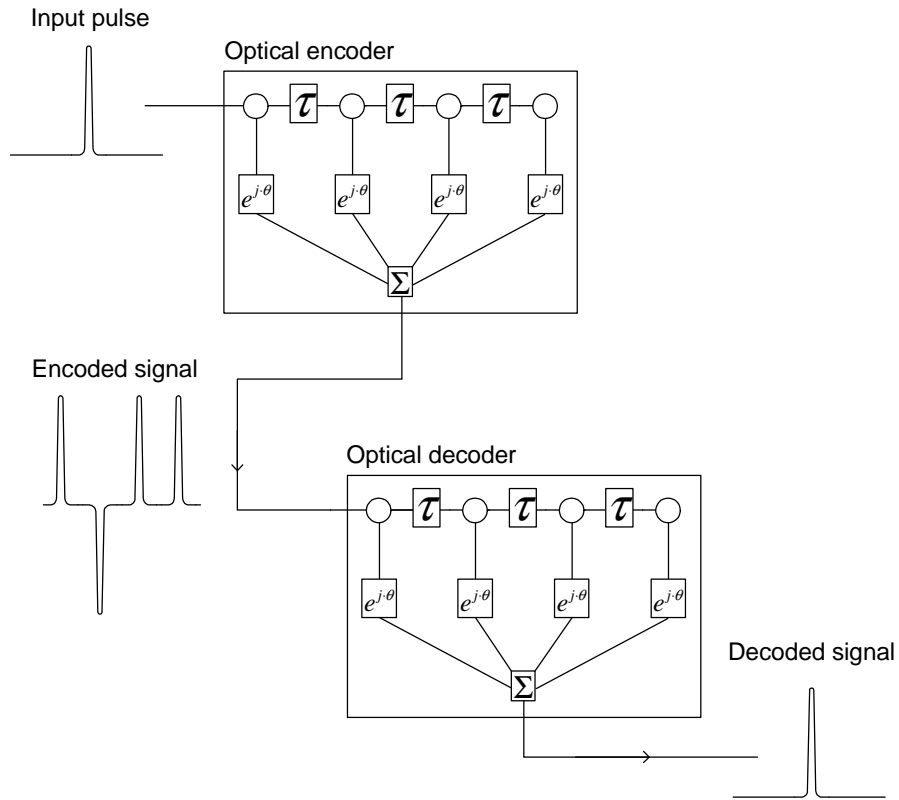


Figure 6-8: Illustration of PLC based OCDMA encoder and decoder.

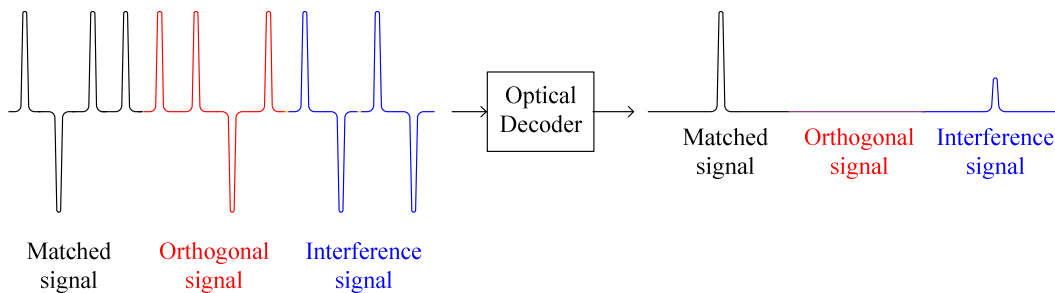


Figure 6-9: Illustration of generation of multiple access interference noise.

Several techniques have been employed to suppress MAI noise, such as optical thresholding based on supercontinuum generation in dispersion flattened fiber (DFF), second harmonic generation (SHG) in periodically poled lithium niobate (PPLN), and non-linear effect in highly non-linear fiber (HNLFF) [234].

In this section the use of cross phase modulation (XPM) non-linear effect in MZI-SOA is used for the first time to suppress MAI noise. As referred above, MZI-SOA based regeneration is in principle similar to MZI-SOA based wavelength conversion, which has

been studied in section 3.5. Regeneration in MZI-SOA has several advantages when compared to other techniques: compactness and ability for integration; regeneration of both '1' and '0' logical levels; reduced input power levels required; high conversion efficiency; allows the use of differential mode to overcome SOA speed limitations; and wide bandwidth operation.

The utilized device is the MZI-SOA cased at Instituto de Telecomunicações in a stand alone box, as described in Appendix II.

### 6.3.1 Experimental Setup and Operation Principle

The setup employed in the experimental tests is depicted in Figure 6-10. A 10 Gb/s 2 ps pulse train at 1545.0 nm, generated by a mode locked laser diode (MLLD) is modulated using a Mach-Zehnder modulator with a  $2^{21} - 1$  PRBS data sequence at 10 Gb/s. The modulated signal is split, and fed to two 8 chip planar lightwave circuit OCDMA encoders, with codes 1 and 2. Polarization controllers are employed to align the polarization of the signal and the encoder. The resultant encoded signals,  $E_1$  and  $E_2$ , are combined and decoded at the *decoder*, which is matched to code 1. On the other hand, code 2 is neither matched nor orthogonal with code 1; hence,  $E_2$  will produce MAI noise on the signal to recover at the *decoder* output. As the pulses are generated by the same source, 200 m of standard single mode fiber (SSMF) are used prior to *encoder2* to avoid coherent distortion when  $E_1$  and  $E_2$  are added; *delay1* is tuned to align the pulses of  $E_1$  and  $E_2$ , maximizing the interference at the *decoder* output; and *VOA1* controls the power of the MAI noise.

After the *decoder* module, the decoded signal with MAI noise is wavelength converted to the *probe* signal wavelength, 1535.0 nm, and simultaneously regenerated in the MZI-SOA. *VOA2* and *delay2* control the differential mode operation. The SOA are operated with currents of 400 mA; the power of the *Probe*, and data signal at arms *A* and *D* are 10, 2.9, and -2.7 dBm, respectively; the delay between arms *A* and *D* (delay 2) is 23 ps. The input and regenerated signals are detected and characterized through bit error rate measurements. The -3 dB bandwidths of the optical filters and photodiode are approximately 105 GHz and 10 GHz, respectively.

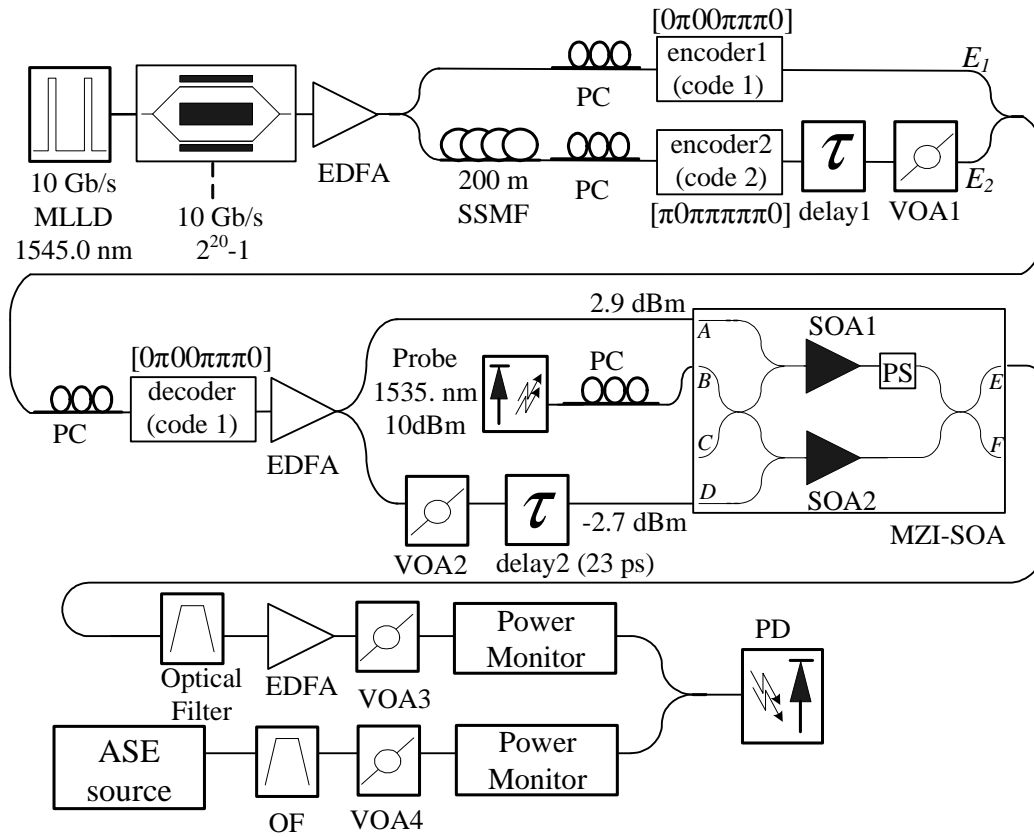


Figure 6-10: Experimental setup for OCDMA MAI 2R regeneration.

The MZI-SOA has been experimentally characterized at 10 Gb/s in section 3.5. Of particular interest is the static characterization of Figure 3-37. From the results, voltage of 7.5 V enables optimum destructive interference; therefore, PS is set at 7.5 V. Moreover, Figure 3-37 also demonstrates that such scheme is fit for 2R regeneration, as over 25 dB of output extinction ratio are obtained with compression at the ‘1’ and ‘0’ logical levels.

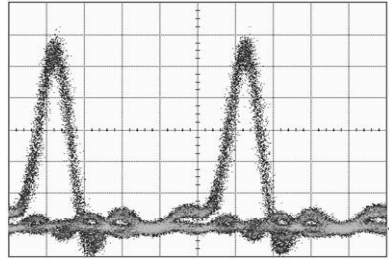
### 6.3.2 Experimental OCDMA Regeneration Results

The OCDMA regenerator is characterized in three situations regarding distortion: in the first, the output of *encoder2* is blocked (without MAI); in the second, the interference signal power at the *decoder* input is -4.7 dBm (MAI case 1), and in the third the interference power is -3.4 dBm (MAI case 2). In all cases the power of the signal coded by *encoder1* at the *decoder* input is 0.5 dBm.

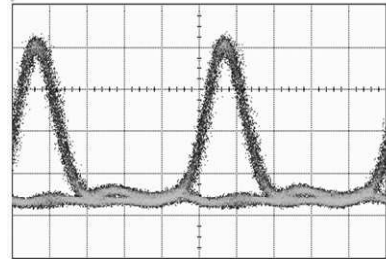
In Figure 6-11 the eye diagrams of the decoded signals after the OCDMA decoder and after the MZI-SOA based regenerator are presented for the three MAI cases. In



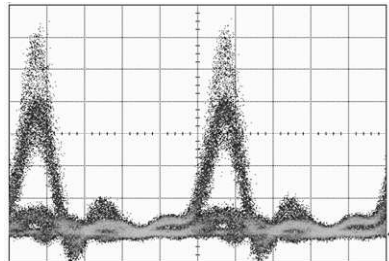
absence of MAI, an undistorted signal is retrieved after the regenerator; however pulse broadening is noticed. When MAI noise is considered, the signals at the regenerator input present very high eye diagram distortion in both logical levels. The regenerator achieves compression of the two logical levels with particular improvements in the '1's, retrieving opened eye diagrams in both cases of MAI noise.



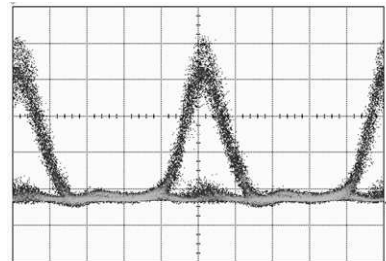
a) Dec. signal without MAI;



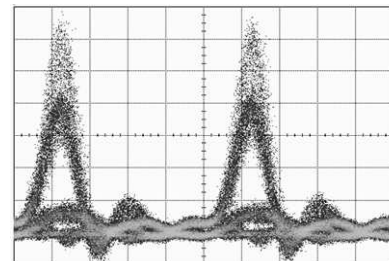
b) Signal after the reg. without MAI;



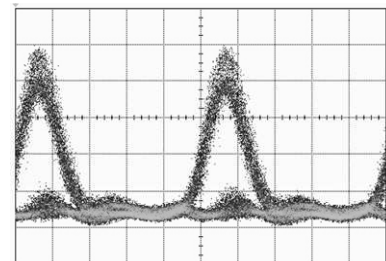
c) Dec. signal with MAI, case 1;



d) Signal after reg. with MAI, case 1;



e) Dec. signal with MAI, case 2;



f) Signal after reg. with MAI, case 2.

Figure 6-11: Eye diagrams (obtained from an oscilloscope with 30 GHz bandwidth) after the ODCMA decoded (dec.) and after the MZI-SOA regenerator (reg.). (20 ps / div)

In Figure 6-12 the BER is presented for the signals after the decoder and the 2R regenerator. For the BER measurements, the OSNR is adjusted at the PD input by changing the ASE noise power (with *VOA4*), while keeping the signal power constant at -1 dBm to ensure linear operation of the PD.

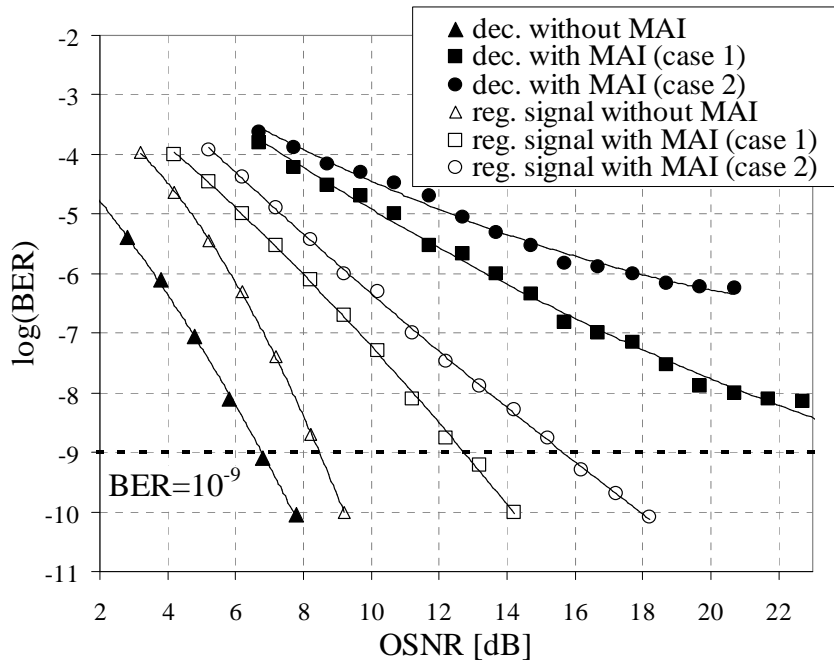


Figure 6-12: BER as a function of the OSNR, of the signals after decoder (dec.) and regenerator (reg.).

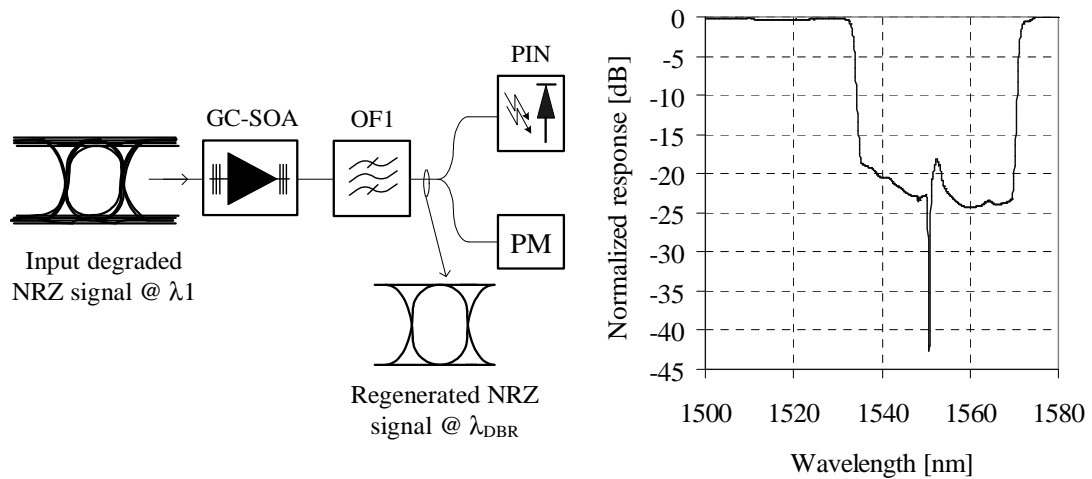
When the signal without MAI crosses the regenerator, 1.8 dB OSNR penalty is verified for a BER of  $10^{-9}$ , comparing to the signal at the decoder output; this penalty is mostly due to the increase of the pulse width after the regenerator, as the regenerated signal does not present distortion or patterning effects (Figure 6-11 a) and b)). In the two cases where MAI is added, clear BER floors are observed above BER of  $5 \cdot 10^{-9}$  (case 1), and of  $5 \cdot 10^{-7}$  (case 2); these are due to the severe eye opening verified in Figure 6-11 c) and e). After the regenerator, both BER floors are eliminated: BER floor-free curves down to  $10^{-10}$  are retrieved.

These results demonstrate the ability of MZI-SOA based regenerators to enhance performance of OCDMA networks by suppression MAI noise. Moreover, improved results are expected if the single MZI-SOA, which is biased to regenerate the two logical levels, is replaced by a cascade of two MZI-SOA; in this configuration the operation point of one MZI-SOA is optimized to regenerate the '0' level, while the other is optimized to regenerate the '1' level [216].

## 6.4 2R Regenerator using a GC-SOA

### 6.4.1 Operation principle

A GC-SOA is a regular SOA with a distributed Bragg reflector (DBR), which create an internal DBR laser, as discussed in 2.8. The gain-clamping mechanism consists in a self-adaptation of the internal laser power, when the power of a signal being amplified varies. As a consequence, the gain of the cavity maintains constant. However, when the power of the input signal increases above a threshold, the carrier density falls below lasing threshold and the gain can no longer be maintained constant and the laser is disabled. Since the gratings have low reflectivity, a considerable power of the laser leaks to the SOA output.



a) Experimental setup;

b) Optical filter (OF1) transfer function.

Figure 6-13: Setup to test the GC-SOA regenerator at 2.5 Gb/s.

Figure 6-13 a) presents the setup of the regenerator based on GC-SOA. A degraded 2.5 Gb/s NRZ signal at  $\lambda_1 = 1550.8$  nm is fed to a GC-SOA. At the GC-SOA output the laser generated by the GC-SOA is encoded with the inverse of the input signal logical information. As will be detailed below, this signal presents notorious re-shaping in relation to input. After the GC-SOA the input wavelength ( $\lambda_1$ ) is removed by an optical filter. The GC-SOA internal laser is centered at 1509.5 nm, which is outside the C-band; therefore, in our facilities there are no means to amplify this signal (regular C-band EDFA do not have

gain at 1509.5 nm); moreover, there is no available filter centered at 1509.5 nm, which can isolate  $\lambda_{\text{DBR}}$ . To remove the input wavelength a cascade of a C-band rejection filter and a fiber Bragg grating (FBG) with a notch at 1509.8 nm are cascaded. The resultant transfer function is depicted in Figure 6-13 b): although not ideal this filter allows removing the input wavelength and also part of the ASE generated by the GC-SOA. The employed photodiode has a 3dB bandwidth of 4.5 GHz.

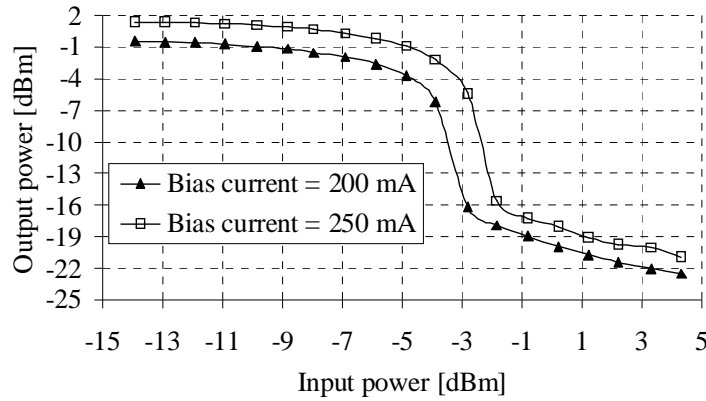


Figure 6-14: Power of the laser generated inside the GC-SOA as a function of the input signal power under static conditions.

In Figure 6-14 the power of the laser generated by the GC-SOA is presented as a function of the power of a signal being amplified, when the input signal is replaced by a continuous wave (CW) signal at the same wavelength (static measurements). This power is measured at the power monitor (PM) module of Figure 6-13. When the power of the input signal is at a low level, small variations are observed in the power of the generated laser. Under such conditions the internal cavity gain is kept constant. Above a threshold power, of about -3 dBm and -4.5 dBm for currents of 250 mA and 200 mA, respectively, the power of the internal laser drops considerably: for a 2 dB variation of the input power, the output power decreases 12 dB. For higher power levels of the input signal, a variation in the laser power of about 0.6 dB per each dB of input power variation is observed. Note that under such conditions, the laser is completely extinct; however, due to our measurement setup, significant amount of ASE is being fed to the power monitor. From observation in an optical spectrum analyzer, the internal laser is extinct for input powers above -2.8 dBm and -1.4 dBm, for currents of 200 mA and 250 mA. Which demonstrates also regeneration of the input logical '1' level. From this static characterization is evident that simple modulation of the GC-SOA internal laser presents reshaping characteristics. This scheme

could be cascaded with a second stage of wavelength conversion in SOA to allow flexible output wavelength. However, our available SOA devices do not have considerable gain at 1509.5 nm.

With the available GC-SOA the maximum operation bit rate is 2.5 Gb/s, for higher bit rates the laser dynamics cause signal distortion, since the bit rate becomes close to the laser maximum modulation rate. Therefore, this work is a proof-of-concept: for real applications at higher bit rates, an improved device would have to be custom designed.

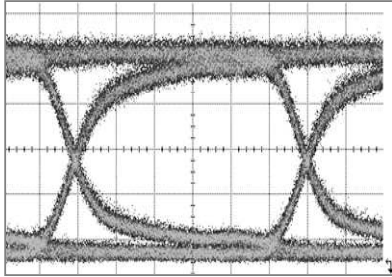
### 6.4.2 Experimental regeneration of a distorted signal

In this section a preliminary characterization of the proposed regenerator is presented. A full characterization is not possible since the GC-SOA internal laser wavelength is 1509.5 nm, and in our facilities there is not experimental equipment appropriate for such wavelength.

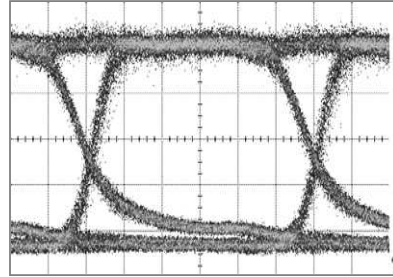
To test the capacities of regeneration of the proposed scheme, a 2.5 Gb/s signal was distorted and then fed to the regenerator under test. Figure 6-15 presents the eye diagrams of the signal before and after the regenerator under three scenarios:

- Figure 6-15 a) presents the back-to-back signal without any distortion and with 10.8 dB of ER. The signal after the 2R (Figure 6-15 a)) is perfectly undistorted, and presents  $Q$ -factor improvement in relation to input. The ER is penalized in relation to input, but this penalization is also due ASE-ASE beating since substantial amount of ASE is fed to the photo-detector. Note that oscillation relaxations are not visible in the GC-SOA modulated laser, because of the low bandwidth of the photo detector;
- Figure 6-15 c) presents a back-to-back signal with reduced ER (3 dB). After the regenerator (Figure 6-15 d)) the signal still presents undistorted eye diagram, but the ER is increased to 8 dB;
- Figure 6-15 e) presents an optical signal which was obtained after cross-gain modulation in a SOA device with recovery times around 800 ps. This

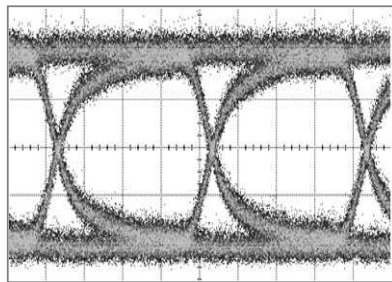
signal presents high degradation when compared to the back to back signal both in  $Q$ -factor and in ER (7.5 dB). After the regenerator (Figure 6-15 f)), this signal is fully recovered: the output signal eye diagram presents no distortion and the ER is increased to 10.2 dB.



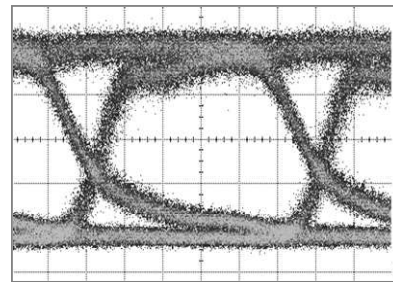
a) Back-to-back signal,  
 $Q$ -factor = 9.9, ER = 10.8 dB;



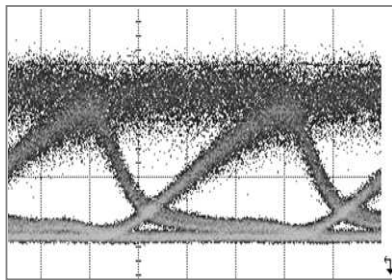
b) Back-to-back signal after 2R,  
 $Q$ -factor = 13.1, ER = 10.1 dB;



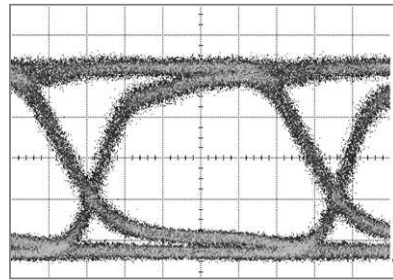
c) Back-to-back signal,  
 $Q$ -factor = 8.7, ER = 3.0 dB;



d) Signal of c after 2R,  $Q$ -factor = 7.5,  
ER = 8.0 dB.



e) Distorted signal via XGM in slow  
SOA,  $Q$ -factor = 4.4, ER = 7.5 dB;



f) Signal of e) after 2R,  
 $Q$ -factor = 10.8, ER = 10.2 dB;

Figure 6-15: Eye diagrams of distorted and regenerated signals at 2.5 Gb/s.

To quantify the regeneration capacities of our setup, the BER of the detected signal is measured for variable added optical noise. Since a noise source at 1510 nm is not available (and commercial C band EDFA have little ASE at this wavelength) out of the band ASE noise is added, which produces mainly ASE-ASE beating noise. For such

purpose ASE with 25 nm of bandwidth and centered at 1530.0 nm was added to the signals under test.

The dependence of the BER with the relation between the power of the signal and the added optical noise (OSNR) is depicted in Figure 6-16 for the signals of Figure 6-15. The back to back signal with ER of 10.8 dB presents approximately the same BER as the same signal after the 2R, demonstrating that the 2R does not cause signal degradation to the back-to-back signal. The back-to-back signal with 3 dB of ER presents an OSNR penalty of around 4 dB in relation to the back-to-back signal with 10.8 dB of ER. However, after the 2R the OSNR penalty is reduced to only 1 dB. For the signal distorted by a slow wavelength converter, a BER floor at approximately  $10^{-9}$  is verified. When this signal is regenerated, a behavior very similar to the back-to-back case is verified and no BER floor is observed for BER down to  $10^{-11}$ . Such results demonstrate that the proposed converter is able to recover from low input ER and from severe eye distortion.

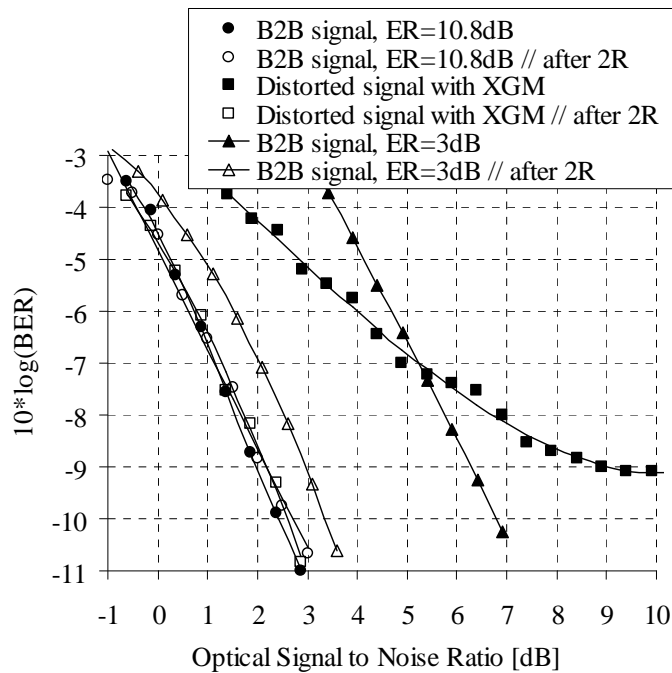


Figure 6-16: Dependence of the BER with the OSNR Only out-of-band ASE noise is considered. B2B – back to back signal.

Ideally, a 2R regenerator should be resilient to variations of the input signal ER. The ER and  $Q$ -factor of the regenerated signal are presented in Figure 6-17 as a function of the input signal ER. It can be verified that for the range of input ER tested, the converter

always enhances the ER; furthermore, for input ER higher than 5 dB, the output ER is always above 10 dB. The regenerated signal  $Q$ -factor is also superior to input for input ER higher than 5 dB.

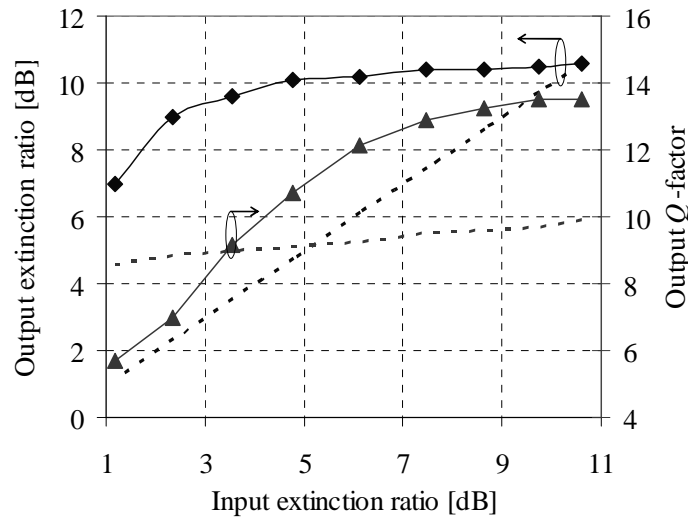


Figure 6-17: Regenerated signal ER and  $Q$ -factor as a function of the input signal ER (dashed lines represent input ER and  $Q$ -factor).

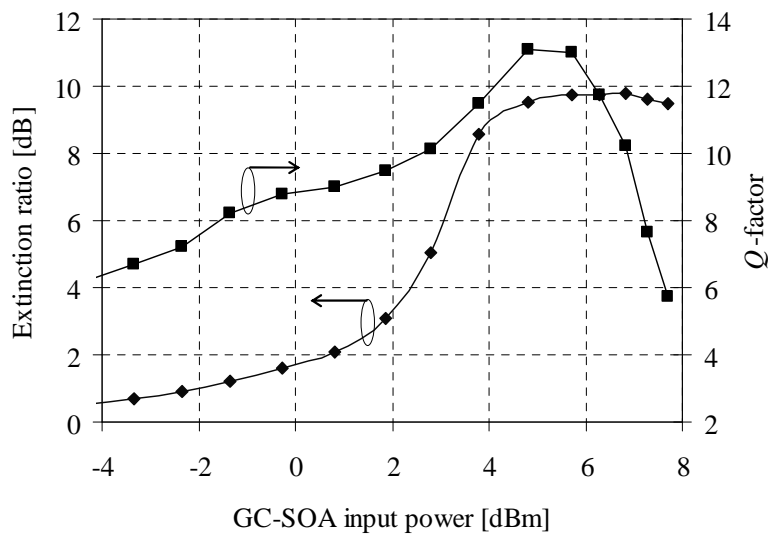


Figure 6-18: Characterization of the regenerator performance for different input optical power.

To assess the constraints of the regenerator in terms of input power, the  $Q$ -factor and the ER of the regenerated signal are plotted as a function of the input power in Figure 6-18; the input signal ER is 10.8 dB. According to the curve, the optimum operation range of input signal power is between 4 and 6 dBm. For lower power, the input laser does not



shutdown; therefore the output signal ER is not optimum. For higher input powers are severe distortions at the laser wavelength due to cross gain modulation.

In this section we have demonstrated optical 2R regeneration of a 2.5 Gb/s signal using GC-SOA. We have demonstrated  $Q$ -factor, ER and required OSNR improvements over wide range of input ER and when the input signal presents amplitude degradation. Further studies of such method would require a faster GC-SOA device which is designed so that the internal laser wavelength is in the C-band.

## 6.5 Summary

This chapter is devoted to all-optical regeneration schemes; from which we focused in optical reshaping, which is essential to 2R regeneration. Two 2R schemes have been experimentally exploited.

A cross-phase modulation (XPM) based regenerator using Mach-Zehnder interferometer with semiconductor optical amplifiers (MZI-SOA) was experimentally tested for multiple access interference (MAI) noise suppression of coherent OCDMA signals. To the authors knowledge this is the first application of MZI-SOA regenerators in OCDMA networks for 2R purposes. Experimental results demonstrate clear noise compression of both logical levels in an 8 chip, 10 Gb/s OCDMA signal. After regeneration, signals with BER floors at  $5 \cdot 10^{-7}$  and  $5 \cdot 10^{-9}$  retrieve BER free curves and improved receiver sensitivities. These results demonstrate promising application of SOA based technology for OCDMA networks.

A novel 2R regeneration method was proposed. In this method the gain-clamped SOA (GC-SOA) internal laser is modulated via XGM by an input distorted signal. Due to the non-linear power transfer from input to the laser wavelength, optical regeneration is obtained. The converter was experimentally characterized for an input 2.5 Gb/s signal, demonstrating true regeneration characteristics and extinction ratio improvements. With the GC-SOA device considered the maximum bit rate was 2.5 Gb/s, above which the bit rate becomes close to the laser maximum modulation rate and distortion occurs; therefore,

for real network applications at high bit rates faster GC-SOA devices would have to be designed.

# Chapter 7

## Conclusions

### *7.1 Summary and conclusions*

This thesis has investigated all-optical signal processing based on semiconductor optical amplifier (SOA) non-linear effects. The main objective was to develop key functionalities which can replace optic-electro-optic (OEO) conversions in photonic cross-connects (PXC). The work developed is mostly based in cross-gain modulation (XGM) and cross-phase modulation (XPM) non-linear effects.

Chapter 2 has presented a high level overview of the history of SOA development, the principle behind amplification in semiconductor materials, and techniques employed for the design of SOA. Different SOA-based solutions for various network applications have been presented, like multi-electrode SOA (ME-SOA), gain-clamped SOA (GC-SOA) or reflective SOA (R-SOA). SOA non-linear gain and phase dynamics are the base of all applications studied throughout this work and have been detailed in this chapter, together with the simulation model employed in the simulation tests throughout the rest of the thesis. Finally, the state-of-the-art regarding several applications of SOA has been presented.

The work developed in the context of this thesis can be divided in four groups:

- Wavelength conversion,
- Format modulation conversion,

- Pulse format conversion,
- Regeneration.

**Wavelength conversion** is the most basic all-optical functionality and has been studied in chapter 3, which has presented an overview of the main SOA-based schemes. Such schemes can be divided based on the main non-linear effect involved: cross-phase modulation, cross-gain modulation, cross-polarization rotation, and four-wave mixing. From these, cross-phase modulation and cross-gain modulation have been chosen to perform the required functionalities, due to their superior characteristics: robustness to variations in the input signal like polarization, power and wavelength; simple processing schemes are allowed, which operate at ultra-high bit rates; and these two non-linear effects can be used together to achieve versatile configurations.

Cross-gain modulation wavelength conversion is likely the simplest non-linear functionality in SOA; however, it is usually limited to operation over few GHz by slow inter-band processes. We have proposed and studied XGM bandwidth enhancement by detuned optical filtering, which converts phase modulation to intensity modulation. By means of simulations, we have verified that a simple first order Gaussian shaped filter allows promising results: the *slow* SOA device, which was designed to operate at 2.5 Gb/s, has allowed conversion up to 40 Gb/s. Moreover, at 10 Gb/s higher output extinction ratio (12 dB) has been enabled. The simulation results have been supported by experimental tests.

We proposed and experimentally demonstrated the use of a detuned optical filter to convert the cross-phase modulation of the probe signal at the output of a GC-SOA in intensity modulation. This method is commonly used to convert return-to-zero signals in common SOA; however, it is expected that when combined with GC-SOA, the carrier recovery time is enhanced and the conversion efficiency is increased. Operation has been demonstrated at 2.5 Gb/s and at 10 Gb/s with improved extinction ratio and  $Q$ -factor, when compared to the input.

Phase-to-intensity conversion in a Mach-Zehnder interferometer with SOA (MZI-SOA) was characterized at 10 Gb/s with standard and differential mode operation with an

optical signal to noise ratio (OSNR) penalty below 1 dB when compared to input. The impact of several converter parameters, such as polarization, optical power, and relative delay between arms, has been experimentally evaluated. A similar scheme was exploited to allow 40 Gb/s multi-wavelength conversion. Conversion of a single input to four output signals has been reported for the first time. We have verified that the main source of distortion is four-wave mixing between the several channels and the data signal; nevertheless, open and undistorted eye diagrams have been obtained with high extinction ratio.

All-optical **modulation format conversion** is a key functionality to allow transparent inter-connection of networks which utilize different modulation formats. In chapter 4 we have proposed two novel all-optical modulation format conversion schemes with operation up to 40 Gb/s.

First, conversion from optical double sideband (oDSB) to optical vestigial sideband (oVSB) has been proposed. To the author's knowledge this is the first all-optical method for such format conversion which does not require optical filtering or Hilbert transform filters. The converter is based on the frequency chirp generated by the self-phase modulation non-linearity in a SOA. To avoid distortion caused by self-gain modulation, a continuous wave signal is amplified simultaneously in the SOA with the information signal. Experimental and simulation characterization at 10 Gb/s retrieved high sideband suppression ratio (15 dB) and improved  $Q$ -factor when compared to input. Enhanced tolerance to chromatic dispersion accumulation, characteristic of oVSB signals, was obtained: transmission over 160 km of standard single mode fiber (SSMF) was enabled without any dispersion compensation, doubling the reach of oDSB. With simple electrical dispersion compensation (EDC) simulation results demonstrated transmission beyond 400 km. The converter is resilient to input power variations, provided that the continuous signal power is adapted accordingly: operation over 13 dB power variation has been reported without degradation of the output signal  $Q$ -factor or sideband suppression ratio. Similarly, high tolerance to variations of the input signal extinction ratio and wavelength has been experimentally verified. Promising results at 40 Gb/s have also been obtained with transmission over 10 km of SSMF without dispersion compensation (the reach of oDSB was 6 km), and over 14 km with EDC realized by an adjustable transversal filter.

Since this work was developed in an industrial environment, stand alone prototypes were developed for 10 Gb/s and 40 Gb/s operation; these are described in detail in appendix IV.

The second modulation format converter is an all-optical scheme to convert on-off-keying signals to the carrier suppressed format. This simple scheme is based on a mix of cross-phase and cross-gain modulations in SOA, when the input signal is amplified together with a high power optical clock signal. The proposed converter is able to convert both non-return-to-zero and return-to-zero input signals. The conversion scheme has been compared to the common transmitter through simulation tests, with similar resilience to tight optical filtering, and enhanced tolerance to linear and non-linear transmission. Single- and multi-channel operation up to four channels has been experimentally assessed at 40 Gb/s. Carrier suppressed spectrum and clear RZ eye diagrams have been obtained at the converter output for all input configurations.

**Pulse format conversion** is required at the interfaces between ultra-fast transport networks, which preferably use return-to-zero pulse format, and lower bit rate access networks, which are likely to employ non-return-to-zero pulse. Chapter 5 reports two schemes to convert return-to-zero signals to the non-return-to-zero format.

In the first method a wavelength converted signal by cross-gain modulation in SOA is filtered with a detuned optical filter. The ideal optical filter shape has been investigated, and approximated experimentally cascading two filters. Converted NRZ signals have been obtained at 10 Gb/s and at 40 Gb/s with high extinction ratios and undistorted eye patterns. At 40 Gb/s, the converter input pulses had 3 ps full-width-at-half-maximum, demonstrating the potential for support of 160 Gb/s networks. Similar tolerance to chromatic dispersion as a conventional NRZ signal was obtained, demonstrating that the transmission capabilities are not prejudiced by the SOA induced chirp. By means of simulation we have demonstrated 40 Gb/s operation with the *slow* SOA device, since the optical filter also enhances the SOA recovery times.

A second method, based on the modulation of a gain-clamped SOA internal laser and on a second cross-gain modulation stage in a common SOA, has been proposed. The operation of the converter was experimentally demonstrated at 10 Gb/s. The resulting signal is non-inverted and features eventual wavelength conversion. Robustness to the

input pulse width was verified, since 5 ps and 40 ps pulses were successfully converted to the NRZ format. The main drawback of this scheme is the limited output extinction ratio, which can be improved if the cross-gain modulation wavelength conversion stage is replaced by cross-phase modulation.

All-optical **Optical regeneration** is one of the most desired functionalities for an all-optical network, since transmission and processing of optical signals generally introduce jitter and amplitude distortion.

We have demonstrated for the first time suppression of multiple-access interference (MAI) noise of coherent optical code division multiple access (OCDMA) signals using a 2R scheme based in MZI-SOA. The converter demonstrated recovery of severely distorted eye diagrams in an 8 chip 10 Gb/s OCDMA signal and eliminated error floors. It is expected that further improvements are possible if two cascaded MZI-SOA stages are employed.

We have proposed a simple 2R regeneration scheme where the internal laser of a gain-clamped SOA is modulated with the input distorted signal. Due to the clamping mechanism, the modulated laser signal presents reshaping when compared to input. The scheme operation has been demonstrated at 2.5 Gb/s with true regeneration characteristics and extinction ratio improvements. To allow regeneration of higher bit rate signal, gain-clamped SOA with faster lasing are required.

## 7.2 *Directions for future work*

It is commonly stated that “*the only constant in technology is change*”. As a consequence the work developed in the scope of this thesis is far from being a closed-topic. Subsequent investigations are recommended:

- In the past years, gain-clamped SOA have generally been forgotten by research in all-optical processing. We have demonstrated the potential of such devices by proposing several functionalities. Simulation models, fit for high bit rates, are required for gain-clamped SOA. The simulation model

detailed in this thesis (appropriate for common SOA) could be developed to consider the dynamics of the internal laser. Such model could be used to perform more accurate comparisons between regular SOA and GC-SOA. To allow operation over higher bit rates, modern design techniques, which allow operation at bit rates around 40 Gb/s, should be applied to the development of GC-SOA with faster lasing mechanisms.

- Wavelength converters are usually limited to one of the four main non-linear effects. In this work we exploited intensively scenarios where cross-phase and cross-gain are combined. One step ahead would be to combine cross-polarization rotation with cross-phase modulation in MZI-SOA. We expect that such schemes allow MZI-SOA to operate as true switches with high extinction ratio in both output ports.
- The topic of modulation formats is one of the most evolving areas in research and development. Currently, it is foreseen that signals with only intensity modulation will have reduced application in real optical networks beyond 40 Gb/s. The study of wavelength conversion should then be extended to allow conversion of the most modern modulation formats (such as differential phase shift keying (DPSK), and coherent polarization-multiplexed quadrature phase shift keying (CP-QPSK). Similarly, format converters which are able to cope with complex modulation formats must be developed to enable the all-optical networks of the future.
- In [45] we proposed a scheme based on multi-electrode SOA, which is expected to allow optical intensity modulation in SOA without phase distortion and phase modulation without intensity distortion. However, further simulations and experimental tests are required, to assess the full potential of this method.



# References

- [1] International Telecommunication Union, *Measuring the Information Society – The ICT Development index*. 2009. Available online at [http://www.itu.int/ITU-T/ict/publications/idi/2009/material/IDI2009\\_w5.pdf](http://www.itu.int/ITU-T/ict/publications/idi/2009/material/IDI2009_w5.pdf).
- [2] Information retrieved from several portuguese internet service providers, e.g. [www.meo.pt](http://www.meo.pt)
- [3] G. Agrawal, *Fiber-optical Communications systems*, Wiley, third edition, 2002.
- [4] E. Desurvire, D. Bayart, B. Desthieux, and S. Bigo, *Erbium-Doped Fiber Amplifiers, Device and System Developments*, Wiley-Interscience, 2002.
- [5] J. Cai, Y. Cai, I. Sun., R. Davidson, D. Foursa, A. Lucero, O. Sinkin, W. Patterson, A. Pilipetskii, G. Mohs, N. Bergano, Neal “112×112 Gb/s transmission over 9,360 km with channel spacing set to the baud rate (360% spectral efficiency)”, in *proc. ECOC 2010*, Torino, Sep. 2010
- [6] Information retrieved on-line at <http://www.nokiasiemensnetworks.com/news-events/press-room/press-releases/nsn-takes-industry-s-first-concrete-step-toward-400g-optical-n>
- [7] Information retrieved on-line at [http://telecomengine.com/newsglobe/article.asp?HH\\_ID=AR\\_5533](http://telecomengine.com/newsglobe/article.asp?HH_ID=AR_5533)
- [8] G. Zarris, E. Hugues-Salas, N. Gonzalez, R. Weerasuriya, F. Parmigiani, D. Hillerkuss, P. Vorreau, M. Spyropoulou, S. Ibrahim, A. Ellis, R. Morais, P. Monteiro, P. Petropoulos, D. Richardson, I. Tomkos, J. Leuthold, D. Simeonidou, “Field Experiments With a Grooming Switch for OTDM Meshed Networking,” *J. Lightwave Technol.*, vol. 28, no. 4, pp. 316–327, Feb. 2010.
- [9] R. Morais, R. Meleiro, P. Monteiro, and P. Marques, “OTDM-to-WDM conversion based on wavelength conversion and time gating in a single optical gate,” in *proc OFC 2008*, San Diego, CA, Paper OTuD5, 2008.
- [10] X. Liu, S. Chandrasekhar, P. Winzer, S. Draving, J. Evangelista, N. Hoffman, B. Zhu, D. Peckham, “Single coherent detection of a 606-Gb/s CO-OFDM signal with 32-QAM subcarrier modulation using 4×80-Gsamples/s ADCs,” in *proc. ECOC 2010*, Torino, Sep. 2010
- [11] G. Agrawal, *Nonlinear Fiber Optics*, Academic Press, 2001.
- [12] L. Occhi, Semiconductor optical amplifiers made of ridge waveguide bulk InGaAsP/InP: Experimental characterization and numerical modeling of gain, phase, and noise (Ph.D. thesis, ETHZ No. 14788), Zurich, 2001.

- [13] C. Schubert, *Interferometric gates for all-optical signal processing (Ph.D. thesis, TUEB No. D 83)*, Berlin, 2004.
- [14] M. Galili, H. Mulvad, L. Oxenlowe, H. Ji, A. Clausen, and P. Jeppesen, "640 Gbit/s wavelength conversion," in *proc. OFC 2008, San Diego*, Feb. 2008, paper OTuD4.
- [15] C. Schubert, C. Schmidt, S. Ferber, R. Ludwig, and H. G. Weber, "Error-free all optical add-drop multiplexing at 160 Gbit/s," *Electron. Lett.*, vol. 39, no. 14, pp. 1074–1076, July 2003.
- [16] J. Simon, "GaInAsP semiconductor laser amplifiers for single-mode fiber communications," *J. Lightwave Technol.*, vol. 5, no. 9, pp. 1286–1295, Sept. 1987.
- [17] C. E. Zah, C. Caneau, F. K. Shokoohi, S. G. Menocal, F. Favire, L. A. Reith, and T. P. Lee, "1.3  $\mu\text{m}$  GaInAsP near-travelling-wave laser amplifiers made by combination of angled facets and antireflection coatings," *Electron. Lett.*, vol. 24, no. 20, pp. 1275–1276, Sept. 1988.
- [18] M. J. O'Mahony, "Semiconductor laser optical amplifiers for use in future fiber systems," *J. Lightwave Technol.*, vol. 6, no. 4, pp. 531–544, Apr. 1988.
- [19] J. Crowe, and W. Ahearn, "9B8--Semiconductor laser amplifier," *IEEE J. Quantum Electron.*, vol. 2, no. 8, pp. 283–289, Aug. 1966.
- [20] I. Hayashi, M. Panish, and P. Foy, "A low-threshold room-temperature injection laser," *IEEE J. Quantum Electron.*, vol. 5, no. 4, pp. 211–212, Apr. 1969.
- [21] Y. Yamamoto, "Characteristics of AlGaAs Fabry-Perot cavity type laser amplifiers," *J. Lightwave Technol.*, vol. 16, no. 10, pp. 1047–1052, Oct. 1980.
- [22] S. Yamamoto, K. Mochizuki, H. Wakabayashi, and Y. Iwamoto, "Long-haul high-speed optical communication systems using a semiconductor laser amplifier," *J. Lightwave Technol.*, vol. 6, no. 10, pp. 1554–1558, Oct. 1988.
- [23] C. Holtmann, P.-A. Besse, T. Brenner, and H. Melchior, "Polarization independent bulk active region semiconductor optical amplifiers for 1.3  $\mu\text{m}$  wavelengths," *IEEE Photon. Technol. Lett.*, vol. 8, no. 3, pp. 343–345, Mar. 1996.
- [24] T. Akiyama, H. Kuwatsuka, T. Simoyama, Y. Nakata, K. Mukai, M. Sugawara, O. Wada, and H. Ishikawa, "Nonlinear gain dynamics in quantum-dot optical amplifiers and its application to optical communication devices," *IEEE J. Quantum Electron.*, vol. 37, no. 8, pp. 1059–1065, Aug. 2001.
- [25] P. P. Iannone and N. J. Frigo, "Applications of SOAs in optical access and metro networks," in *OAA '01, Stresa*, July 2001, Paper OTuC1.
- [26] J. Prat, C. Arellano, V. Polo, and C. Bock, "Optical network unit based on a bidirectional reflective semiconductor optical amplifier for fiber-to-the-home networks," *IEEE Photon. Technol. Lett.*, vol. 17, no. 1, pp. 250–252, Jan. 2005.
- [27] G. Maxwell, B. Manning, M. Nield, M. Hariow, C. Ford, M. Clements, S. Lucas, P. Townley, R. McDougall, S. Oliver, R. Cecil, L. Johnston, A. Poustie, R. Webb, I. Lealman, L. Rivers, J. King, S. Perrin, R. Moore, I. Reid, and D. Scrase, "Very low coupling loss, hybrid-integrated all-optical regenerator with passive assembly," in *ECOC '02, Copenhagen*, Sept. 2002, paper PD3.5.

- [28] A. Poustie, "SOA-based All-optical Processing," in *Proc. Optical Fiber Communication Conference (OFC)*, p. OWF1, March 2007.
- [29] J. Baliga, R. Ayre, K. Hinton, W. Sorin, and R. Tucker, "Energy Consumption in Optical IP Networks," *J. Lightwave Technol.*, vol. 27, pp. 2391–2403, July, 2009.
- [30] D. J. Blumenthal and M. Usami, "Optical signal processing: The roadmap towards high-speed optical packet/burst switching," in *Proc. European Conference on Optical Communication (ECOC)*, p. 5.6.1, 2009.
- [31] G. Agrawal, and N. Dutta, *Semiconductor lasers*, Van Nostrand Reinhold, 1993.
- [32] M. Connelly, *Semiconductor optical amplifiers*, Kluwer Academic Publishers, 2002.
- [33] C. Vassallo, "Polarisation-independent antireflection coatings for semiconductor optical amplifiers," *Electron. Lett.*, vol. 24, no. 1, pp. 61–62, Jan. 1988.
- [34] A. Vukovic, P. Sewell, T. M. Benson, and P.C. Kendall, "Advances in facet design for buried lasers and amplifiers," *IEEE J. Select. Topics Quantum Electron.*, vol. 6, no. 1, pp.175–84, Jan.-Feb. 2000.
- [35] I. Cha, M. Kitamura, H. Honmou, and I. Mito, "1.5 $\mu$ m band travelling-wave semiconductor optical amplifiers with window facet structure," *Electron. Lett.*, vol. 25, no. 18, pp. 1241–1242, Aug. 1989.
- [36] N. Yasuoka, K. Kawaguchi, H. Ebe, T. Akiyama, M. Ekawa, K. Morito, M. Sugawara, and Y. Arakawa, "1.55- $\mu$ m polarization-insensitive quantum dot semiconductor optical amplifier," in *ECOC 2008, Brussels*, paper Th1C1.
- [37] T. Akiyama, M. Sugawara, and Y. Arakawa, "Quantum-Dot Semiconductor Optical Amplifiers," *Proc. IEEE*, vol. 95, no. 9, pp. 1757–1766, Sept. 2007.
- [38] J. Segarra, V. Sales, and J. Prat, "An All-Optical Access-Metro Interface for Hybrid WDM/TDM PON Based on OBS," *J. Lightwave Technol.*, vol. 25, no. 4, pp. 1002–1016, April 2007.
- [39] Jeung-Mo Kang, and Sang-Kook Han, "A novel hybrid WDM/SCM-PON sharing wavelength for up- and down-link using reflective semiconductor optical amplifier," *IEEE Photon. Technol. Lett.*, vol. 18, no.3, pp. 502–504, Feb. 2006.
- [40] M.C.R. Medeiros, I. Darwazeh, L. Moura, A. Teixeira, P.S. Andre, M. Lima, and J. Ferreira da Rocha, "DAWN – Dynamically allocated wavelength WDM network demonstrator", in *ICTON '01, Cracow*, July 2001, paper We.A.4.
- [41] R. N. Nogueira, A. L. J. Teixeira, P. S. André, J. F. da Rocha, and J. L. Pinto, "Wide tuning range self-generated orthogonal pumps source based on a reflective semiconductor optical amplifier," in *CLEO/Europe '03, Munich*, June 2003, pp. 545.
- [42] T. Rampone, Hong-Wu Li, and A. Sharaiha, "Semiconductor optical amplifier used as an in-line detector with the signal DC-component conservation," *J. Lightwave Technol.*, vol. 16, no. 7, pp. 1295–1301, July 1998.
- [43] G. Giuliani, P. Cinguino, and V. Seano, "Multifunctional characteristics of 1.5- $\mu$ m two-section amplifier-modulator-detector SOA," *IEEE Photon. Technol. Lett.*, vol. 8, no. 3, pp. 367–369, Mar. 1996.

- [44] T. N. Nielsen, N. Storkfelt, U. Gliese, B. Mikkelsen, T. Durhuus, K. E. Stubkjaer, B. Fernier, F. Leblond, and A. Accard, "Cancellation of inherent AM in semiconductor optical amplifier phase modulators," *Electron. Lett.*, vol. 28, no. 3, pp. 235–236, Jan. 1992.
- [45] T. Silveira, A. Ferreira, "Amplitude modulator with phase distortion cancellation, and amplitude and phase modulator with amplitude and phase distortion cancellation based on semiconductor optical amplifier technology," Nokia Siemens Networks, patent pending.
- [46] J. M. Wiesenfeld, "Gain dynamics and associated nonlinearities in semiconductor optical amplifiers," *J. of High Speed Electronics and Systems*, vol. 7, no. 1, pp. 179–222, Mar. 1996.
- [47] G. Toptchiyski, S. Kindt, K. Petermann, E. Hilliger, S. Diez, and H. G. Weber, "Time-domain Modeling of Semiconductor Optical Amplifiers for OTDM Applications," *J. Lightwave Technol.*, vol. 17, no. 12, pp. 2577–2583, Dec. 1999.
- [48] G. P. Agrawal, and N. A. Olsson, "Self-phase modulation and spectral broadening of optical pulses in semiconductor laser amplifiers," *IEEE J. Quantum Electron.*, vol. 25, no. 11, pp. 2297–2306, Nov. 1989.
- [49] A. Mecozzi and J. Mørk, "Saturation effects in nondegenerate four-wave mixing between short optical pulses in semiconductor laser amplifiers," *IEEE J. Select. Topics Quantum Electron.*, vol. 3, no. 5, pp. 1190–1207, Oct. 1997.
- [50] G. Toptchiyski, S. Kindt, K. Petermann, E. Hilliger, S. Diez, and H. G. Weber, "Time-domain modeling of semiconductor optical amplifiers for OTDM applications," *J. Lightwave Technol.*, vol. 17, no. 12, pp. 2577–2583, Dec. 1999.
- [51] T. Durhuus, B. Mikkelsen, and K. E. Stubkjaer, "Detailed dynamic model for semiconductor optical amplifiers and their crosstalk and intermodulation distortion," *J. Lightwave Technol.*, vol. 10, no. 8, pp. 1056–1065, Aug. 1992.
- [52] R. P. Schrieck, *Ultrafast Dynamics in InGaAsP/InP Optical Amplifiers and Mode Locked Laser Diodes (Ph.D. thesis, ETHZ No. 14337)*, Zurich, 2001.
- [53] D. C. Hutchings, M. Sheik-Bahae, D. J. Hagan, and E. W. van Stryland, "Kramers-Krönig relations in nonlinear optics," *Opt. Quantum Electron.*, vol. 24, no. 1, pp. 1–30, Jan. 1992.
- [54] C. Henry, "Theory of the linewidth of semiconductor lasers," *IEEE J. Quantum Electron.*, vol. 18, no. 2, pp. 259–264, Feb 1982.
- [55] M. Osinski and J. Buus, "Linewidth broadening factor in semiconductor lasers--An overview," *IEEE J. Quantum Electron.*, vol. 23, no. 1, pp. 9–29, Jan. 1987.
- [56] A. Reale, A. Di Carlo, and P. Lugli, "Gain dynamics in traveling-wave semiconductor optical amplifiers," *IEEE J. Select. Topics Quantum Electron.*, vol. 7, no. 2, pp. 293–299, March/April 2001.
- [57] SOA catalog from Thorlabs, retrived online in 01-12-2010 at [http://www.thorlabs.de/NewGroupPage9.cfm?ObjectGroup\\_ID=3901](http://www.thorlabs.de/NewGroupPage9.cfm?ObjectGroup_ID=3901).
- [58] J. H. E. Cartwright and O. Piro, "The Dynamics of Runge-Kutta Methods," *Int. J. Bifurcations Chaos*, no. 2, pp. 427–449, 1992.

- [59] B. Bauer, F. Henry, R. Schimpe, "Gain stabilization of a semiconductor optical amplifier by distributed feedback," *IEEE Photon. Technol. Lett.*, vol. 6, no. 2, pp. 182–185, Feb. 1994.
- [60] J. Simon, et al., "Travelling wave semiconductor optical amplifier with reduced nonlinear distortions," *Electron. Lett.*, vol. 30, no. 1, pp. 49–50, Jan. 1994.
- [61] D. Francis, et al., "A single-chip linear optical amplifier," in *OFC 2001, Anaheim*, March 2001, vol. 4, pp. PD13-1– PD13-3.
- [62] V. Mutalik, G. Hoven, L. Tiemeijer, "Analog performance of 1310-nm gain-clamped semiconductor optical amplifiers," in *OFC 1997, Dallas*, March 1997, pp. 266–267.
- [63] R. Manning and D. Davies, "Three-wavelength device for all-optical signal processing", *Opt. Lett.*, vol 19, pp 889–891, June 1994.
- [64] T. Silveira, A. Teixeira, G. Beleffi, D. Forin, P. Monteiro, H. Furukawa, and N. Wada, "All-optical conversion from RZ to NRZ using gain-clamped SOA," *IEEE Photon. Technol. Lett.*, vol. 19, no. 6, pp. 357–359, Mar. 2007.
- [65] G. Morthier, et al., "Experimental demonstration of an all-optical 2R regenerator with adjustable decision threshold and "true" regeneration characteristics," *IEEE Photon. Technol. Lett.*, vol. 12, no. 11, pp. 1516–1518, Nov. 2000.
- [66] J. Tae et al., "Low input power wavelength converter using gain-clamped semiconductor optical amplifier," *Electron. Lett.*, vol. 38, no. 18, pp. 1045–1047, Aug. 2002.
- [67] F. Dorgeuiele, et al., "1.28 Tbit/s throughput 8×8 optical switch based on arrays of gain-clamped semiconductor optical amplifier gates," in *OFC 2000, Baltimore*, March 2000, vol. 4, pp. 221– 223.
- [68] Z. Bakonyi, "10 Gbit/s RZ transmission over 5000 km with gain-clamped semiconductor optical amplifiers and saturable absorbers," *Electron. Lett.*, vol. 36, no. 21, pp. 1790– 1791, Oct. 2000.
- [69] H. Lee, et al., "Demonstration of 16 x 10 Gb/s WDM transmissions over 5 x 80 km using gain-clamped semiconductor optical amplifiers in combination with distributed Raman fiber amplifiers as inline amplifiers under dynamic add-drop situations," *IEEE Photon. Technol. Lett.*, vol. 15, no. 11, pp. 1621–1623, Nov. 2003.
- [70] L. Spiekman, D. Piehler, P. Iannone, K. Reichmann and Han-Hyub Lee, "Semiconductor Optical Amplifiers for FTTx," in *ICTON 2007, Rome*, vol. 2, pp. 48–50, July 2007.
- [71] D. Nasset, D.B. Payne, R. Davey, and T. Gilfedder, "Demonstration of Enhanced Reach and Split of a GPON System Using Semiconductor Optical Amplifiers," in *ECOC 2006, Cannes*, 2006, paper Mo4.5.1.
- [72] A. Shipulin, G. Onishchukov, P. Riedel, D. Michaelis, U. Peschel, and F. Lederer, "10 Gbit/s signal transmission over 550 km in standard fibre at 1300 nm using semiconductor optical amplifiers," *Electron. Lett.*, vol. 33, no. 6, pp. 507–509, Mar. 1997.

- [73] Li Zhihong, Yi Dong, Mo Jinyu, Wang Yixin, and Lu Chao, "1050-km WDM transmission of 8\*10.709 Gb/s DPSK signal using cascaded in-line semiconductor optical amplifier," *Photon. Technol. Lett.*, vol. 16, no. 7, pp. 1760–1762, July 2004.
- [74] Yi Dong, Mo Jinyu, Li Zhihong, Li Zhaohui, Wang Yixin, and Lu Chao, "WDM transmission of 16\*10.709 Gb/s over 640-km SSMF using cascaded semiconductor optical amplifiers and DPSK modulation format," *Photon. Technol. Lett.*, vol. 16, no. 10, pp. 2359–2361, Oct. 2004.
- [75] T. Silveira, A. Teixeira, A. Ferreira, P. Monteiro, and P. Andre, "Influence of SOA based devices on optical single sideband signals," in *ICTON 2005, Barcelona*, vol. 2, pp. 234–237, July 2005.
- [76] M. Feuer, J. Wiesenfeld, J. Perino, C. Burrus, G. Raybon, S. Shunk, and N. Dutta, "Single-port laser-amplifier modulators for local access," *IEEE Photon. Technol. Lett.*, vol. 8, no. 9, pp. 1175–1177, Sept. 1996.
- [77] G. Berrettini, A. Simi, A. Malacarne, A. Bogoni, and L. Poti, "Ultrafast integrable and reconfigurable XNOR, AND, NOR, and NOT photonic logic gate," *IEEE Photon. Technol. Lett.*, vol. 18, no. 8, pp. 917–919, April 2006.
- [78] P. Li, D. Huang, X. Zhang, "SOA-Based Ultrafast Multifunctional All-Optical Logic Gates With PolSK Modulated Signals," *IEEE J. Quantum Electron.*, vol. 45, no. 12, pp. 1542–1550, Dec 2009.
- [79] J. Kim, J. Kang, T. Kim, S. Han, "All-optical multiple logic gates with XOR, NOR, OR, and NAND functions using parallel SOA-MZI structures: theory and experiment," *J. Lightwave Technol.*, vol. 24, no. 9, pp. 3392–3399, Sep. 2006.
- [80] J. Leuthold, J. Eckner, C. Holtmann, R. Hess, and H. Melchior, "All-optical 2× 2 switches with 20 dB extinction ratios," *IEE Electronics Letters*, vol. 32, no. 24, pp. 2235–2236, 1996.
- [81] S. Nakamura, Y. Ueno, and K. Tajima, "Error-free all-optical demultiplexing at 336Gb/s with a hybrid-integrated Symmetric-Mach-Zehnder switch," in *OFC '02, Anaheim*, March 2002, paper FD3.
- [82] M. Heid, S. L. Jansen, S. Spalter, E. Meissner, W. Vogt, and H. Melchior, "160-Gbit/s demultiplexing to base rates of 10 and 40 Gbit/s with a monolithically integrated SOA-Mach-Zehnder interferometer," in *ECOC 2002, Copenhagen*, Sept. 2002, paper All-optical Demultiplexing 8.4.3.
- [83] C. Schubert, C. Schmidt, C. Börner, E. Dietrich, S. Ferber, R. Ludwig, and H. G. Weber, "A gain-transparent Ultrafast-Nonlinear Interferometer (GT-UNI) in a 160 Gb/s optical sampling system," in *OAA '02, Vancouver*, July 2002, paper OTuD5.
- [84] P. J. Winzer and R.-J. Essiambre, "Advanced Modulation Formats for High-Capacity Optical Transport Networks," *J. Lightwave Technol.*, vol. 24, no. 12, pp. 4711–4728, Dec. 2006.
- [85] P. P. Iannone, K. C. Reichman, and N. J. Frigo, "Broadcast digital video delivered over WDM passive optical networks," *IEEE Photon. Technol. Lett.*, vol. 8, no. 7, pp. 930–932, July 1996.

- [86] N. Pleros, C. Bintjas, M. Kalyvas, G. Theophilopoulos, K. Vlachos, and H. Avramopoulos, "50 channel and 50 GHz multiwavelength laser source," in *ECOC '01, Amsterdam*, Oct. 2001, vol. 3, pp. 410–411.
- [87] K. Kikuchi and K. Matsuura, "Transmission of 2-ps optical pulses at 1550 nm over 40-km standard fiber using midspan optical phase conjugation in semiconductor optical amplifiers," *IEEE Photon. Technol. Lett.*, vol. 10, no. 10, pp. 1410–1412, Oct. 1998.
- [88] F. Futami and K. Kikuchi, "Generation of 113 GHz, 1.8 ps optical pulse trains by Fourier synthesis of four-wave mixing signals obtained from semiconductor optical amplifiers," *Opt. Lett.*, vol. 22, no. 24, pp. 1873–1875, Dec. 1997.
- [89] R. Clavero, F. Ramos, J. M. Martinez, and J. Marti, "All-Optical Flip-Flop Based on a Single SOA-MZI," *IEEE Photon. Technol. Lett.*, vol. 17, no. 4, pp. 843–845, April 2005.
- [90] L. Stampoulidis, E. Kehayas, D. Apostolopoulos, P. Bakopoulos, K. Vysokinos, and H. Avramopoulos, "On-the-Fly All-Optical Contention Resolution for NRZ and RZ Data Formats Using Packet Envelope Detection and Integrated Optical Switches," *IEEE Photon. Technol. Lett.*, vol. 19, no. 8, pp. 538–540, 2007.
- [91] E. Varvarigos, "The "packing" and the "scheduling packet" switch architectures for almost all-optical lossless networks," *J. Lightwave Technol.*, vol. 16, no. 10, pp. 1757–1767, 1998.
- [92] T. Durhuus, B. Mikkelsen, C. Joergensen, S. Lykke Danielsen, and K. Stubkjaer, "All-optical wavelength conversion by semiconductor optical amplifiers," *J. Lightwave Technol.*, vol. 14, no. 6, pp. 942–954, June 1996.
- [93] R. Ramaswami and K. Sivarajan, *Optical Networks: A Practical Perspective*, Morgan Kaufmann, 2001.
- [94] C. Siva Ram Murthy and Mohan Gurusamy, *WDM Optical Networks: Concepts, Design and Algorithms*, Prentice Hall, 2001.
- [95] S. Yoo, "Wavelength conversion technologies for WDM network applications," *J. Lightwave Technol.*, vol. 14, no. 6, pp. 955–966, 1996.
- [96] T. Silveira, A. Teixeira, P. Monteiro, and G. Tosi Bellefi, "Cross Gain modulation bandwidth Enhancement in SOA by Means of a Detuned Optical Filter", *Electron. Lett.*, vol. 41, no. 13, pp. 53–54, June 2005.
- [97] T. G. Silveira, A. L. J. Teixeira, and P. N. P. Monteiro, "Increase of the Cross Gain Modulation Bandwidth in Semiconductor Optical Amplifiers", in *SEON 2005, Aveiro*, June 2005.
- [98] T. G. Silveira, A. L. J. Teixeira, and P. N. P. Monteiro. "Filter Optimization for Cross Gain Modulation Bandwidth Enhancement", in *LEOS 2005, Sydney*, pp. 67–68, Oct. 2005.
- [99] T. Silveira, A. Teixeira, A. Ferreira, and P. Monteiro, "Cross Gain Modulation Bandwidth Enhancement", in *2<sup>nd</sup> E-Photon One Summer School, Cesenatico*, Aug. 2005.

- [100] T. Silveira, A. Teixeira, G. Tosi-Beleffi, and P. Monteiro; “All – Optical Wavelength conversion and reshape based on a single Gain Clamped SOA”, in *CLEO 2006, Long Beach*, May 2006, paper JThC99.
- [101] T. Silveira, A. Teixeira, A. Ferreira, S. Stevan Jr, P. Monteiro, G. Tosi Beleffi, and D. Forin, “All-Optical Signal Processing using Gain-Clamped Semiconductor Optical Amplifiers”, in *ICTON 2007, Rome*, vol. 3, pp. 307– 310, July, 2007.
- [102] T. Silveira, A. Teixeira, N. Kataoka, A. Ferreira, N. Wada, and P. Monteiro, “Experimental characterization of Cross Phase Modulation wavelength conversion,” in *CONFTELE 2007, Peniche*, pp. 585–588, May 2007.
- [103] N. Yan, T. Silveira, A. Teixeira, A. Ferreira, E. Tangdionga, P. Monteiro, and A.M.J. Koonen, “40 Gb/s all-optical multi-wavelength conversion via a single SOA-MZI for WDM wavelength multicast,” in *OECC 2007, Yokohama*, pp. 530–531, Jul. 2007.
- [104] N. Yan, T. Silveira, A. Teixeira, A. Ferreira, E. Tangdionga, P. Monteiro, and A. M. J. Koonen, “40 Gbit/s wavelength multicast via SOA-MZI and applications,” *Electron. Lett.*, vol. 43, no. 23, Nov. 2007.
- [105] N. Yan, J. del Val Puente, T. G. Silveira, A. Teixeira, A. Ferreira, E. Tangdionga, P. Monteiro, and A. Koonen, “Simulation and Experimental Characterization of SOA-MZI-Based Multiwavelength Conversion,” *J. Lightwave Technol.*, vol. 27, no.2, pp. 117–127, Jan. 2009.
- [106] C. Joergensen, S. Danielsen, K. Stubkjaer, M. Schilling, K. Daub, P. Doussiere, F. Pommerau, P. Hansen, H. Poulsen, A. Kloch, M. Vaa, B. Mikkelsen, E. Lach, G. Laube, W. Idler, and K. Wunstel, “All-optical wavelength conversion at bit rates above 10 Gb/s using semiconductor optical amplifiers,” *IEEE J. Select. Topics Quantum Electron.*, vol. 3, no. 5, pp. 1168–1180, Oct. 1997.
- [107] Nesset, D.; Kelly, T.; Marcenac, D., “All-optical wavelength conversion using SOA nonlinearities”, *Comm. Magazine*, vol. 36, no. 12, pp. 56 – 61, 1998.
- [108] R. Ramaswami and S. Sivarajan, *Optical Networks*, Morgan Kaufmann, 2002.
- [109] J. Leuthold, D. M. Marom, S. Cabot, J. J. Jaques, R. Ryf, and C. R. Giles, “All-optical wavelength conversion using a pulse reformatting optical filter,” *J. Lightwave Technol.*, vol. 22 , no. 1, pp. 186–192, Jan. 2004.
- [110] J. Leuthold, D. M. Marom, S. Cabot, J. J. Jaques, R. Ryf, and C. R. Giles, “All-optical wavelength conversion using a pulse reformatting optical filter”, *J. Lightwave Technol.*, vol. 22, no. 1, pp. 186–192, Jan. 2004.
- [111] Y. Liu, E. Tangdionga, Z. Li, H. de Waardt, A. Koonen, G. Khoe, S. Xuwen, I. Bennion, and H. Dorren, “Error-Free 320-Gb/s All-Optical Wavelength Conversion Using a Single Semiconductor Optical Amplifier,” *J. Lightwave Technol.*, vol. 25, no. 1, pp. 103–108, Jan. 2007.
- [112] M. L. Nielsen, M. Nord, M. N. Petersen, B. Dagens, A. Labrousse, R. Brenot, B. Martin, S. Squedin, and M. Renaud, “40 Gbit/s standard-mode wavelength conversion in all-active MZI with very fast response,” *Electron. Lett.*, vol. 39, no. 4, pp. 385–386, Feb. 2003.



- [113] B. Mikkelsen, T. Durhuus, C. Joergensen, R. J. S. Pedersen, C. Braagaard, K. E. Stubkjaer, "Polarisation insensitive wavelength conversion of 10 Gbit/s signals with SOAs in a Michelson interferometer," *Electron. Lett.*, vol. 30, no. 3, pp. 260–261, Feb. 1994.
- [114] D. Wolfson, A. Kloch, T. Fjelde, C. Janz, B. Dagens, and M. Renaud, "40-Gb/s all-optical wavelength conversion, regeneration, and demultiplexing in an SOA-based all-active Mach-Zehnder Interferometer," *IEEE Photon Technol. Lett.*, vol. 12, no. 3, pp. 332–334, Mar. 2000.
- [115] Y. Ueno, S. Nakamura, H. Hatakeyama, T. Tamanuki, T. Sasaki, and K. Tajima, "168 Gb/s OTDM wavelength conversion using an SMZ-type all-optical switch," in *ECOC '00, Munich*, vol. 1, pp. 13–14, Sept. 2000.
- [116] J. Sokoloff, P. Prucnal, I. Glesk, and M. Kane, "A terahertz optical asymmetric demultiplexer (TOAD)," *IEEE Photon. Technol. Lett.*, vol. 5, no. 7, pp. 787–790, July 1993.
- [117] M. Eiselt, W. Pieper, and H. Weber, "SLALOM: semiconductor laser amplifier in a loop mirror," *J. Lightwave Technol.*, vol. 13, no. 10, pp. 2099–2112, Oct. 1995.
- [118] S. Diez, R. Ludwig, and H. G. Weber, "Gain-transparent SOA-switch for high-bitrate OTDM add/drop multiplexing," *IEEE Photon. Technol. Lett.*, vol. 11, no. 1, pp. 60–62, Jan. 1999.
- [119] J. Yu, X. Zheng, C. Peucheret, A. Clausen, H. Poulsen, and P. Jeppesen, "All-optical wavelength conversion of short pulses and NRZ signals based on a nonlinear optical loop mirror," *J. Lightwave Technol.*, vol. 18, no. 7, pp. 1007–1017, July 2000.
- [120] S. Nakamura, Y. Ueno, and K. Tajima, "168-Gb/s all-optical wavelength conversion with a symmetric-Mach-Zehnder-type switch," *IEEE Photon. Technol. Lett.*, vol. 13, no. 10, pp. 1091–1093, Oct. 2001.
- [121] G. P. Agrawal, "Population pulsations and nondegenerate four-wave mixing in semiconductor lasers and amplifiers," *J. Opt. Soc. Amer. B*, vol. 5, no. 1, pp. 147–158, 1988.
- [122] J. Zhou, N. Park, J. W. Dawson, K. J. Vahala, M. A. Newkirk, and B. I. Miller, "Terahertz four-wave mixing spectroscopy for study of ultrafast dynamics in a semiconductor optical amplifier," *Appl. Phys. Lett.*, vol. 63, no. 9, pp. 1179–1181, Aug. 1993.
- [123] A. Uskov, J. Mørk, and J. Mark, "Wave mixing in semiconductor laser amplifiers due to carrier heating and spectral-hole burning," *IEEE J. Quantum Electron.*, vol. 30, no. 8, pp. 1769–1781, Aug. 1994.
- [124] A. Mecozzi, S. Scotti, A. D'Ottavi, E. Iannone, and P. Spano, "Fourwave mixing in traveling-wave semiconductor amplifiers," *IEEE J. Quantum Electron.*, vol. 31, no. 4, pp. 689–699, Apr. 1995.
- [125] I. Koltchanov, S. Kindt, K. Petermann, S. Diez, R. Ludwig, R. Schnabel, and H. G. Weber, "Gain dispersion and saturation effects in four-wave mixing in semiconductor laser amplifiers," *IEEE J. Quantum Electron.*, vol. 32, no. 4, pp. 712–720, Apr. 1996.

- [126] A. Uskov, J. Mork, and J. Mark, "Wave mixing in semiconductor laser amplifiers due to carrier heating and spectral-hole burning," *IEEE J. Quantum Electron.*, vol. 30, no. 8, pp. 1769–1781, Aug. 1994.
- [127] C. Politi, D. Klonidis, and M. J. O'Mahony, "Dynamic behavior of wavelength converters based on FWM in SOAs," *IEEE J. Quantum Electron.*, vol. 42, no. 2, pp. 108–125, Feb. 2006.
- [128] S. Arahira and Y. Ogawa, "160-Gb/s all-optical encoding experiments by four-wave mixing in a gain-clamped SOA with assist-light injection," *IEEE Photon. Technol. Lett.*, vol. 16, no. 2, pp. 653–655, Feb. 2004.
- [129] N. Calabretta, Y. Liu, F. Huijskens, M. Hill, H. de Waardt, G. Khoe, and H. Dorren, "Optical signal processing based on self-induced polarization rotation in a semiconductor optical amplifier," *J. Lightwave Technol.*, vol. 22, no. 2, pp. 372–381, Feb. 2004.
- [130] H. J. S. Dorren, D. Lenstra, Yong Liu, M. T. Hill, G.-D. Khoe, "Nonlinear polarization rotation in semiconductor optical amplifiers: theory and application to all-optical flip-flop memories," *IEEE J. Quantum Electron.*, vol. 39, pp. 141–148, Jan. 2003.
- [131] G. Contestabile, N. Calabretta, M. Presi, E. Ciaramella, "Single and multicast wavelength conversion at 40 Gb/s by means of fast nonlinear polarization switching in an SOA," *IEEE Photon. Technol. Lett.*, vol. 17, no. 12, pp. 2652–2654, Dec. 2005.
- [132] N. Storkfelt, B. Mikkelsen, D. S. Olesen, M. Yamaguchi, and K. E. Stubkjaer, "Measurement of carrier lifetime and linewidth enhancement factor for 1.5- $\mu\text{m}$  ridge-waveguide laser amplifier," *IEEE Photon. Technol. Lett.*, vol. 3, no. 7, pp. 632–634, July 1991.
- [133] "1550 Non-Linear SOA product Specification," Kamelian, retrieved online in 2010/10/29 from [http://www.kamelian.com/data/nlsoa\\_ds.pdf](http://www.kamelian.com/data/nlsoa_ds.pdf).
- [134] "Preliminary datasheet, SOA-NL-OEC-1550," CIP Technologies, retrieved online in 2010/10/29 from [http://www.ciphotonics.com/PDFs\\_Sept09/SOA\\_NL\\_OEC\\_1550\\_L.pdf](http://www.ciphotonics.com/PDFs_Sept09/SOA_NL_OEC_1550_L.pdf)
- [135] R. J. Manning, D. A. O. Davies, S. Cotter, and J. K. Lucek, "Enhanced recovery rates in semiconductor laser amplifiers using optical pumping," *Electron. Lett.*, vol. 30, no. 4, pp. 787–788, May 1994.
- [136] L. Casperson and A. Yariv, "The time behavior and spectra of relaxation oscillations in a high-gain laser," *IEEE J. Quantum Electron.*, vol. 8, no. 2, pp. 69–73, Feb. 1972.
- [137] M. Asghari, I. H. White, and R. V. Penty, "Wavelength conversion using semiconductor optical amplifiers," *J. Lightwave Technol.*, vol. 15, no. 7, pp. 1181–1190, July 1997.
- [138] N. Yan, A. Teixeira, T. Silveira, G. M. Tosi Beleffi, F. Curti, D. Forin, F. Dalla Longa, I. Tafur Monroy, P. Monteiro, and T. Koonen, "Theoretical and experimental performance evaluation of all-optical multi-wavelength conversion by four-wave mixing in fiber at 10/20/40 Gb/s for optical layer multicast," *Microwave & Optics Tech. Lett.*, vol. 49, no. 5, pp. 1067–1071, Mar. 2007.

- [139] M. Karasek, J. Kanka, P. Honzatko, J. Vojtech, and J. Radil, "10 Gb/s and 40 Gb/s Multi-wavelength conversion based on nonlinear effects in HNLF," in *ICTON 2006, Nottingham*, June 2006, paper Tu.D1.7.
- [140] L. Xu, N. Chi, K. Yvind, L. J. Christiansen, L. K. Oxenløwe, J. Mørk, and P. Jeppesen, "7 x 40 Gb/s base-rate RZ all-optical broadcasting utilizing an electroabsorption modulator," *Opt. Expr.*, vol. 12, no. 3, pp. 416–420, Feb. 2004.
- [141] G. Contestabile, N. Calabretta, M. Presi, and E. Ciaramella, "Single and multicast wavelength conversion at 40 Gb/s by means of fast nonlinear polarization switching in an SOA," *IEEE Photon. Technol. Lett.*, vol. 17, no. 12, pp. 2652–2654, Dec. 2005.
- [142] G. Contestabile, M. Presi, and E. Ciaramella, "Multiple wavelength conversion for WDM multicasting by FWM in an SOA," *IEEE Photon. Technol. Lett.*, vol. 16, no. 7, pp. 1775–1777, Jul. 2004.
- [143] B. H. L. Lee, R. Mohamad, and K. Dimyati, "Performance of all-optical multicasting via dual-stage XGM in SOA for grid networking," *IEEE Photon. Technol. Lett.*, vol. 18, no. 21, pp. 2215–2217, Nov. 2006.
- [144] M. Karasek, J. Kanka, P. Honzatko, J. Vojtech, and J. Radil, "10 Gb/s and 40 Gb/s multi-wavelength conversion based on nonlinear effects in HNLF," in *ICTON 2006, Nottingham*, Jun. 2006, paper Tu.D1.7.
- [145] J.L. Pleumeekers, J. Leuthold, M. Kauer, P.G. Bernasconi, C.A. Burrus, M. Cappuzzo, E. Chen, L. Gomez, and E. Laskowski, "All-optical wavelength conversion and broadcasting to eight separate channels by a single semiconductor optical amplifier delay interferometer," in *OFC 2002, Anaheim*, Mar. 2002, paper ThDD4.
- [146] H.S. Chung, R. Inohara, K. Nishimura, and M. Usami, "All-optical multiwavelength conversion of 10 Gbit/s NRZ/RZ signals based on SOA-MZI for WDM multicasting," *Electron. Lett.*, vol. 41, no. 7, pp. 432–433, Mar. 2005.
- [147] D. Reading-Picopoulos, F. Wang, Y.J. Chai, R.V. Penty, and I.H. White, "10 Gb/s and 40 Gb/s WDM multi-casting using a hybrid integrated Mach-Zehnder interferometer," in *OFC 2006, Anaheim*, Mar. 2006, paper OFP2.
- [148] N. Yan, H.-D. Jung, I. Tafur Monroy, H. de Waardt, and T. Koonen, "All-optical multi-wavelength conversion with negative power penalty by a commercial SOA-MZI for WDM wavelength multicast," in *OFC 2007, Anaheim*, Mar. 2007, paper JWA36.
- [149] G. Contestabile, N. Calabretta, R. Proietti, and E. Ciaramella, "Doublestage cross-gain modulation in SOAs: an effective technique for WDM multicasting," *IEEE Photon. Technol. Lett.*, vol. 18, no. 1, pp. 181–183, Jan. 2006.
- [150] L. Xu, N. Chi, K. Yvind, L.J. Christiansen, L.K. Oxenløwe, J. Mørk, P. Jeppesen, and J. Hanberg, "8x40 Gb/s RZ all-optical broadcasting utilizing an electroabsorption modulator," in *OFC 2004, Los Angeles*, Feb. 2004, paper MF71.
- [151] G. Contestabile, N. Calabretta, M. Presi, and E. Ciaramella, "Single and multicast wavelength conversion at 40 Gb/s by means of fast nonlinear polarization switching in an SOA," *IEEE Photon. Technol. Lett.*, vol. 17, no. 12, pp. 2652–2654, Dec. 2005.

- [152] T. J. Paul, E. A. Swanson, J. C. Livas, R. S. Bondurant, and R. J. Magliocco, "3 Gbit/s optically preamplified direct detection DPSK receiver with 116 photon/bit sensitivity," *Electron. Lett.*, vol. 29, no. 7, pp. 614–615, April 1993.
- [153] R. A. Griffin, and A. C. Carter, "Optical differential quadrature phase-shift key (oDQPSK) for high capacity optical transmission," in *OFC 2002, Anaheim*, pp. 367–368, Mar. 2002.
- [154] K. Yonenaga, S. Kuwano, S. Norimatsu, and N. Shibata, "Optical duobinary transmission system with no receiver sensitivity degradation," *Electron. Lett.*, vol. 31, no. 4, pp. 302–304, Feb. 1995.
- [155] C. Fludger, T. Duthel, D. van den Borne, C. Schullien, E. Schmidt, T. Wuth, J. Geyer, E. De Man, G. Khoe, H. de Waardt, "Coherent Equalization and POLMUX-RZ-DQPSK for Robust 100-GE Transmission," *J. Lightwave Technol.*, vol. 26, no. 1, pp. 64–72, Jan. 2008.
- [156] Y. Miyamoto, A. Hirano, K. Yonenaga, A. Sano, H. Toba, K. Murata, and O. Mitomi, "320 Gbit/s (8×40 Gbit/s) WDM transmission over 367 km with 120 km repeater spacing using carrier-suppressed return-to-zero format," *Electron. Lett.*, vol. 35, no. 23, pp. 2041–2042, Nov. 1999.
- [157] M. Sieben, J. Conradi, and D. E. Dodds, "Optical single sideband transmission at 10Gbit/s using only electrical dispersion compensation," *J. Lightw. Technol.*, vol. 17, no. 10, pp. 1742–1749, Oct. 1999.
- [158] D. Fonseca, A. Cartaxo, P. Monteiro, R. Sousa, T. Silveira, A. Ferreira, and M. Violas, "40 Gbit/s OSSB-NRZ transmitter for high capacity systems," in *ECOC 2005, Glasgow*, vol. 4, pp. 787–788, Sept. 2005.
- [159] A. P. S. Ferreira, T. G. Silveira, P. M. N. P. Monteiro, and R. F. G. S. Ribeiro, "On the use of return-to-zero formats in electrical dispersion compensated optical single sideband transmission systems," *IET Optoelectron.*, vol. 2, no. 4, pp. 148–157, Aug. 2008.
- [160] R.-J. Essiambre, P.J. Winzer, Xun Qing Wang, W. Lee, C.A. White, and E.C. Burrows, "Electronic predistortion and fiber nonlinearity," *IEEE Photon Technol. Lett.*, vol. 18, no. 17, pp. 1804–806, Sept. 2006.
- [161] R.I. Killey, P.M. Watts, V. Mikhailov, M. Glick, and P. Bayvel, "Electronic dispersion compensation by signal predistortion using digital Processing and a dual-drive Mach-Zehnder Modulator," *IEEE Photon. Technol. Lett.*, vol. 17, no. 3, pp. 714–716, Mar. 2005.
- [162] J. McNicol, M. O'Sullivan, K. Roberts, A. Comeau, D. McGhan, and L. Strawczynski, "Electrical domain compensation of optical dispersion", in *OFC/NOFC 2005, Anaheim*, vol. 4, pp. 269–271, Mar. 2005.
- [163] D. McGhan, C. Laperle, A. Savchenko, Chuandong Li, G. Mak, and M. O'Sullivan, "5120-km RZ-DPSK transmission over G.652 fiber at 10 Gb/s without optical dispersion compensation", *IEEE Photon. Technol. Lett.*, vol. 18, no. 2, pp. 400–402, Jan. 2006.

- [164] T. Silveira, A. Ferreira, P. Monteiro, M. Violas, R. Ribeiro, and F. Rocha, "Electrical dispersion compensation at 10 Gb/s optical single sideband transmission systems," in *LEOS 2004, Puerto Rico*, vol. 2, pp. 759–760, 2004.
- [165] P. M. Watts, V. Mikhailov, M. Glick, P. Bayvel, and R. I. Killey, "Performance of optical single sideband signal transmission systems using adaptive electronic dispersion compensators," in *ECOC 2005, Glasgow*, vol. 2, pp. 259–260, Sept. 2005.
- [166] A. Ferreira, T. Silveira, R. Ribeiro, P. Monteiro, M. Violas, and A. Teixeira, "Mitigation of chromatic dispersion effects on optical single sideband signals by Butterworth filtering," in *ICTON 2005, Barcelona*, vol. 2, pp. 76–79, July 2005.
- [167] P. Winzer and R. Essiambre, "Advanced Modulation Formats for High-Capacity Optical Transport Networks," *J. Lightwave Technol.*, vol. 24, no. 12, pp. 4711–4728, Dec. 2006.
- [168] G. Raybon, "Performance of advanced modulation formats in optically-routed networks," in *OFC 2006, Anaheim*, Mar. 2006, paper OThR1.
- [169] D. Grosz, A. Agarwal, S. Banerjee, D. Maywar, and A. Kung, "All-Raman ultralong-haul single-wideband DWDM transmission systems with OADM capability," *J. Lightw. Technol.*, vol. 22, no. 2, pp. 423–432, Feb. 2004.
- [170] K. Yonenaga and N. Takachio, "Dispersion compensation for homodyne detection systems using a 10 Gb/s optical PSK-VSB signal," *IEEE Photon. Technol. Lett.*, vol. 7, no. 8, pp. 929–931, Aug. 1995.
- [171] K. Tanaka, K. Takano, K. Kondo, and K. Nakagawa, "Improved sideband suppression of optical SSB modulation using all-optical Hilbert transformer," *Electron. Lett.*, vol. 38, no. 3, pp. 133–134, Jan. 2002.
- [172] W. Li, M. Chen, and Y. Dong, "All-optical format conversion from NRZ to CSRZ and between RZ and CSRZ using SOA-based fiber loop mirror," *IEEE Photon. Technol. Lett.*, vol. 16, no. 1, pp. 203–205, Jan. 2004.
- [173] T. Silveira, P. Monteiro, A. Teixeira, "Optical single sideband modulator", Nokia Siemens Networks, European patent application number EP1772860.
- [174] T. Silveira, A. Teixeira, A. Ferreira, and P. Monteiro, "All Optical Vestigial Sideband Generation Using Semiconductor Optical Amplifier," *IEEE Photon. Technol. Lett.*, vol. 18, no. 21, pp. 2212–2214, Nov. 2006.
- [175] T. Silveira, D. Fonseca, A. Ferreira, R. Morais, M. Madureira, A. Teixeira, and P. Monteiro, "40 Gb/s All-Optical Vestigial-Sideband Generation using SOA", in *ECOC 2006, Cannes*, vol. 3, pp. 305–306, Sept. 2006.
- [176] T. Silveira, A. Ferreira, A. Teixeira, and P. Monteiro, "40-Gb/s Multichannel NRZ to CSRZ Format Conversion Using an SOA," *IEEE Photon. Technol. Lett.*, vol. 20, no. 19, pp. 1597–1599, Oct 2008.
- [177] D. Fonseca, A. V. T. Cartaxo, and P. Monteiro, "On the use of electrical precompensation of dispersion in optical single-sideband transmission systems," *IEEE J. Select. Topics Quantum Electron.*, vol. 12, no. 4, pp. 603–614, July-Aug. 2006.
- [178] S. L. Hahn, *Hilbert Transforms in Signal Processing*. Artech House Publishers, 1996.

- [179] D. Fonseca, A. V. T. Cartaxo, and P. Monteiro, "Optical single-sideband transmitter for various electrical signaling formats," *J. Lightwave Technol.*, vol. 24, no. 5, pp. 2059–2069, May 2006.
- [180] D. Fonseca, A. Cartaxo, P. Monteiro, "adaptive optoelectronic filter for improved optical single sideband generation," *IEEE Photon. Technol. Lett.*, vol. 18, no. 2, pp. 415–417, Jan. 2006.
- [181] T. Silveira, A. Ferreira, P. Monteiro, A. Teixeira, and R. Ribeiro, "Fully Integrable Optical Single Sideband Transmitter", in *ICT 2006, Madeira*, May 2006.
- [182] T. Silveira, A. Ferreira, R. Ribeiro, A. Teixeira, P. Monteiro, "Optical vestigial sideband signal producing arrangement for transmitting optical signal, has production arrangement producing one of modulation signals, and with differentiating unit and low pass filter", Nokia Siemens Networks, German patent application number DE102006020166.
- [183] T. Maia, R. Ribeiro, and P. Monteiro; "Impact of the modulation depth on self homodyne optical single sideband systems," in *LEOS '01, San Diego*, vol. 2, pp. 675–676, Nov. 2001.
- [184] U.-S. Lee, H. Jung, and S. Han, "Optical single sideband signal generation using phase modulation of semiconductor optical amplifier", *IEEE Photon. Technol. Lett.*, vol. 16, no. 5, pp. 1373–1375, May 2004.
- [185] F. Liu, X. Zheng, R. Pedersen, and P. Jeppesen, "Interferometric crosstalk suppression using polarization multiplexing technique and an SOA", in *CLEO '00, San Francisco*, pp. 91–92, May 2000.
- [186] T. Silveira, A. Ferreira, P. Monteiro, M. Violas, R. Ribeiro, and F. Rocha, "Electrical dispersion compensation at 10Gb/s optical single sideband transmission systems," in *LEOS '04, Puerto Rico*, pp. 759–760, 2004.
- [187] A. Ferreira, T. Silveira, R. Ribeiro, P. Monteiro, and M. Violas, "10Gbit/s evaluation of electrical dispersion compensation methods for Optical Single Sideband systems," in *CONFTELE 2007, Peniche*, pp. 493–496, May 2007.
- [188] R. E. Massara, *Optimization methods in electronic circuit design*, Longman Scientific & Technical, 1991.
- [189] M. A. M. Madureira, D. Fonseca, A. V. T. Cartaxo, R. L. Aguiar, and P. M. P. Monteiro, "Adjustable Electrical Dispersion Compensation in a 40-Gb/s Optical Single Sideband System," *IEEE Photon. Technol. Lett.*, vol. 18, no. 24, pp. 2689–2691, Dec. 2006.
- [190] D. Norte and A. Willner, "Experimental demonstrations of all-optical conversions between the RZ and NRZ data formats incorporating noninverting wavelength shifting leading to format transparency," *IEEE Photon. Technol. Lett.*, vol. 8, no. 5, pp. 712–714, May 1996.
- [191] X. Yang, A.K. Mishra, R.J. Manning, and R. Giller, "All-optical 40 Gbit/s NRZ to RZ format conversion by nonlinear polarization rotation in SOAs," *Electron. Lett.*, vol. 43, no. 8, pp. 469–471, Apr. 2007.

- [192] J. Dong, X. Zhang, J. Xu, and D. Huang, "40 Gb/s all-optical NRZ to RZ format conversion using single SOA assisted by optical bandpass filter," *Opt. Expr.*, vol. 15, no. 6, pp. 2907–2914, Mar. 2007.
- [193] L. Xu, B. C. Wang, V. Baby, I. Glesk, and P. R. Prucnal, "All-Optical Data Format Conversion Between RZ and NRZ Based on a Mach–Zehnder Interferometric Wavelength Converter," *IEEE Photon. Technol. Lett.*, vol. 15, no. 2, pp. 308–310, Feb. 2003.
- [194] C. H. Kwok and C. Lin, "Simultaneous 4 x 10 Gb/s NRZ-to-RZ Modulation Format Conversion in Nonlinear Optical Loop Mirror With a Photonic Crystal Fiber," *IEEE Photon. Technol. Lett.*, vol. 19, no. 22, pp. 1825–1827, Nov. 2007.
- [195] Chung Ghiu Lee, Yun Jong Kim, Chul Soo Park, Hyuek Jae Lee, and Chang-Soo Park, "Experimental demonstration of 10-gb/s data format conversions between NRZ and RZ using SOA-loop-mirror," *J. Lightwave Technol.*, vol. 23, no. 2, pp. 834–841, Feb. 2005.
- [196] C. W. Chow, C. S. Wong, and H. K. Tsang, "All-optical modulation format conversion and multicasting using injection-locked laser diodes", *J. Lightwave Technol.*, vol. 22, Issue 11, pp.: 2386–2392, Nov. 2004.
- [197] L. Xu, B. C. Wang, V. Baby, I. Glesk, and P. R. Prucnal, "All-optical data format conversion between RZ and NRZ based on a Mach-Zehnder interferometric wavelength converter", *IEEE Photon. Technol. Lett.*, vol 15, no. 2, pp. 308–210, Feb. 2003.
- [198] B. Mikkelsen, M. Vaa, H. N. Poulsen, S. L. Danielsen, C. Joergensen, A. Kloch, P. B. Hansen, K. E. Stubkjaer, K. Wunstel, K. Daub, E. Lach, G. Laube, W. Idler, M. Schilling, and S. Bouchoule, "40 Gbit/s all-optical wavelength converter and RZ-to-NRZ format adapter realised by monolithic integrated active Michelson interferometer", *Electron. Lett.*, vol. 33, no. 2, pp. 133–134, Jan. 1997.
- [199] A. Reale, P. Lugli, and S. Betti, "Format conversion of optical data using four-wave mixing in semiconductor optical amplifiers", *IEEE J. Select. Topics Quantum Electron.*, vol. 7, no. 4, pp. 703–709, July–Sept. 2001.
- [200] T. Silveira, A. Ferreira, D. Fonseca, A. Teixeira, and P. Monteiro, "40 Gb/s all-optical RZ to NRZ format converter based on SOA and detuned filtering," in *ICTON '09, Azores*, June–July 2009.
- [201] T. Silveira, A. Ferreira, L. Costa, A. Teixeira, and Paulo Monteiro, "All Optical Conversion from ODSB to OVSF using a Semiconductor Optical Amplifier", in *proc. SEON 2007, Aveiro*, June 2007
- [202] T. Silveira, A. Teixeira, P. Monteiro, and G. Beleffi, "Cross Gain Modulation Bandwidth Enhancement in Semiconductor Optical Amplifiers by Means of a Detuned Optical Filter", *Electron. Lett.*, vol. 41, no. 23, pp. 761–763, June 2005.
- [203] P. Cho, D. Mahgerefteh, and J. Goldhar, "10 Gb/s RZ to NRZ format conversion using a semiconductor-optical-amplifier/fiber-Bragg-grating wavelength converter," in *ECOC '98, Madrid*, vol. 1, pp. 353–354, 1998.

- [204] D. Fonseca and A. Cartaxo, "On the transition to pseudo-linear regime in dispersion managed systems with NRZ, RZ and duobinary signal formats", *IEE Proc. Part J – Optoelectronics*, vol. 152, no. 3, pp. 181–187, June 2005.
- [205] A. Hodzic, M. Winter, B. Konrad, S. Randel, and K. Petermann, "Optimized filtering for 40-gb/s/ch-based DWDM transmission systems over standard single-mode fiber", *IEEE Photon. Technol. Lett.*, vol. 15, no. 7, pp. 1002–1004, July 2003.
- [206] A. Willner and W. Shieh, "Optimal spectral and power parameters for all-optical wavelength shifting: single stage, fanout, and cascability", *J. Lightwave Technol.*, vol. 13, no. 5, pp. 771–781, May 1995.
- [207] O. Leclerc, B. Lavigne, E. Balmeffre, P. Brindel, L. Pierre, D. Rouvillain, F. Seguin, "Optical regeneration at 40 Gb/s and beyond," *J. Lightwave Technol.*, vol. 21, no. 11, pp.: 2779-2790, Nov. 2003.
- [208] T. Silveira, A. Teixeira, N. Kataoka, A. Ferreira, N. Wada, X. Wang, and P. Monteiro, "MZI-SOA-based 2R Regeneration of OCDMA signals with Multi-Access Interference noise", *Microwave Opt. Technol. Lett.*, vol. 50, no. 6, pp. 1521–1523, June 2008.
- [209] T. G. Silveira, A. Teixeira, N. Kataoka, A. Ferreira, N. Wada, X. Wang, T. Miyazaki, and P. Monteiro, "Coherent Interference 2R Regeneration of Optical CDMA Based on MZI SOA," in *CLEO 2007, Baltimore*, May 2007, paper CMZ2.
- [210] B. Sartorius, "3R All-optical signal regeneration," in *ECOC '01, Amsterdam*, vol. 5, pp. 98–125, Sept./Oct. 2001.
- [211] B. Mikkelsen, S.L. Danielsen, C. Joergensen, R. J. S. Pedersen, H. N. Poulsen, and K. E. Stubkjaer, "All-optical noise reduction capability of interferometric wavelength converters," *Electron. Lett.*, vol. 32, no. 9, pp. 566–567, March 1996.
- [212] Zuqing Zhu, M. Funabashi, Zhong Pan; L. Paraschis, and S. J. B. Yoo, "10 000-hop cascaded in-line all-optical 3R regeneration to achieve 1 250 000-km 10-Gb/s," *IEEE Photon. Technol. Lett.*, vol. 18, no. 5, pp. 718–720, Mar. 2006.
- [213] O. Leclerc, "Optical vs. Electronic in-line Signal Processing in Optical Communication Systems: An exciting challenge for Optical Devices," in *Proc. ECIO'03*, pp.: 55-67, 2003.
- [214] F. Ohman, S. Bischoff, B. Tromborg, J. Mork, "Semiconductor devices for all-optical regeneration," in *proc ICTON 2003*, vol. 2, pp.: 41-46, July 2003.
- [215] D. Wolfson, A. Kloch, T. Fjelde, C. Janz, B. Dagens, M. Renaud, "40-Gb/s all-optical wavelength conversion, regeneration, and demultiplexing in an SOA-based all-active Mach-Zehnder interferometer," *IEEE Photon. Technol. Lett.*, vol. 12, no. 3, pp.: 332-334, Oct 1998.
- [216] B. Lavigne, P. Guerber, P. Brindel, E. Balmeffre, B. Dagens, "Cascade of 100 optical 3R regenerators at 40 Gbit/s based on all-active Mach Zehnder interferometers," in *proc. ECOC 2001*, pp.: 290-291, Amsterdam, Sep. 2001.
- [217] D. Wolfson, T. Fjelde, A. Kloch, C. Janz, A. Coquelin, I. Guillemot, F. Gaborit, F. Poingt, M. Renaud, "Experimental investigation at 10 Gb/s of the noise suppression capabilities in a pass-through configuration in SOA-based interferometric structures," *IEEE Photon. Technol. Lett.*, vol. 12, no. 7, pp.: 837-839, Jul 2000.



- [218] Y. Kim, J. Lee, J. Kang, S. Han, "2R limiter circuit with gain clamped SOA for XGM wavelength converter," *IEE Proc. Part J – Optoelectronics*, vol. 152, no. 1, pp.: 11 – 15, Feb. 2005.
- [219] Mingshan Zhao, J. De Merlier, G. Morthier, R. Baets, "All-optical 2R regeneration based on polarization rotation in a linear optical amplifier," *IEEE Photon. Technol. Lett.*, vol. 15, no. 2, pp.: 305-307, Feb. 2003.
- [220] G. Gavioli, P. Bayvel, "Novel 3R regenerator based on polarization switching in a semiconductor optical amplifier-assisted fiber Sagnac interferometer," *IEEE Photon. Technol. Lett.*, vol. 15, no. 9, pp.: 1261-1263, Sep. 2003.
- [221] G. Contestabile, M. Presi, R. Proietti, E. Ciaramella, "Optical Reshaping of 40-Gb/s NRZ and RZ Signals Without Wavelength Conversion," *IEEE Photon. Technol. Lett.*, vol. 20, no. 13, pp.: 1113-1115, Jul. 2008.
- [222] M. Gay, L. Bramerie, D. Massoubre, A. O'Hare, A. Shen, J. Oudar, J. Simon, "Cascadability assessment of a 2R regenerator based on a saturable absorber and a semiconductor optical amplifier in a path switchable recirculating loop," *IEEE Photon. Technol. Lett.*, vol. 18, no. 11, pp.: 1273-1275, Jun. 2006.
- [223] J. Leuthold, G. Raybon, Y. Su, R. Essiambre, S. Cabot, J. Jaques, M. Kauer, "40 Gbit/s transmission and cascaded all-optical wavelength conversion over 1000000 km," *Electron. Lett.*, vol. 38, no. 16, pp. 890–891, Aug. 2002.
- [224] H. Simos, A. Bogris, D. Syvridis, "Investigation of a 2R all-optical regenerator based on four-wave mixing in a semiconductor optical amplifier," *J. Lightwave Technol.*, vol. 22, no. 2, pp. 595–604, Feb. 2004.
- [225] R. Manning, I. Phillips, A. Ellis, A. Kelly, A. Poustie, K. Blow, "All-optical clock division at 40 GHz using semiconductor optical amplifier based nonlinear interferometer," *Electron. Lett.*, vol. 35, no. 10, pp. 827–829, May 1999.
- [226] C. Boerner, C. Schubert, C. Schmidt, E. Hilliger, V. Marembert, J. Berger, S. Ferber, E. Dietrich, R. Ludwig, H. Weber, B. Schmauss, "160 Gbit/s clock recovery with electro-optical PLL using a bidirectionally operated electroabsorption modulator as phase comparator," in *proc. OFC 2003*, vol. 2, pp. 670-671, March 2003.
- [227] G. Kanellos, N. Pleros, D. Petrantonakis, P. Zakyntinos, H. Avramopoulos, G. Maxwell, and A. Poustie, "40 Gb/s 2R Burst Mode Receiver with a single integrated SOA-MZI switch," *OSA Optics Express*, vol. 15, no. 8, pp. 5043–5049, 2007.
- [228] G. Contestabile, A. D'Errico, M. Presi, and E. Ciaramella, "40-GHz All-Optical Clock Extraction Using a Semiconductor-Assisted Fabry–Pérot Filter," *IEEE Photon. Technol. Lett.*, vol. 16, no. 11, pp. 2523–2525, Nov. 2004.
- [229] O. Kamatani, S. Kawanishi, "Prescaled timing extraction from 400 Gb/s optical signal using a phase lock loop based on four-wave-mixing in a laser diode amplifier," *IEEE Photon. Technol. Lett.*, vol. 8, no. 8, pp.: 1094-1096, Aug. 1996.
- [230] Hyuek Jae Lee, Hae Geun Kim, Jee Yon Choi, Hak Kyu Lee, "All-optical clock recovery from NRZ data with simple NRZ-to-PRZ converter based on self-phase modulation of semiconductor optical amplifier," *Electron. Lett.*, vol. 35, no. 12, pp. 989–990, Jun. 1999.

- [231] W. Mao, Y. Li, M. Al-Mumin, and G. Li, "All-Optical Clock Recovery for Both RZ and NRZ Data," *IEEE Photon. Technol. Lett.*, vol. 14, no. 6, pp. 873–875, June 2002.
- [232] R. Scott, W. Cong, K. Li, V. Hernandez, B. Kolner, J. Heritage, and S. Yoo, "Demonstration of an error-free 4x10 Gb/s multiuser SPECTS O-CDMA network testbed," *IEEE Photon Technol. Lett.*, vol. 16, no. 9, pp. 2186–2188, Sep. 2004.
- [233] X. Wang, and K. Kitayama, "Analysis of beat noise in coherent and incoherent time-spreading OCDMA," *J. Lightw. Technol.*, vol. 22, no. 10, pp. 2226–2235, Oct. 2004.
- [234] X. Wang, N. Wada, T. Hamanaka, K. Kitayama, A. Nishiki, "10-user, truly-asynchronous OCDMA experiment with 511 chip SSFBG en/decoder and SC-based optical threshold," in *OFC 2005, Anaheim*, Mar. 2005, paper PDP33.
- [235] H. Sotobayashi, W. Chujo, and K. Kitayama, "1.6-b/s/Hz 6.4-Tb/s QPSK-OCDM/WDM (4 OCDM X 40 WDM X 40 Gb/s) transmission experiment using optical hard thresholding," *IEEE Photon. Technol. Lett.*, vol. 14, no. 4, pp. 555–557, April 2002.
- [236] Z. Jiang, D. Seo, S. Yang, D. Leaird, R. Roussev, C. Langrock, M. Fejer, and A. Weiner, "Four-user 10-Gb/s spectrally phase-coded O-CDMA system operating at ~30 fJ/bit," *IEEE Photon. Technol. Lett.*, vol. 17, no. 3, pp. 705–707, March 2005.
- [237] R. Essiambre, G. Raybon, and B. Mikkelsen, "Pseudo-linear transmission of high-speed TDM signals: 40 and 160 Gb/s", in I. Kaminow and T. Li, *Optical Fiber Telecommunications IV B – Systems and Impairments*, Academic Press, 2002, pp. 232.
- [238] R. Hui, M. Vaziri, J. Zhou, and M. O'Sullivan, "Separation of noise from distortion for high-speed optical fiber system link budgeting", *IEEE Photon. Technol. Lett.*, vol. 11, no. 7, pp. 910–912, July 1999.
- [239] Optical transport network physical layer interfaces, Standard ITU-T G.959.1, 2003
- [240] T. G. Silveira, A. Teixeira, A. Ferreira, and P. Monteiro, "Optical Vestigial Sideband Generation using counter propagating pumping in Semiconductor Optical Amplifier", in *CLEO-IQEC 2007, Munich*, June 2007.

# Appendix I

## Publications by the author

### *List of work published in the scope of this thesis*

#### Patents

1. T. Silveira, A. Ferreira, “Amplitude modulator with phase distortion cancellation, and amplitude and phase modulator with amplitude and phase distortion cancellation based on semiconductor optical amplifier technology,” Nokia Siemens Networks, patent pending.
2. T. Silveira, A. Ferreira, R. Ribeiro, A. Teixeira, P. Monteiro, “Optical vestigial sideband signal producing arrangement for transmitting optical signal, has production arrangement producing one of modulation signals, and with differentiating unit and low pass filter”, Nokia Siemens Networks, German patent application number DE102006020166.
3. T. Silveira, P. Monteiro, A. Teixeira, “Optical single sideband modulator”, Nokia Siemens Networks, European patent application number EP1775860.

#### Journals

4. T. Silveira, A. Teixeira, P. Monteiro, G. Tosi Bellefi, “Cross Gain modulation bandwidth Enhancement in SOA by Means of a Detuned Optical Filter”, *Electronics Letters*, vol. 41, n. 13, pp. 53 – 54, June 2005.
5. T. Silveira, A. Teixeira, A. Ferreira, P. Monteiro, “All Optical Vestigial Sideband Generation Using Semiconductor Optical Amplifier”, *Photonics Technology Letters*, vol. 18, n. 21, pp. 2212-2214, 2006.
6. N. Yan, A. Teixeira, T. Silveira; G. Tosi-Belleffi; F. Curti; D. Forin; T. Koonen; P. Monteiro; " Theoretical And Experimental Performance Evaluation Of All-Optical Multi-Wavelength Conversion By Four-Wave Mixing In Fiber At 10/20/40 Gb/S For

- Optical Layer Multicast", *Microwave Optical Tech. Letters*, Vol. 49, no. 5, pp.: 1067-1071, May, 2007.
7. T. G. Silveira; A. Teixeira; G. Tosi Beleffi; D. Forin; P. Monteiro; H. Furukawa; N. Wada; "All-Optical Conversion From RZ to NRZ Using Gain-Clamped SOA", *Photonics Technology Letters*, Vol. 19, no. 6, pp. 357 – 359, March 2007.
  8. T. Silveira, A. Teixeira, N. Kataoka, A. Ferreira, N. Wada, X. Wang, and P. Monteiro, "MZI-SOA-based 2R Regeneration of OCDMA signals with Multi-Access Interference noise", *Microwave Opt. Technol. Lett.*, vol. 50, no. 6, pp. 1521–1523, June 2008.
  9. N. Yan, J. del Val Puente, T. G. Silveira, A. Teixeira, A. Ferreira, E. Tangdiongga, P. Monteiro, and A. Koonen, "Simulation and Experimental Characterization of SOA-MZI-Based Multiwavelength Conversion," *J. Lightwave Technol.*, vol. 27, no.2, pp. 117–127, Jan. 2009.
  10. T. Silveira, A. Ferreira, A. Teixeira, and P. Monteiro, "40-Gb/s Multichannel NRZ to CSRZ Format Conversion Using an SOA," *IEEE Photon. Technol. Lett.*, vol. 20, no. 19, pp. 1597–1599, Oct 2008.
  11. N. Yan, T. Silveira, A. Teixeira, A. Ferreira, E. Tangdiongga, P. Monteiro, and A. M. J. Koonen, "40 Gbit/s wavelength multicast via SOA-MZI and applications," *Electron. Lett.*, vol. 43, no. 23, Nov. 2007.

## International peer-reviewed conferences

12. A. Teixeira, T. Silveira, A. Ferreira, R. Nogueira, P. André. M. Lima, P. Monteiro, J. Rocha, "All optical router based on OCDMA codes and SOA based devices", invited paper, *in proc. ICTON 2005*, Barcelona, pp.: 183-188, July 2005.
13. T. Silveira, A. Teixeira, A. Ferreira, P. Monteiro, P. André, "Influence of SOA Based Devices on Optical Single Sideband Signals", *in proc. ICTON 2005*, Barcelona, pp.: 234-238, July 2005.
14. N. Yan, T. Koonen, I. Tafur Monroy, A. Teixeira, T. Silveira, P. Monteiro G. Tosi Beleffi, D. Forin, "Simultaneous multi-wavelength signal conversion for transparent optical multicast", *in proc. NOC 2005*, London, pp. 155-162, July 2005.
15. Tiago G. Silveira, António L. J. Teixeira, and Paulo N. P. Monteiro. "Filter Optimization for Cross Gain Modulation Bandwidth Enhancement", *in Proc. LEOS 2005*, Sydney, pp.: 67-68, Sydney, October 2005.
16. T. Silveira, A. Teixeira, A. Ferreira, P. Monteiro, "Cross Gain Modulation Bandwidth Enhancement", *2<sup>nd</sup> E-Photon One Summer School*, Cesenatico, August 2005.
17. A. Teixeira, T. Silveira, A. Ferreira, P. André, P. Monteiro, M. Lima, R. Nogueira, J. Rocha, "OCDMA Headers Properties Impact on an All-Optical Packet Router Module", *in proc. CONTEL 2005*, Croatia, Vol.: 2, pp.: 541- 545, June 2005.

18. A. Teixeira, T. Silveira, P. André, R. Nogueira, G. Tosi-Belleffi, P. Monteiro, J. Da Rocha, "All-optical switching with SOA based devices", CAOL 2005, Ukraine, vol.: 1, pp.: 52- 55, vol. 1, September 2005
19. T. Silveira, A. Teixeira, G. Tosi-Belleffi, P. Monteiro; "All – Optical Wavelength conversion and reshape based on a single Gain Clamped SOA", in *proc Conf. on Lasers and Electro-optic - CLEO* , Anaheim , United States, May , 2006 .
20. A. Teixeira, A.T.; G. Tosi-Belleffi; T. Silveira; " RZ to NRZ Format Converter based on a Semiconductor Optical Amplifier with a Saturable Absorber ", *Proc Conf. on Lasers and Electro-optic - CLEO* , Anaheim , United States, May , 2006.
21. T. Silveira, D. Fonseca, A. Ferreira R. Morais M. Madureira, A. Teixeira, P. Monteiro, "40 Gb/s All-Optical Vestigial-Sideband Generation using SOA", in *proc. ECOC 2006*, Cannes, France, vol.3, pp. 305-306.
22. N. Yan, A. Teixeira, T. Silveira, I. Tafur Monroy, P. Monteiro, G. Tosi Belleffi, T. Koonen, "Optical Multicasting Performance Evaluation using Multi-Wavelength Conversion by Four-Wave Mixing in DSF at 10/20/40 Gb/s", in *proc. PS'2006*, Crete, 2006, Greece.
23. Tiago Silveira, Ana Ferreira, Paulo Monteiro, Antonio Teixeira, Rui Ribeiro, "Fully Integrable Optical Single Sideband Transmitter", in *Proc. ICT 2006*, May 2006, Madeira.
24. Tiago G. Silveira, Antonio Teixeira, Nobuyuki Kataoka, Ana Ferreira, Naoya Wada, Xu Wang, Tetsuya Miyazaki, Paulo Monteiro; "Coherent Interference 2R Regeneration of Optical CDMA Based on MZI SOA, in *proc. CLEO 2007*, Baltimore, paper CMZ2.
25. Tiago G. Silveira, Antonio Teixeira, Ana Ferreira, Paulo Monteiro, "Optical Vestigial Sideband Generation using counter propagating pumping in Semiconductor Optical Amplifier", in *proc CLEO europe 2007*, Munich.
26. Tiago Silveira, António Teixeira, Ana Ferreira, Sérgio Stevan Jr, Paulo Monteiro, G. Tosi Belleffi, Davide Forin, "All-Optical Signal Processing using Gain-Clamped Semiconductor Optical Amplifiers", *invited paper in proc ICTON 2007*, Rome
27. N. Yan, T. Silveira, A. Teixeira, A. Ferreira, E. Tangdionga, P. Monteiro, A. Koonen, "40 Gb/s All-Optical Multi-Wavelength Conversion via a Single SOA-MZI for WDM Wavelength Multicast," in *proc OECC 2007*, Japan.
28. P. Teixeira, L. Oliveira, T. Silveira, P. André, R. Nogueira, M. Lima, A. Teixeira, "MZI-SOA based all-optical router implementation with OCDMA header recognition," in *proc. OECC 2007*, Japan.
29. T. Silveira, A. Ferreira, D. Fonseca, A. Teixeira, and P. Monteiro, "40 Gb/s all-optical RZ to NRZ format converter based on SOA and detuned filtering," in *ICTON '09, Azores*, June–July 2009.

30. T. Silveira, A. Ferreira, A. Teixeira, and P. Monteiro, "All-optical conversion to vestigial sideband through self-phase modulation in semiconductor optical amplifier," in *ICTON '09, Azores*, June–July 2009.

## Local conferences

31. Tiago Silveira, Xin Xiangjun, António Teixeira, Paulo Monteiro, Ana Ferreira, Paulo André, "2R regeneration of an OSSB signal, based on a single SOA", in *proc. Conftele2005*, Tomar, Portugal, April 6 – 8, 2005.
32. Tiago G. Silveira, António L. J. Teixeira, and Paulo N. P. Monteiro, "Increase of the Cross Gain Modulation Bandwidth in Semiconductor Optical Amplifiers", in *proc. SEON 2005*, Aveiro, June 2005.
33. Tiago Silveira; António Teixeira; Nobuyuki Kataoka; Ana Ferreira; Naoya Wada; Paulo Monteiro "Experimental characterization of Cross Phase Modulation wavelength conversion", in *proc. CONFTELE 2007*, Peniche, pp.: 585-588.
34. Leandro Oliveira; Tiago Silveira; Paulo André; Rogério Nogueira; Mário Lima, "Mach-Zehnder Based All-Optical Switch Implementation", in *proc. CONFTELE 2007*, Peniche, pp.: 481-484. poster
35. Tiago Silveira, A. Ferreira, L. Costa, A Teixeira, and Paulo Monteiro, "All Optical Conversion from ODSB to OVSF using a Semiconductor Optical Amplifier", in *proc. SEON 2007*, Aveiro, June 2007.

## Other publications

## Journals

36. P. Monteiro, D. Fonseca, A. Ferreira, T. Silveira, N. Garcia, M. Hajduczenia; C. Santiago, J. Pedro, R. Luís, L. Pellegrino; "Optical Communications Research Activities at COM RD1 Siemens S.A", *Fiber and Integrated Optics*, Vol. 24, No. -, pp. 395 - 410, June, 2005.
37. Xin Xiangjun, P. André, A. Teixeira, A. Ferreira, T. Silveira, P. Monteiro, R. F. Rocha, J. L. Pinto; "The improvement of ASK signal quality by employing an effective spectrum equalization method in a combined ASK/FSK modulation scheme", *Chinese Physics Letters*, Vol. 22, No. 8, pp. 1948 - 1950, August, 2005.
38. X Xiangjun, P. André, A.T. Teixeira, A. Ferreira, T. Silveira, P. Monteiro; J. Rocha; J. Pinto; "The Influence Of Pump Wavelength On The Performance Of Wavelength Conversion Of 10-Gb/s Single-Side-Band Optical Signal Based On Four-Wave Mixing

- In Dispersion-Shifted Fiber", *Microwave and Optical Tech. Letters* , Vol. 46 , No. 5 , pp. 493 - 493 , September , 2005 .
39. Xiangjun Xin, P. P. André, A. Teixeira, A. Ferreira, T. Silveira, P. Monteiro, F. da Rocha, J. Pinto, "Detailed numerical analysis of a four-wave mixing in dispersion-shifted fiber based all-optical wavelength converter of 10 Gb/s single sideband optical signal", *Optical Fiber Technology*, vol. 12, no. 3, pp. 288-295, 2006.
  40. Xin Xiangjun, P. S. Andre , A. L. J. Teixeira, Ana Ferreira, Tiago Silveira, P. M. Monteiro, F. da Rocha, J. L. Pinto, Deng Chaogong,"Spectrum Equalization Employing Reshaping Filter To Improve Ask Signal Quality In Combined Fsk/Ask Modulation Scheme", *Microwave Optical Tech. Letters* , Vol. 48, No. 11 , pp. 2208 - 2210, November, 2006.
  41. A. P. S. Ferreira, T. G. Silveira, P. M. N. P. Monteiro, and R. F. G. S. Ribeiro, "On the use of return-to-zero formats in electrical dispersion compensated optical single sideband transmission systems," *IET Optoelectron.*, vol. 2, no. 4, pp. 148–157, Aug. 2008.
  42. A Ferreira, T. Silveira, D. Fonseca, R. Ribeiro, P. Monteiro, "Highly Linear Integrated Optical Transmitter for Subcarrier Multiplexed Systems," *IEEE Photon. Technol. Lett.*, vol. 21, no. 7, pp. 438-440, April 2009.

## International peer-reviewed conferences

43. T. Silveira, A. Ferreira, P. Monteiro, M. Violas, R. Ribeiro, F. Rocha, "Electrical Dispersion Compensation at 10Gb/s Optical Single Sideband Transmission Systems", *in proc. LEOS 2004*, Puerto Rico, November 2004, pp. 759-760.
44. T. Silveira, A. Ferreira, P. Monteiro, M. Violas, R. Ribeiro, J. Rocha, "Robustness analysis of a 10 Gb/s Optical Single Side Band Transmitter", *in proc. SEON 2004*, June 2004.
45. T. Silveira, A. Teixeira, R. Nogueira, P. André, P. Monteiro, A. Ferreira, S. Stevean, J. Rocha, "Optimization of Wavelength Interleaved Radio-over-Fiber Systems"*I<sup>st</sup>E-Photon Summer School*, Mons Setembro de 2004.
46. Tiago Silveira, Ana Ferreira, Paulo Monteiro, António Teixeira, "Electrical dispersion compensation in OSSB systems at 10G/s," *I<sup>st</sup>E-Photon Winter School*, Aveiro, March 2004.
47. P. S. André, A. L. J. Teixeira, P. M. Monteiro, T. Maia, Xin Xiangjun, T. G. Silveira, A. P. S. Ferreira, "All Optical wavelength conversion of 10 Gbps single side band optical signals in DSF fibres", *in proc. NOC 2004*, Eindhoven, June 29 – July 1, pp.: 207-214, 2004.
48. D. Fonseca, A. Cartaxo, P. Monteiro, R. Sousa, T. Silveira, A. Ferreira, M. Violas, "40 Gbit/s OSBS-NRZ transmitter for High Capacity Systems," *in proc. ECOC 2005*, Glasgow, vol. 4, pp.: 787 – 788, 2005.

49. A. Ferreira, T. Silveira, R. Ribeiro, P. Monteiro, M. Violas, "Mitigation of Chromatic Dispersion Effects on OSSB Signals by Butterworth Filtering", in *proc. ICTON 2005*, Barcelona, vol. 2, pp.: 76-79, July 2005.
50. Antonio Teixeira, T. Silveira, S. Stevan Jr, R. Nogueira, Giorgio Tosi Beleffi, Franco Curti, Andrea Reale, Michele Guglielmucci, "Optical Gain Characteristics of Rayleigh Backscattered Lasing in Several Fibre Types", in *proc. NOC 2005*, London, July 2005.
51. A. Teixeira, P. André; S. Junior; T. Silveira; "Raman Amplification based on Multiple Low-Power lasers", in *proc. AICT*, Guadeloupe , Antigua & Barbuda , pp.: 85, February , 2006.
52. S. Stevan Jr., A. Teixeira, T. Silveira, P. André, Giorgio M. Tosi Beleffi, A. Reale and A. Pohl, "Double shifted Raman amplification by means of spontaneous Rayleigh Backscattering lasing control", in *Proc. ICT 2006*, May 2006, Madeira.
53. Ana Ferreira, Tiago Silveira, Rui Ribeiro, Paulo Monteiro, Manuel Violas, "Sinusoidal pulse formatting in Optical Single Sideband transmission systems" in *Proc. ICT 2006*, May 2006, Madeira.
54. R. Nogueira, A. Teixeira, M. Violas, R. Sousa, P. Andre, T. Silveira, R. Okina, S. Sales, "Tuneable Optical Dispersion Compensators for Dynamic Optical Networks", in *proc ICTON 2007*, Rome.
55. Ana Ferreira, Tiago Silveira, Paulo Monteiro, and Rui Ribeiro, "40 Gb/s optical Single Sideband DWDM transmission system using polar return-to-zero signalling format", in *proc ICTON 2007*, Rome.
56. S. Stevan, M. Fugihara, G. Beleffi, P. Andre, T. Silveira, R. Nogueira, A. Teixeira, A. Pohl, "Experimental analysis of an all optical gate based in Gain Clamping Semiconductor Amplifier Chip , in *proc CLEO europe 2007*, Munich.
57. A. Ferreira, T. Silveira, D. Fonseca, P. Monteiro, R. Ribeiro, "Highly linear radio-over-fiber transmitter for subcarrier multiplexed systems", in *proc ECOC 2008*, Brussels, 2008
58. Stevan, S.; Beleffi, G.T.; Andre, P.; Silveira, T.; Teixeira, A.; Reale, A.; Pohl, A.; "Triple C, L and U-band wide amplification system by means of Rayleigh backscattering control", IMOC, Oct. 29 2007-Nov. 1 2007, pp. 680 – 682.
59. A. Ferreira, T. Silveira, D. Fonseca, R. Ribeiro, P. Monteiro, "External modulator linearization techniques for high performance radio over fiber transmission systems," in *ICTON '09, Azores*, June–July 2009.

## Local conferences

60. A. Ferreira, T. Silveira, P. Monteiro, R. F. S. Ribeiro, M. Violas, R. F. Rocha; "Robustness analysis of a 40Gb/s Optical Single Side Band Transmitter with electrical



- dispersion compensation”, *Proc Conf. on Telecommunications - ConfTele*, Tomar, April, 2005.
61. P. André, A. Teixeira, X. Xiangjun, A. Ferreira, T. Silveira, P. Monteiro, R. F. Rocha, J. L. Pinto; “Study of Optical Labeling Transmission Performance in IP-over-WDM Networks Based on Combined FSK/ASK Modulation Format”, *Proc Conf. on Telecommunications - ConfTele*, Tomar, Portugal, April, 2005.
  62. Vitor Silva; Luís Amaral; Paulo Monteiro; Ana Ferreira; Tiago Silveira; Miguel Madureira; Rui Ribeiro; Daniel Fonseca, “Optical Single-Sideband Transmitter for High Capacity Systems”, *in proc. CONFTELE 2007*, Peniche, pp: 109-112. -poster
  63. Ana Ferreira; Tiago Silveira; Rui Ribeiro; Paulo Monteiro; Manuel Violas, “10Gbit/s evaluation of electrical dispersion compensation methods for Optical Single Sideband systems,” *in proc. CONFTELE 2007*, Peniche, pp.: 493-496. poster
  64. Ruben Sousa; Manuel Violas; Ana Ferreira; Tiago Silveira; Paulo Monteiro, “10 Gbit/s Optical Single Sideband Prototype”, *in proc. CONFTELE 2007*, Peniche, pp.: 553-556. poster
  65. M. Drummond, A. Ferreira, T. Silveira, R. Nogueira, D. Fonseca, P. Monteiro, “107 Gb/s optical vestigial sideband system with fiber Bragg grating filtering”, *in proc. SEON 2007*, Aveiro, June 2005.



## Appendix II

### SOA devices used in this work

The most relevant semiconductor optical amplifier (SOA) devices considered in the experimental tests are a bulk device from OptoSpeed (1550MRI/P: R1408 – L932) and a multi-quantum well device from CIP (SOA-NL-OEC-1550 - 1.55 $\mu$ m Non-Linear). The former device is called throughout this work as *slow SOA* and the latter as *fast SOA*. The main characteristics of these devices are summarized in Table II-1.

Parameter	Typical value	
	<i>Slow SOA</i>	<i>Fast SOA</i>
Peak wavelength	1555.0 nm	1550.0 nm
Polarization dependent gain	0.8 dB	0.5 dB
Noise figure (NF)	9.6 dB	8 – 11 dB
Saturation output power (-3dB)	6.1 dBm	7 dBm
Maximum gain	21.3 dB	34 dB
Unsaturated recovery time (10-90%)	380 ps	80 ps

Table II-1: Typical parameters of the two devices used in this work. Slow SOA refers to OptoSpeed (1550MRI/P: R1408 – L932) and Fast SOA to CIP (SOA-NL-OEC-1550 - 1.55 $\mu$ m Non-Linear).

The parameters considered in the simulations are detailed in Table II-2. These parameters are fit to the simulation model described in detail in sections 2.6 and 2.7.

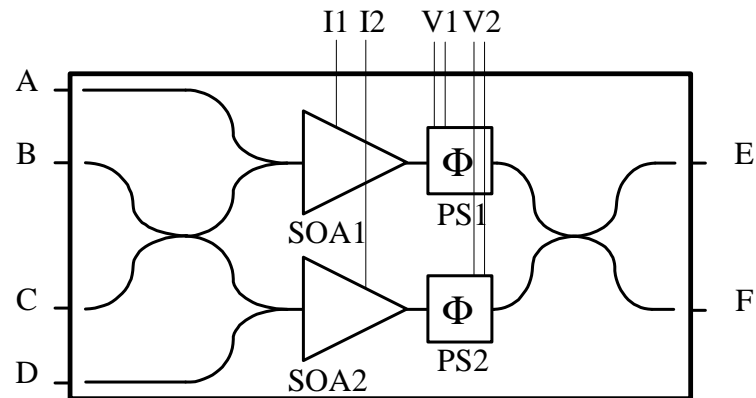
Parameter	<i>Slow SOA</i>	<i>Fast SOA</i>
Number of sections ( $N_S$ )	1	5
Differential gain ( $dg/dN$ )	$2.8 \cdot 10^{-20} \text{ m}^3$	$2.2 \cdot 10^{-20} \text{ m}^3$
Carrier density at transparency ( $N_{tr}$ )	$1.2 \cdot 10^{24} \text{ m}^{-3}$	$1.0 \cdot 10^{24} \text{ m}^{-3}$
Injection Current ( $I$ )	0.25 A	0.30 A
Active layer volume ( $V$ )	$1.1 \cdot 10^{-16} \text{ m}^3$	$2.2 \cdot 10^{-16} \text{ m}^3$
SOA cavity length ( $L$ )	$0.45 \cdot 10^{-3} \text{ m}$	$1.0 \cdot 10^{-3} \text{ m}$
Optical confinement ( $\Gamma$ )	0.15	0.35
Absortion coefficient ( $\alpha_{int}$ )	$2.5 \cdot 10^3 \text{ m}^{-1}$	$4.0 \cdot 10^3 \text{ m}^{-1}$
Rec. rate related to non-radiative processes	$1.8 \cdot 10^8 \text{ s}^{-1}$	$1.0 \cdot 10^8 \text{ s}^{-1}$
Rec. related to spontaneous emission ( $B_{sp}$ )	$1.4 \cdot 10^{-16} \text{ m}^3 \cdot \text{s}^{-1}$	$0.8 \cdot 10^{-16} \text{ m}^3 \cdot \text{s}^{-1}$
Rec. rate related to Auger recombination	$3.2 \cdot 10^{-41} \text{ m}^6 \cdot \text{s}^{-1}$	$1.5 \cdot 10^{-41} \text{ m}^6 \cdot \text{s}^{-1}$
Relaxation time related to CH ( $\tau_{CH}$ )	$5.1 \cdot 10^{-13} \text{ s}$	$5.1 \cdot 10^{-13} \text{ s}$
NL gain compression related to CH ( $\epsilon_{CH}$ )	$1.2 \cdot 10^{-24} \text{ m}^3$	$1.2 \cdot 10^{-24} \text{ m}^3$
NL gain compression related to SHB ( $\epsilon_{SHB}$ )	$4.0 \cdot 10^{-25} \text{ m}^3$	$4.0 \cdot 10^{-25} \text{ m}^3$
Linewidth enhancement factor for CDP ( $\alpha_N$ )	6.0	5.5
Linewidth enhancement factor for CH ( $\alpha_{CH}$ )	0.0	1.2
Linewidth enhancement factor for SHB	0.0	0.0

Table II-2: Simulation parameters of the two devices used in this work. Slow SOA refers to OptoSpeed (1550MRI/P: R1408 – L932) and Fast SOA to CIP (SOA-NL-OEC-1550 - 1.55 $\mu\text{m}$  Non-Linear). Rec.: recombination; CH – carrier heating; SHB: spectral hole burning; CDP: carrier density pulsation.

Apart from the two referred devices, a gain-clamped SOA (GC-SOA) from Alcatel was utilized in the scope of a joint experiment. This device was gently lended by Instituto Superiore delle Comunicazioni e delle Tecnologie dell' Informazione (ISCOM), Rome, Italy. Since this device is no longer commercially available and we had limited access to it, there was very few information available: maximum gain of 15 dB; output saturation power of 10.3 dBm ; and noise figure of 6.8 dB.

The Mach-Zehnder interferometer with SOA (MZI-SOA) included SOA with characteristics similar to the ones of the *Fast SOA*. The utilized MZI-SOA device was operated in a stand alone box at Instituto de Telecomunicações, pictured in Figure II-3, with

electrical circuitry which performs variable current injection, temperature control and phase shift adaptation. Figure II-3 a) presents the SOA schematic, with independent current control for the two SOA, and independent phase shift control in the two output arms. Generally  $V_2$  is set to zero and the phase shift is controlled by  $PS1$  only. Figure II-3 b) presents a photography of the MZI-SOA inside the custom made box.



a) MZI-SOA schematic;



a) Photography of the MZI-SOA inside the stand alone configuration.

Figure II-3: MZI-SOA in a box with electrical stand alone control.



## Appendix III

### Performance assessment in simulations

The simulation tests performed in this work focus mainly in assessing the deterministic distortion induced by semiconductor optical amplifiers (SOA) based schemes. Since SOA induced optical noise is not considered in the utilized model, performance is assessed via the eye opening penalty (EOP).

The EOP does not depend on the signal optical signal to noise ratio (OSNR); therefore, it is fit to account for deterministic signal distortions. Moreover, it has the advantage that low computation effort is required for its calculation. There are numerous definitions of the EOP in the literature [237], [238]. In this thesis the following definition is considered:

$$EOP = -10 \cdot \log \left( \frac{\Delta I_E}{\Delta I_{Ref}} \right), \quad (III-1)$$

Where  $\Delta I_E$  is the height of the highest rectangle, with a width of  $\Delta T$ , that can fit inside the eye diagram of the signal to analyze; and  $\Delta I_{Ref}$  refers to the highest rectangle with similar width that can be fitted inside the eye diagram of a reference signal. In this work  $\Delta T$  is considered 20% of the bit period and the reference signal is an unfiltered NRZ signal with extinction ratio (ER) of 9 dB and 10 dB for 10 Gb/s and 40 Gb/s, respectively, according to the standard data for long-haul systems [239].

Figure III-1 illustrates an eye diagram with the defined rectangle of  $\Delta T = 0.2 T_B$ , with  $T_B$  the bit period. EOP is adequate to account for signal degradation, but also for ER degradation.

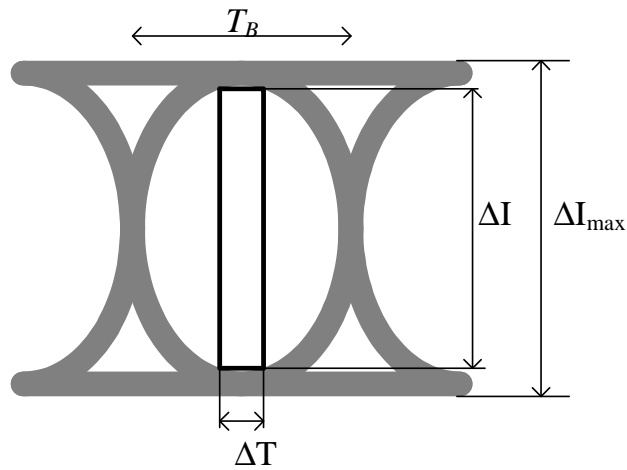


Figure III-1: Illustration of eye opening penalty calculation.

To characterize the opening of a signal eye diagram independently of its ER, a modified version of the EOP, MEOP is also considered in this work:

$$MEOP = -10 \cdot \log \left( \frac{\Delta I_E}{\Delta I_{\max}} \right), \quad (\text{III-2})$$

With  $\Delta I_{\max}$  the difference between the maximum and minimum levels of the signal under analysis. This figure of merit is appropriate to characterize reshaping systems which do not alter the signal ER, but enhance its opening.



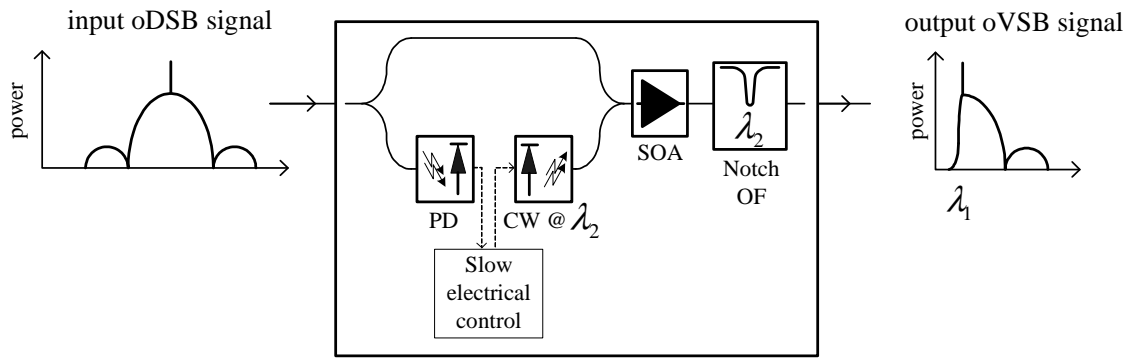
## Appendix IV

# Optimization and development of a prototype to convert optical DSB to VSB

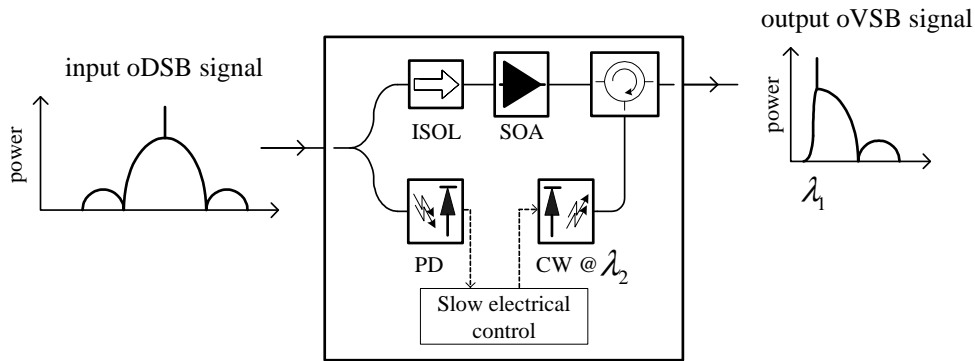
In Chapter 4 we have proposed a novel format converter from optical double sideband (oDSB) to vestigial sideband (oVSB). The converter operation is based on self-phase modulation (SPM) non-linearity in a semiconductor optical amplifier (SOA). SPM induces a frequency chirp which has similarities with that of a vestigial sideband signal. Due the promising results obtained by the converter, such as: high tolerance to input power variations, extinction ratio, or wavelength, and the low cost potential of SOA devices, Siemens Networks filed a patent for the proposed converter [173] and requested that stand-alone prototypes were developed for 10 Gb/s and 40 Gb/s.

Figure IV-1 presents two stand-alone configurations for the proposed converter. Figure IV-1 a) presents a co-propagating scheme; the input signal is split in two replicas by a 90/10 coupler. The lower power replica is detected in a slow photo-detector – the bandwidth of this photo-detector can be as low a few MHz. The current at the photo-detector output is measured by slow electrical processing, which then adapts the current that controls an optical laser source. The continuous wave (CW) signal is coupled (in a 50/50 coupler) to the higher power replica of the input signal and fed to the SOA. At the SOA output a notch optical filter removes the CW signal wavelength. This scheme has the advantage of using low cost optical components; however, the input signal passes by a splitter and coupler, suffering high losses; moreover, an optical filter is required to remove

the CW signal wavelength. Figure IV-1 b) represents a counter-propagating scheme, where the CW signal is back-fed to the SOA, through a circulator. Since the CW signal counter-propagates in the SOA, an isolator is required at the input. This scheme does not require optical filtering at the output, has lower insertion losses than the co-propagating scheme, and has potential for lower costs since a coarse laser can be used and the CW signal suffers less attenuation before being fed to the SOA, enabling the use of a lower power laser (higher power lasers are usually more expensive).



a) Co-propagating scheme;



b) Counter-propagating scheme.

Figure IV-1: Stand-alone configurations to convert optical DSB to VSB.

## 10 Gb/s prototype

For the 10 Gb/s prototype the counter-propagating scheme was employed due to its potential for low costs and simplicity. In this section we first characterize the optical equipment required to build the 10 Gb/s prototype; afterwards, the prototype is experimentally characterized.

## Equipment characterization and optimization

### Laser characterization

A low price coarse laser was employed as probe signal. The optical spectrum of the laser is depicted in Figure IV-2. The laser spectrum is very broad (it is a Fabry Perot laser); however, since it travels in counter propagation with the signal, this should not be an impairment to the operation of the setup. The spectral bandwidth at -20 dB of the peak spectral power is around 6.5 nm.

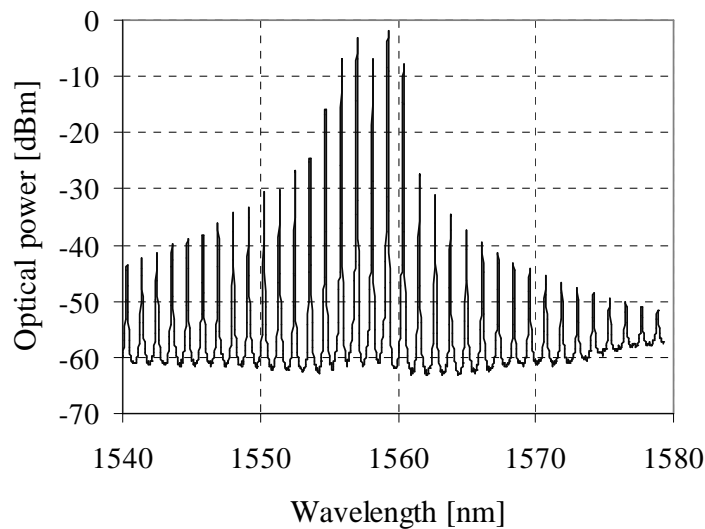


Figure IV-2: Coarse laser optical spectrum (driving current of 34 mA).

As concluded in Chapter 4, a wide range of power for the input signal is allowed, provided that the CW probe power is adapted accordingly. The CW power at the SOA input can be adapted either by using an external variable optical attenuator (VOA) or by varying the laser driving current. To enable lower costs, the second alternative was adopted. In Figure IV-3 a) the optical power at the laser output is plotted as a function of the electrical current, from where we verify that the laser power can vary from 2.9 to -9.0 dBm. In Figure IV-3 b) linear units are used, and a linear approximation is presented. The linear approximation, which presents an excellent fit to the measured power, was used for the peripheral interface controller (PIC), which performed the “slow electrical control” block.

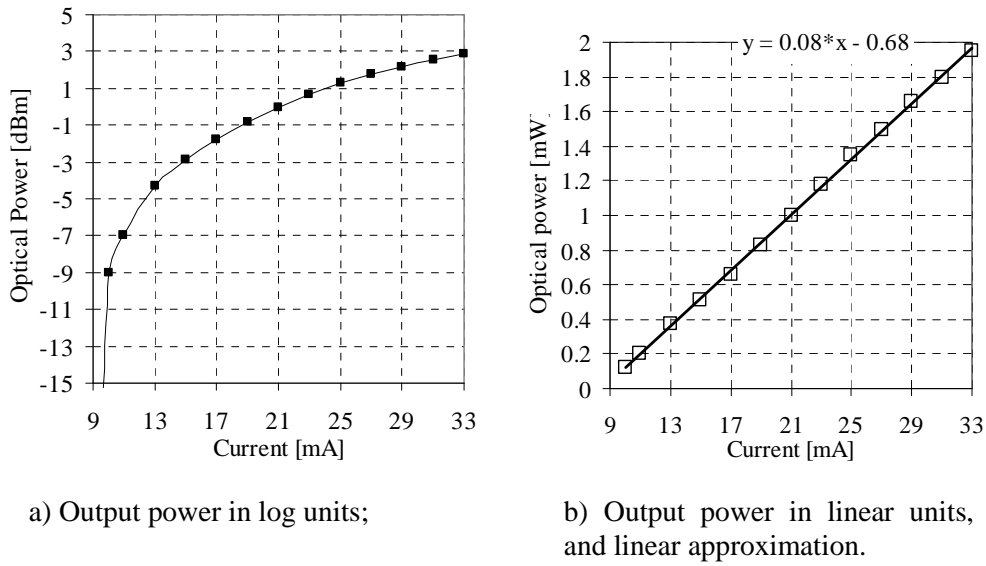


Figure IV-3: Optical power at the output of the coarse as a function of the driving current.

#### Photo-detector characterization

The input signal power measurement was done by splitting the input signal in a 80/20 splitter, with the lower power copy feeding a slow photo-detector. The photo-detector was assembled in a setup similar to Figure IV-4.  $V_{out}$  was measured by an ADC (analog to digital converter).

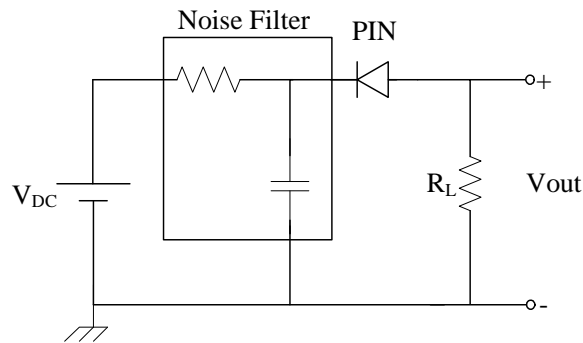
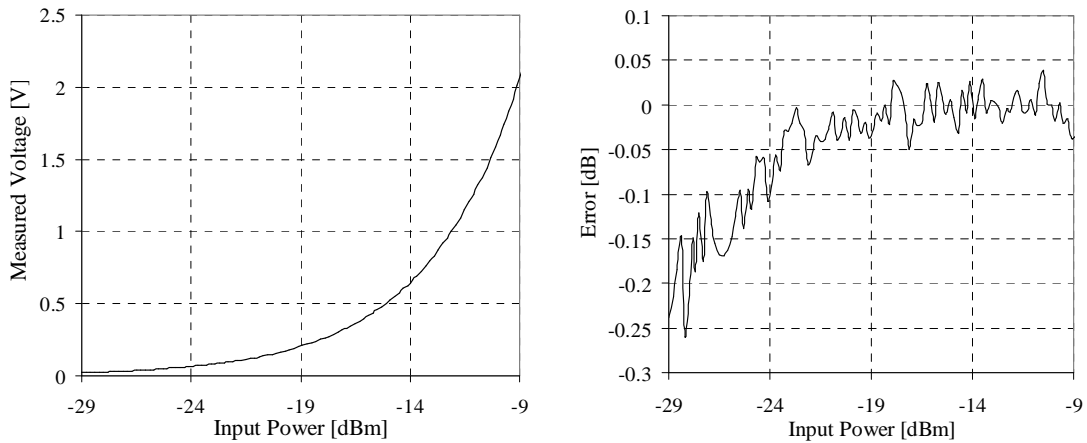


Figure IV-4: Setup for measuring the input power using a slow photo-detector.

There are two critical parameters for the operation of the photodiode setup: the values of  $V_{DC}$  and  $R_L$ .  $V_{DC}$  should be as high as possible to allow a big sensitivity to the input power; however increasing  $V_{DC}$  above a threshold value will provoke an increase in the dark current. The value of  $V_{DC}$  was optimized as 2.9 V, which was the maximum possible value at which the dark current was negligible.  $R_L$  is also a compromise, since a

high value of  $R_L$  allows a high range of input powers; however the system becomes more sensible to the electrical noise.  $R_L$  was chosen to be  $18\text{ k}\Omega$  to allow a maximum power of about  $-10\text{ dBm}$ .

In Figure IV-5 a) the voltage measured at  $R_L$  is presented. Figure IV-5 b) presents the error between the optical power at the photo-detector input and the optical power expected from the measured Voltage:  $P = V_{out} / R_L / \mathfrak{R}$ , with  $\mathfrak{R} = \text{Responsivity} = 0.9$ . A range of input power from  $-9\text{ dBm}$  to  $-22\text{ dBm}$  is allowed with an error smaller than  $\pm 0.05\text{ dB}$ .



a) Voltage measured at  $R_L$ ;

b) Error between optical power at photo detector input and expected power.

Figure IV-5: Photodiode output voltage and power error as a function of the input optical power.

#### CW power optimization

After characterizing the laser and photodiode, it is necessary to find the relation between the optical power measured at the photo-detector and the optimum power of the CW signal when using the counter-propagation scheme. The optimum CW laser power was obtained as the value which allows the optimum relation between SSR and  $Q$ -factor at the converter output. In Figure IV-6 the measured optimum laser power is plotted as a function of the input power. The continuous line in the figure depicts the estimated laser power value for each power at the photo-detector input. It was obtained as:

$$P_{laser} = I_{laser} \cdot 0.08 - 0.68. \quad (IV-1)$$

This relation was obtained from Figure IV-3 b). The relation between the laser current and the measured voltage at  $R_L$  was optimized to be:

$$I_{laser} = -V_{out}^2 \cdot 17.0 + V_{out} \cdot 47.3 + 4.1, \quad (IV-2)$$

With  $V_{out}$  obtained from:

$$V_{out} = \frac{(P_{in} \cdot \Re)}{R_L}. \quad (IV-3)$$

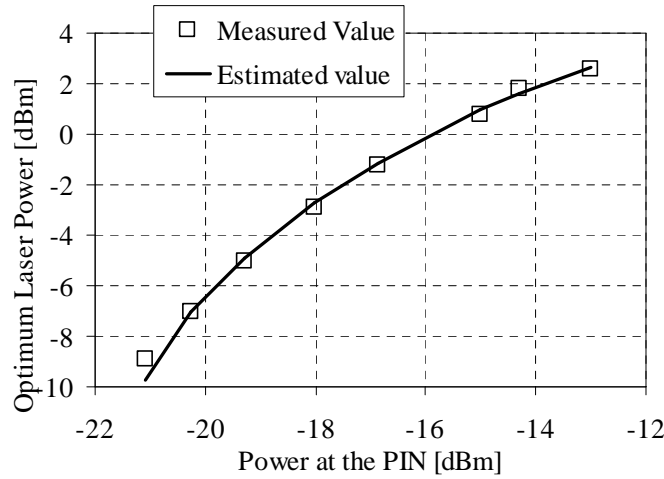


Figure IV-6: Optimum laser power as a function of the power at the photodiode.

## Final prototype and results

### Back-to-back results

The 10 Gb/s experimental prototype setup is similar to that represented in Figure IV-2 b). Figure IV-7 presents the photography of the setup, including the configuration where the PIC was assembled together with the local CW laser and photo-detector to measure the input power. The prototype results have been presented in [240] and [201].

In Figure IV-8 the SSR and  $Q$ -factor of the output converted signal are plotted as a function of the input signal power, measured at the input of the 90/10 coupler. The local CW laser power was optimized by the PIC, based on the results of previous section; therefore a stand alone adaptive system is implemented. The input signal ER was 6 dB and had a  $Q$ -factor = 6.5, the signal wavelength was 1547.51 nm. The converted signal  $Q$ -factor is always above input for input powers below 3.4 dBm. The SSR of the converted signal is above 12 dB for input powers above -6.6 dBm; and is above 13 dB for input powers above -4.6 dBm. This represents an allowed 9 dB input power variation for SSR above 13 dB and  $Q$ -factor above input; which is a considerable increase to the 3 dB obtained in section 4.2.3.1 for the case where the pump power was constant.

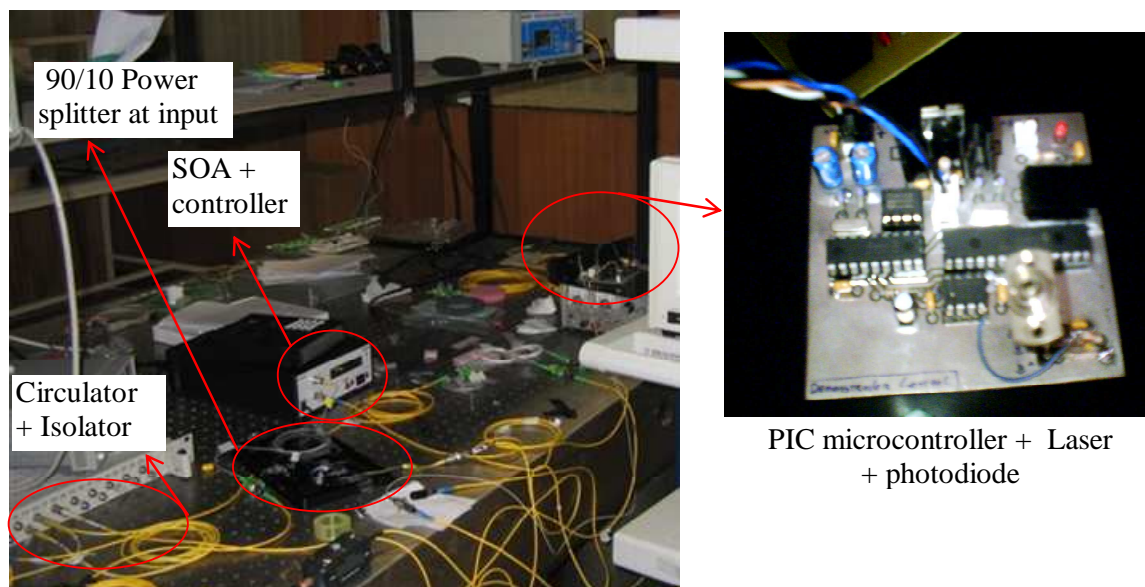


Figure IV-7: Photography of experimental 10 Gb/s prototype.

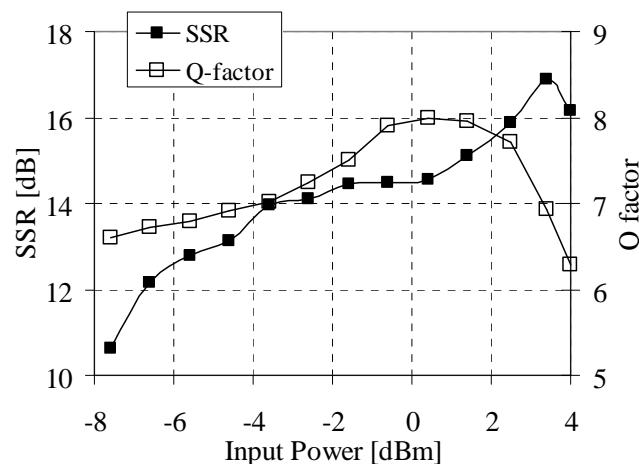


Figure IV-8: SSR and  $Q$ -factor as a function of the input signal power.

The converter output power is plotted in Figure IV-9 as a function of the input power, measured at the 90/10 splitter input. For the 9 dB input power range where SSR is above 13 dB and the  $Q$ -factor is better than the  $Q$ -factor at the converter input, the power varied less than 0.7 dB. The converter then acts also as a amplifier / attenuator with constant output power.

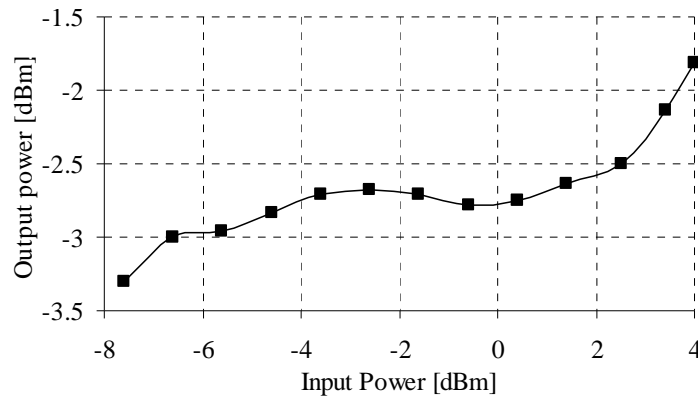
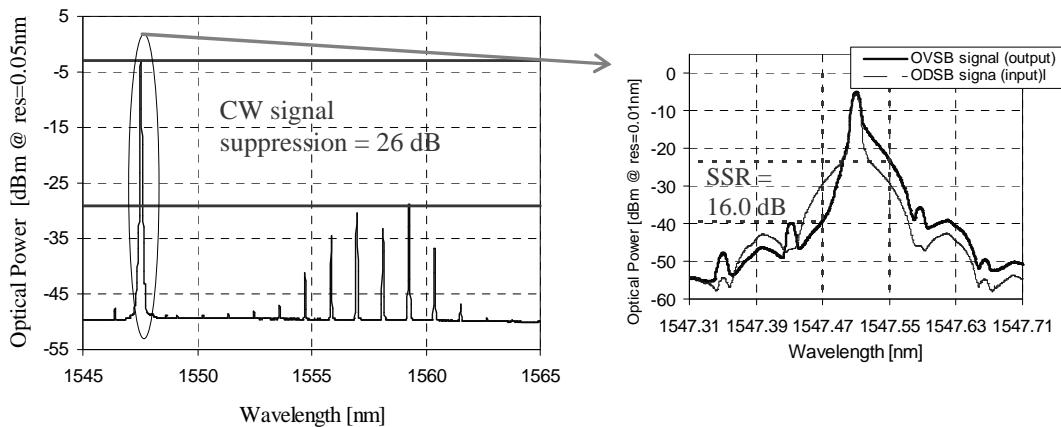
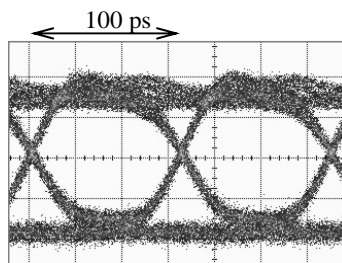


Figure IV-9: Power of the output signal as a function of the input signal power.



a) Optical spectrum (inset: zoom in the interest area, with input signal as reference);



b) Eye diagram.

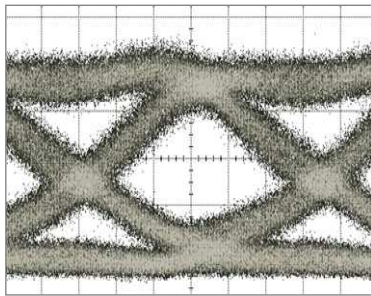
Figure IV-10: Converted signal characterization for input power of 2.5 dBm.



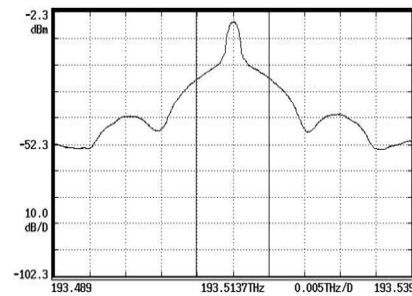
In Figure IV-10 the optical spectrum at the converter output is depicted for an input power of 2.5 dBm. The output optical spectrum reveals a residue of the coarse laser; this is mostly due to reflections in the fiber splicing and due to a finite isolation of the optical circulator, however the data signal carrier is 26 dB superior to the highest power spectral component of the residual laser. The converted presents an open eye diagram with reduced distortion due to SGM non-linearity.

#### VSB signal generation after transmission over fiber

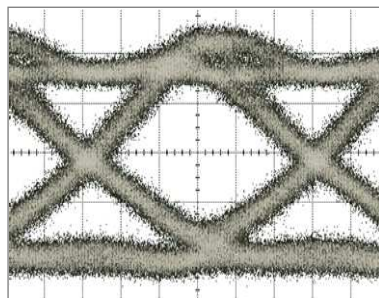
In Chapter 4 we have demonstrated that the VSB signal obtained after conversion with the proposed method presents enhanced dispersion tolerance when compared to common DSB signals. Moreover, it also allows simple and effective EDC after direct detection. However, in all presented tests format conversion has been performed over undistorted oDSB signals. In a meshed network the DSB signal can travel through several kilometers before being converted to VSB.



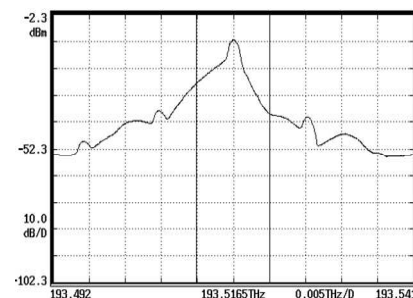
a) Input oDSB signal eye diagram ( $Q$ -factor = 6.15);



b) Input oDSB signal spectrum;



c) Converted oVSB signal eye diagram ( $Q$ -factor = 6.4);



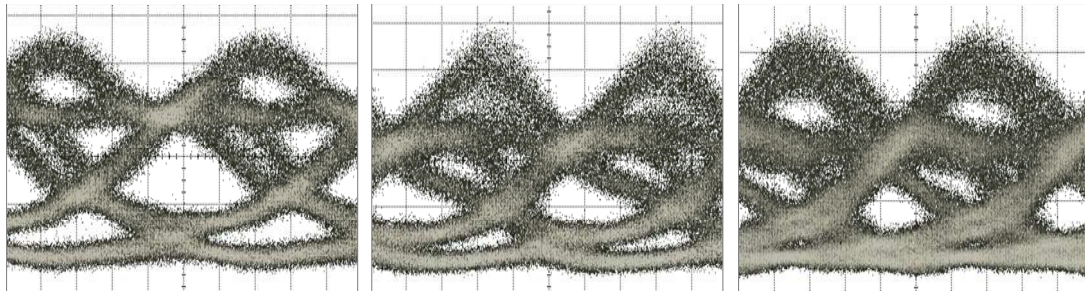
d) Converted oVSB signal Spectrum (SSR = 11.4 dB).

Figure IV-11: Eye diagrams and optical spectrum of an oDSB signal after 40 km of fibre and of the oVSB signal obtained after conversion.

To test the impact of an input DSB signal with dispersion induced degradation in converted signal eye diagram and SSR, an oDSB signal was transmitted over 40 km of SSMF and then converted with the proposed setup.

Figure IV-11 a) and b) presents the eye diagram and spectrum of the experimental oDSB signal after 40 km of SSM fiber (680 ps/nm of dispersion). The reference oDSB signal was obtained similarly to that of section 4.2.3.1. Figure IV-11 c) and d) characterize the converted oVSB signal. The SSR achieved with this scheme was 4.2 dB smaller compared to the case when the conversion is performed over an undistorted signal. This penalty is due to the transitions of the oDSB signal being less sharp (due to the accumulated dispersion).

The oVSB signal converted in the current scenario - the input oDSB signal has already been transmitted over 40 km – should still present enhanced dispersion tolerance. Figure IV-12 presents the eye diagrams of the oVSB signal after it has been transmitted over more 40, 80 and 120 km – total transmission lengths of 80, 120 and 160 km, respectively. The obtained eye diagrams are still open, even for 160 km of total transmission length. These results demonstrate the resilience of the converter to dispersion induced degradation of the input signal.



a) Total length = 80 km;

b) Total length = 120 km;

c) Total length = 160 km.

Figure IV-12: Eye diagrams of the oVSB signal when it is transmitted over 40 km, 80 km and 120 km of fiber. The VSB generation is performed after the oDSB signal has already been transmitted over 40 km of fiber.

## 40 Gb/s prototype

Due to the promising results of the counter-propagating scheme for 10 Gb/s, it was tested also for 40 Gb/s. The SSR results are similar in the co- and counter-propagating modes. Figure IV-13 compares the eye diagram of the converted signal in co- and counter-propagating modes. In the counter-propagating mode, the signal presents increased distortion and jitter when compared to the co-propagating mode: the jitter of the converted signal in co-propagating mode is 5.2 ps and in the counter-propagating mode is 8.0 ps. The penalties in the counter-propagating mode eye diagram are due to counter propagating interaction between the data and CW signals, since the SOA cavity length is around 0.5 mm, which corresponds to approximately one fifth of the bit period.

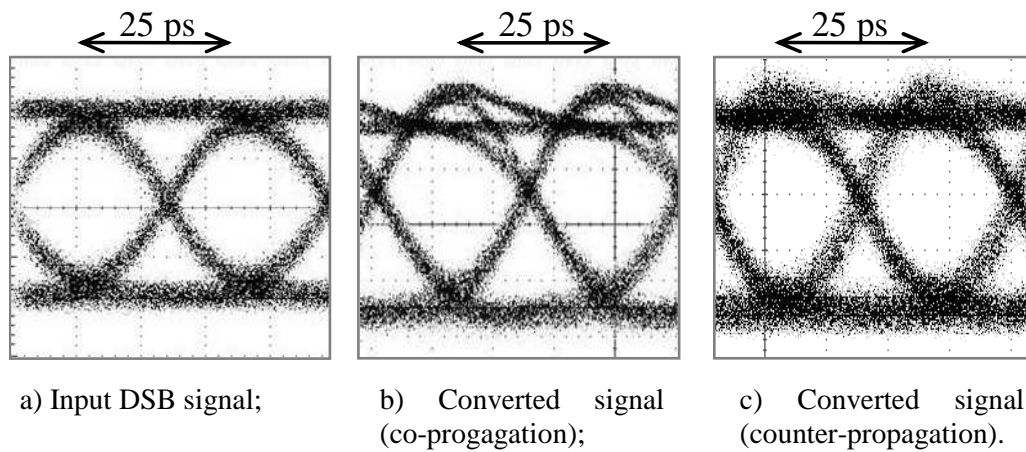


Figure IV-13: Input and converted signals eye diagrams.

Due to the signal distortion caused by counter-propagation, the co-propagating scheme was chosen for the 40 Gb/s prototype. As a consequence, a CW laser with central wavelength around 1530.0 nm was employed. However, lower wavelengths are farther from the SOA gain peak (1560.0 nm); as a consequence higher probe powers are required. The required CW probe power as a function of data signal input power is plotted in Figure IV-14 for CW wavelength of 1530.0 nm and 1540.0 nm. It can be observed that using a laser at 1530.0 nm with maximum power of around 5 dBm lowers the maximum allowed input to -3 dBm. It should be noted that the CW signal maximum output power is a key issue, since low cost lasers are usually limited to few dBm of maximum output power.

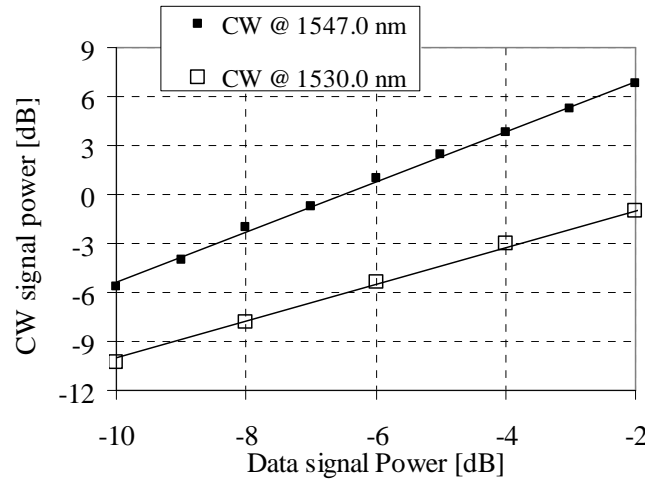


Figure IV-14: Optimum laser power as a function of the data signal at the SOA input, when laser wavelength is 1530.0 nm and 1547.0 nm.

The detailed equipment characterization will not be repeated here for 40 Gb/s, since the basic design rules of 10 Gb/s can be applied. The 40 Gb/s prototype was assembled in a stand alone setup, appropriated for transportation, as presented in the photos of Figure IV-15 and Figure IV-16.

The prototype includes the current source and temperature control for the SOA as well as the PIC controller for the CW probe current optimization and the passive optical equipment (splitters at the SOA input). Since the pump is co-propagated, an optical filter is required at the prototype output to remove its wavelength. The prototype allows for operation with and without local laser, so that the SOA device can also be used for other purposes.



Figure IV-15: Photography of 40 Gb/s prototype external view.

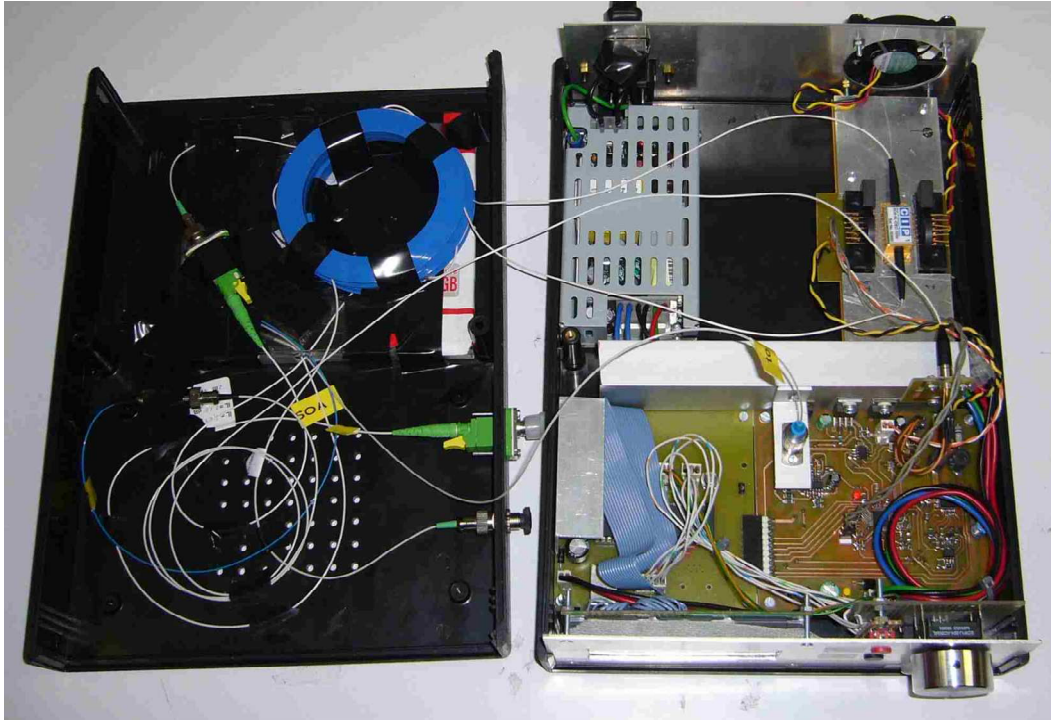


Figure IV-16: Photography of 40 Gb/s prototype internal view.

Figure IV-17 presents the converted signal spectrum and eye diagram when the input power is -1.8 dBm and wavelength is 1551.55 nm. A SSR around 14 dB is retrieved and the converted signal presents patterning, but is still open.

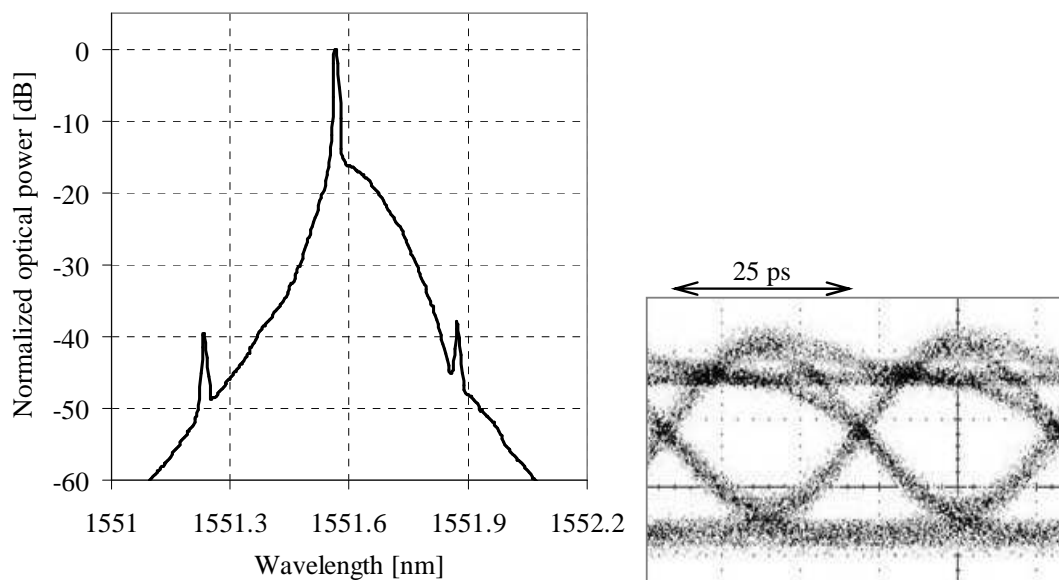


Figure IV-17: converted signal spectrum and eye diagram when input power is -1.8 dBm.



For the characterization of the prototype a pre-amplified receiver composed by an EDFA, an optical filter with -3 dB bandwidth of 90 GHz, and a photo-detector with -3 dB bandwidth of 37 GHz was considered.

In Figure IV-18 the power of the output signal and of the CW signal are depicted as a function of the input power. For input powers below 3 dBm the CW signal power varies proportionally to the input power (since the control system reads the input power and adapts the CW driving current) and the output power is kept constant with a variation below 0.5 dB. For input powers higher than 3 dBm the maximum output power of the CW is reached and the output power increases proportionally to the input power.

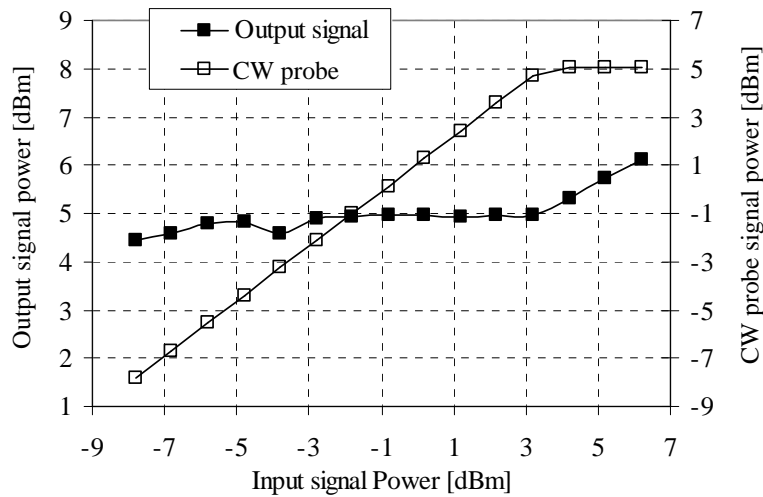


Figure IV-18: Output and CW signals power as a function of the input power.

In Figure IV-19 the output signal BER and SSR are plotted as a function of the input signal power measured at the input of the 90/10 splitter at input. The power at the pre-amplified receiver was maintained at -18.5 dBm, which corresponds to a BER of  $10^{-9}$  for the input oDSB signal; the input signal wavelength was 1551.72 nm and the ER was 8 dB. The converter presents a BER penalty (already verified in section 4.2.3.2) due to a decrease in the converted signal ER, caused by the gain compression in the signal logical '1' level. The prototype presents a high input power range: the input signal power can vary from -5 to 6 dBm (11 dB of variation) maintaining the SSR above 13.0 dB and the BER below  $10^{-5}$ .

Finally, the data signal wavelength dependence is verified in Figure IV-20, where all the control system was kept unchanged, and the input power was constant at -4 dBm.

The SSR is above 13 dB for data wavelengths between 1551 nm and 1563 nm. This range could be extended if the calibration curve of the CW driving signal was optimized for each wavelength.

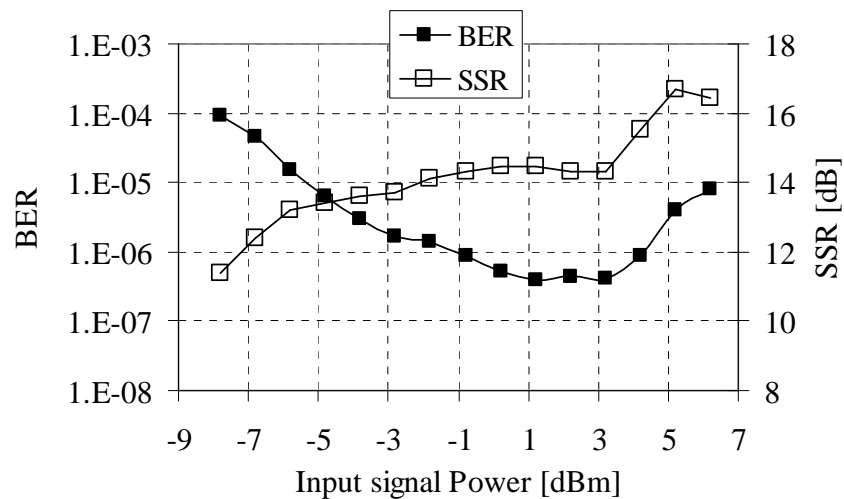


Figure IV-19: BER and SSR as a function of the input signal power.

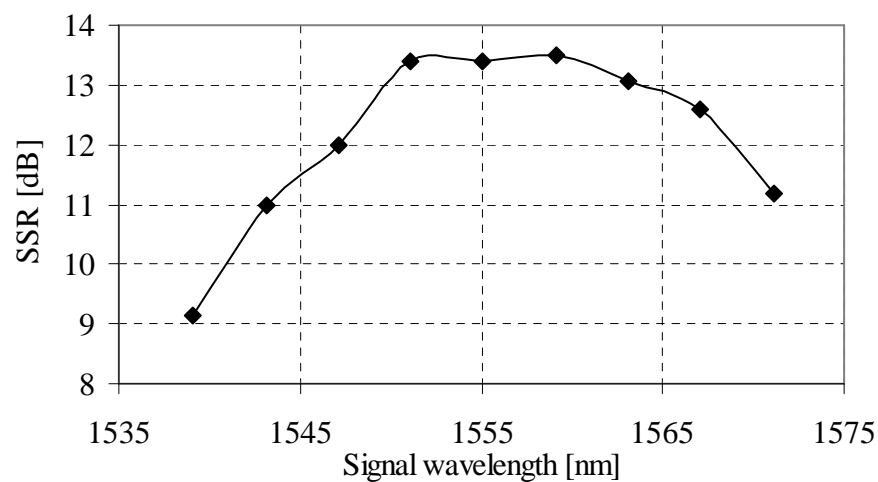


Figure IV-20: SSR variation with the signal wavelength.